

BRNO UNIVERSITY OF TECHNOLOGY

Faculty of Mechanical  
Engineering

HABILITATION THESIS

Brno, 2021

Ing. JAN BOHACEK, Ph.D.





**BRNO UNIVERSITY OF TECHNOLOGY**

VYSOKÉ UČENÍ TECHNICKÉ V BRNĚ

**FACULTY OF MECHANICAL ENGINEERING**

FAKULTA STROJNÍHO INŽENÝRSTVÍ

**HEAT TRANSFER AND FLUID FLOW LABORATORY**

LABORATOŘ PŘENOSU TEPLA A PROUDĚNÍ

**SIMULATION AND MODELING OF HORIZONTAL  
CENTRIFUGAL CASTING**

SIMULACE A MODELOVÁNÍ ODTŘEDIVÉHO LITÍ OCELI

in **APPLIED MECHANICS**

v **APLIKOVANÉ MECHANICE**

**HABILITATION THESIS**

HABILITAČNÍ PRÁCE

**AUTHOR**

AUTOR PRÁCE

Ing. Jan Bohacek, Ph.D.

BRNO 2021



## ABSTRACT

Numerical modeling of horizontal centrifugal casting of rolls forms a central topic of this work. It is a collection of author's efforts to simulate the whole casting process starting with pouring the liquid steel into a rotating cylindrical mould and finishing when all the liquid becomes solid. The modeling part is preceded by a theoretical part giving a background in rotating flows. A list of common issues encountered during the casting process is provided, such as violent vibrations, unexplained microstructural variations and flow related phenomena. In order to get a more general picture about the process, the perspective of a research group from the foundry is supplied. In the second part, several numerical models were presented in the order they were developed. The shallow water model, also known as a 2.5D model, was suggested to accelerate calculations while maintaining important features of the casting. Applying it through the Euler-Euler model in ANSYS FLUENT was substituted by a more efficient and much faster approximate Riemann solver. As an alternative, on request of the industry partner, a 2D free-surface model based on full Navier-Stokes equations was assembled and incorporated within the Graphical User Interface. The thesis is a compilation of the author's articles on the topic of horizontal centrifugal casting. It is possible to redevelop the numerical models as well as to reproduce most of the numerical results thereof.

## KEYWORDS

horizontal centrifugal casting; metallurgy; simulation; computational fluid dynamics; free-surface flow; shallow water equations.

## ABSTRAKT

Numerické modelování horizontálního odstředivého lití válců pro válcovací stolice představuje ústřední téma habilitační práce. Jedná se o sbírku autorova úsilí simulovat celý proces od prvního kontaktu taveniny s formou po ukončenou fázi tuhnutí. Výpočtovou část předchází část teoretická, v níž je na obecné úrovni popsáno proudění s vlivem rotace. Dále se zde mluví o problémech, které se běžně při odstředivém lití oceli vyskytují, např. náhlé vibrace, lokální změny v mikrostruktuře odlévaného materiálu nebo další jevy související s prouděním. Teoretická část končí kapitolou věnující se dané tematice z pohledu průmyslového partnera. V druhé části práce je představeno několik výpočtových modelů v pořadí, v jakém byly vyvinuty. Model založený na rovnicích mělké vody, též známý jako 2,5D model, byl navrhnout za účelem snížení výpočtového času oproti běžným komerčním softwarům. Řešení rovnic mělké vody bylo zprvu realizováno důmyslně s pomocí Euler-Euler modelu uvnitř ANSYS FLUENTu, avšak později bylo vystřídáno efektivnějším a přesnějším Riemannovým řešičem. Jako alternativa k němu byl na podnět průmyslového partnera dovyvinut 2D model proudění s volnou hladinou založený na Navier-Stokesových rovnicích, který byl později zahrnut do uživatelsky přívětivého grafického rozhraní. Práce je kompilací autorových odborných článků na dané téma. Na jejich základě je možné výpočtové modely a některé z výsledků zopakovat.

## KLÍČOVÁ SLOVA

horizontální odstředivé lití; metalurgie; simulace; výpočtové modelování proudění; proudění s volnou hladinou; rovnice mělké vody.

BOHACEK, Jan. *Simulation and modeling of horizontal centrifugal casting*. Brno, 2021, 131 p. Habilitation thesis. Brno University of Technology, Faculty of Mechanical Engineering, Heat Transfer and Fluid Flow Laboratory.

## DECLARATION

I declare that I have written the Habilitation Thesis titled "Simulation and modeling of horizontal centrifugal casting" independently, using exclusively the technical references and other sources of information cited in the thesis and listed in the comprehensive bibliography at the end of the thesis.

As the author I furthermore declare that, with respect to the creation of this Habilitation Thesis, I have not infringed any copyright or violated anyone's personal and/or ownership rights. In this context, I am fully aware of the consequences of breaking Regulation § 11 of the Copyright Act No. 121/2000 Coll. of the Czech Republic, as amended, and of any breach of rights related to intellectual property or introduced within amendments to relevant Acts such as the Intellectual Property Act or the Criminal Code, Act No. 40/2009 Coll., Section 2, Head VI, Part 4.

Brno .....

.....

author's signature



## ACKNOWLEDGEMENT

I wish to express my sincere gratitude to my professor, Prof. Miroslav Raudensky, for his tireless and friendly encouragement.

I am forever thankful that Prof. Jaroslav Horsky let me return to the Heat Transfer and Fluid Flow Laboratory in Brno. I wish he could know that.

I also very appreciate a long term support of Assoc. Prof. Pavel Rudolf.

I would like to thank Prof. Andreas Ludwig for giving me a chance to work for nine beautiful years in his group. I really enjoyed doing research at the Chair of Simulation and Modeling of Metallurgical Processes (SMMP), Leoben, Austria. It was a great honour to work under supervision of Assoc. Prof. Abdellah Kharicha. I want to gratefully acknowledge his scientific help and support. I also want to thank Assoc. Prof. Menghuai Wu for making working days a little informal, for creating a friendly environment for all of us.

I especially thank my colleagues in SMMP, Dr. Ebrahim Karimi-Sibaki and Dr. Alexander Vakhrushev for becoming so fantaaastic friends that no words can describe.

I extend my gratitude to all present and former members of SMMP. It was a great pleasure working with them.

Special thanks go to people from Materials Center Leoben and Eisenwerk Sulzau-Werfen (ESW), Tenneck, Austria for supporting funding my projects. Extra thanks to Sir Thomas (Tommy Nylén), Dipl.-Ing. Thomas Trickl, Dr. Armin Paar, and Dipl.-Ing. Leonel Elizondo for having wonderful project meetings together.

Respectful thanks to all my friends.

And last, but foremost, many thanks go to my outstanding family in Mladkov, the Czech Republic who who always supported me and believed in me.



# Contents

<b>Introduction</b>	<b>13</b>
<b>1 A review on the centrifugal casting</b>	<b>15</b>
1.1 Rotating flows . . . . .	15
1.1.1 Equations of motion of non-isothermal rotating flow . . . . .	15
1.1.2 Typical configurations with rotating flows . . . . .	17
1.1.3 Horizontal vs. vertical cylinder . . . . .	20
1.1.4 Inertial waves . . . . .	21
1.2 Horizontal centrifugal casting . . . . .	22
1.2.1 The view point of R&D in the plant . . . . .	26
<b>2 Numerical modeling of centrifugal casting</b>	<b>29</b>
2.1 Shallow water equations - Euler-Euler multiphase approach . . . . .	31
2.2 Shallow water equations - approximate Riemann solver . . . . .	54
2.3 (Non-)hydrostatic free-surface model to model . . . . .	83
2.4 Air gap modeling . . . . .	103
2.5 Software for industry . . . . .	118
<b>Conclusions</b>	<b>121</b>
<b>Bibliography</b>	<b>123</b>
<b>Author's publications on centrifugal casting</b>	<b>125</b>
<b>Authored and co-authored publications on other topics</b>	<b>127</b>
<b>List of symbols, quantities and abbreviations</b>	<b>131</b>



# List of Figures

1.1	Taylor-Couette flow between two cylinders. . . . .	17
1.2	Demonstration of negligible effect of inertia and dominance of viscous effect in a Taylor-Couette experiment [6]. . . . .	18
1.3	A schematic picture of Taylor vortex flow and photos from experiment [7]. . . . .	19
1.4	The Ekman spiral. . . . .	19
1.5	A schematic picture of azimuthal flow in a horizontally rotating cylinder	21
1.6	Inertial waves in a partially filled horizontal cylinder, reprinted from [12] . . . . .	22
1.7	A shark-teeth pattern in the liquid pool formed at the bottom of a plexi-glass cylinder rotating at low <i>angular velocity</i> ( $\vec{\Omega}$ ), the photo taken by BOHACEK J. at SMMP, MUL, Leoben. . . . .	23
1.8	Difference between vertical (left) and horizontal (right) centrifugal casting of a transparent alloy; the courtesy of prof.Esaka [14]. . . . .	24
1.9	Vibrations of a support roll holding a chill for horizontal centrifugal casting of the outer shell of a work roll; the measurement conducted in Eisenwerk Sulzau-Werfen in Tenneck, Austria. . . . .	25
1.10	The banding phenomenon, a multi-layered structure, clearly visible on a metallographic sample (the courtesy of Eisenwerk Sulzau-Werfen). . . . .	25
1.11	Another possible explanation of banding phenomena in HSC products. . . . .	26
1.12	An undesired occurrence of a long columnar MC crystal (the courtesy of Eisenwerk Sulzau-Werfen). . . . .	27
2.1	A schematic picture of azimuthal flow in a horizontally rotating cylinder	29
2.2	Taylor-Couette flow between two cylinders. . . . .	30
2.3	An accuracy test of two solvers: A collapse of a liquid bump over a solid paraboloid at a specific time. . . . .	55
2.4	A chronological chart of HSC solver developments . . . . .	83
2.5	The GUI's main panel. . . . .	118
2.6	Step 1: solver options . . . . .	118
2.7	Step 2: setting up the dimensions and the mesh. . . . .	119
2.8	Step 3: reading material from database (or creating a new material). . . . .	119
2.9	Step 4: imposing initial and boundary conditions. . . . .	120
2.10	Step 5: Run simulation and save data in <i>vtk</i> format. . . . .	120



# Introduction

The author of the present work started his scientific path in the field of the Computational Fluid Dynamics (CFD) with modeling of an ejector-type cooling nozzle back in 2005. In 2006, he joined as a PhD candidate the Heat Transfer and Fluid Flow Laboratory at BUT BRNO where he further extended his background in CFD, particularly in modeling of immiscible multiphase flows and heat&mass transfer phenomena. He defended his doctoral thesis entitled "Effect of flow parameters of water and air atomized sprays on cooling intensity of hot surfaces" after he got a postdoctoral position at the Chair of Simulation and Modeling of Metallurgical Processes at Montanuniversitaet Leoben, Austria in 2011. Therein, he spent several years in modeling of horizontal centrifugal casting, followed by developing linear solvers for graphical processing units (GPU) and helping his colleague with a project on the electro-slag remelting. In 2017, the author returned back at Brno University of Technology BRNO, where he is involved in several CFD projects about, e.g. thermal management systems of battery modules for electric vehicles, calculation of pressure drop of heat exchangers with polymeric hollow fibers, Lattice-Boltzmann calculations with complex porous media, etc. Apart from that, he gives lectures "Advanced use of ANSYS FLUENT" for PhD students.

This work is a logical outcome of the author's research activities at the Chair in Leoben between years 2010 and 2020. Funded by the Austrian COMET Competence Centre Programme (K2) and the industry partner, Eisenwerk Sulzau-Werfen, R. & E. Weinberger AG, simulation and numerical modeling of horizontal centrifugal casting of rolls for mills was done.

In fact, words "Simulation and Modeling" can have multiple meanings in this respect. The R&D people from the foundry would probably name a few projects involving simulation of modeling, however, with totally different topics of interest, such as:

- simulation of residual stresses in the casting,
- thermodynamic simulations of (new) materials,
- Phase-Field and similar simulations of microstructure,
- macroscopic simulations of flow and heat transfer including solidification.

This work is solely focused on the last topic of a macroscopic simulation of the whole casting process. Prior to that, various flow phenomena inherent to rotating flows are highlighted in section 1.1. In the same section, a difference between the horizontal and vertical centrifugal casting is discussed. The horizontal configuration is further connected with the field of vibromechanics. Next, in section 1.2 the topic of solidification is of a central importance. It is described as it was a view point of someone from the casting community. It is explained why a structure of a

horizontally centrifuged product is so much different compared to that obtained with a vertical configuration. Actual problems e.g. related to defects etc. of the horizontal centrifugal casting are listed. In addition, a sort of comments of the industry partner are supplemented to inform the reader about his activities in a broader extent.

Section 1 is followed by various modeling efforts of the author in section 2. In section 2.1, a numerical model of horizontal centrifugal casting is introduced, which was based on the shallow water equations (SWE) and implemented via the Euler-Euler model available in ANSYS FLUENT. In 2.2, drawbacks of the preceding efforts are analysed and circumvented by choosing approximate Riemann solver over the Euler-Euler model for obtaining more accurate solution of SWE. Despite having a accurate solution of SWE, which can simulate the whole casting process in literally three spatial dimensions in a very reasonable amount of time, it was decided to develop a full Navier-Stokes model for free-surface flows. The numerical model is detailed in 2.3. In addition, the section also presents work which was devoted to formation of a gap between the casting and the mold and consequently the heat transfer coefficient at the interface. Before concluding the work, section 2.5 briefly presents a user friendly graphical user interface that was prepared for the industry partner. Main highlights of the horizontal centrifugal casting projects of the author are provided in conclusions.

# 1 A review on the centrifugal casting

Solidification is of central importance in many natural and industrial processes. However, coupling of thermodynamics (generally departing from equilibria in thermal and solutal gradients) and fluid dynamics makes the topic of solidification very complex and challenging. Fortunately, solidification has been in the scope of researchers for about one century and currently available mathematical models can nowadays quantify most of the principles and phenomena occurring in various time and length scales [1, 2]. However, there yet exist many vaguely or even not at all explored topics, which without a doubt deserve more attention. The *centrifugal casting* involves a complex interplay between fluid flow and solidification phenomena which are discussed separately in sections 1.1 and 1.2 respectively.

## 1.1 Rotating flows

As will be discussed in section 1.2, flow phenomena present in the centrifugal casting are inherently connected with the physics behind the rotating flows. Therefore, the following text gives a concise overview of well-studied configurations with liquid flows subjected to rotations. Prior to that, the governing equations of rotating flow are introduced.

### 1.1.1 Equations of motion of non-isothermal rotating flow

Equations of motion of *rotating flows* can be formulated in inertial (stationary) as well as non-inertial (rotating) frame of reference. Generally, it is preferred to work with the rotating frame of reference as the definition of boundary conditions becomes more convenient.

In the rotating frame of reference, the fluid is exposed to additional body forces referred to as fictitious forces, also known as d’Alambert forces. The fictitious forces are the centrifugal force, the Coriolis force, and the Euler force. In the equation of isothermal fluid motion the forces are conveniently written as acceleration source terms on the right-hand side of the well-known Navier-Stokes equations, which can be written as:

$$\begin{aligned} \frac{\partial \vec{u}}{\partial t} + \vec{u} \cdot \nabla \vec{u} = & -\frac{1}{\rho_0} \nabla p + \nu \nabla^2 \vec{u} - \nabla \Phi + \vec{f} \\ & - \vec{\Omega} \times (\vec{\Omega} \times \vec{r}) - 2\vec{\Omega} \times \vec{u} - \frac{d\vec{\Omega}}{dt} \times \vec{r} \end{aligned} \quad (1.1)$$

Equations of isothermal fluid motion (or the Navier-Stokes equations) are written for an incompressible Newtonian liquid. The first four terms on the right-hand side

of Eq. (1.1) represent the gradient of the *static pressure* ( $p$ ), the Newtonian viscous term with the *kinematic viscosity* ( $\nu$ ), the gradient of the *gravitational potential* ( $\Phi$ ), and additional *body forces* ( $\vec{f}$ ) respectively. When the vector of *gravitational acceleration* ( $\vec{g}$ ) is constant in the given reference frame, the gradient of gravitational potential can be rewritten as  $\vec{g}z$ , where  $z$  is the vertical coordinate.

Often, temperature and concentration gradients changes locally the *fluid density* ( $\rho$ ), which leads to *natural convection*. Assuming that the density fluctuations, denoted by  $\rho'$ , are small compared to the *reference fluid density* ( $\rho_0$ ), the *Boussinesq approximation* can be used [3]. If a term with  $\rho_0$  is not a gradient, then it is the leading-order term, and the corresponding  $\rho'$  term can be neglected. The opposite holds for the terms with gradients and thus, such  $\rho'$  terms must be kept. Practically, this means that only  $-\rho'/\rho_0\nabla\Phi$  and  $-\rho'/\rho_0\vec{\Omega} \times (\vec{\Omega} \times \vec{r})$  additionally appear in Eq. (1.1). The resulting momentum equations for non-isothermal rotating incompressible flow read:

$$\begin{aligned} \frac{\partial \vec{u}}{\partial t} + \vec{u} \cdot \nabla \vec{u} = & -\frac{1}{\rho_0} \nabla p + \nu \nabla^2 \vec{u} - \frac{\rho'}{\rho_0} \nabla \Phi + \vec{f} \\ & - \frac{\rho'}{\rho_0} \vec{\Omega} \times (\vec{\Omega} \times \vec{r}) - 2\vec{\Omega} \times \vec{u} - \frac{d\vec{\Omega}}{dt} \times \vec{r} \end{aligned} \quad (1.2)$$

Details on derivation of the equations of motion of isothermal rotating flow can be found e.g. in [4]. When the buoyancy is involved due to local density changes, the equations must be modified, which is carefully discussed in [5]. Therein, the importance of modifying the advection term by adding  $\frac{\rho'}{\rho_0} \nabla(\frac{1}{2}u^2)$  to lhs of Eq. (1.2) was argued. Equation (1.2) becomes

$$\begin{aligned} \frac{\partial \vec{u}}{\partial t} + \vec{u} \cdot \nabla \vec{u} = & -\frac{1}{\rho_0} \nabla p + \nu \nabla^2 \vec{u} - \frac{\rho'}{\rho_0} \nabla \Phi + \vec{f} \\ & - \frac{\rho'}{\rho_0} \vec{\Omega} \times (\vec{\Omega} \times \vec{r}) - 2\vec{\Omega} \times \vec{u} - \frac{d\vec{\Omega}}{dt} \times \vec{r} + \frac{\rho'}{\rho_0} \nabla(\frac{1}{2}u^2) \end{aligned} \quad (1.3)$$

There yet exist other approximations in the literature, especially those devoted to problems of astrophysics such as stellar flows, accretation disks, etc. Among them, the *shearing sheet model* and the *anelastic approximation* are to be mentioned. In [5], the author pointed out that the term  $\frac{\rho'}{\rho_0} \nabla(\frac{1}{2}u^2)$  is considered in neither of the approximations. The effect of including the term in the momentum equations was demonstrated on examples with rotating cylinders. Further, it was stated that the term plays an important role either when there is global rotation or strong vortices in the flow.

## 1.1.2 Typical configurations with rotating flows

The topic of the habilitation is *the horizontal centrifugal casting*. As the process resembles the flow in a rotating cylinder, the well-known configurations and flow phenomena in rotating cylinders are worth mentioning.

### Laminar Taylor-Couette flow between cylinders

We start discussion with the isothermal *Taylor-Couette flow* between two cylinders. Rotating Couette flow is a laminar flow between two vertical rotating cylinders. The cylinders are close to each other, similar to the configuration shown in Fig. 1.1. The flow is dominated by viscous effects while the inertial effects are negligible. Until the *critical Taylor number* ( $Ta_{cr}$ ) is reached, the flow remains completely azimuthal and the analytical solution of the Navier-Stokes equations can be found. The *Taylor number* ( $Ta_m$ ) is defined according to the following formula:

$$Ta_m = \frac{\Omega r_m^{0.5} (b - a)^{1.5}}{\nu} \quad (1.4)$$

where  $r_m = (a + b)/2$  with  $a$  and  $b$  being radii of the smaller and larger cylinder respectively. The solution has a practical use, namely the formula for the torque, is used in some viscometers to determine the viscosity of a liquid. In Fig. 1.2, the

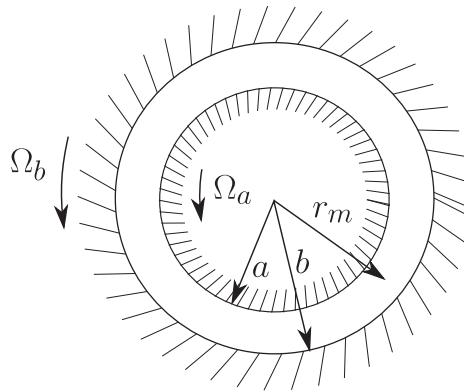


Fig. 1.1: Taylor-Couette flow between two cylinders.

physics behind the laminar Couette flow between the concentric cylinders is nicely demonstrated on mixing and unmixing a high viscous liquid with three colored spots. When performing several rotations in one direction, the colors get smeared. When the rotations are reversed, the colored spots are recovered. The experiment clearly confirms that the inertial effects are negligible.

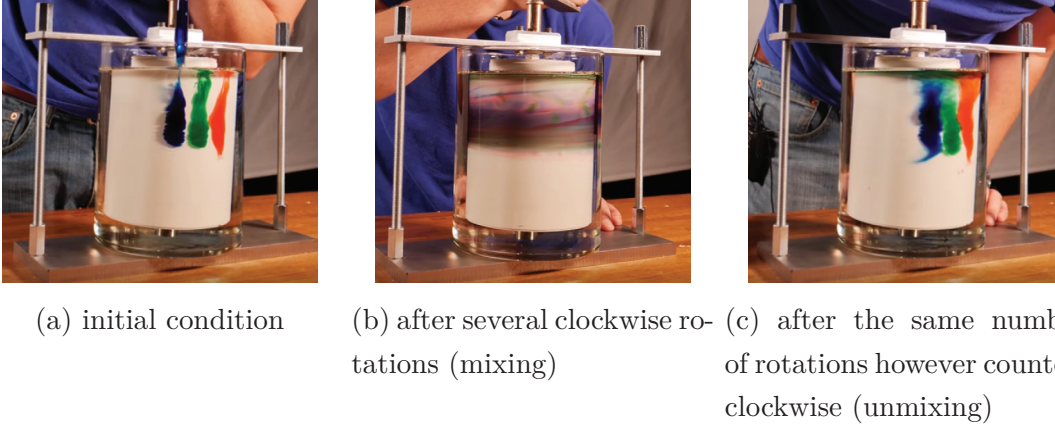


Fig. 1.2: Demonstration of negligible effect of inertia and dominance of viscous effect in a Taylor-Couette experiment [6].

### Taylor-Couette flow at high Reynolds numbers

When the  $\vec{\Omega}$  is increased, viscous forces and the radial pressure gradient fail to dampen small flow disturbances and the unidirectional azimuthal flow is replaced by a secondary flow, which is known as the *Rayleigh instability*. According to the stability analysis, the flow is stable if the following condition is fulfilled:

$$\frac{d}{dr}(ru_\phi)^2 > 0, \quad (1.5)$$

meaning that if the outer cylinder rotates faster, the flow is stable. If the inner cylinder rotates faster, the flow is unstable. If the cylinders rotate in opposite directions, the flow is stable near the outer cylinder and unstable near the inner cylinder. The most typical flow pattern of instabilities are toroidal vortices that are known as the *Taylor vortices* or the *Taylor vortex flow*. The Taylor vortices are schematically shown in Fig. 1.3a. With the inner cylinder rotating and the outer one fixed, a sequence of well-established flow states is known. With the Reynolds number increasing, the azimuthal flow and subsequently the Taylor vortex flow are replaced with the *wavy vortex flow*. It is characterized by travelling waves and a strong hysteresis. The fundamental frequency corresponds to the travelling circumferential waves. Additional frequency appears at higher Reynolds numbers and it is responsible for modulation of the travelling waves. In Fig. 1.3b and Fig. 1.3c, the Taylor vortex flow and a transition to the wavy vortex flow respectively were visualized in the experiment. Further increase of the Reynolds number leads to the turbulent-like states, namely chaotic wavy vortex flow, wavy turbulent vortex flow, and turbulent Taylor vortex flow.

Transitional pathway becomes more complicated when the outer cylinder co- or counter-rotates. The transition comprises several interesting flow patterns such as

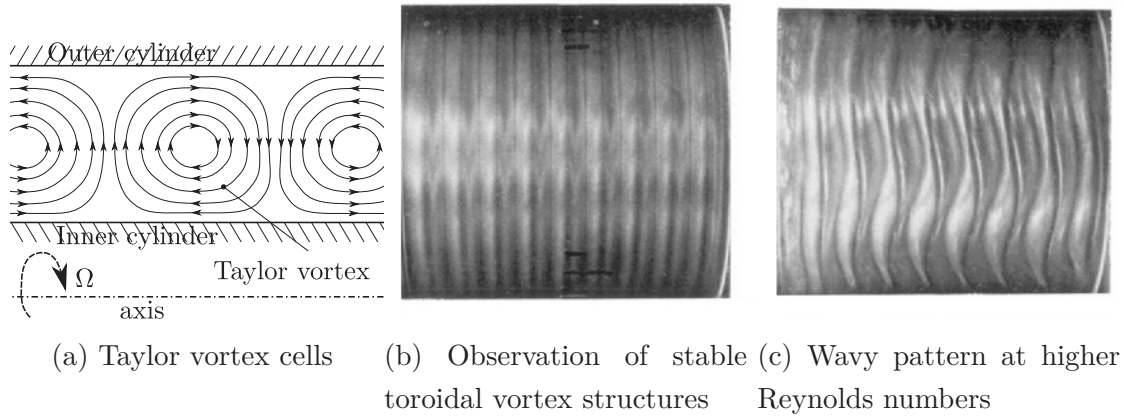


Fig. 1.3: A schematic picture of Taylor vortex flow and photos from experiment [7].

spiral vortex flow, interpenetrating spirals, wavy interpenetrating spirals, intermittent turbulent spots, and spiral turbulence.

In reality, the rotating cylinders are finite, thus having circular walls at extremities. When  $\vec{\Omega}$  is perturbed, so-called *Ekman layer* appears with some characteristic features. In the boundary layer, viscous stresses cause imbalance of the pressure gradient in the radial direction and the Coriolis force, thus leading to rotation of the flow, as shown in Fig. 1.4. The Coriolis deflection relates to the *geostrophic flow* and is particularly known from circulation patterns in the *ocean gyres*. The topic-related keywords are *the Ekman transport, cyclone, anticyclone, upwelling, downwelling*, etc. Coriolis effects are also often studied with intracelestial problems.

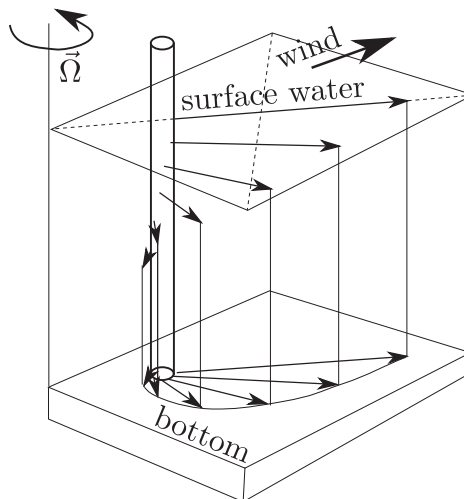


Fig. 1.4: The Ekman spiral.

## Thermal Taylor-Couette flow

In general, the Taylor-Couette flow is sensitive to the radial temperature gradient that can have both stabilizing as well as destabilizing effect. The axial buoyant forces compete with the centrifugal forces to generate *the spiral vortex flow*. The *Richardson number* that characterizes the ratio between buoyant and centrifugal forces is used to classify three distinct flow regimes: (1) centrifugal dominant, (2) mixed-convection regime, and (3) buoyant dominant, which significantly destabilizes the flow resulting in the formation of *the helicoidal flow pattern*. As remarked in [8], many intriguing flow states may appear depending on Reynolds numbers, Prandtl number, Richardson number, length-to-gap ratio, and some other parameters. Common tools or quantities used in analysis are contour plots of azimuthal, axial and radial velocities, and temperature. Further, turbulent kinetic energy, power spectral density and spatial autocorrelation of velocity components. Similar to the isothermal Taylor-Couette flow, the importance of the Ekman layer was demonstrated in [9].

### 1.1.3 Horizontal vs. vertical cylinder

The orientation of the cylinder axis, i.e. whether it is horizontal or parallel, has an influence on spatiotemporal flow structures. However, in the case of isothermal Taylor-Couette flow between two cylinders, significant differences are not anticipated, especially when the centrifugal forces are large compared to the gravity. To the best extend of our knowledge, we have not found any comprehensive research in the public literature. When the inner cylinder is removed and  $\vec{\Omega}$  is large enough so that a liquid layer is formed around the circumference of the outer cylinder, differences become eminent. With the outer cylinder held vertically, the shape of the free-surface is a parabola. In the rotating frame of reference, the vector of the gravitational acceleration is invariant with respect to time. The flow is stable, i.e. disturbances are dampened. A rigid-body motion is observed. With the outer cylinder oriented horizontally, the gravitational acceleration rotates in the rotating frame of reference, i.e. it acts as perturbation of the centrifugal acceleration. By no means is the annular layer thickness uniform around the circumference of the cylinder and so it is not the field of azimuthal velocities. The oscillatory motion of the annular layer was demonstrated on a drift of a marker placed on the free-surface. The marker reveals a retrograde azimuthal streaming of the free-surface, as schematically shown in Fig. 1.5b. In experiment, it was shown that the layer is thicker at the top than it is at the bottom [10], as schematically shown in Fig. 1.5a. Consequently, resulting from the continuity, the relative velocity is higher at the bottom than at the top. The *Ekman pumping* takes place at the ends of the cylinder because the

centrifugal forces there are larger than in the bulk fluid. The liquid is centrifuged outwards along the ends of the cylinder. Then, it turns to continue inwards to the center of the cylinder. Eventually, two counter-rotating loops are formed. The axial streaming is weak compared to the azimuthal streaming. The azimuthal streaming is caused by production of vorticity in the Stokes layer. The basic azimuthal flow is represented by a single azimuthal wave sitting at the top of the cylinder in the non-rotating frame of reference. However, much more intriguing flow patterns may appear related to instabilities generated in the Stokes layer. This phenomena deserve a separate section 1.1.4. From the view point of solidification and a casting process, differences between the horizontal and vertical centrifugal casting will be described later in section 1.2.

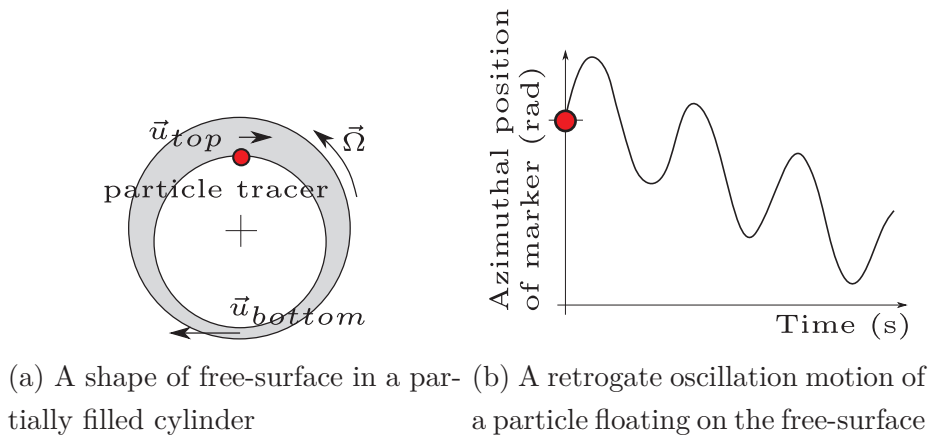


Fig. 1.5: A schematic picture of azimuthal flow in a horizontally rotating cylinder

### 1.1.4 Inertial waves

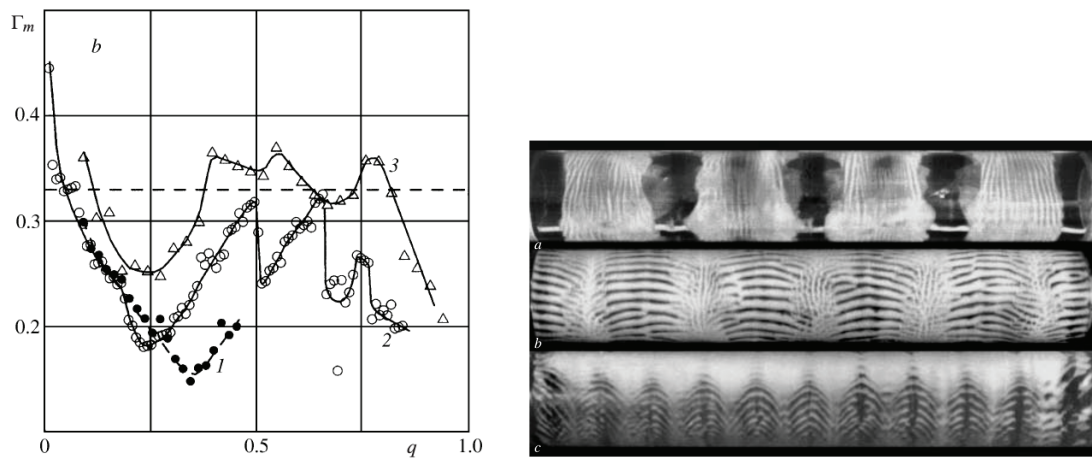
A fluid rotating at  $\vec{\Omega}$  supports formation of inertial waves [11] propagating through the interior of the fluid, when a precession or a periodic variation of  $\vec{\Omega}$ , also known as longitudinal librations, are applied. In a cylinder with the horizontal axis of rotation, the gravity force acts as an oscillating force in the rotating frame, therefore, the problem could be looked at from the viewpoint of *vibrational mechanics* supporting excitation of *inertial waves*. When the fluid is enclosed in a container, it is referred to as *inertial modes*.

The presence of inertial waves was confirmed experimentally by observing a non-monotonic behavior of the collapse limit of a liquid layer in a partially filled rotating cylinder [12]. At some relative occupancies of the cylinder the collapse limit agreed well with the theoretical limit, while it was greatly overestimated at some others. The collapse limit  $\Gamma_m$  is defined as an inverse value of the square of *Froude number*

equal to  $1/3$ , calculated with the free-surface radius  $a$ . Equation 1.6 was theoretically derived using the linear stability analysis in [13] and reads:

$$\Gamma = \frac{g}{\Omega^2 R} \quad (1.6)$$

A clear example of non-monocity is shown in 1.6a. Each curve represents a cylinder with the length  $L$  and radius  $b$ . The relative occupancy of the cylinder,  $q$ , is given on the horizontal axis. The collapse limit  $\Gamma_m$  is plotted on the vertical axis. The theoretical limit,  $\Gamma_m = 1/3$  is also depicted. The local minima signify deviations from the basic azimuthal flow i.e. secondary vortex structures, as can be seen in 1.6b.



(a) A non-monocity of the collapse limit (b) Flow patterns visualized by granular of a liquid layer. medium.

Fig. 1.6: Inertial waves in a partially filled horizontal cylinder, reprinted from [12]

Below the collapse limit i.e. when a liquid pool is formed in bottom of the cylinder, interesting flow structures and instabilities occur. Formation mechanisms however do not fall in the class of rotating flows; therefore, it is not further discussed. This class of flows belongs to *coating flows* or *rimming flows*.

## 1.2 Horizontal centrifugal casting

In the casting process, the mold/chill is a cylinder rotating around its axis at  $\vec{\Omega}$ . This suggests the same flow phenomena as discussed in the previous section 1.1 on rotating flows although the solidification interferes. In addition to buoyancy driven by thermal-solutal gradients, the gradually solidifying melt interacts with the flow.



Fig. 1.7: A shark-teeth pattern in the liquid pool formed at the bottom of a plexi-glass cylinder rotating at low  $\vec{\Omega}$ , the photo taken by BOHACEK J. at SMMP, MUL, Leoben.

At this point, it makes sense to distinguish between *columnar crystals* growing from the wall and *equiaxed crystals* nucleating and growing in the melt. To best illustrate characteristic features of the horizontal centrifugal casting, sometimes referred to as *horizontal spin casting* (HSC), it is compared to the *vertical spin casting*.

With the axis of rotation being vertical, the latter is not suitable for casting long products such as seamless tubes, rolls, etc. For the present work more importantly, the vector of gravity acceleration  $\vec{g}$  is fixed in the rotating frame of reference and a truly rigid motion is identified. As result, the melt solidifies exclusively from the wall in a form of long columnar crystals growing towards the axis of rotation (Fig. 1.8a). In contrast, the vector  $\vec{g}$  oscillates in the rotating frame, which leads to the azimuthal flow, secondary flow, and consequently a better mixing. The better mixing enhances the heat transfer, which supports the formation and growth of free equiaxed crystals, as can be seen in Fig. 1.8b.

It is indeed the oscillatory  $\vec{g}$  and inherent vibrations induced by imperfections of the mold and an unbalanced mass that are responsible for outstanding mechanical properties of HSC cast products. Vibrations are sometimes introduced intentionally in other casting techniques to refine the structure and thus improve the quality of the product. Obviously, the HSC rig is simple and can deliver superior products. However, there is a catch with it.

- (i) In the horizontal centrifugal casting of work rolls a uniform thickness of the liquid layer is essential. Considering the large momentum of the spinning system, any disruption of the layer may result in a catastrophe. Therefore, knowing the collapse limit is vital. In section 1.1, the non-monocity of the

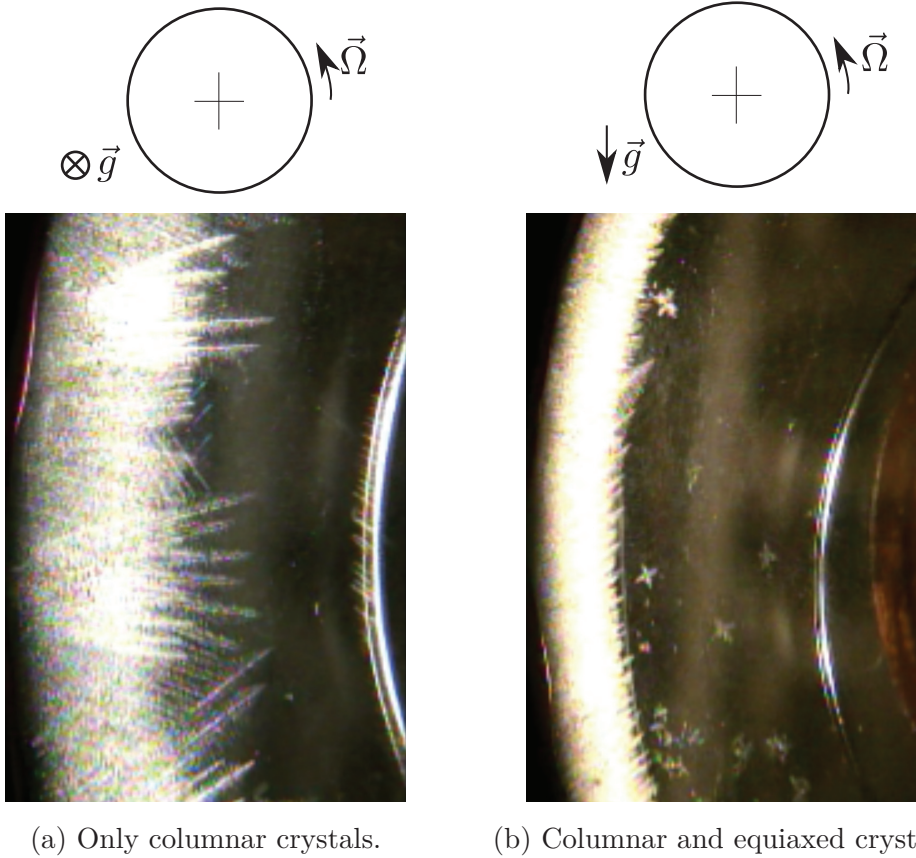
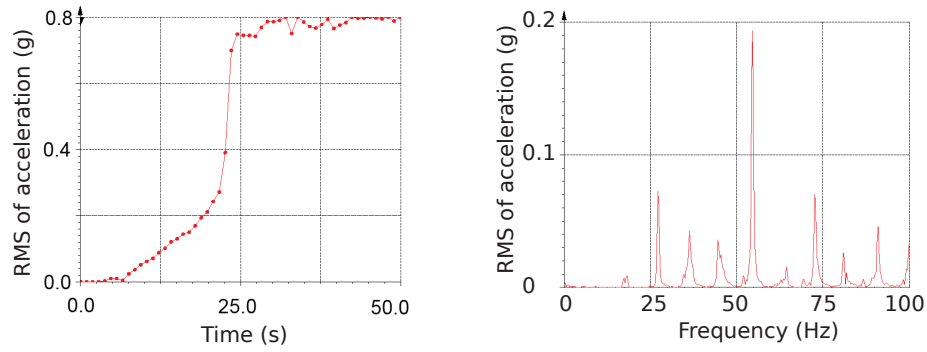


Fig. 1.8: Difference between vertical (left) and horizontal (right) centrifugal casting of a transparent alloy; the courtesy of prof.Esaka [14].

collapse limit has been already. highlighted.

- (ii) During a typical casting, vibrations of carrying rollers are continuously monitored and normally stay at low levels, as can be seen in Fig. 1.9. Sometimes, as the solidification proceeds, vibrations rise considerably. In such an event, the rate  $\vec{\Omega}$  must be quickly adjusted in order to calm the situation and prevent potential risks. We believe that the progressing solidification is responsible for an abrupt transition to a resonant flow regime.
- (iii) Several theories have been proposed to explain *banding* (Fig. 1.10), an undesired condition encountered in a horizontally cast products. The theories [15] range from the influence of vibrations in producing independently nucleated growth bands under conditions of constitutional supercooling leading to entrapment of solute rich liquid, to bands created by flow instabilities appearing as sporadic surging of liquid metal restricted to lower rotation rates. Until now, the origin of the banding has not yet been clearly identified. Herein, an explanation from the perspective of vibromechanics is suggested. Liquid oscillations and steady streaming generated by gravity field can form ripples of



(a) An onset of vibrations at the moment the first incoming melt touches the chill. (b) A frequency spectra of vibration with harmonics corresponding to integer multiples of  $\vec{\Omega}$ .

Fig. 1.9: Vibrations of a support roll holding a chill for horizontal centrifugal casting of the outer shell of a work roll; the measurement conducted in Eisenwerk Sulzau-Werfen in Tenneck, Austria.

equiaxed crystals (Fig. 1.11a), which may eventually ‘freeze’ and thus appear in the final structure (Fig. 1.11b).

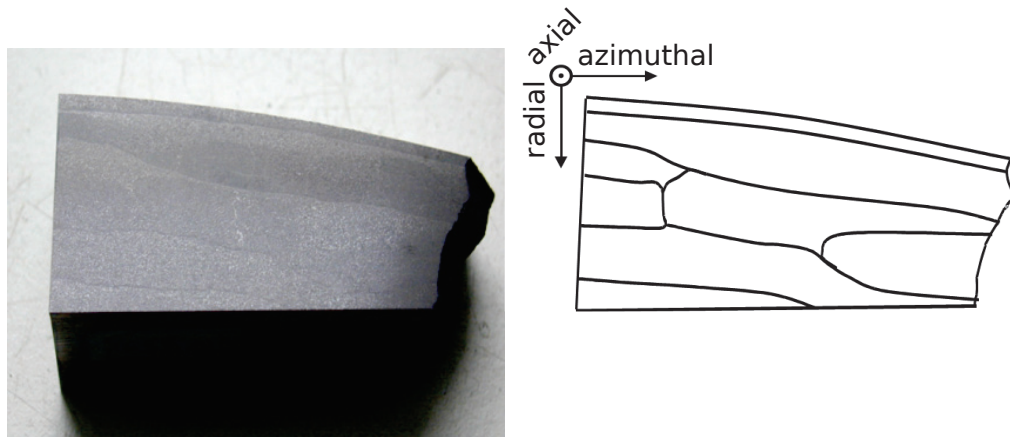
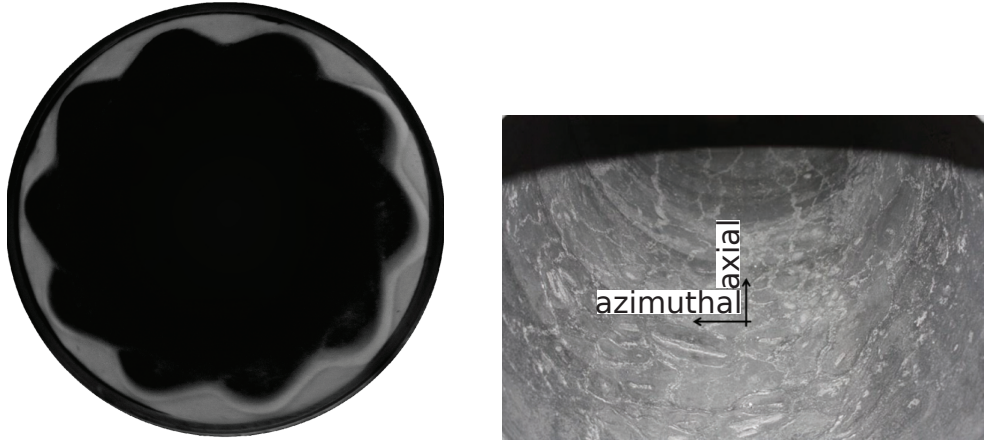


Fig. 1.10: The banding phenomenon, a multi-layered structure, clearly visible on a metallographic sample (the courtesy of Eisenwerk Sulzau-Werfen).

(iv) During the horizontal centrifugal casting, a typical structure is formed by fine equiaxed crystals of martensite reinforced with MC carbides, where the letter M stands for an alloying element, e.g. Vanadium. Interestingly, very long (cm), isolated columnar crystals can be occasionally identified deteriorating the cast quality, as shown in Fig. 1.12. The cause of such a columnar crystal growth still remains unexplained.



(a) A horizontally rotating cylinder completely filled with a water-glycerol solution seeded with glass spheres. Regular ripples formed at the boundary of the sedimented granular medium can be static or migrating in the cylinder frame [16].

(b) Regularly spaced annular waves visible on the solidified free surface (the courtesy of Eisenwerk Sulzau-Werfen).

Fig. 1.11: Another possible explanation of banding phenomena in HSC products.

- (v) The list of encountered issues with the horizontal centrifugal casting could be certainly longer. As the cast alloys are often very complex and centrifugal acceleration massively promotes buoyancy, the manufacturer must cope with problems related to *macrosegregation*.

### 1.2.1 The view point of R&D in the plant

Although the author concentrates on the topics which were involved during his spin casting projects, a more general viewpoint of a roll manufacturer is given here. Naturally, the money is the key parameter in the plant. The R&D expenditures are low ( $\sim 2\%$ ) compared to other types of business. The main goal is to deliver to the customer a roll that is wear, breakage and crack resistant, and that can be easily grinded, redressed and tested. In other words, the roll maker wants to increase the life of the roll without adversely influencing the quality of the rolled product or the mill performance [17].

In essence, the R&D is working with three different types of projects namely development, strategic and competence projects. A development project is initiated by customers needs. Typically, it is related to changes of chemical composition of the roll material or the heat treatment. The goal is clearly defined and it should be

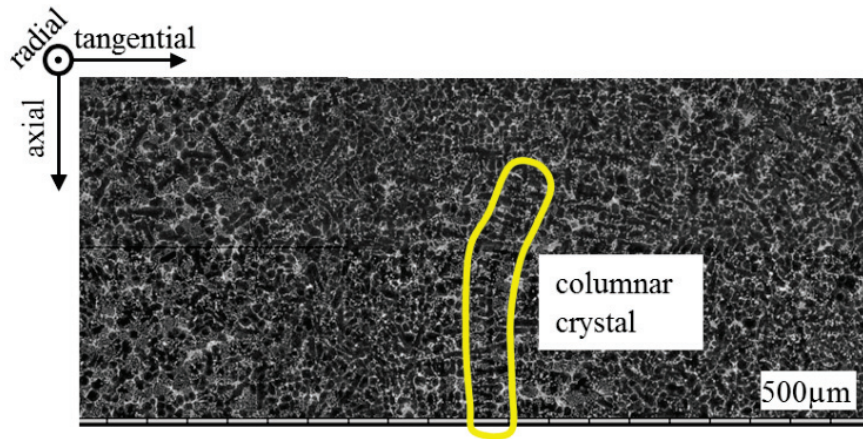


Fig. 1.12: An undesired occurrence of a long columnar MC crystal (the courtesy of Eisenwerk Sulzau-Werfen).

fulfilled in a relatively short time. On the contrary, a strategic project foresees the market situation in the future and it tries to develop or at least build up knowledge about technologies of the highest potential significance. For example, remember that the *Chrome Steel* roll has been replaced by *HSS* rolls at all stands of HSM stands. It is possible that the future will bring a roll made of ceramics ( $\text{SiAlON}$ ), which is currently limited by the size requirements [18]. Furthermore, engagement of *Cemented Carbide* rolls may lead to significant performance improvements [19]. In addition to new materials, new processes may be the main topic of strategic projects. For example, *cladding* is one such a process in which two dissimilar metals are bonded together by application of a high pressure. Remember that currently the roll is made by combination of two processes: gravity casting of the core and preceded by centrifugal casting of the outer shell. The *Osprey* process is another technology that has a potential to eliminate problems related to segregation, large grain sizes or brittle phases [20]. Unfortunately, the process requires complex and expensive steps of preparing the input material, the powder. The process belongs to *Powder metallurgy*. The main benefit is that the carbide size can be significantly reduced when the melt is atomized and solidified at very high cooling rates.

Finally, concerning competence projects, the research is often conducted together with university and simulation and modeling tools are involved. The topics worth mentioning are modeling of life cycle of HSM work rolls, study on welding a wear resistant coating on the roll, modeling of the phase transformation and residual stress in a composite mill roll during heat treatment, simulation of the static core filling after spin casting of the shell, and simulation of *horizontal centrifugal casting*.

Apart from that, duties of the R&D also include after sales consultancy and

performance follow up. The roll manufacturer keeps track records of his customers and therefore, the rolls on different stands can be optimized with the help of the roll history. The roll manufacturer is very well aware of the total cost of ownership (TCO) of the customer; thus, the manufacturer is able to offer the best solution for him [21].

For a careful reader it is easy to notice much broader scope of the R&D in roll making than the topic of this work, which is mainly focused on numerical simulation of *horizontal centrifugal casting* detailed in section 2.

## 2 Numerical modeling of centrifugal casting

Horizontal centrifugal casting of a roll, also known as horizontal spin casting (HSC), is an opaque process involving high temperatures ( $>1200^{\circ}\text{C}$ ) of a liquid steel and high inertia moments of rotating system ( $\sim 100$  tons rotating at  $\sim 600$  rpm). Concerning



(a) A slag removal after HSC

(b) A filling process during HSC

Fig. 2.1: A schematic picture of azimuthal flow in a horizontally rotating cylinder

methods of investigation related to a complex flow field, a numerical simulation is the first choice. In the plant an experiment would be very difficult to design namely for the following reasons:

- The flowing media is a superheated liquid steel, which excludes intrusive velocity measurement techniques.
- The liquid steel is situated in a steel mould rotating around its axis at around 600 rpm, which excludes attachment of expensive measurement devices or significantly rises the need for devices sampling at high frequency.
- The liquid steel is enclosed partly by the steel mould and the endcores at both extremities. Therefore, only a small portion of the free surface of the liquid steel is optically accessible through a limited view angle.

At the laboratory scale, the water model would be also hard to design namely for the reasons:

- Vibrations and mould deformations may significantly influence the resulting structure. Unfortunately, both parameters are unlikely to be correctly accounted for in the laboratory experiment.
- Thermal conditions cannot be reproduced.
- In order to take into account effects of solidifying liquid metal, a semi-transparent alloy would have to be considered.

The numerical simulation of the horizontal centrifugal casting may take different forms depending on the approach selected and the specific topic studied. For example, while the Newton's law is sufficient for simulation of segregating  $MC$  carbides, it

is necessary to consider 3D Navier-Stokes equations with free-surface tracking/capturing algorithms to describe the flow field in detail. Furthermore, while the user of commercial CFD software will most likely choose the *Volume of Fluid* (VOF) model, another user will try to avoid resolving flow fields in the ambient air. The user of common CFD packages will stick to *Finite Volume Methods*, while the user of, e.g., *ProCAST* should have a background in *Finite Element Methods*.

The author of this work was given the project entitled "Simulation of Horizontal Spin Casting" at the Chair of Simulation and Modeling Metallurgical Processes (SMMP) at Montanuniversitaet Leoben in 2011. As ANSYS FLUENT was the main tool for most of the SMMP members, it was selected also for the author's task. He started where his colleague ended with simulations in ANSYS FLUENT when he decided to leave the Chair. The colleague performed two types of simulations. In both of them, the VOF model was enabled to capture the position of the free-surface of the melt. Initially, 2D axisymmetric simulations were considered together with the built-in solidification model. A relatively small grid size allowed to complete the solidification process in an acceptable amount of computational time. The 2D result is shown at the top of Fig. 2.2. The 2D domain corresponds to an axial cut

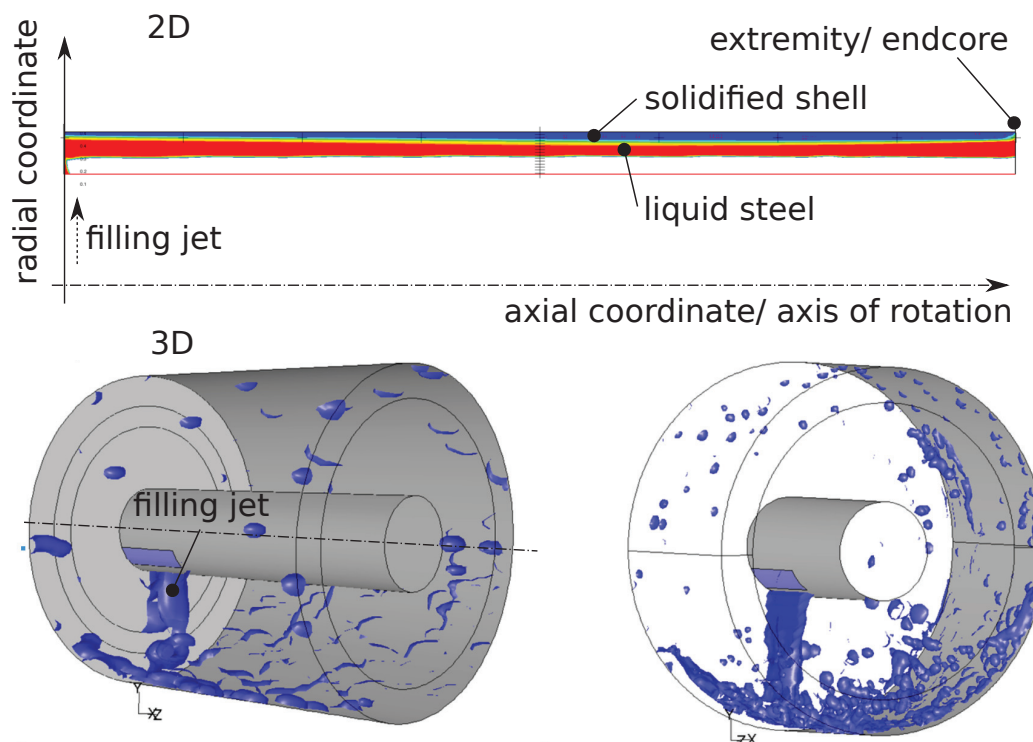


Fig. 2.2: Taylor-Couette flow between two cylinders.

through the outer shell as well as the permanent steel mould. Such model provides approximate information on progress of solidification. However, the results are likely

to be biased by the absence of the third dimension; therefore, the missing term with the Coriolis acceleration in the momentum equations. Perhaps, that was the reason why a full 3D model was set up. At the bottom of Fig. 2.2, the early stage of centrifugal casting is shown. The colored surfaces represent the liquid steel. Unlike the 2D model, this case suffered from a slow convergence. Moreover, the liquid droplets were not picking up the speed of the rotating mould. Last but not least, to simulate just fractions of seconds already took an enormous amount of time. At that moment, the author of this group joined the group of Prof. A. Ludwig and took over the project. At that time, Dr. A. Kharicha came up with an idea of so-called *shallow water equations* (SWE) to combine, so to simply say, the calculation performance of the 2D model and the accuracy of the 3D model.

Since then, the author further developed his idea, derived the equations and implemented them in the commercial system ANSYS FLUENT. The section 2.1 is dedicated to this topic.

## 2.1 Shallow water equations - Euler-Euler multiphase approach

This section is compiled from two articles that were published in *ISIJ International* and *Journal of Fluid Engineering*.

The first one entitled "Simulation of Horizontal Centrifugal Casting: Mold Filling and Solidification" is primarily aimed at the casting community as it presents data related to solidification such as details about the heat transfer, solidification model including simplistic radiation and stochastic mould filling, and results about time dependent thickness of solidifying shell. The solidification front is tracked by solving 1D heat conduction together with the Stefan problem in a dimensionless form. Two cases were analyzed, namely the case A with a perfectly cylindrical mold and the case B with a deformed mould. 3D solidification fronts are compared both in time and space. Non-uniform distribution of the melt is found during the filling stage, which will cause mass imbalance and consequent vibrations.

The second one entitled "Modified Shallow Water Equations with Application for Horizontal Centrifugal Casting" is oriented on those who are more involved in pure fluid dynamics. Shallow water equations (SWE) are described in detail including the extra source terms resulting from vibrations and mould deformations. The main objective was to investigate a response of the free surface of the liquid layer to various initial conditions such as different rotation rate, thickness of the layer, vibrations yes or no, bending of the mould axis and the initial perturbation.

In both articles, introductions concisely summarize efforts of others working on

similar topics. Shallow water equations follow as the governing equations; however, the process of implementing them in ANSYS FLUENT was not revealed to the reader. The approach is concisely explained here. The most general Euler-Euler model was selected from the multi-phase models available. The continuity and momentum equations take the following form:

$$\frac{\partial \alpha_i \vec{u}}{\partial t} + \vec{u} \cdot \nabla (\alpha_i \vec{u}) = S_i \quad (2.1)$$

$$\frac{\partial \alpha_i \vec{u}}{\partial t} + \vec{u} \cdot \nabla (\alpha_i \vec{u}) = -\frac{\alpha_i}{\rho_i} \nabla p + \alpha_i \nu \nabla^2 \vec{u} + \vec{F}_i \quad (2.2)$$

In a general multiphase problem, the volume fraction of the phase  $i$  is denoted by  $\alpha_i$  and  $\sum_i^N \alpha_i = 1$  where  $N$  is the total count of phases. The pressure  $p$  is shared by the phases. The mass and momentum exchange between them happen through the terms  $S_i$  and  $\vec{F}_i$  respectively. In order to transform SWE into 2.1 and 2.2, a dummy phase must be added to fulfill the condition that the total volume fraction equals 1. This is the only role of the dummy phase, say, air resting upon the liquid layer. Then,  $\alpha_i$  stands for the thickness of the layer  $i$ . In 2.2, the pressure term becomes meaningless as SWE put in balance hydrostatic and inertial forces. Hydrostatic forces are hidden in  $\vec{F}_i$ .

*Shallow water equations* can be implemented by using the Euler-Euler model, which is available in most of the CFD packages including ANSYS FLUENT. However, the efficiency and accuracy is questionable as will be discussed in the next section 2.2.



The Iron and Steel Institute of Japan

# Simulation of Horizontal Centrifugal Casting: Mold Filling and Solidification

Jan BOHACEK,<sup>1)\*</sup> Abdellah KHARICHA,<sup>2)</sup> Andreas LUDWIG<sup>1)</sup> and Menghuai WU<sup>2)</sup>

1) Dept. of Metallurgy, Montanuniversitaet Leoben, Franz-Joseph Strasse 18, Leoben, 8700 Austria.

2) Christian Doppler Lab for Advanced Simulation of Solidification and Melting, Dept. of Metallurgy, Montanuniversitaet Leoben, Franz-Joseph Strasse 18, Leoben, 8700 Austria.

(Received on July 8, 2013; accepted on November 28, 2013)

In order to simulate the mold filling and solidification of the outer shell of large work rolls being cast by horizontal centrifugal casting, the shallow water equations were adopted to solve the 2D average flow dynamics of the melt spreading inside the cylindrical mold. The model accounts for centrifugal force, Coriolis force, shear force, gravity and convective and diffusive energy transport. The solidification front was tracked by fulfilling the Stefan condition. Radiative and convective heat losses were included from both, the free surface and the outer wall of the mold. By introducing a stochastic factor to account for the irregular filling jet behavior an uneven spreading of liquid from the center of the mold towards the extremities was predicted. Thus, the formation of the first solid layer also happens unevenly. However, when the mold is covered everywhere with a solid layer, the solidification rate decreases and further filling increases the height of the liquid layer. With increase liquid height the amplitude of the free surface waves also increases.

KEY WORDS: horizontal centrifugal casting; work roll; shallow water equations; Coriolis force; Stefan condition; mold deformation.

## 1. Introduction

The centrifugal casting process has two distinct branches, the vertical and horizontal centrifugal (or spin) casting, where vertical and horizontal define the placement of the axis of revolution of the mold. The vertical centrifugal casting is commonly used for casting non-cylindrical parts such as valves, propellers, sprockets *etc.* On the other hand, cylindrical parts such as pipes, sleeves, tubes are cast using the second technique provided that the length of the casting is greater than the diameter and that the casting contains a cylindrical bore through. The main difference between the vertical and horizontal centrifugal casting is in the resultant force acting on the melt. With a vertical mold axis the resultant force is constant, whereas with a horizontal mold axis the centrifugal force is periodically disturbed by the gravity and by inherent vibrations. A common advantage of both centrifugal casting processes dwells in obtaining superior mechanical properties of the products compared to the conventional gravity castings.<sup>1)</sup> Now, putting the vertical centrifugal casting<sup>2)</sup> aside, the horizontal centrifugal casting can be discussed in more details. A schematic of the process is shown in **Fig. 1**. The filling starts with the relatively cold mold ( $\sim 433$  K) already rotating at constant rpm ( $\sim 680$  rpm). Solidification occurs immediately, when the melt firstly hits the mold wall. A cloud of fine crystals nucleate close to the

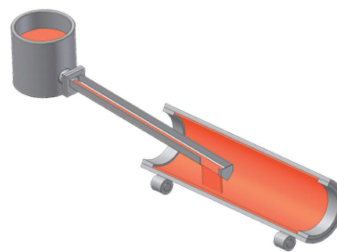


**Fig. 1.** A schematic of the horizontal centrifugal casting of an outer shell of a large work roll. (Online version in color.)

mold. Due to the interaction between the forces of inertia and the extreme shear force, nuclei are evenly distributed in the bulk, where they mostly survive and continue growing, which then results in a very fine structure throughout.<sup>3)</sup> Possible columnar crystals solidifying from the mold wall are usually washed out by severe tangential forces and further support the fine structure. Next, the centrifugal force can easily exceed 100 G in magnitude, which helps to suppress the shrinkage and pushes possible inclusions and impurities towards the mold center due to the density difference. The second phenomenon enhancing mechanical properties is the inherent vibration, which promotes the solidification rate and enhances turbulence. The angular frequency  $\Omega$  has to be carefully chosen. Too low  $\Omega$  causes the liquid to fail to adhere to the mold wall, which is known as “raining” *i.e.* a curtain of metal droplets falling down from the top of the

\* Corresponding author: E-mail: jan.bohacek@unileoben.ac.at  
DOI: <http://dx.doi.org/10.2355/isijinternational.54.266>

mold.<sup>4)</sup> On the other hand, excessive angular frequencies generally lead to inadmissible strong vibrations, which may result in longitudinal cracks caused by the hoop stress in the initially solidified shell. Besides, even for very little density difference between two alloy elements a too high angular frequency  $\Omega$  can result in significant segregation.<sup>5)</sup> For this reasons, the angular frequency  $\Omega$  along with many other process parameters such as the pouring temperature, pouring rate, the way how the melt is poured *etc.* require an optimal control.

Some papers written by other researchers on this topic were oriented on the experimental trials, usually some cold experiments; some papers were dealing with mathematical models and numerical simulations. A paper<sup>6)</sup> describing various flow regimes during the horizontal centrifuging was done to study the influence of the angular frequency  $\Omega$  and the liquid height  $h$  on waves appearing on the free surface. It was surprisingly found that with increasing the angular frequency the free surface was more disturbed mainly due to inherent mechanical vibrations. For low  $\Omega$  the free surface formed purely cylindrical pattern. With increasing  $\Omega$  a free surface pattern was passing through the regime with helical waves, then orthogonal, and eventually “orange skin” waves. Mathematical formulas were stated for vibrations and axial deformation of the mold to analytically investigate free surface patterns. Recently, in-situ experiments were performed,<sup>7)</sup> in which the Succinonitrile-1 mass% water alloy was poured in the rotating glass cell and the movement of the equiaxed crystals was observed by means of the high-speed camera. They found that the relative path of the arbitrarily chosen equiaxed crystal associated with a fix point on the mold oscillates and travels in the anti-rotational direction. This phenomenon can be attributed to the interaction between the inertia of the crystal and the 3D flow influenced by effects of the gravity and vibrations. Very interesting experimental work<sup>8)</sup> comparing mechanical properties of the Al-Si specimens cast using the centrifugal and gravitational casting technique was done revealing that the tensile and rupture strength was increased for the centrifugal castings. The authors claimed that it is possible to split effects of the centrifugal force into three separate mechanisms: the centrifugal pressure, the inherent vibration, and the fluid dynamics.

In addition to these experimental works, not many numerical studies were devoted to the horizontal centrifugal casting. In,<sup>9)</sup> a full 3D simulation of the horizontal centrifugal casting was performed in the commercial software STAR-CD V4 using the VOF method to track the free surface. The whole cylindrical domain was meshed with rather coarse polyhedral elements, which allowed notably large time step ( $\sim 0.01$ ). Only the flow was solved without taking into account the heat transfer and solidification. Results from simulations showed roughly how the melt is spreading during the filling, but no details are given on how the filling was realized and whether the model could capture some free surface patterns or not. Next, a solidification model<sup>10)</sup> was developed for a description of the centrifugal casting process of a metal matrix composite reinforced by dispersed ceramic particles. The numerical model ignored the flow, but forces acting on the particles were taken into account by means of solving ODE for the force balance. A planar solid-

ification front was considered. A study on a similar topic<sup>11)</sup> was performed, in which the solidification of the centrifugally cast particle reinforced metal matrix composite was influenced by the particles travelling through the liquid metal matrix. From the force balance on the particle, they found that the Coriolis force can be disregarded when the particle diameter  $d$  or the angular frequency  $\Omega$  is small. In other words, the Coriolis force can be only neglected when the ratio between the coefficient  $2\rho_p V\Omega$  (related to the Coriolis force) and the coefficient  $6\pi\mu d$  (related to the drag force) is much smaller than unity. In general, the Coriolis force cannot be however neglected. A full 3D numerical model<sup>12)</sup> of the horizontal centrifugal casting was recently introduced simulating the interface between the metal and air reconstructed by the VOF method for tracking free surfaces. The main goal was to study the effect of two different filling systems on the temperature distribution on the outer wall of the mold. It was found that with the filling arm moving to and fro more uniform temperature distribution can be achieved compared to the classical static filling. Another numerical study<sup>13)</sup> concerning the horizontal centrifugal casting namely casting of pipes was done using the commercial CFD package FLOW3D. In order to avoid extremely low time steps, momentum equations were solved in the rotating frame of reference. However, due to a very small wall-to-length thickness ratio, one simulation still took considerably long time ( $\sim 20$  days).

Nowadays, the commercial CFD packages are along with hyper-threading computing very powerful tools, which can be successfully used to simulate many physical and engineering processes. However, the importance of the proper choice of the equations to be solved and how it should be solved still remains inarguable. In this particular case of the horizontal centrifugal casting of a work roll we believe it is practically impossible to simulate the full casting process ( $\sim 35$  min) by solving the full 3D Navier-Stokes equations for two immiscible phases (the metal and air) in a reasonable time. On the other hand, we are convinced that the main features of the flow and the whole casting can be reliably captured with the help of the 2D shallow water equations (SWE).<sup>14,15)</sup> The original 2D SWE were derived from the 3D N-S equations assuming that the pressure is strictly hydrostatic and that the vertical components in the momentum equation for the radial direction can be ignored. For the characteristic length scale much greater than the characteristic height it is a very good approximation. In our system the order of magnitude of the ratio between the characteristic height (liquid metal height) and the characteristic length scale is 0.01 and thus; the simplification by assuming a shallow water flow is reasonable. It is important to note that no assumption is made about the amplitude of waves. The SWE still retains the nonlinear convective terms from the N-S equations. In general, the SWE are used for modeling purposes in oceanography,<sup>16)</sup> river management,<sup>17)</sup> and meteorology.

In this paper modified SWE are introduced for simulating the average flow dynamics of the melt inside a horizontally rotating mold. The flow is exposed to some sort of vibrations induced by a poor roundness of the mold (or a mass imbalance) and a mold deformation due to thermal effects. The flow equations are coupled with a solidification model

assuming a microscopically planar solid-liquid interface. The diffusive and convective energy transport is solved in the liquid taking into account convective and radiative heat losses from the free surface. A simple heat diffusion model is applied in the solidifying shell and the mold. In Fig. 2, a general configuration demonstrates aspects of the SWE model such as a melt flowing over a solidifying shell, heat transfer to the mold, and heat losses from the free surface and the outer wall of the mold.

**2. Model Description**

The centrifugal force is evidently the most dominant force (~100 G) always pushing the liquid towards the mold wall. From observations during the real casting the liquid perfectly adhered to the rotating mold even during first stages of the filling. This suggests solving the flow in the rotating frame of reference *i.e.* taking into account fictitious forces such as the centrifugal force and Coriolis force. The SWE were derived in the Cartesian coordinate system constructed by unfolding the inner wall of the mold into the *x-y* plane, where *x* and *y* denote the axial and the circumferential position. Despite the cylindrical geometry, the Cartesian coordinate system was chosen mainly due to the rather small ratio between the liquid height *h* and the mold radius *R*. The model assumptions are summarized below:

- The momentum equation can be written in the rotating frame of reference due to the high centrifugal force (~100 G).
- The radial momentum is negligible compared to the momentum in the axial and the tangential direction of the cylindrical mold. Higher order terms in the asymptotic series of the static pressure can be neglected and only the hydrostatic pressure is retained.
- A fully developed laminar flow is assumed; therefore, a parabolic velocity profile is forced within the liquid height *h* (Fig. 2) with a no slip boundary condition on the underlying topography and zero stress on the free surface.
- Surface tension effects can be neglected.

The continuity equation remains unchanged for our con-

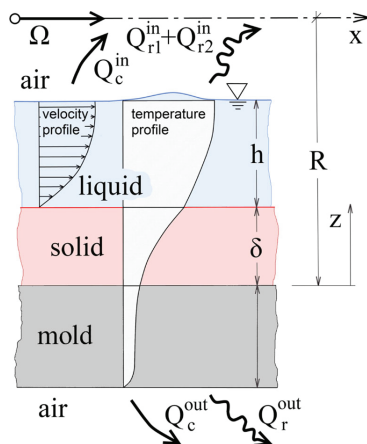


Fig. 2. A schematic of the SWE model. (Online version in color.)

figuration and takes the form:

$$\frac{\partial(\rho h)}{\partial t} + \frac{\partial(\rho hu)}{\partial x} + \frac{\partial(\rho hv)}{\partial y} = 0, \dots\dots\dots (1)$$

where *h* is the liquid height, *x* and *y* denote the axial and tangential direction, and *u* and *v* are respective components of mass weighted average of the velocity. In the axial direction, the velocity *u* is defined by:

$$u = \int_{\delta}^{h+\delta} u(z) dz \dots\dots\dots (2)$$

The mass weighted average *v* of the velocity in the tangential direction is computed analogically. The momentum equations for both directions *x* and *y* are given by:

$$\frac{\partial(\rho hu)}{\partial t} + u \frac{\partial(\rho hu)}{\partial x} + v \frac{\partial(\rho hu)}{\partial y} + F_{cx} + F_{cy} = F_{gx} + F_{rx} \dots (3)$$

and

$$\frac{\partial(\rho hv)}{\partial t} + u \frac{\partial(\rho hv)}{\partial x} + v \frac{\partial(\rho hv)}{\partial y} + F_{cy} + F_{cx} = F_{gy} + F_{ry} \dots (4)$$

where the terms on the left hand side represent the inertia forces including the centrifugal force *F<sub>c</sub>* and Coriolis force *F<sub>C</sub>*. On the right hand side, *F<sub>r</sub>* denotes the shear force. *F<sub>g</sub>* stands for the gravity force (possibly perturbed by vibrations). Obviously, the centrifugal force acts purely in the radial direction, but its effect emerges in the momentum equations for *x* and *y* direction. Thus, any acceleration acting in the radial direction needs to be firstly expressed as the integral of the equivalent hydrostatic pressure over the liquid height *h*. Then the gradient of such an integral gives the correct *x* and *y* components of the corresponding force. Components of the centrifugal force exerted over the liquid are defined by:<sup>18)</sup>

$$F_c = \rho \Omega^2 (R - h - \delta) \nabla (h + \delta) \dots\dots\dots (5)$$

where *R* is the inner radius of the mold and  $\delta$  is the height of the solidifying shell. For the derivation of the Coriolis force dependent on the relative velocity we introduce an additional assumption on the velocity profile within the liquid height *h*. We expect the flow to be fully developed laminar. Hence, a parabolic velocity profile was considered with a no slip boundary condition on the wall and zero friction on the free surface. In the case of a perfectly cylindrical mold, the Coriolis force acts only radially and becomes:<sup>18)</sup>

$$F_C = \rho \Omega h \left( \frac{5}{2} v \nabla h + 2v \nabla \delta + \frac{5}{4} h \nabla v \right) \dots\dots\dots (6)$$

From Eq. (6) it is clear that when the relative motion of the liquid is in the rotational direction, the Coriolis force pushes the liquid towards the mold wall and vice versa. Next, since the relative velocity is maximal on the free surface and zero on the underlying topography, the Coriolis force should be more important at the free surface than on the solid relief. This is indicated by the analytical constants 5/2 and 2 by the terms with the gradient of the liquid height *h* and the solid height  $\delta$ , respectively. The assumption of a parabolic velocity profile is also used in derivation of the bed shear stress<sup>19)</sup> for the Newtonian fluid. The shear force invoked by the bed shear stress acting in the axial direction can be written as:

$$F_{\tau} = -3\mu \frac{u}{h} \dots\dots\dots (7)$$

where  $\mu$  is the dynamic viscosity ( $\sim 0.006$  Pa s) and  $\rho$  is the density ( $\sim 6800$  kg/m<sup>3</sup>). The shear force in the tangential direction is defined using the same formula (Eq. (7)) except that the velocity component  $u$  is replaced by the velocity component  $v$ . The shear force  $F_{\tau}$  plays an important role and balances the centrifugal force, when the liquid height  $h$  diminishes. Finally, the gravity force  $F_g$  has components in both  $x$  and  $y$  directions; however, it is prevailing in the  $y$  (tangential direction). In the axial direction the gravity force  $F_{gx}$  becomes:

$$F_{gx} = -\rho gh \cos(\Omega t) \frac{\partial(h+\delta)}{\partial x} \dots\dots\dots (8)$$

In the tangential direction, the component  $F_{gy}$  of the gravity force becomes:

$$F_{gy} = -\rho gh \left( \cos(\Omega t) \frac{\partial(h+\delta)}{\partial y} + \left(1 - \frac{h}{2R}\right) \sin(\Omega t) \right) \dots\dots (9)$$

where  $g$  is the gravitational acceleration ( $\sim 9.81$  m/s<sup>2</sup>) and  $t$  is the current time. In Eqs. (8) and (9), the terms with the slope of the free surface represent the gradient components of the hydrostatic pressure integrated over the liquid height  $h$ . In other words, in the SWE these terms correctly reflect the effect of the radial component of the gravitational acceleration  $g$ , which has an impact on the flow in both, the axial and the tangential, directions. As already discussed, the real casting is accompanied by inherent vibrations, which are induced by a poor circularity of the carrying rollers or the tracks, and also by deformation of the mold axis due to pouring the hot metal inside the mold. In the numerical model, the vibrations are simply applied by perturbing the gravity force, whereas the mold deformation modifies all other forces except of the shear force  $F_{\tau}$ . The mold deformation was realized by assuming the axis following a sine function with the nodes in the position of carrying rollers and the antinode in the center of the mold representing the lowest axial mode shape of a vibrating cylindrical shell.<sup>20)</sup> Higher axial mode shapes were not considered in this study. The exaggerated picture of such an imperfect mold is shown in **Fig. 3**. Details on the derivation of the SWE including the influence of the vibrations and mold deformation are given in our papers.<sup>21,22)</sup> The first paper<sup>21)</sup> is focused on the investigation of free surface patterns influenced by vibrations and axial mold deformations. Free surface patterns were studied on the initially uniform distribution of the liquid height  $h$ .

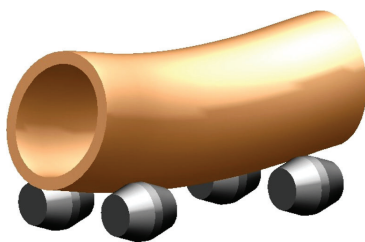


**Fig. 3.** An exaggerated schematic of the deformed mold for Case B. (Online version in color.)

Neither the solidification nor the mold filling were discussed. The second paper<sup>22)</sup> deals with the solidification of the initially uniform thickness of the liquid and analyses the effect of different heat transfer mechanisms on heat losses from the free surface inside the mold. The mold filling was not included in the model.

Concerning the solidification model, we assume that the liquid solidifies exclusively from the mold wall and that there is no slip and also no thermal resistance between the solidifying shell and the mold. Further, it is known that for Prandtl number less than unity, the hydrodynamically fully developed flow is also thermally fully developed. In other words, in our case we believe that the thermal diffusivity is much stronger than the viscous forces; therefore, the thermally fully developed flow is considered. Such a flow is characterized by a parabolic temperature profile (Fig. 1). Further assumptions for the solidification model can be itemized as the following:

- A planar solid/liquid interface is considered between the solid and the liquid ( $s/l$ ). At the current stage of the model, a possible mushy zone is not accounted for.
- The solidifying shell is perfectly attached to the internal mold wall; hence, it rotates with the same angular frequency  $\Omega$  as the mold. In other words, there is no velocity slip between the mold and the solidifying shell.
- Although a separating refractory material ( $ZrO_2$ ) is used to separate mold from the casting, a zero thermal resistance is currently considered.
- Heat fluxes are dominant in the radial direction due to the high pouring temperature ( $\sim 1755$  K) and relatively low initial temperature of the mold ( $\sim 433$  K). For this reason, the heat diffusion equation is simplified and solved only in the radial direction. Lateral heat fluxes are neglected.
- Convective and radiative heat losses are modeled inside and outside the mold. During the real casting the mold fronts are insulated by sand cores; therefore, the heat losses from the fronts are neglected.

In the liquid, the heat advection-diffusion equation (Eq. (10)) is solved for the average temperature  $\bar{T}$  given by:

$$\bar{T} = \frac{1}{h} \int_{\delta}^{h+\delta} T(z) dz \dots\dots\dots (9)$$

The heat advection-diffusion equation can be written as:

$$\frac{\partial(h\bar{T})}{\partial t} + \frac{\partial(h\bar{T})}{\partial x} u + \frac{\partial(h\bar{T})}{\partial y} v = \left( \frac{\partial}{\partial x} h\alpha \frac{\partial \bar{T}}{\partial x} + \frac{\partial}{\partial y} h\alpha \frac{\partial \bar{T}}{\partial y} \right) + S_T \dots\dots\dots (10)$$

where  $\alpha$  is the thermal diffusivity and  $S_T$  is the source term due to solidification and heat transfer to the mold. In the present study the thermal diffusivity  $\alpha$  is kept constant and the same for the liquid, solid, and mold ( $\sim 5.88 \times 10^{-6}$  m<sup>2</sup>/s). In the future, the effective thermal diffusivity will be implemented in order to account for the variable thermal resistance due to the shell shrinkage<sup>23)</sup> and the insulating refractory material ( $ZrO_2$ ). The  $s/l$  interface of the solidifying shell is supposed to be planar fulfilling the Stefan condition<sup>24)</sup> given by:

$$\rho L_f c = k \frac{\partial T_s}{\partial z} - k \frac{\partial T_l}{\partial z}, \dots\dots\dots (11)$$

where  $L_f$  is the latent heat (~250 kJ/kg),  $c$  is the velocity of the  $s/l$  interface normal to the interface and the right hand side denotes the net heat flux through the  $s/l$  interface. The temperature of the  $s/l$  interface corresponds to the temperature of liquidus  $T_{LQ}$  (~1586 K). The subscripts  $s$  and  $l$  denote the solid and the liquid. The thermal conductivity  $k$  is constant (~30 W/(m K)) and same for both, the solid and liquid. The same holds for the density. The Stefan condition is coupled with the 1D heat equation, which is solved numerically on each quadrilateral element of the 2D grid and in cylindrical coordinates has the following form:

$$\frac{\partial T}{\partial t} = \alpha \frac{1}{r} \frac{\partial}{\partial r} \left( r \frac{\partial T}{\partial r} \right), \dots\dots\dots (12)$$

Equation (12) describes the heat conduction through the solidifying shell to the mold. Only the 1D heat equation is solved because the lateral heat fluxes are compared to the radial heat fluxes negligible. The Dirichlet boundary condition is applied on the solid/liquid interface ( $T_l=1586$  K). On the outer wall of the mold the Neumann boundary condition is employed representing convective and radiative heat losses (described below). The convective and radiative heat transfer from the free surface inside the mold was taken into account. The convective losses were simplified by considering a constant heat transfer coefficient  $HTC_{in}$  of 100 W/(m<sup>2</sup>K). Outside of the mold convective heat losses were also accounted for, but due to higher circumferential velocity the heat transfer coefficient  $HTC_{out}$  was increased (~150 W/(m<sup>2</sup>K)). The model of the radiative heat transfer inside the mold is split into two parts. The first part denotes the heat losses via extremities, whereas the second part denotes the heat exchange inside the mold due to the fact that some regions are hotter (or colder) than others. The theory of a black body was applied to simplify the problem.<sup>25)</sup> The radiative heat losses via extremities (mold openings) from each surface element were formulated as the following:

$$Q_{r1}^{in} = A(1 - F_w) \sigma (T^4 - T_a^4), \dots\dots\dots (13)$$

where  $A$  is the area of the quadrilateral free surface element,  $\sigma$  is the Stefan-Boltzmann constant (~5.67e-08 W/(m<sup>2</sup>K<sup>4</sup>)),  $T$  is the temperature of the free surface and  $T_a$  is the temperature of the ambient (~323 K).  $F_w$  represents a geometrical resistance or a view factor, which generally depends on the distance between two radiating surfaces and angles between them. Unfortunately, even for this simple case of a cylindrical mold with two openings, the view factor  $F_w$  cannot be determined analytically. A numerical approximation of the view factor  $F_w$  is however feasible<sup>26)</sup> and is given by the polynomial of the fourth order as the following:

$$F_w = ax^4 + bx^3 + cx^2 + dx + e, \dots\dots\dots (14)$$

where  $x$  is the axial position, which is zero at one extremity. The constants  $a, b, c, d,$  and  $e$  are -0.1539, 0.7795, -1.502, 1.34, and 0.4981. The constants were determined for the specific case with the mold internal radius  $R=0.372$  m and the mold length  $L=3.2$  m. However, the view factor  $F_w$  is related to the actual shape of the free surface inside the mold; therefore, it is time dependent. Qualitatively we can

say that as the liquid height  $h$  increased during the filling, the radiative heat exchange inside the mold becomes more important, whereas the radiative heat losses via extremities diminish. On the other hand, the percentage rate of change of the view factor  $F_w$  is small. Therefore, rather than applying computationally expensive approximation of the constants in Eq. (13) every time step, we accepted a certain error and used the time independent constants  $a, b, c, d,$  and  $e$ . The summation rule applies for any enclosure; therefore, the view factor  $F_w$  can be used to determine the radiative heat exchange inside the mold, which takes the following form:

$$Q_{r2}^{in} = AF_w \sigma (T^4 - T_w^4), \dots\dots\dots (15)$$

where  $T_w$  is the mean surface temperature, which is determined from the energy conservation inside the mold given by:

$$\sum_{i=1}^4 AF_w \sigma (T^4 - T_w^4) = 0, \dots\dots\dots (16)$$

Using Eq. (15) the mean average temperature  $T_w$  becomes:

$$T_w = \sqrt[4]{\frac{\sum F_{iw} T_i}{\sum F_{iw}}}, \dots\dots\dots (17)$$

in which we need to evaluate sums of  $F_{iw} T_i$  and  $F_{iw}$  over all grid elements. The relation for the radiative heat losses from the outer wall of the mold is much simpler, since the view factor from an arbitrary surface element to the ambient is always equal unity. The corresponding formula is given by:

$$Q^{out} = A \sigma (T^4 - T_a^4), \dots\dots\dots (18)$$

The filling of the mold was realized through a circular mass source in the center of the mold. Since the SWE were solved in the rotating frame of reference, the mass source had to travel in the anti-rotational direction. From the observations during the real casting the momentum of the impinging jet presumably did not have an effect on the initial formation of the liquid ring around the circumference (Fig. 4). In addition, the filling jet evidently did not have sufficient momentum to penetrate through the initial liquid ring and come closer to the mold extremities. Therefore, the momentum of the filling jet was ignored in the simulations. The profile of



Fig. 4. An early stage of the filling ( $t < 5$  s); a filling jet emitting from the filling arm, splashing on the rotating inner wall of the mold ( $R=0.372$  m,  $\Omega=71.2$  rad/s), and forming a ring around the mold circumference. (Online version in color.)

the mass source for the filling jet was naturally approximated by a normal distribution with the standard deviation  $\sigma$  estimated from the real casting observations (~90 mm). The real footprint of the filling jet is however far away from a smooth normal distribution. Therefore, the profile of the impingement density was perturbed by means of a Box-Muller transform around the center of the filling jet, which is generally given by:

$$N = \sqrt{-2 \ln U_1} \cos(2\pi U_2), \dots \dots \dots (19)$$

where  $U_1$  and  $U_2$  are randomly sampled numbers from the interval (0, 1]. For a set of  $U_1, U_2$  the resulting  $N$  number follows a normal distribution. Using this algorithm the elements in the vicinity of the filling jet center were visited and for each element a number of visits was counted. The ratio between a number of visits and total number of tries gave a strength  $s$  of the mass source term  $S_m$ , which takes the following form:

$$S_m = 30.2035(1 - \exp(-t)) \frac{s}{A}, \dots \dots \dots (20)$$

where the time dependent exponential function applies to the variable mass flow rate during the first 5 seconds of the casting, after which the mass flow rate is kept constant of 30 kg/s. Although the end of the filling was not reached in the present simulation results, in the real casting the filling is stopped at  $t=90$  s.

Flow and thermal boundary conditions are summarized in **Table 1**. Second order discretization schemes were used for time and space. The algorithm was stable for the convective condition  $CFL \leq 1$ . A computational domain for the flow computation consisted of  $160 \times 117$  (the mold length  $L \times$  the mold circumference  $2\pi R$ ) orthogonal quadrilateral elements. The heat diffusion in the radial direction was performed on 200 equally spaced grid points. The grid size dependency was tested on a 1D cold flow simulation (without the solidification) of a collapsing liquid column hitting a solid obstacle. The tested number of grid points was 100, 300, and 1000 s. A wave speed was slightly overestimated for a small number of grid points (100). For a larger number of grid points a wave speed error can be neglected (**Fig. 5**).

**3. Results and Discussion**

The list of dimensions used in simulations is the following: the length of the mold  $L$  of 3.2 m, the internal mold radius  $R$  of 0.372 m, and the mold wall thickness of 0.203 m. Material properties and other model settings were mentioned

**Table 1.** Boundary conditions.

location for BC	flow BC	thermal BC
free surface of the liquid	$\left( \frac{\partial u(z)}{\partial z}, \frac{\partial v(z)}{\partial z} \right) = 0$	
free surface of the solid	$(u(z), v(z)) = 0$	$Q$ (convection, radiation)
dry inner wall of the wall	-	
outer wall of the mold	-	
$s/l$ interface	$(u(z), v(z)) = 0$	$T = T_{LIQ}$
mold extremities	Reflective wall $hu_{GHOST} = -hu$	$Q = 0$ (adiabatic wall)

in the previous section. As the initial conditions ( $t=0$  s), we considered an empty mold rotating in the positive direction with the angular frequency  $\Omega$  of 71.2 rad/s. During the simulation the angular frequency  $\Omega$  was held constant, although in the real casting especially during the filling a certain drop in  $\Omega$  is always recorded. At both extremities reflective boundary condition was applied for the flow and zero flux for the enthalpy. Two types of simulations were carried out differing only in the geometrical configuration. The Case A simulation was performed assuming a perfectly cylindrical mold *i.e.* Eqs. (1)–(4) were solved, whereas the Case B simulation was done for a slightly deformed mold with the amplitude of 2 mm at the antinode (**Fig. 3**). The results are presented on the inner mold wall unfolded in the horizontal plane as depicted in **Fig. 6**.

In the early stage of the filling, when the mass flow rate was still rising according to the exponential function given in Eq. (19) and the cold mold wall was not exposed to the hot liquid yet, the solidification rate is extremely high and newly incoming liquid solidifies almost instantly. In **Fig. 7**, the actual free surface situation is visualized by means of the free surface temperatures at  $t=0.5$  s. The liquid free surface is depicted by the pear-shaped region, from where the position of the jet center is clear (shown as a circle). The filling jet is travelling in the anti-rotational direction. In the neighboring zone the liquid solidified completely; thus, only the solid can be seen. The rest of the surface was not touched by the liquid metal, which is indicated by a significantly lower temperature very close to the initial temperature of the

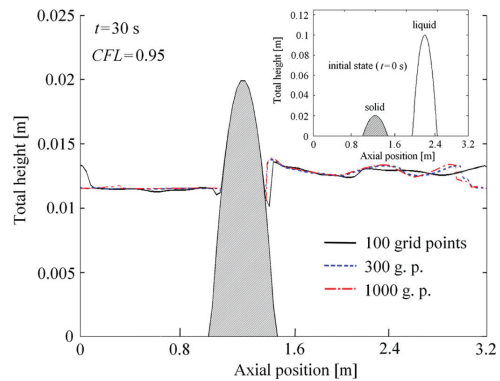


**Fig. 5.** A free surface of the liquid after a collapse of the liquid column with a wave reflection from the solid obstacle at  $t=30$  s; Initial state ( $t=0$  s) shown in a smaller scale. (Online version in color.)

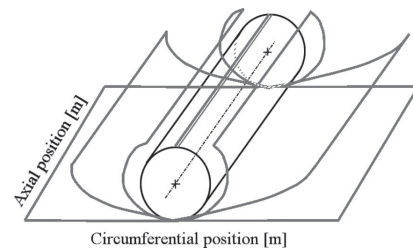


**Fig. 6.** A cylindrical surface of the inner mold wall unfolded into the horizontal plane.

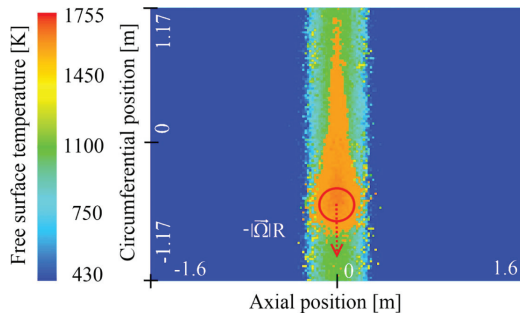


Fig. 7. Contours of the free surface temperature at the early stage of the filling at  $t=0.5$  s with the solid free surface, the liquid free surface, and a dry wall of the mold.; the actual position of the jet is shown as a circle. (Online version in color.)

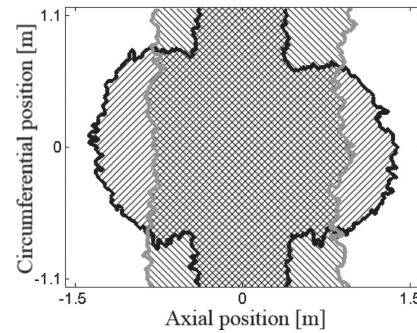


Fig. 8. Position of the moving contact line for results of Case A and Case B at  $t=6$  s shown in grey and black, respectively.

mold ( $\sim 433$  K). As the solidification and filling proceed, the moving contact lines (where the mold is for the first time being wetted by the metal) are travelling to both extremities with an average speed of around 0.15 m/s. At around 2 seconds the results of Case A deviate from that of Case B. In Fig. 8, we compare the actual position of the moving contact line of Case A and B at  $t=6$  s. Obviously, in the case of the perfectly cylindrical mold the moving contact lines remain approximately parallel to the extremities (grey), which does not apply to the case with a deformed mold. Even a very small deformation of the mold (which was considered in Case B), controls the spreading of the melt towards the extremities. Note that we considered only one specific shape of deformed mold. However, this will hold also for many other shapes. The mold extremities are reached at around 10 seconds, however; the way how the extremities are reached is completely different for a deformed mold compared to an ideal non-deformed one. In the Case B nearly symmetric bulges on both sides from the jet continue to grow. Once the bulge touches itself after surrounding the whole circumference, the liquid height increases in that place and high centrifugal force generates a stream that quickly fills up the empty space close to the extremities (see Fig. 8 Case B). Note that the bulge is shifted slightly upwards due to the Coriolis force, which accelerates the liquid relatively moving in the rotating direction and decelerates the liquid moving in the anti-rotational direction. As shown in Fig. 8, in Case A it is small disturbances in the filling jet that are defining the shape of the contact line, and not the deformation of the mold. In the early stage of the casting (Fig. 7), the contact lines are relatively parallel to the extremities. Later, instabilities occur and form regions with bulges and depressions, which then in a random manner proceed towards the extremities (see Fig. 10 of the real casting). To confirm this random behavior of the liquid spreading, the Case A simulation was run three times. In Fig. 9, the asymmetry of the liquid spreading is much more notable for Case A. This asymmetry also causes that in some regions the liquid solidifies completely. Later, a newly coming liquid inundates the solid again and remelting occurs. Such an occurrence of dry regions is shown in grey in Fig. 11 at  $t=30$  s. The liquid free surface is shown in white. Black dotted arrows highlight the original filling streams whereby the liquid is mainly transported towards the extremities. In Fig.

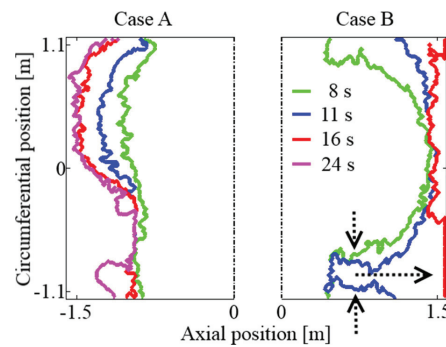


Fig. 9. Actual positions of the contact lines for the Case A and Case B at several time instants. The vertical arrows indicate a tangential spreading of the bulge, whereas the horizontal arrow shows the position and flow orientation of the future dominating filling stream. (Online version in color.)

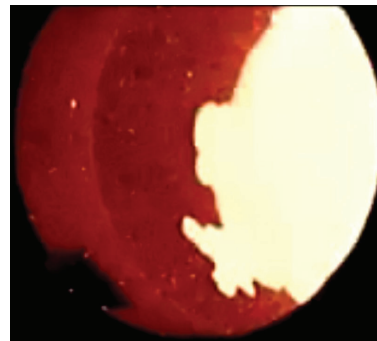


Fig. 10. A snapshot taken during the real casting at approximately  $t=8$  s showing uneven spreading of the melt towards the extremity (a sand core); the filling rate of 30 kg/s, the angular frequency  $\Omega=30$  rad/s, the mold radius  $R=0.372$  m, and the mold length  $L=3.2$  m. (Online version in color.)

12, a complex wavy relief of the solid/liquid interface is excavated after removing the liquid layer. The position of the filling streams shown in the previous figure now corresponds to the distinct valleys that are a consequence of a reduced solidification rate due to the fresh hot liquid. The same mechanism was applied along the footprint of the filling jet resulting in the formation a pool. Although the solidification starts firstly in the mold center *i.e.* where the filling jet firstly touches the wall, the shell is after some time

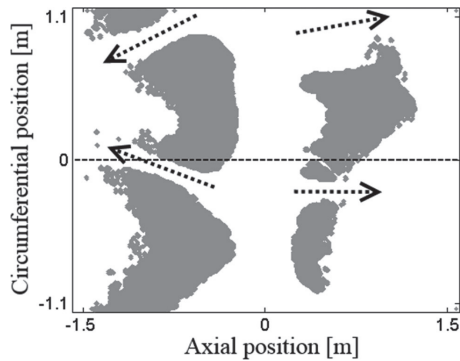


Fig. 11. Dry regions (grey) occurring due to uneven spreading of the liquid towards the left and right extremity for Case A at  $t=30$  s; the liquid free surface shown in white with dashed arrows highlighting the position of the filling streams.

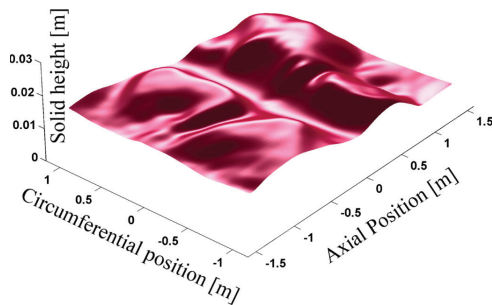


Fig. 12. A 3D relief of the solid/liquid interface for Case A at  $t=30$  s. (Online version in color.)

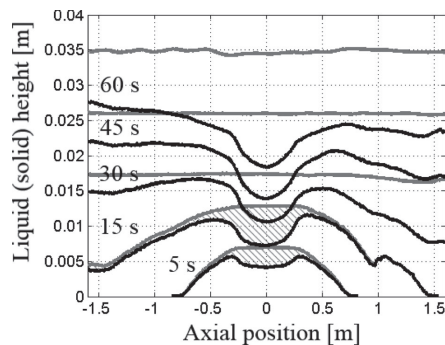


Fig. 13. A time evolution of the solid/liquid interface (black) with the respective liquid free surface (grey) along the axial direction for Case A.

(~30 s) thicker at the extremities. This is mainly caused by the centered position of the filling jet, but also due to increased radiative heat losses at the extremities. A time evolution of the  $s/l$  interface profile (black) with the respective liquid free surface (grey) is shown along the mold axis (dashed line in Fig. 11) for both Case A and Case B in Figs. 13 and 14, respectively. In Case B (Fig. 14), the profile of the  $s/l$  interface is evidently much more symmetric than in Case A (Fig. 13). Moreover, the pool formed in the center is wider open, which is demonstrated by a two sided arrow in Fig. 14. In addition, on the free liquid surface waves are

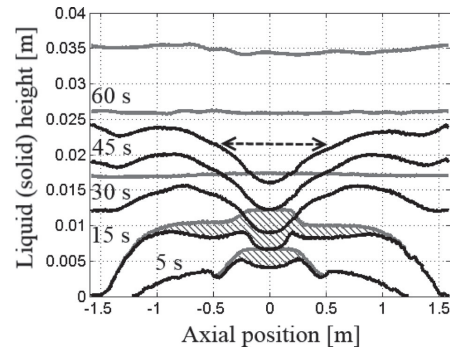


Fig. 14. A time evolution of the solid/liquid interface (black) with the respective liquid free surface (grey) along the axial direction for Case B; The two sided arrow demonstrates a wider pool compared to Case A.

induced by interaction of the forces and the underlying topography, which is more noticeable at later stages of the casting (~60 s) when the liquid height is higher. Various wave patterns appearing on the free surface are beyond the scope of this paper. More details on this topic can be found in our papers.<sup>21,22)</sup>

#### 4. Conclusions

A complexity of a 3D flow during the horizontal centrifugal casting of a large work roll was reduced with the aid of the shallow water equations (SWE) by solving only the axial and tangential velocity components, neglecting momentum in the radial direction, but still resolving the height of the liquid. Using the SWE we save a great amount of the computational power, which consequently allows us to perform parameter studies. The original SWE were modified to account for forces such as the centrifugal force, the Coriolis force, the bed shear stress and the gravity. In addition, a deformation of the mold due to the thermal effects was taken into account assuming a specific shape of the mold (Fig. 3). A simple solidification model was added to the flow equations assuming a dominant heat flow in the radial direction and thus, solving only the 1D heat equation the solid and the mold for each element of the 2D grid. The Stefan condition was applied at the solid/liquid interface to determine its speed. In the paper we focused on the early stage of the casting including the modeling of the filling, which was done by applying a randomly sampled mass source resembling a normal distribution of the impingement density around the jet center. Two different cases were studied, Case A representing a perfectly cylindrical mold and Case B representing a slightly deformed mold. In both cases, the filling jet was responsible for a delayed solidification underneath, which led to the formation of a pool surrounding the circumference. The mold extremities were reached approximately at the same time (~10 s) as during the real casting. However, even in the real casting the liquid does not move towards the extremities uniformly, the contact line forms into finger-like patterns. In Case A, the contact line was more disturbed by the filling jet, whereas in the B) simulation the shape of the contact line was rather controlled by the deformed mold resulting in a more symmetric profile of

the solid/liquid interface along the axial direction. Note that in all simulations a zero thermal resistance was considered in contact between the solidifying shell and the mold. In practice, a refractory material such as  $ZrO_2$  is used to separate the mold from the casting. At the same time, such coating can be used to passively control the heat transfer from the casting by varying the coating thickness along the mold axis. In the present paper only the outer shell (or one layer) was concerned. As a next step we plan to include the second layer (the intermediate layer), which serves as a blending bridge between the outer shell and the gravitationally cast core.

#### Acknowledgements

Financial support by the Austrian Federal Government (in particular from the Bundesministerium fuer Verkehr, Innovation und Technologie and the Bundesministerium fuer Wirtschaft, Familie und Jugend) and the Styrian Provincial Government, represented by Oesterreichische Forschungsforderungsgesellschaft mbH and by Steirische Wirtschaftsforderungsgesellschaft mbH, within the research activities of the K2 Competence Centre on "Integrated Research in Materials, Processing and Product Engineering", operated by the Materials Center Leoben Forschung GmbH in the framework of the Austrian COMET Competence Centre Programme, is gratefully acknowledged. This work is also financially supported by the Eisenwerk Sulzau-Werfen R. & E. Weinberger AG.

#### Nomenclature

$A$ : area of the quadrilateral free surface element ( $m^2$ )  
 $c$ : speed of the solidifying front in radial direction (m/s)  
 $a, c, b, d, e$ : constant for the analytical expression of the view factor (–)  
 $d$ : diameter of a particle (m)  
 $F$ : force (N.m/kg)  
 $F_w$ : view factor (geometrical resistance)  
 $h$ : liquid height (m)  
 $HTC$ : heat transfer coefficient ( $W/(m^2K)$ )  
 $k$ : thermal conductivity ( $W/(m.K)$ )  
 $L$ : length of the mold (m)  
 $L_f$ : latent heat of fusion (J/kg)  
 $N$ : randomly sampled number from a normal distribution (–)  
 $Q$ : heat flux (W)  
 $r$ : radial position (m)  
 $R$ : inner mold radius (m)  
 $s$ : strength of the mass source (–)  
 $S_m$ : mass source ( $kg/(m^2s)$ )  
 $S_T$ : heat source term ( $W/m^2$ )  
 $t$ : time (s)  
 $T$ : temperature (K)  
 $T_{LID}$ : temperature of liquidus (K)  
 $u$ : mass weighted average of velocity in axial direction (m/s)  
 $U_1, U_2$ : numbers from interval (0, 1] (–)  
 $v$ : mass weighted average of velocity in tangential direction (m/s)

$V$ : volume of a particle ( $m^3$ )  
 $x$ : axial position (m)  
 $y$ : tangential position (m)  
 $z$ : radial position (m)  
 $\alpha$ : thermal diffusivity ( $m^2/s$ )  
 $\delta$ : solid height (m)  
 $\mu$ : dynamic viscosity (Pa.s)  
 $\rho$ : density ( $kg/m^3$ )  
 $\sigma$ : Stefan-Boltzmann constant ( $W/(m^2K^4)$ )  
 $\Omega$ : angular frequency of the mold (rad/s)

#### Indices:

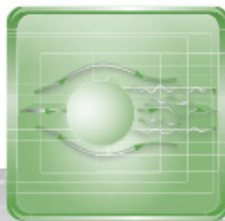
$a$ : ambient air  
 $c$ : centrifugal force  
 $C$ : Coriolis force  
 $g$ : gravity  
 $GHOST$ : ghost cell  
 $i$ : cell index  
 $in$ : inside the mold  
 $l$ : liquid  
 $out$ : outside the mold  
 $P$ : particle  
 $r1$ : radiative losses via extremities  
 $r2$ : radiative heat redistribution inside the mold  
 $s$ : solid  
 $\tau$ : bed shear stress

#### REFERENCES

- G. Chirita, I. Stefanescu, J. Barbosa, H. Puga, D. Soares and F. S. Silva: *Int. J. Cast Met. Res.*, **22** (2009), 382.
- R. Zagórski and J. Śleziona: *Arch. Mater. Sci. Eng.*, **28** (2007), 441.
- S. R. Chang, J. M. Kim and C. P. Hong: *ISIJ Int.*, **41** (2001), 738.
- K. S. Keerthiprasad, M. S. Murali, P. G. Mukunda and S. Majumdar: *Front. Mater. Sci. China*, **4** (2010), 103.
- N. Abu-Dheir, M. Khraisheh, K. Saito and A. Male: *Mater. Sci. Eng.*, **A393** (2004), 109.
- G. Martinez, M. Garnier and F. Durand: *Appl. Sci. Res.*, **44** (1987), 225.
- H. Esaka, K. Kawai, H. Kaneko and K. Shinozuka: *IOP Conf. Series: Mater. Sci. Eng.*, **33** (2012), 012041.
- G. Chirita, I. Stefanescu, D. Soares and F. S. Silva: *Anales de Mecánica de la Fractura*, **1** (2006), 317.
- K. S. Keerthiprasad, M. S. Murali, P. G. Mukunda and S. Majumdar: *Metall. Mater. Trans. B*, **42** (2010), 144.
- P. S. S. Raju and S. P. Mehrotra: *Mater. Trans. JIM*, **41** (2000), 1626.
- L. Drenchev, J. Sobczak, S. Malinoc and W. Sha: *Model. Simul. Mater. Sci. Eng.*, **11** (2003), 635.
- Z. Xu, N. Song, R. V. Tol, Y. Luan and D. Li: *IOP Conf. Series: Mater. Sci. Eng.*, **33** (2012), 012030.
- E. Kaschnitz: *IOP Conf. Series: Mater. Sci. Eng.*, **33** (2012), 012031.
- P. J. Dellar and R. Salmon: *Phys. Fluid.*, **17** (2005), 1.
- C. W. Hirt and J. E. Richardson: *Flow Sci. Tech. Note.*, **48** (1999), 1.
- R. J. Leveque: *Finite Volume Methods for Hyperbolic Systems*, Cambridge University Press, New York, (2002), 429.
- P. Garcia-Navarro, P. Brufau, J. Burguete and J. Murillo: *Monografías de la Real Academia de Ciencias de Zaragoza*, **31** (2008), 89.
- A. Kharicha, J. Bohacek, A. Ludwig and M. Wu: to be published.
- J. Murillo and P. Garcia-Navarro: *J. Comput. Phys.*, **231** (2012), 1963.
- A. E. H. Love: *Phil. Trans. Roy. Soc. London (ser. A)*, (1888), 495.
- J. Bohacek, A. Kharicha, A. Ludwig and M. Wu: Proc. Int. Conf. Experimental Fluid Mechanics, Vol. 2, Technical University of Liberec, Liberec, (2011), 564.
- J. Bohacek, A. Kharicha, A. Ludwig and M. Wu: *IOP Conf. Series: Mater. Sci. Eng.*, **33** (2012), 012032.
- E. Panda, D. Mazumdar and S. P. Mehrotra: *Metall. Mater. Trans.*, **37** (2006), 1675.
- J. A. Dantzig and M. Rappaz: *Solidification*, EPFL Press, Lausanne, (2009), 134.
- F. P. Incropera and D. P. DeWitt: *Fundamentals of Heat and Mass Transfer*, 5th ed., John Wiley & Sons, Hoboken, (2001), 790.
- J. Bohacek, A. Kharicha, A. Ludwig and M. Wu: to be published.



JOURNAL OF FLUIDS  
ENGINEERING



November 2015

ASME JOURNALS  
SETTING THE STANDARD FOR ENGINEERING KNOWLEDGE SHARING

## Abdellah Kharicha<sup>1</sup>

Department of Metallurgy,  
University of Leoben,  
Franz Josef-Strasse 18,  
Leoben 8700, Austria  
e-mail: abdellah.kharicha@unileoben.ac.at

## Jan Bohacek

Department of Metallurgy,  
University of Leoben,  
Franz Josef-Strasse 18,  
Leoben 8700, Austria  
e-mail: jan.bohacek@unileoben.ac.at

## Andreas Ludwig

Professor  
Department of Metallurgy,  
University of Leoben,  
Franz Josef-Strasse 18,  
Leoben 8700, Austria  
e-mail: andreas.ludwig@unileoben.ac.at

## Menghuai Wu

Laboratory for Advanced Simulation  
of Solidification and Melting  
Department of Metallurgy,  
University of Leoben,  
Franz Josef-Strasse 18,  
Leoben 8700, Austria  
e-mail: menghuai.wu@unileoben.ac.at

# Modified Shallow Water Equations With Application for Horizontal Centrifugal Casting of Rolls

*A numerical model based on the shallow water equations (SWE) was proposed to simulate the two-dimensional (2D) average flow dynamics of the liquid metal spreading inside a horizontally rotating mold. The SWE were modified to account for the forces, such as the centrifugal force, Coriolis force, shear force with the mold wall, and gravity. In addition, inherent vibrations caused by a poor roundness of the mold and the mold deformation due to temperature gradients were applied explicitly by perturbing the gravity and the axis bending, respectively. Several cases were studied with the following initial conditions: a constant average height of the liquid metal (5, 10, 20, 30, and 40 mm) patched as a flat or a perturbed surface. The angular frequency  $\Omega$  of the mold ( $\varnothing 1150$ – $3200$ ) was 71.2 (or 30) rad/s. Results showed various wave patterns propagating on the free surface. In early stages, a single longitudinal wave moved around the circumference. As the time proceeded, it slowly diminished and waves traveled mainly in the axial direction. It was found that the mean amplitude of the oscillations grows with the increasing liquid height. [DOI: 10.1115/1.4030760]*

## 1 Introduction

The horizontal centrifugal casting (HSC) is a casting process that has several advantages over the traditional gravity casting processes. The schematic of the HSC process is shown in Fig. 1. Centrifugally cast products have a high degree of metallurgical purity and homogeneous microstructure. A significant gain is observed for the rupture strength, the rupture strain, the fatigue resistance, and the Young's modulus as discussed, e.g., by Shailesh et al. [1]. These properties naturally depend on the centrifugal force and thus, the best mechanical properties can be found at the largest distance from the axis of rotation. However, a proper selection of the angular frequency  $\Omega$  has to be done in order to prevent the so-called "metal raining," i.e., metal droplets falling down from the upper part of the mold due to a too weak centrifugal acceleration. In the same time, excessive speeds can lead to the appearance of longitudinal cracks caused by the hoop stress in the initially solidified layer. From empirical knowledge, other parameters have an important influence on the casting products, it includes the pouring temperature, the pouring rate, the mold coating, etc. Recently, Chirita et al. [2] identified natural or forced vibrations as possible additional factors to be taken into account. Although mechanisms are not yet clear, the vibrations influence the solidification structure and the level of porosity. Earlier, Chirita et al. [3] observed a transition from the lamellar to the fibrous morphology with the increase of the vibration amplitude. An

influence on the eutectic fraction was also observed. If the acceleration related to the vibration reaches a critical magnitude, the grains tend to coarsen. It is generally assumed that during the centrifugal casting, the melt first solidifies on the mold wall, then due to the turbulent flow, fragments are moved back into the melt and stand as a new nucleation sites as described by Chang et al. [4]. It is believed that vibrations can significantly enhance this grain refining process.

In most of the scientific papers, numerical studies of the centrifugal casting usually rely on commercial CFD packages. Certainly, the most common approach for solving the free-surface flows is



Fig. 1 A schematic of the horizontal centrifugal casting of the outer shell of a work roll

<sup>1</sup>Corresponding author.

Contributed by the Fluids Engineering Division of ASME for publication in the JOURNAL OF FLUIDS ENGINEERING. Manuscript received February 24, 2014; final manuscript received May 28, 2015; published online July 21, 2015. Assoc. Editor: Samuel Paolucci.

the volume of fluid (VOF) method by Hirt and Nichols [5], which is very robust and applicable to various free-surface flows. Unfortunately, to accurately track the interface a very fine grid is usually required and moreover, one has to solve the flow also in the ambient phase, which is rather redundant in the case of the HSC. In the paper by Keerthiprasad et al. [6], an effort for a comprehensive description of the flow dynamics of the melt inside the horizontally rotating mold including the mold filling was done using the VOF model (STAR-CD). Two phases were considered, the liquid metal and the surrounding air. The time step was notably large ( $\sim 0.01$  s), which implies a very rough calculation. Nevertheless, the results were found to be in quite good agreement with experimental data. The VOF method was also used in work done by Zagorski and Sleziona [7] to study the initial stage of mold filling during the vertical centrifugal casting of metal matrix composite reinforced with SiC. Additionally, a discrete phase model was used to track SiC particles. The problem was solved as 2D axisymmetric with swirl component of velocity and all calculations were terminated at 1 s of real-time. At a sufficiently high rotating speed of the mold, the liquid metal rotates with the mold. Therefore, it is convenient to solve the task in the rotating frame of reference, i.e., to take into account fictitious forces such as the centrifugal and Coriolis force. This approach naturally allows using much larger time steps resulting in a significant speed-up of calculations. Recently, this solution strategy was adopted by Kaschnitz [8], where the horizontal centrifugal pipe casting process was solved using *FLOW-3D*. Although the flow algorithm does not consider the flow within the ambient air, the normal computation still took around 20 days for a relatively rough mesh. To overcome mesh-dependent results, the numerical model was tuned by adjusting the viscosity, turbulent properties, and comparing numerical results with the experiment. Next, the effect of fictitious forces on the mold filling during the vertical centrifugal casting was investigated again by using the VOF model [9]. They found that the Coriolis force can cause remarkable variations in the flow patterns in the casting-part-cavities of a large horizontal-section area and directly connected to the sprue. Another recent study of the mold filling was performed by Xu et al. [10], in which the effect of the static and moveable filling on the temperature distribution during the HSC of a work roll was studied. The second naturally produces a more uniform temperature distribution, which could lead to the elimination of the so-called sapling defects. The flow algorithm is based on the VOF free-surface tracking method. Since simulations were focused on the filling ( $\sim 30$  s), the full HSC process ( $\sim 35$  mins) was not of concern and the algorithm performance or computational times were not discussed. Fjeld and Ludwig [11] performed a numerical study of the casting of a work roll core. The popular VOF method was employed to track the interface between the liquid metal and air. The remelting of the outer shell was mainly investigated (more details related to simulations of multiphase phenomena are clearly discussed in the work by Ludwig et al. [12]).

The aim of the present model is a development of an effective flow algorithm for tracking the free surface of a thin liquid layer inside a horizontally rotating cylindrical mold representing the outer shell of a work roll. Numerical simulations are focused on the investigation of wave patterns appearing on the free surface due to the interaction of the inertia forces including fictitious forces and other body forces, such as the gravity and forces resulting from mold vibrations. In the future, the current numerical model will be extended to account for the solidification and the heat transfer including the radiation inside the mold. From a long-term perspective, we target on the simulation of the full HSC process, i.e., the casting of both the outer (the high-speed steel) and the intermediate (the gray cast iron) layer. The HSC process is finished after approximately 35 mins when the mold is turned in the vertical position and the gravity casting of the core takes place. By comparing the HSC time ( $\sim 35$  mins) with relatively high velocities of the liquid metal ( $\sim 1$  m/s), we can conclude that the algorithm has to be extremely fast and efficient.

## 2 Numerical Model

The present model is based on the SWE. The SWE are widely used for modeling purposes in oceanography and also meteorology. Its original form can be found in the book by Leveque [13] and are used for a mathematical description of the so-called gravity waves. The SWE can be generalized to account for various physical phenomena, such as the Coriolis force, flow over variable topography, and bed shear stress, which are discussed, e.g., in Dellar and Salmon [14] and Hirt and Richardson [15]. The SWE usually refer to the modeling of the so-called gravity waves. In the literature, the SWE can be found derived in the Cartesian coordinate system as well as in the spherical coordinate system [16], but no application of the SWE could be found for the cylindrical geometry. Note that by using the SWE, the momentum equation in the direction perpendicular to the underlying topography is always omitted. In other words, under certain conditions a three-dimensional (3D) problem can be transformed into a 2D problem, which can still resolve the height in the vertical (or radial) direction.

Here, we present a shallow water model for modeling the average flow dynamics of the thin liquid layer inside a horizontally rotating mold (see Fig. 1). The SWE were derived in the rotating frame of reference, i.e., fictitious forces were included in the model. The SWE were further modified in order to account for the variable topography representing the liquid/solid interface. The solidification and heat transfer are, however, out of the scope of this paper. A general situation is depicted in Fig. 2, in which the parabolic velocity profile indicates the assumption of the fully developed laminar flow.

Next, we assume a no-slip boundary condition (BC) with the underlying topography. On the free surface, the friction with air and surface tension effects is neglected. The liquid height  $h$  is small compared to the internal radius  $R$  of the mold; therefore, the

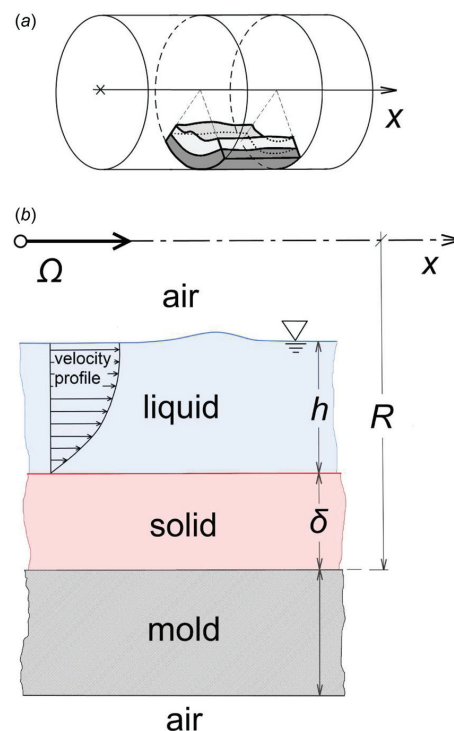


Fig. 2 A schematic of a part of the HSC section

problem can be still solved in the Cartesian coordinates  $(x, y)$  representing the axial and tangential direction, respectively. Perhaps, the most important assumption applies to neglecting all vertical (or radial) components in momentum equations except the gradients of the hydrostatic pressure. In the shallow water terminology, this is often called the condition of the hydrostatic balance discussed by Audusse et al. [17].

The continuity equation takes the form

$$\frac{\partial(h\rho)}{\partial t} + \nabla \cdot (h\rho\bar{\mathbf{u}}) = 0 \quad (1)$$

where the liquid density  $\rho$  is a constant in the model ( $\sim 6800 \text{ kg/m}^3$ ), and  $\bar{\mathbf{u}}$  is the mass flow averaged velocity of the liquid. The momentum equations can be expressed in the vectorial form as follows:

$$\frac{\partial(h\rho\bar{\mathbf{u}})}{\partial t} + \bar{\mathbf{u}} \cdot (\nabla(h\rho\bar{\mathbf{u}})) + \mathbf{F}_c + \mathbf{F}_C = -h\nabla p + h\mu\nabla^2\bar{\mathbf{u}} + \mathbf{F}_\tau + \mathbf{F}_g \quad (2)$$

where the terms on the left-hand side represent the inertia forces including the fictitious forces. The centrifugal force  $\mathbf{F}_c$  is derived from the centrifugal acceleration  $\mathbf{a}_c$  given by

$$\mathbf{a}_c = \Omega \times (\Omega \times \mathbf{r}) \quad (3)$$

where  $\mathbf{r}$  is the position vector. The centrifugal force  $\mathbf{F}_c$  always pushes the liquid outward. For a perfectly cylindrical mold, the only nonzero component of the centrifugal acceleration  $\mathbf{a}_c$  is the radial component  $a_{cr}$ . The radial component  $a_{cr}$  cannot be, however, applied directly in Eq. (2). It has to be first expressed as an equivalent hydrostatic pressure. Then, the integral of the gradient of this hydrostatic pressure over the liquid height  $h$  gives the axial and tangential components of the centrifugal force  $\mathbf{F}_c$  used in Eq. (2). The same procedure is applied on all other body forces having a nonzero radial component. A detailed derivation of the centrifugal force  $\mathbf{F}_c$  can be found in Appendix B. The Coriolis force  $\mathbf{F}_C$  is derived from the Coriolis acceleration  $\mathbf{a}_C$ , which depends on the relative velocity  $\mathbf{u}$  and is given by

$$\mathbf{a}_C = 2\Omega \times \mathbf{u} \quad (4)$$

Unlike the centrifugal force  $\mathbf{F}_c$ , the Coriolis force  $\mathbf{F}_C$  either pushes the liquid inward or outward depending on the orientation of the relative velocity  $\mathbf{u}$ . Note that this is only true for a perfectly cylindrical mold and the angular frequency  $\Omega$  parallel to the mold axis. For more details, see Appendix C. On the right-hand side of Eq. (2), the first two terms represent the force resulting from the static pressure difference and the viscous force derived from the shear stresses in the plane  $(x, y)$ , respectively. Note that the viscous force does not account for the shear force with the mold due

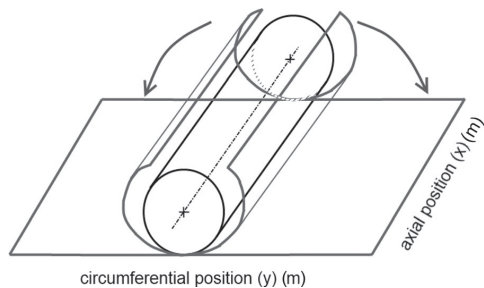


Fig. 3 A schematic of the computational domain created by unfolding the internal cylindrical surface of the mold into the plane  $(x, y)$

to the no-slip BC imposed. The bed shear force with the mold depends on the parabolic velocity profile and is applied separately denoted by  $\mathbf{F}_\tau$  (Appendix F). The last term in Eq. (2) refers to the gravity force  $\mathbf{F}_g$ , which in the rotating frame of reference is a vector rotating in the opposite direction of the rotating mold  $(-\Omega)$ . The final formulas for  $\mathbf{F}_g$  used in Eq. (2) are discussed in detail in Appendix D. In addition to the free-surface BCs and the BCs on the liquid/solid interface both described earlier, we apply a reflective wall at the mold extremities. In Fig. 3, this corresponds to the boundaries parallel to the circumferential position. Finally, periodic boundary conditions are used at the boundaries denoting the axial position.

### 3 Vibrations and Mold Deformation

The HSC of work rolls is always accompanied by inherited vibrations induced by a static imbalance of the mold, a poor circularity of rolling tracks or carrying rollers, and also by an axial deformation of the mold due to thermal expansion effects (Martinez et al. [18]). Fundamental principles about vibrations of cylindrical shells are stated in Love's [19] and Donnell's [20] theory both based on the thin shell equations. Each object with a certain mass and a stiffness including the cylindrical mold prefers to oscillate at its natural frequencies  $f_n$ . Each of these frequencies is associated with a mode shape and a damping coefficient. The natural frequency  $f_n$  is a function of the mass and the stiffness, which depends on the dimensions of the object and the Young's modulus. For geometrically simple objects, such as a beam or a cantilever, a unique mode shape  $m$  exists for each natural frequency  $f_n$ . This is, however, not true for cylindrical shells, for which a unique pair of mode shapes  $m$  and  $n$  exists for each natural frequency  $f_n$  as discussed in Ref. [21]. The mode shape  $m$  refers to a number of axial half waves, whereas the mode shape  $n$  applies to a number of circumferential full waves (Fig. 4). For a static cylinder, each mode shape is represented by a standing

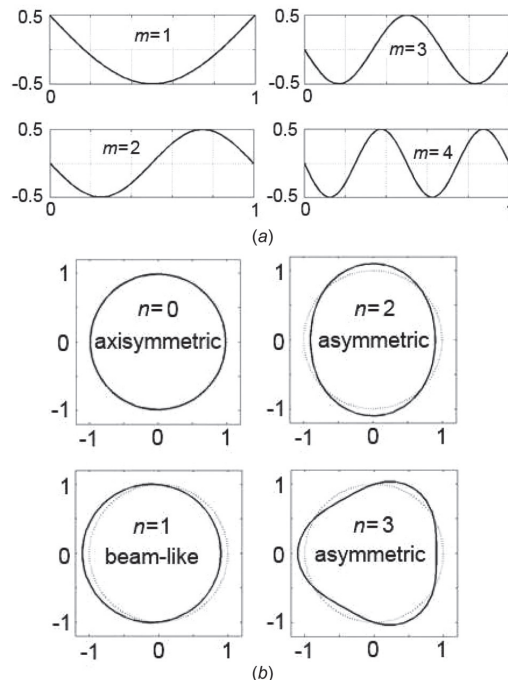
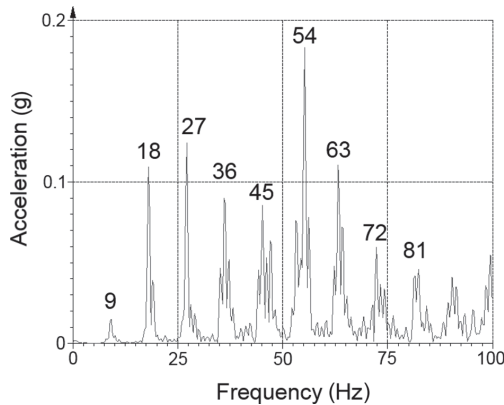


Fig. 4 Mode shapes of a vibrating cylindrical shell: (a) axial mode shapes and (b) circumferential mode shapes



**Fig. 5 A frequency spectrum of the horizontally accelerating carrying roller perpendicular to the mold axis**

wave oscillating around its nodes. However, in rotating cylindrical shells mode shapes travel and lag behind the rotation of the cylinder, which is called the Bryan effect [22].

Experimentally, a link between mode shapes and the vibration recorded during the real casting was found with the help of a frequency spectrum of the acceleration of the arbitrary carrying roller measured in a horizontal plane and perpendicular to the mold axis. An example of the experimental data is shown in Fig. 5 for a particular casting with the angular frequency  $\Omega$  of the rotating mold corresponding to 9 Hz. The obvious harmonics are integer multiples of the angular frequency  $\Omega$ , which implies a qualitative connection with the mode shapes. Higher harmonics correspond to more complicated mode shapes.

The present paper aims to study a response of the free surface to a specific vibration mode. The study is simplified by only considering one pair of the axial and the circumferential mode shape. We introduce the bending of the axis to reproduce the axial mode shape ( $m=1$ ) (see Appendix A). The presence of the axis bending modifies all body forces mentioned in Eq. (2) (a derivation of these forces is detailed in Appendices B, C, and D). The circumferential mode shape ( $n=2$ ) is applied directly by perturbing the gravity with details given in Appendix E.

#### 4 Results and Discussion

All simulations were run with constant physical properties of the liquid metal ( $\rho = 6800 \text{ kg/m}^3$  and  $\mu = 0.006 \text{ kg/m s}$ ). The mold is 3.2 m long and the inner mold radius is  $R = 0.372 \text{ m}$ . Two

**Table 1 List of model settings for the cases N1–N12**

	$\Omega$ (rad/s)	$h$ (mm)	Vibrations	Axis bending	Initial perturbation
N1	71.2	5	Yes	No	Yes
N2		10			
N3		20			
N4		30			
N5		40			
N6		5			No
N7		10			
N8	30	20			
N9					Yes
N10			No		No
N11				Yes	
N12			Yes		

different angular frequencies  $\Omega$  were considered: 30 rad/s and 71.2 rad/s. Several liquid layer heights  $h$  were simulated (5, 10, 20, 30, and 40 mm). An initial distribution of the liquid height  $h$  was imposed. Two distinct initial liquid height distributions were considered, either a flat surface with a constant liquid height  $h$  or a surface perturbed by the following function:

$$h = \bar{h} \left[ \sin(p(x-q)^2) + \sin(r(y-s)^2) \right] \quad (5)$$

where  $\bar{h}$  is the mean liquid height. Constants  $p$ ,  $q$ ,  $r$ , and  $s$  are 10, 0.4, 12, and 0.3, respectively. The function given by Eq. (5) was chosen in order to perturb the free surface with different wavelengths in both directions,  $x$  and  $y$ . Several cases (N1–N12) corresponding to different model settings (Table 1) were calculated. The time step was held constant ( $\Delta t = 0.001 \text{ s}$ ) so that the local Courant number was always smaller than 0.1 for both angular frequencies  $\Omega$  used. Second-order schemes were used for the space and time discretization.

Examples of an instantaneous shape of the free surface are shown in the  $xy$ -plane representing the axial and tangential direction in Figs. 6 and 7. At early stage of the simulation, a single wave travels along the cylinder circumference. In the case without the axis bending, the longitudinal wave does not vary along the axial direction (Fig. 6(a)). On the contrary, the longitudinal wave immediately responds to the nonzero axis bending and varies along the axial direction (Fig. 6(b)). In a fully developed flow regime, the longitudinal wave is no longer visible and a complex wave pattern is formed (Fig. 7). Without the axis bending, the pattern of the free surface resembles annular waves (Fig. 7(a)), whereas with the axis bending the pattern is more chaotic (Fig. 7(b)).

The results were compared by means of the mean amplitude defined as

$$\bar{A}_h = \frac{h_{\max} - h_{\min}}{2} \quad (6)$$

where  $h_{\max}$  and  $h_{\min}$  are the maximum and the minimum liquid height found in the entire computational domain. Such an

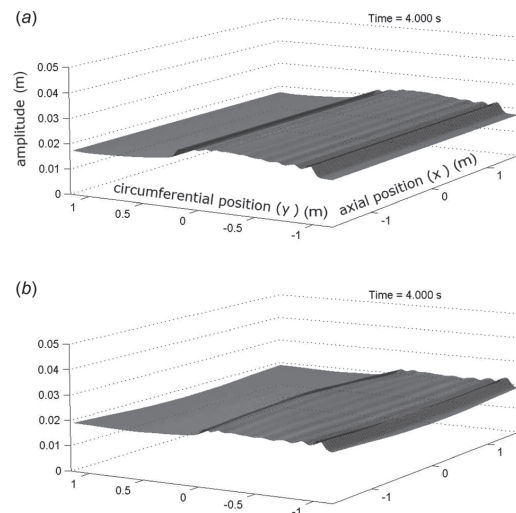


**Fig. 6 An instantaneous shape of the free surface at 4 s for N8 and N12, respectively. (a) A constant liquid height  $h$  along the axial direction. (b) An influence of the axis bending on the longitudinal wave formed during the early stage of the simulation.**

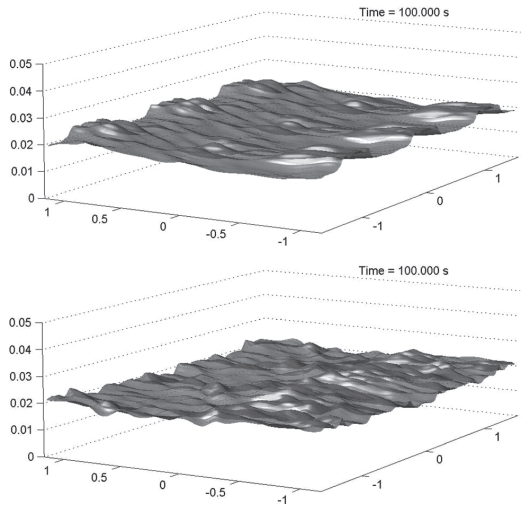


**Fig. 7** A fully developed pattern at 100s for *N8* and *N12*, respectively. (a) A pattern resembling annular waves and (b) A pattern disrupted by the presence of the axis bending.

amplitude, however, shows strong fluctuations (a thickly fluctuating signal in Fig. 8); therefore, the resulting data were convolved with the Gaussian kernel (a line with a circle marker in Fig. 8) to obtain the main evolution. The evolution of the mean amplitudes is shown in Fig. 8 for the angular frequency  $\Omega$  of 71.2 rad/s and in Fig. 9 for  $\Omega = 30$  rad/s. Several general features can be drawn from the results:

- (1) Mean amplitudes never drop to zero within the calculated time range ( $\approx 180$ s). Certain waves survive even for small liquid heights.
- (2) A single longitudinal wave is formed in early stages due to the gravity and the inertia interaction no matter whether the free surface was initially perturbed or not. As the velocity field develops, the longitudinal wave diminishes within an apparent relaxation time ranging from 20s to 40s.
- (3) The higher the liquid height  $h$ , the higher is the mean amplitude of the oscillations.

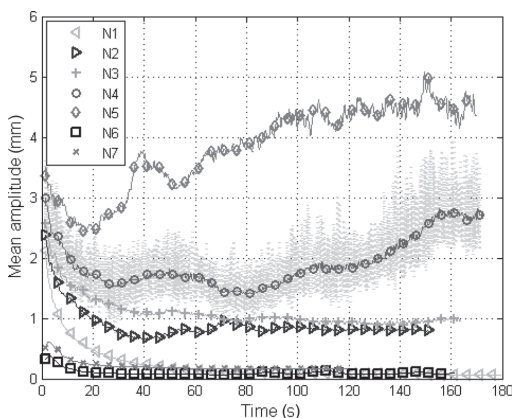


**Fig. 8** An evolution of the mean amplitude of the free surface for  $\Omega = 71.2$  rad/s

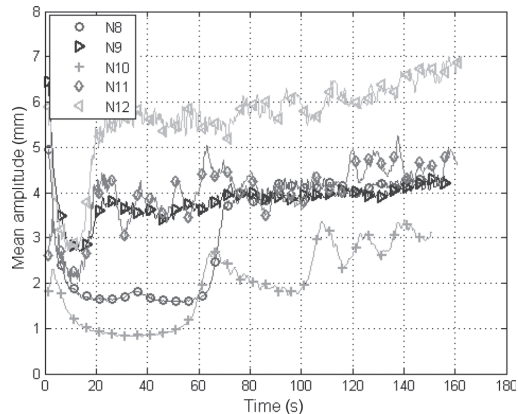


**Fig. 9** An evolution of the mean amplitude of the free surface for  $\Omega = 30$  rad/s

- (4) In all final states, waves are traveling mainly in the axial direction. This transfer of momentum from the circumferential and radial directions (gravity and vibrations) to the axial direction is due to the rotational nature of the Coriolis force.

Almost no influence of the initial perturbation on the final state can be observed between the cases *N1* and *N6* (Fig. 8). Without the perturbation case, *N7* converges toward a relatively quiet state, with the perturbation the same case converges toward a state where the oscillations are four times larger. At lower rotation speed, a transition between a calm and dynamic state occurs after 60s real-time. In Fig. 9, notice the relatively low amplitude region from 20s to 60s with a sudden transition to instability at 60s. *N10* with no vibrations involved is significantly different compared to *N8*. By comparing case *N10* with cases *N8* and *N9*, it can be stated that vibrations amplify and stabilize the amplitude of oscillations of the interface. The same behavior is found for the cases *N11* and *N12* both with the axis bending and without and with the vibrations, respectively. The origin of the stabilizing effects of the perturbations is not yet clear. From Fig. 9, it is also evident that the axis bending significantly reduces the time necessary for the transition to instability.

A verification of the SWE model was done using the hydrostatic free-surface model discussed in detail, e.g., in the paper by Casulli [23]. The hydrostatic free-surface model is an intermediate step between the SWE model and a fully nonhydrostatic free-surface model such as the VOF and the level set method [24]. Unlike these generally expensive nonhydrostatic free-surface models, the hydrostatic free-surface model neglects effects of the

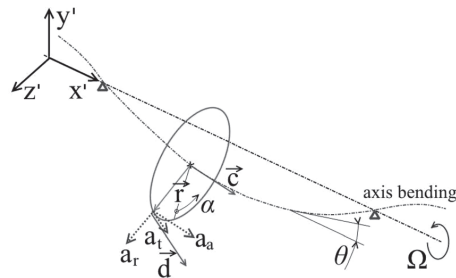


**Fig. 10** A verification of the SWE model; a comparison with the hydrostatic free-surface model by Casulli [23]

nonhydrostatic pressure. However, the efficiency of the algorithm is greatly improved. On the other hand, when compared with the SWE model, the complexity of the hydrostatic free-surface model is increased by resolving horizontal velocity components along the height of the liquid layer and reconstructing the vertical velocity components using the continuity equation. Here, the verification was realized by comparing waves propagating after a collapse of the liquid parabola. The initial liquid height was defined by the following formula:

$$h_0(x, 0) = 0.03 + \max(0, 0.03 - 5(x - 0.5)^2) \quad (7)$$

Other simulation settings were identical to those used in the aforementioned simulations with the angular frequency  $\Omega$  of 71.2 rad/s. In Fig. 10, the dot-and-dash line represents the initial liquid height (Eq. (7)) and the solid and the dash line show the wave pattern of the hydrostatic free-surface model and the SWE model at 0.05 s, respectively. The velocity vector field is naturally an output of the hydrostatic free-surface model. Both wave patterns are in a good agreement, despite a little phase error caused by the complete friction matrix used in the hydrostatic free-surface model.

## 5 Conclusions and Future Prospects

A shallow water model (SWE) for the flow of liquid metal layer on the inside surface of a rotating cylinder was developed. The objective was to study wave patterns of the free surface, wave birth, propagation, and death. Besides, the aim was also to study a response of the system on different initial conditions, i.e., the initial liquid height was either constant or perturbed using a sinelike function. The main assumptions of the model are: The angular frequency  $\Omega$  of the mold is so high that the fluid is mainly rotating with the cylinder. For this reason, the model was defined in the rotating frame of reference. A parabolic velocity profile along the liquid height was taken into account with a no-slip boundary condition on the cylindrical wall. The model was further extended in order to account for vibrations and an axis bending. The origin of the vibrations and the axis bending was explained by means of the natural frequencies and the corresponding mode shapes. It was shown that despite extremely high centrifugal forces ( $\sim 100$  G) acting on a liquid layer, the interaction between the inertia, the gravity, and the vibrations can lead to the formation of waves on the free surface. The higher the liquid height, the more it is prone to instabilities. The SWE model was successfully validated against a more complex, well-established hydrostatic free-surface model using a wave propagation test. In the future, a solidification model will be included using two layers approach, one for the liquid and one for the solidified layer by taking into account the heat conduction inside the mold and also heat losses into the ambient air. The magnitude of accelerations and flow velocities predicted by the present model leads to the idea that strong fragmentation of the solidified elements occurs. In order to take into account this phenomenon, a three-layer model will be under consideration.

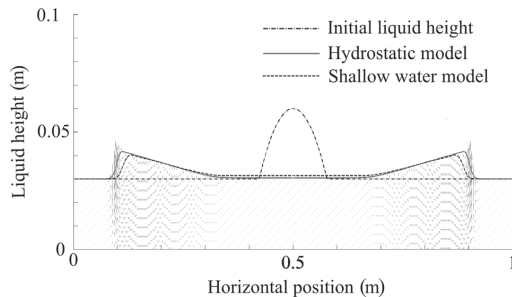


Fig. 11 Schematic of vectors

## Acknowledgment

Financial support by the Austrian Federal Government (in particular from the Bundesministerium für Verkehr, Innovation und Technologie and the Bundesministerium für Wirtschaft, Familie und Jugend) and the Styrian Provincial Government, represented by Österreichische Forschungsförderungsgesellschaft mbH and by Steirische Wirtschaftsförderungsgesellschaft mbH, within the research activities of the K2 Competence Centre on "Integrated Research in Materials, Processing and Product Engineering," operated by the Materials Center Leoben Forschung GmbH in the framework of the Austrian COMET Competence Centre Programme, is gratefully acknowledged. This work was also financially supported by the Eisenwerk Sulzau-Werfen, R. & E. Weinberger AG.

## Appendix A: Bending of Mold Axis

Since the SWE are solved in the rotating frame of reference, it is convenient to introduce a global coordinate system  $C_G(x', y', z')$  rotating with the angular velocity of the mold  $\Omega$ . A deformation of the mold axis (bending) is given by the following trigonometric function with nodes exactly positioned in the carrying rollers:

$$B = -A \cos\left(\frac{\pi x'}{\lambda}\right) \quad (A1)$$

where  $\lambda$  is the distance between the two coaxial rollers,  $A$  is the maximum amplitude of the bending (in the simulations  $A = 2$  mm), and  $B$  is the local amplitude, which is zero in the nodes, negative toward the mold center, and positive toward extremities (Fig. 11). The  $x'$  coordinate is zero at the center of the mold. The tangent  $\mathbf{c}$  of the deformed axis is defined by the slope of the  $B$ , which is given by

$$\begin{aligned} \tan \theta &= \frac{\partial B}{\partial x'} \\ &= A \frac{\pi}{\lambda} \sin\left(\frac{\pi x'}{\lambda}\right) \end{aligned} \quad (A2)$$

The tangent  $\mathbf{c}$  is then defined as

$$\mathbf{c} = \begin{bmatrix} 1 \\ \tan \theta \\ 0 \end{bmatrix} \quad (A3)$$

and denotes the axial direction. Similarly, in the radial direction we can define vector  $\mathbf{r}$  pointing outward from the  $x'$  axis

$$\mathbf{r} = \begin{bmatrix} R \sin \theta \cos \alpha \\ -R \cos \theta \cos \alpha \\ -R \sin \alpha \end{bmatrix} \quad (A4)$$

where  $R$  is the inner radius of the mold, and the angle  $\alpha$  defines the tangential position in radians around the circumference as follows:

$$\alpha = \frac{y}{R} \quad (A5)$$

where  $y$  is the circumferential position in meters. Finally, the cross product  $\mathbf{c} \times \mathbf{r}$  gives a vector  $\mathbf{d}$  representing the tangential direction

$$\mathbf{d} = \mathbf{c} \times \mathbf{r} = \begin{bmatrix} -R \sin \alpha \tan \theta \\ R \sin \alpha \\ -R(\cos \theta \cos \alpha + \sin \theta \cos \alpha \tan \theta) \end{bmatrix} \quad (A6)$$

The vectors  $\mathbf{c}$ ,  $\mathbf{d}$ , and  $\mathbf{r}$  are normalized.

## Appendix B: Centrifugal Force

In order to determine the centrifugal acceleration  $\mathbf{a}_c$  for each point inside the mold, we need to determine its distance from the  $x$ -axis in vectorial form. Let us call this vector as  $\mathbf{r}^*$ . The vector  $\mathbf{r}^*$  is defined as follows:

$$\mathbf{r}^* = \begin{bmatrix} 0 \\ B - R \cos \theta \cos \alpha \\ -R \sin \alpha \end{bmatrix} \quad (\text{B1})$$

The vector  $\mathbf{r}^*$  has the same orientation as the vector  $\mathbf{r}$ , i.e., from the mold center outward. The centrifugal acceleration  $\mathbf{a}_c$  is fully defined by the angular velocity  $\Omega$  and the vector  $\mathbf{r}^*$  by the formula

$$\mathbf{a}_c = \Omega \times (\Omega \times \mathbf{r}^*) \quad (\text{B2})$$

where  $\Omega$  is a vector with nonzero component only in  $x$ -direction.

$$\Omega = \begin{bmatrix} |\Omega| \\ 0 \\ 0 \end{bmatrix} \quad (\text{B3})$$

The resulting centrifugal acceleration  $\mathbf{a}_c$  points radially outward from the mold axis and is defined as follows:

$$\mathbf{a}_c = \begin{bmatrix} 0 \\ \Omega^2 (B - R \cos \theta \cos \alpha) \\ -\Omega^2 R \sin \alpha \end{bmatrix} \quad (\text{B4})$$

The centrifugal acceleration  $\mathbf{a}_c$  defined in this way cannot be, however, directly applied in the SWE model. The vector  $\mathbf{a}_c$  has to be transformed into the local coordinate system given by vectors  $\mathbf{c}$ ,  $\mathbf{r}$ , and  $\mathbf{d}$  denoting the axial, radial, and tangential direction, respectively (Appendix A). The axial component  $a_{ca}$  of centrifugal acceleration  $\mathbf{a}_c$  is obtained by projecting it into the axial direction given by vector  $\mathbf{c}$ , which is done simply by applying dot product as follows:

$$a_{ca} = \mathbf{a}_c \cdot \mathbf{c} \quad (\text{B5})$$

Similarly, the tangential  $a_{ct}$  and the radial  $a_{cr}$  components of centrifugal acceleration  $\mathbf{a}_c$  are derived as follows:

$$a_{ct} = \mathbf{a}_c \cdot \mathbf{d} \quad (\text{B6})$$

and

$$a_{cr} = \mathbf{a}_c \cdot \mathbf{r} \quad (\text{B7})$$

respectively. After evaluating the dot product of  $\mathbf{a}_c$  and  $\mathbf{r}$ , the radial component  $a_{cr}$  of the centrifugal acceleration  $\mathbf{a}_c$  finally becomes:

$$a_{cr} = \Omega^2 (R \sin^2 \alpha - \cos \theta \cos \alpha (B - R \cos \theta \cos \alpha)) \quad (\text{B8})$$

Note that  $a_{cr}$  stands for the radial component of the centrifugal acceleration  $\mathbf{a}_c$  but only at the inner mold surface. In order to calculate  $a_{cr}(z)$  as a function of radial distance  $z$  from the wall,  $R$  has to be replaced by  $R - z$ . Then, Eq. (B8) becomes

$$a_{cr}(z) = \Omega^2 (R - z) \sin^2 \alpha - \Omega^2 \cos \theta \cos \alpha (B - (R - z) \cos \theta \cos \alpha) \quad (\text{B9})$$

Since the flow (continuity and momentum equations) is solved using the SWE,  $a_{cr}$  from Eq. (B9) has to be first expressed as a hydrostatic pressure  $p_h$ . At an arbitrary point  $z_0$  within the liquid layer, the hydrostatic pressure  $p_h(z_0)$  is defined by the following formula:

$$p_h(z_0) = -\rho \int_{h+\delta}^{z_0} a_{cr}(z) dz \quad (\text{B10})$$

where  $h$  and  $\delta$  denote the height of liquid metal and the height of solid metal, respectively. Integration of Eq. (B10) results in rather lengthy formula and is not mentioned here. For the special case, when there is no axis deformation ( $B=0$  and  $\theta=0$ ), the hydrostatic pressure  $p_h$  at  $z_0$  reduces to

$$p_h(z_0) = -\frac{1}{2} \rho \Omega^2 (z_0 - h - \delta)(2R - z_0 - h - \delta) \quad (\text{B11})$$

Replacing  $z_0$  with  $z$  in Eq. (B10) and integrating the gradient of the hydrostatic pressure  $p_h(z)$  over the liquid height  $h$  gives us the force  $\mathbf{F}_c$  with the axial and tangential component, which then can be applied as source terms in momentum equations. This force  $\mathbf{F}_c$  is given by

$$\mathbf{F}_c = - \int_{\delta}^{h+\delta} \nabla p_h(z) dz \quad (\text{B12})$$

where  $\nabla p_h(z)$  is the gradient of hydrostatic pressure  $p_h(z)$ .  $\nabla p_h(z)$  has two components, axial and tangential. (The same procedure is also applied to other forces having a nonzero component in the radial direction  $z$ .) Let us first analyze the axial component of the force  $\mathbf{F}_c$  and let us again start with the special case, when there is no axis deformation ( $B=0$  and  $\theta=0$ ). (We suppress the subscripts  $c$  here and below for clarity, since we need to add other subscripts.) In this special case, the axial component of the force  $\mathbf{F}$  is simplified to

$$F_{rx} = -\rho \Omega^2 h (R - h - \delta) \frac{\partial (h + \delta)}{\partial x} \quad (\text{B13})$$

The tangential component  $F_{ry}$  is the same except that  $x$  is replaced by  $y$

$$F_{ry} = -\rho \Omega^2 h (R - h - \delta) \frac{\partial (h + \delta)}{\partial y} \quad (\text{B14})$$

In the general case, when the axis is deformed ( $B \neq 0$  and  $\theta \neq 0$ ), the formula for the force  $\mathbf{F}$  gets inconveniently long; nevertheless, for the sake of completeness it is given below. We again start with the force component  $F_{rx}$  exploded into several terms

$$\begin{aligned} F_{rx} = & \rho \Omega^2 ((Bbc - b^2 c^2 R - a^2 R) \left( h \frac{\partial (h + \delta)}{\partial x} \right) \\ & + (a^2 + b^2 c^2) \left( h^2 \frac{\partial (h + \delta)}{\partial x} \right) \\ & + (a^2 + b^2 c^2) \left( \delta h \frac{\partial (h + \delta)}{\partial x} \right) \\ & + \frac{1}{2} \frac{\partial B}{\partial x} bc (h^2) \\ & + \frac{1}{6} \frac{\partial c}{\partial x} (3Bb - 6b^2 c R) (h^2) \\ & + \frac{1}{6} \frac{\partial c}{\partial x} 4b^2 c (h^3) \\ & + \frac{1}{6} \frac{\partial c}{\partial x} 6b^2 c (\delta h^2) \end{aligned} \quad (\text{B15})$$

where  $a$ ,  $b$ , and  $c$  are substitutions for  $\sin \alpha$ ,  $\cos \alpha$ , and  $\cos \theta$ , respectively. These substitutions are also used in the definition of the force component  $F_{ry}$ , which is given by

$$\begin{aligned}
F_{ry} = & \rho\Omega^2((Bbc - b^2c^2R - a^2R)\left(h\frac{\partial(h+\delta)}{\partial y}\right) \\
& + (a^2 + b^2c^2)\left(h^2\frac{\partial(h+\delta)}{\partial y}\right) \\
& + (a^2 + b^2c^2)\left(\delta h\frac{\partial(h+\delta)}{\partial y}\right) \\
& - \frac{\partial a}{\partial y}aR(h^2) \\
& + \frac{2}{3}\frac{\partial a}{\partial y}a(h^3) \\
& + \frac{\partial a}{\partial y}a(\delta h^2) \\
& + \frac{1}{6}\frac{\partial b}{\partial y}(3Bc - 6bc^2R)(h^2) \\
& + \frac{1}{6}\frac{\partial b}{\partial y}4bc^2(h^3) \\
& + \frac{1}{6}\frac{\partial b}{\partial y}6bc^2(\delta h^2)
\end{aligned} \tag{B16}$$

Let us try to check the correctness of Eqs. (B15) and (B16) by setting  $B$  and  $\theta$  again equal to zero ( $c = \cos \theta = 1$ ), which means the mold axis is perfectly straight. Last four terms in Eq. (B15) cancel out and the equation reduces to Eq. (B13). Regarding Eq. (B16), last six terms also cancel out and the equation reduces to Eq. (B14).

To summarize, the radial component of centrifugal acceleration  $\mathbf{a}_c$  cannot be applied directly. It has to be expressed first as a hydrostatic pressure, then gradient of this pressure has to be calculated in tangential and axial direction. Finally, both components of pressure gradient have to be integrated over the liquid height  $h$ . The corresponding results than represent momentum source terms due to the radial component of centrifugal acceleration  $\mathbf{a}_c$ .

In addition to the radial component, the centrifugal acceleration  $\mathbf{a}_c$  can generally have also components in the tangential and the axial direction. The derivation of corresponding momentum sources is straightforward and easier than in the previous case of  $\mathbf{a}_{cr}$ , since neither a computation of hydrostatic pressure nor its gradient is needed. The momentum source term for the axial direction resulting from the axial component of  $\mathbf{a}_c$  takes the following form:

$$F_{ax} = \int_{\delta}^{h+\delta} \rho a_{ca} dz \tag{B17}$$

where  $a_{ca}$  is the axial component of the centrifugal acceleration  $\mathbf{a}_c$ . Similarly, the momentum source term for the tangential direction resulting from the tangential component of  $\mathbf{a}_c$  is given by

$$F_{ly} = \int_{\delta}^{h+\delta} \rho a_{ct} dz \tag{B18}$$

After the integration of Eq. (B17),  $F_{ax}$  becomes

$$\begin{aligned}
F_{ax} = & \rho\Omega^2 \frac{1}{|c|} ((Be - bde)R)(h) \\
& + \frac{1}{2}(bde)(h^2) \\
& + (bde)(\delta h^2)
\end{aligned} \tag{B19}$$

where  $b$ ,  $d$ , and  $e$  are substitutions for  $\cos \alpha$ ,  $\cos \theta$ , and  $\tan \theta$ , respectively. For a mold without the axis bending  $\theta = 0$ , then  $\tan \theta = 0$  and thus,  $F_{ax}$  is zero. Similarly, after the integration of Eq. (B18),  $F_{ly}$  becomes

$$\begin{aligned}
F_{ly} = & \rho\Omega^2 \frac{aR}{|d|} ((B + bef)R)(h) \\
& - \frac{1}{2}(bef)(h^2) \\
& - (bef)(\delta h^2)
\end{aligned} \tag{B20}$$

where  $a$ ,  $b$ ,  $e$ , and  $f$  are substitutions for  $\sin \alpha$ ,  $\cos \alpha$ ,  $\tan \theta$ , and  $\sin \theta$ , respectively. In Eqs. (B19) and (B20),  $|c|$  and  $|d|$  correspond to vectors defined in Eqs. (A3) and (A6), respectively, i.e., those not normalized yet. Note again that for a mold without the axis bending  $\tan \theta = 0$  and thus,  $F_{ly}$  is zero.

## Appendix C: Coriolis Force

The general vector formula for the Coriolis acceleration  $\mathbf{a}_c$  is

$$\mathbf{a}_c = -2\boldsymbol{\Omega} \times \mathbf{u} \tag{C1}$$

where  $\boldsymbol{\Omega}$  is the angular velocity described in Appendix B and  $\mathbf{u}$  is the relative velocity defined in the global coordinate system  $C_G(\mathbf{x}', \mathbf{y}', \mathbf{z}')$ . The components of the Coriolis acceleration  $\mathbf{a}_c$  in the global coordinate system  $C_G$  are

$$\mathbf{a}_c = \begin{bmatrix} 0 \\ a_{cy'} \\ a_{cz'} \end{bmatrix} \tag{C2}$$

The  $x$ -component  $a_{cy'}$  is zero because the angular velocity  $\boldsymbol{\Omega}$  is parallel to the  $x'$  axis. The relative velocity  $\mathbf{u}$  is computed in the local coordinate system  $C_L(\mathbf{c}, \mathbf{d}, \mathbf{r})$  with the following nonzero components:

$$\mathbf{v} = \begin{bmatrix} u_x \\ u_y \\ 0 \end{bmatrix} \tag{C3}$$

One of the assumptions of the SWE model is a negligible flux in the radial direction and thus, the radial component  $u_z$  of the relative velocity  $\mathbf{u}$  is zero. In order to transform the Coriolis acceleration  $\mathbf{a}_c$  into momentum source terms it is first projected onto the vectors  $\mathbf{c}$ ,  $\mathbf{d}$ , and  $\mathbf{r}$  as it was done for the centrifugal acceleration  $\mathbf{a}_c$  in Appendix B. After the projection the Coriolis acceleration  $\mathbf{a}_c$  in the local coordinate system,  $C_L$  becomes:

$$\mathbf{a}_c = \begin{bmatrix} a_{Ca} \\ a_{Ct} \\ a_{Cr} \end{bmatrix} = \begin{bmatrix} \mathbf{a}_c \cdot \mathbf{c} \\ \mathbf{a}_c \cdot \mathbf{d} \\ \mathbf{a}_c \cdot \mathbf{r} \end{bmatrix} \tag{C4}$$

First, the axial component  $a_{Ca}$  of the Coriolis acceleration  $\mathbf{a}_c$  is expressed as

$$\begin{aligned}
a_{Ca} = & 0c_{x'} + a_{cy'}c_{y'} + a_{cz'}0 \\
= & 2\Omega u_y c_{y'} d_{z'}
\end{aligned} \tag{C5}$$

after the substitution for  $c_{y'}$  and  $d_{z'}$  from Eqs. (A3) and (A6), respectively, Eq. (C5) would expand into an inconveniently long term; hence, it is not shown here. Similar relations can be found for the tangential  $a_{Cd}$  and the radial  $a_{Cr}$  components of the Coriolis acceleration  $\mathbf{a}_c$ , given by

$$\begin{aligned}
a_{Ct} = & 0d_{x'} + a_{cy'}d_{y'} + a_{cz'}d_{z'} \\
= & -2\Omega u_x c_{y'} d_{z'}
\end{aligned} \tag{C6}$$

and

$$\begin{aligned} a_{Cr} &= 0r_y' + a_{Cy'}r_y' + a_{Cz'}r_z' \\ &= 2\Omega(u_y d_z r_y' - u_x r_z' c_y' - u_y d_y' r_z') \end{aligned} \quad (C7)$$

respectively. The axial  $u_x$  and the tangential  $u_y$  components (Eq. (C3)) of the relative velocity  $\mathbf{u}$  of the liquid are functions of the radial coordinate  $z$  and resemble the parabolic velocity profile with the no-slip BC on the mold wall (or the solid) and the zero stress on the free surface. The axial component  $u_x(z)$  can be expressed as a function of the radial coordinate  $z$  and the axial component of the mass averaged velocity  $\bar{u}_x$  as follows:

$$u_x(z) = -\frac{3\bar{u}_x(\delta - z)(\delta + 2h - z)}{2h^2} \quad (C8)$$

In a similar way, the tangential component  $u_y(z)$  can be written. Substituting  $u_y(z)$  into Eq. (C5) and applying the same integral as in Eq. (B17) lead to the momentum source term for the axial direction resulting from the axial component of the Coriolis acceleration  $\mathbf{a}_C$

$$F_{Cax} = -2\rho\Omega bf\bar{u}_y h \quad (C9)$$

where  $b$  and  $f$  are  $\cos \alpha$  and  $\sin \theta$ , respectively. In the case without the axis bending,  $\sin \theta$  is zero and thus, the Coriolis force in the axial direction  $F_{Cax}$  becomes zero. Comparing Eqs. (C5) and (C6) reveals that the momentum source term  $F_{Ciy}$  in the tangential direction resulting from the tangential component of the Coriolis acceleration  $\mathbf{a}_C$  is very much similar, given by

$$F_{Ciy} = 2\rho\Omega bf\bar{u}_x h \quad (C10)$$

Note again that without the axis bending ( $\sin \theta = 0$ ), the Coriolis force in the tangential direction  $F_{Ciy}$  also cancels out. In addition to  $F_{Ca}$  and  $F_{Ct}$ , the radial component  $F_{Cr}$  is derived following the same steps that were used for the derivation of the centrifugal force (Appendix B). Final formulas of both components,  $F_{Crx}$  and  $F_{Cry}$ , are

$$\begin{aligned} F_{Crx} &= -\rho h \Omega \left( d \left( \frac{5}{2} \bar{u}_y \frac{\partial h}{\partial x} + 2 \bar{u}_y \frac{\partial \delta}{\partial x} + \frac{5}{4} h \frac{\partial \bar{u}_y}{\partial x} \right) \right. \\ &\quad + af \left( \frac{5}{2} \bar{u}_x \frac{\partial h}{\partial x} + 2 \bar{u}_x \frac{\partial \delta}{\partial x} + \frac{5}{4} h \frac{\partial \bar{u}_x}{\partial x} \right) \\ &\quad \left. + \frac{5}{4} (ad \bar{u}_x - f \bar{u}_y) h \frac{\partial \theta}{\partial x} \right) \end{aligned} \quad (C11)$$

and

$$\begin{aligned} F_{Cry} &= -\rho h \Omega \left( d \left( \frac{5}{2} \bar{u}_y \frac{\partial h}{\partial y} + 2 \bar{u}_y \frac{\partial \delta}{\partial y} + \frac{5}{4} h \frac{\partial \bar{u}_y}{\partial y} \right) \right. \\ &\quad \left. + af \left( \frac{5}{2} \bar{u}_x \frac{\partial h}{\partial y} + 2 \bar{u}_x \frac{\partial \delta}{\partial y} + \frac{5}{4} h \frac{\partial \bar{u}_x}{\partial y} \right) + \frac{5}{4R} bf \bar{u}_x h \right) \end{aligned} \quad (C12)$$

respectively. The constants  $a$ ,  $b$ ,  $d$ , and  $f$  stand for  $\sin \alpha$ ,  $\cos \alpha$ ,  $\cos \theta$ , and  $\sin \theta$ . In the case without the axis bending, Eqs. (C11) and (C12) reduce to a simple formula, given by

$$F_{Crx,y} = -\rho h \Omega \left( \frac{5}{2} \bar{u}_y \nabla h + 2 \bar{u}_y \nabla \delta + \frac{5}{4} h \nabla \bar{u}_y \right) \quad (C13)$$

#### Appendix D: Gravity Force

The acceleration of gravity  $\mathbf{a}_g$  is written in the global coordinate system  $C_G(\mathbf{x}', \mathbf{y}', \mathbf{z}')$  as follows:

$$\mathbf{a}_g = \begin{bmatrix} 0 \\ -g \cos(\Omega t) \\ g \sin(\Omega t) \end{bmatrix} \quad (D1)$$

where  $t$  is the time in seconds, and  $g$  is the magnitude of the gravitational acceleration. Note that the vector  $\mathbf{a}_g$  rotates against the angular velocity  $\Omega$  defined by Eq. (B3), which reflects the rotating frame of reference used. The initial position of the global coordinate system  $C_G$  with respect to the acceleration  $\mathbf{a}_g$  is fixed, since any possible phase shift  $\varphi_0$  might play a significant role only during the very first rotations of the mold. Momentum source terms are derived in the same way as those for the centrifugal force and the Coriolis force. After the projection of the vector  $\mathbf{a}_g$  onto the unit vector in the axial direction  $\mathbf{c}$ , the resulting axial component  $a_{ga}$  multiplied by the liquid height  $h$  and density  $\rho$  leads to the following source term:

$$F_{gax} = -\rho h g f \cos(\Omega t) \quad (D2)$$

which becomes zero in the case without axis bending ( $f \cong \sin \theta = 0$ ). Similarly, the source term resulting from the tangential component  $a_{gt}$  obtained by projecting it onto the unit vector  $\mathbf{d}$  is

$$F_{gty} = \rho h g (b \sin(\Omega t) + ad \cos(\Omega t)) \quad (D3)$$

When the axis bending is zero, after a few trigonometric operations it reduces to

$$F_{gty} = -\rho h g \sin(\Omega t + \alpha) \quad (D4)$$

Finally, the momentum source terms resulting from the radial component  $a_{gr}$  are obtained by integrating the gradient of the hydrostatic pressure over the liquid height, multiplying it by the density  $\rho$ , and switching the sign. Both,  $F_{grx}$  and  $F_{gry}$  can be written as

$$\begin{aligned} F_{grx} &= -\rho h g \left( (bd \cos(\Omega t) - a \sin(\Omega t)) \frac{\partial(h + \delta)}{\partial x} \right. \\ &\quad \left. - \frac{1}{2} bf \cos(\Omega t) h \frac{\partial \theta}{\partial x} \right) \end{aligned} \quad (D5)$$

and

$$\begin{aligned} F_{gry} &= -\rho h g \left( (bd \cos(\Omega t) - a \sin(\Omega t)) \frac{\partial(h + \delta)}{\partial y} \right. \\ &\quad \left. - \frac{1}{2R} (ad \cos(\Omega t) + b \sin(\Omega t)) h \right) \end{aligned} \quad (D6)$$

respectively. Without the axis bending, Eq. (D5) reduces to

$$F_{grx} = -\rho h g \cos(\Omega t + \alpha) \frac{\partial(h + \delta)}{\partial x} \quad (D7)$$

whereas Eq. (D6) simplifies to

$$\begin{aligned} F_{gry} &= -\rho h g \cos(\Omega t + \alpha) \frac{\partial(h + \delta)}{\partial y} \\ &\quad + \rho \frac{h^2 g}{2R} \sin(\Omega t + \alpha) \end{aligned} \quad (D8)$$

#### Appendix E: Gravity Force Perturbed Due to the Imperfect Roundness of the Mold

Vibrations induced in the horizontally rotating mold due to the noncircularity of the mold or the carrying rollers are taken into account by a time-dependent perturbation of gravity  $g(1 + \xi \cos(\omega t + \beta_0))$ , where  $\xi$  is a nonzero real number (in the simulations  $\xi = 2$ ),  $\omega$  is the angular frequency of the perturbation (in the simulations  $\omega = 2\Omega$ ), and  $\beta_0$  is the phase (in the simulations  $\beta_0 = \pi/2$ ). Labeling the perturbed gravity as  $g_p$ , the acceleration of the perturbed gravity  $\mathbf{a}_{gp}$  in the global coordinate system  $C_G(\mathbf{x}', \mathbf{y}', \mathbf{z}')$  can be expressed as

$$\mathbf{a}_{gp} = \begin{bmatrix} 0 \\ -g_p \cos(\Omega t) \\ g_p \sin(\Omega t) \end{bmatrix} \quad (E1)$$

Comparing Eq. (D1) and Eq. (E1) leads to the conclusion that exactly the same formulas as derived in Appendix D can be used to determine components of the gravity force perturbed due to the imperfect roundness of the mold provided that  $g$  in Eqs. (D2)–(D7) is replaced by  $g_p$ .

### Appendix F: Bed Shear Force

The viscous term in Eq. (2) does not account for the shear force with the mold (or the solidified metal shell) following from the assumption of the parabolic velocity profile. The bed shear force can be, however, easily derived from the 3D stress tensor  $\tau$  and applied as an additional source term in both the axial and tangential direction. The stress tensor  $\tau$  can be expressed as a function of the symmetric part of the velocity gradient tensor as follows:

$$\tau = -\mu(\nabla \mathbf{u} + \nabla \mathbf{u}^T) \quad (F1)$$

which is in exploded form given by

$$\tau = -\mu \begin{bmatrix} 2 \frac{\partial u_x}{\partial x} & \frac{\partial u_y}{\partial x} + \frac{\partial u_x}{\partial y} & \frac{\partial u_z}{\partial x} + \frac{\partial u_x}{\partial z} \\ \frac{\partial u_x}{\partial y} + \frac{\partial u_y}{\partial x} & 2 \frac{\partial u_y}{\partial y} & \frac{\partial u_z}{\partial y} + \frac{\partial u_y}{\partial z} \\ \frac{\partial u_x}{\partial z} + \frac{\partial u_z}{\partial x} & \frac{\partial u_y}{\partial z} + \frac{\partial u_z}{\partial y} & 2 \frac{\partial u_z}{\partial z} \end{bmatrix} \quad (F2)$$

Generally, in momentum equations the viscous acceleration  $\mathbf{a}_\tau$  is expressed as a divergence of the stress tensor  $\tau$  divided by the density  $\rho$ , which for the incompressible flow results in

$$\mathbf{a}_\tau = \nu \nabla^2 \mathbf{u} = \nu \left( \frac{\partial^2 \mathbf{u}}{\partial x^2} + \frac{\partial^2 \mathbf{u}}{\partial y^2} + \frac{\partial^2 \mathbf{u}}{\partial z^2} \right) \quad (F3)$$

In Eq. (E3), the last term  $\nu \partial^2 \mathbf{u} / \partial z^2$  is the missing part in the viscous term in Eq. (2) representing components of a shear force acting on a  $z$ -plane parallel to the axial and tangential direction, respectively. In order to apply such a force in the SWE, we have to first substitute for the velocity  $\mathbf{u}$  from Eq. (C8) and integrate it over the liquid height  $h$ . This leads to the final components  $F_{\tau a}$  and  $F_{\tau t}$  of the bed shear force in the axial and tangential direction

$$F_{\tau a} = -3\nu \frac{\bar{u}_x}{h} \quad (F4)$$

and

$$F_{\tau t} = -3\nu \frac{\bar{u}_y}{h} \quad (F5)$$

respectively.

### References

- [1] Shailesh, P., Kumar, B. P., Sundararajan, S., and Komariahia, M., 2012, "Experimental Investigation on Centrifugal Casting of 5500 Alloy: A Taguchi Approach," *Sci. Res. Essays*, **7**(44), pp. 3797–3808.
- [2] Chirita, G., Stefanescu, I., Barbosa, J., Puga, H., Soares, D., and Silva, F. S., 2009, "On Assessment of Processing Variables in Vertical Centrifugal Casting Technique," *Int. J. Cast Met. Res.*, **22**(5), pp. 382–389.
- [3] Chirita, G., Stefanescu, I., Soares, D., and Silva, F. S., 2006, "Centrifugal Versus Gravity Casting Techniques Over Mechanical Properties," *An. Mec. Fractura*, **1**, pp. 317–322.
- [4] Chang, S. R., Kim, J. M., and Hong, C. P., 2001, "Numerical Simulation of Microstructure Evolution of Al Alloys in Centrifugal Casting," *ISIJ Int.*, **41**(7), pp. 738–747.
- [5] Hirt, C. W., and Nichols, B. D., 1981, "Volume of Fluid (VOF) Method for the Dynamics of Free Boundaries," *J. Computat. Phys.*, **39**(1), pp. 201–225.
- [6] Keerthirasad, K. S., Murali, M. S., Mukunda, P. G., and Majumdar, S., 2010, "Numerical Simulation and Cold Modeling Experiments on Centrifugal Casting," *Metall. Mater. Trans. B*, **42**(1), pp. 144–155.
- [7] Zagorski, R., and Sleziona, J., 2007, "Pouring Mold During Centrifugal Casting Process," *Arch. Mater. Sci. Eng.*, **28**(7), pp. 441–444.
- [8] Kaschnitz, E., 2012, "Numerical Simulation of Centrifugal Casting of Pipes," *IOP Conf. Ser.: Mater. Sci. Eng.*, **33**(1), p. 012031.
- [9] Daming, X., Limin, J., and Hengzhi, F., 2008, "Effects of Centrifugal and Coriolis Forces on the Mold-Filling Behavior of Titanium Melts in Vertically Rotating Molds," *China Foundry*, **5**(4), pp. 249–257.
- [10] Xu, Z., Song, N., Tol, R. V., Luan, Y., and Li, D., 2012, "Modelling of Horizontal Centrifugal Casting of Work Roll," *IOP Conf. Ser.: Mater. Sci. Eng.*, **33**(1), p. 012030.
- [11] Fjeld, A., and Ludwig, A., 2009, "Flow Patterns and Re-Melting During the Filling of a Large Composite Casting," *Int. J. Cast Met. Res.*, **22**(1–4), pp. 111–114.
- [12] Ludwig, A., Kharicha, A., and Wu, M., 2014, "Modeling of Multiscale and Multiphase Phenomena in Materials Processing," *Metall. Mater. Trans. B*, **45**(1), pp. 36–43.
- [13] Leveque, R. J., 2002, *Finite Volume Methods for Hyperbolic Systems*, Cambridge University Press, New York.
- [14] Dellar, P. J., and Salmon, R., 2005, "Shallow Water Equations With a Complete Coriolis Force and Topography," *Phys. Fluids*, **17**(10), pp. 1–23.
- [15] Hirt, C. W., and Richardson, J. E., 1999, "The Modeling of Shallow Flows," *Flow Sci. Tech. Notes*, **48**, pp. 1–14.
- [16] Lanser, D., Blom, J. G., and Verwer, J. G., 2001, "Time Integration of the Shallow Water Equations in Spherical Geometry," *Modell. Anal. Simul.*, **171**(1), pp. 373–393.
- [17] Audusse, E., Bouchut, F., Bristeau, M.-O., Klein, R., and Perthame, B., 2004, "A Fast and Stable Well-Balanced Scheme With Hydrostatic Reconstruction for Shallow Water Flows," *SIAM J. Sci. Comput.*, **25**(6), pp. 2050–2065.
- [18] Martinez, G., Garnier, M., and Durand, F., 1987, "Stirring Phenomena in Centrifugal Casting of Pipes," *Appl. Sci. Res.*, **44**(1–2), pp. 225–239.
- [19] Love, A. E. H., 1888, "The Small Free Vibrations and Deformations of a Thin Elastic Shell," *Philos. Transl. R. Soc. London, Ser. A*, **179**, pp. 491–546.
- [20] Donnell, L. H., 1935, "Stability of Thin-Walled Tubes Under Torsion," *N.A.C.A. Report No. 479*.
- [21] Li, H., Lam, K.-Y., and Ng, T.-Y., 2005, *Rotating Shell Dynamics*, Elsevier, London.
- [22] Bryan, G. H., 1890, "On the Beats in the Vibration of Revolving Cylinder or Bell," *Proc. Cambridge Philos. Soc.*, **7**(3), pp. 101–111.
- [23] Casulli, V., 1999, "A Semi-Implicit Finite Difference Method for Non-Hydrostatic, Free-Surface Flows," *Int. J. Numer. Methods Fluids*, **30**(4), pp. 425–440.
- [24] Osher, S., and Sethian, J. A., 1988, "Fronts Propagating With Curvature-Dependent Speed: Algorithms Based on Hamilton-Jacobi Formulations," *J. Comput. Phys.*, **79**(1), pp. 12–49.

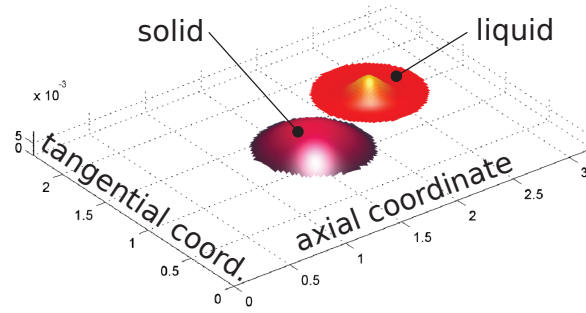
## 2.2 Shallow water equations - approximate Riemann solver

In the previous section 2.1, the idea behind *shallow water equations* (SWE) was introduced. With ANSYS FLUENT in hand, it was enticing to exploit functionalities of the most general multiphase model, the *Euler-Euler model*. The original shallow water equations were modified to take into account effects of centrifugal and Coriolis accelerations influenced by the presence of the underlying relief of a gradually solidifying liquid metal.

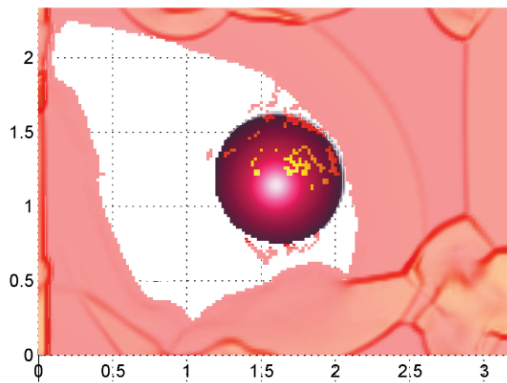
Recall that the SWE were selected to merge advantages of 2D and 3D models. Often, the SWE is referred to as a 2.5D model because a complex 3D free-surface flow is retained but the  $z$ -velocity component is omitted from the governing equations. Moreover, the pressure term only comprises the hydrostatic pressure. In other words, the flow motion is controlled by balance between the inertial and hydrostatic forces. The SWE is a set of hyperbolic partial differential equations. Shocks and rarefaction waves appear on the free surface; therefore, numerical schemes should treat it in an appropriate manner.

When the SWE were applied using the Euler-Euler model, as discussed in the previous section 2.1, the following shortcomings were encountered:

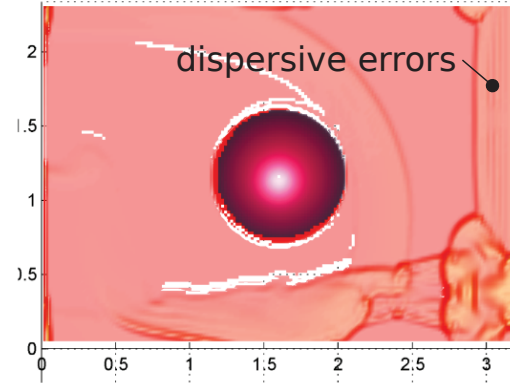
- There was a necessity to consider an additional layer (air above the liquid layer) to fulfill the condition that  $\sum \alpha = 1$ . Two extra momentum equations had to be added, which increased the number of unknowns to be solved and consequently resulted in a slower convergence.
- More importantly, the Poisson's equation had to be solved for the pressure  $p$ . As an elliptic partial differential equation, it is much more computationally demanding than solving the momentum equations. Note that the pressure  $p$  does not appear in the SWE at all. Thus, when implementing it by using the Euler-Euler model, it was a necessary burden dramatically slowing down the calculation.
- Last but not least, often in the horizontal centrifugal casting of rolls, an intermediate layer is centrifuged, which is located between the outer shell and the core material. There would be three layers required in the Euler-Euler model. After several tests, it was shown that our approach did not work for more than two layers. Therefore, the intermediate layer could not be further considered.
- Finally, using the upwind discretization schemes for the convective term in the momentum equations turn out to incorrectly handle wave patterns appearing on the free surface of the liquid layer. It is known that the first order upwind suffers from a numerical diffusion while the second order upwind produces dispersive errors i.e. it brings energy into the system (Fig. 2.3).



(a) An initial condition



(b) An approximate Riemann solver



(c) ANSYS FLUENT (the Euler-Euler model)

Fig. 2.3: An accuracy test of two solvers: A collapse of a liquid bump over a solid paraboloid at a specific time.

Figure 2.3 shows a comparison between the Euler-Euler model in ANSYS FLUENT and an approximate Riemann solver, which is the main subject of this section 2.2. In [22], it is argued that to solve a hyperbolic PDE correctly conservative Godunov's schemes should be considered. A system of hyperbolic PDEs are decomposed into eigenvalues and eigenvectors in order to eventually end up with an accurate discretization of the fluxes as well as explicit updating formulas. In what follows, the article entitled "An approximate Riemann solver for shallow water equations and heat advection in horizontal centrifugal casting" presents the modified shallow water equations with application to HSC. Apart from details about the algorithm, five important topics are covered:

1. The Coriolis force is treated as a flux, not as a source term.
2. The stop&go mechanism is described for dealing with Non-Newtonian fluids.
3. Having a complicated solid bathymetry as well as various source terms, the numerical algorithm is preserving the steady state.
4. The heat advection equation is added to the modified SWE as a part of the

approximate Riemann solver.

5. Lastly, the solver is applied to simulate solidification of a single layer of the liquid steel in the horizontally rotating mould. The model includes heat conduction in the mould and the mould filling.

The approximate Riemann solver of the modified SWE runs much faster (around 10 times) than the Euler-Euler equivalent mentioned earlier. Moreover, the precision is also significantly better due to the explicit treatment of the hyperbolic system, due to distinguishing between shocks and rarefactions. It is recommended not to use the Euler-Euler model to solve the SWE. Instead, the approximate Riemann solver is as a rule of thumb preferred.

The article is supplemented with another article of the author entitled "An approximate Riemann solver for two layer shallow water equations in horizontal centrifugal casting". It provides details about the derivation of an approximate Riemann solver for two layers, for simplicity in one spatial dimension though. Results from simulation of centrifugal casting of two layers is shown and compared with an experiment. In one spatial dimension, the two layer SWE system breaks down into four eigenspeeds, resulting in a much more complex system than the one layer system has, namely only two external wave speeds. The two layer SWE solved by the approximate Riemann solver developed herein is a robust approach, efficient and accurate approach. The main limitation comes from the conditionally real eigenvalues, namely the density of the bottom layer must be higher than that of the top layer. In two spatial dimensions, an additional condition exists to keep real eigenvalues, namely the one related to the Coriolis acceleration.

Although the approximate Riemann solver is very efficient as it can quickly calculate the whole casting process (around 1 hour), it neglects some important parts of physics, as particularly pointed out by the industry partner:

- Mixing between the layers cannot be captured. The two layers are immiscible in the model. In fact, the upper layer must have a lower density than the layer at the bottom, as already stated above.
- The SWE were derived in Cartesian coordinates; therefore, are valid small ratios defined as the layer thickness over the mould radius.
- In the SWE, the velocity components represent average velocities over the thickness of the layer. In the present work, a general parabolic velocity profile was considered. This assumption is certainly violated with more realistic complex flows.
- The buoyant flows due to density differences cannot be simulated.



Volume 267, 15 September 2015

ISSN 0096-3003

APPLIED  
MATHEMATICS  
AND  
COMPUTATION



Contents lists available at ScienceDirect

## Applied Mathematics and Computation

journal homepage: [www.elsevier.com/locate/amc](http://www.elsevier.com/locate/amc)

# An approximate Riemann solver for shallow water equations and heat advection in horizontal centrifugal casting



Jan Boháček<sup>a,\*</sup>, Abdellah Kharicha<sup>b</sup>, Andreas Ludwig<sup>a</sup>, Menghuai Wu<sup>b</sup>

<sup>a</sup>Department of Metallurgy, Montanuniversitaet Leoben, Franz-Joseph Strasse 18, 8700 Leoben, Austria

<sup>b</sup>Christian Doppler Lab for Advanced Simulation of Solidification and Melting, Dept. of Metallurgy, Montanuniversitaet Leoben, Franz-Joseph Strasse 18, 8700 Leoben, Austria

## ARTICLE INFO

### Keywords:

Approximate Riemann solver  
Godunov's splitting  
Shallow water equations  
Liquid film  
Centrifugal  
Coriolis

## ABSTRACT

An approximate Riemann solver was developed for solving modified shallow water equations (SWE) and energy transport describing the average flow dynamics of a single layer spreading inside a horizontally rotating cylinder. The numerical model was particularly developed for simulating the horizontal centrifugal casting (HSC) of the outer shell of a work roll. The SWE were derived in the rotating frame of reference; therefore, fictitious forces (the centrifugal force and the Coriolis force) were considered. In addition, other forces such as the bed shear force, the force of gravity, the wind shear force and forces arising from the variable liquid/solid interface were taken into account. The Jacobian matrix of the nonlinear hyperbolic system of PDEs was decomposed into a set of eigenvalues and corresponding eigenvectors using standard and corrected Roe averages. A Harten–Hyman entropy fix was used to prevent expansion shocks (entropy violating solutions) typically occurring during transonic rarefactions. Source terms were applied as a stationary discontinuity and were physically bounded and well-balanced for steady states (producing non-oscillatory solutions). Each wave was upwinded using the explicit Godunov's method. The high resolution corrections with flux limiters were used to achieve second order of accuracy and dispersion free solutions at discontinuities. In addition to the Riemann solver, a central scheme FV model was used to solve the heat diffusion inside the cylinder (mold) and partially solidified liquid layer, coupled with the solidification model. Several simulations were performed, results were analyzed and discussed.

© 2015 The Authors. Published by Elsevier Inc. This is an open access article under the CC BY-NC-ND license (<http://creativecommons.org/licenses/by-nc-nd/4.0/>).

## 1. Introduction

The present paper describes in detail an approximate Riemann solver for solving modified shallow water equations and energy transport of a single liquid layer spreading inside a horizontally rotating cylinder. The horizontal centrifugal casting (HSC) of the outer shell of a work roll is an industrial application of such a process. In brief, the HSC process (Fig. 1) can be summarized as the following: A cylindrical mold is horizontally placed on four carrying rollers, from which two coaxial are always driven, whereas other two are driving. While the mold is rotating at a high speed (~600 rpm), a liquid metal is poured from the crucible via the statically mounted runner approximately in the center of the mold. Due to high centrifugal forces the liquid metal spreads uniformly and creates a sleeve of a constant thickness. This particular process of casting a work roll

\* Corresponding author.

<http://dx.doi.org/10.1016/j.amc.2015.04.028>

0096-3003/© 2015 The Authors. Published by Elsevier Inc.

This is an open access article under the CC BY-NC-ND license (<http://creativecommons.org/licenses/by-nc-nd/4.0/>).

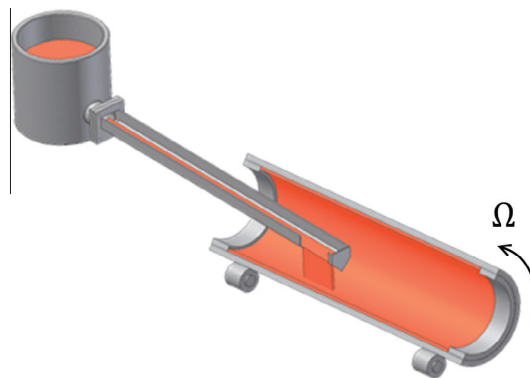


Fig. 1. A schematic of the horizontal centrifugal casting.

takes approximately 35 min. Generally, a centrifugally cast product has a superior mechanical properties compared to conventional gravitational castings [1].

Among other research papers published recently, mathematical models differ mainly in whether the flow was solved or not. Numerical studies solving the flow dynamics were mostly using the VOF method [2] to capture the interface between the liquid layer and the surrounding air. The simulations performed by Xu [3] were terminated at 30 s and thus; only the filling stage of the casting could be analyzed. In the paper, the time dependent distribution of the surface temperature on the external mold wall was obviously the main objective. The solidification model was not however mentioned in the text. Another interesting paper by Kaschnitz [4] presented a HSC simulation of seamless pipes performed using the commercial package FLOW3D. In order to avoid extremely low time steps, momentum equations were solved in the rotating frame of reference. However, due to a very small wall-to-length thickness ratio, one simulation still took considerably long time ( $\sim 20$  days). A commercial code (STAR-CD V4) was used also in a work done by Prasad [5]. The mesh inside the mold was entirely constructed out of rather coarse polyhedral elements, which allowed notably large time steps ( $\sim 0.01$  s). Only the continuity and momentum equations were solved for the flow. Heat transfer and solidification were not discussed in the paper. Results from simulations showed roughly how the melt is spreading during the filling stage, however no details are given on how the filling was imposed and whether the model could capture some free surface patterns or not. It can be concluded that such multiphase (VOF) simulations can successfully resolve a flow field of the liquid metal during the HSC process, however; only a limited period of time is usually concerned. Moreover, these simulations are solely covering the topic of solidification of the liquid layer. On the other hand, several research papers can be found dealing with the complete solidification of the liquid layer yet omitting the flow. The main object of consideration is a time dependent thickness of the solidifying shell often influenced by a segregation of some element due to a density difference and extremely high centrifugal pressure. For example in [6], Drenchev introduced a numerical model discussing some aspects of macrosegregation of reinforcing particles in a metal matrix. The enthalpy equation was the primary equation to solve with thermal physical properties determined from the segregation model. Since the flow (or the mold filling) was not included, the initial thickness of the liquid layer was uniform and identical to the final thickness of the shell. Similar numerical models can be found in [7,8]. The main bottleneck is the fact that the model lacks variances in the mold and shell temperatures due to the localized filling, which in turn affects the local thickness of the solidified shell and the macrostructure pattern consequently.

In the present paper, a fruitful effort was made to develop a novel approach, which would take the flow into consideration and still allow for a complete solidification of the shell in a reasonable computational time. The flow during the HSC process can be characterized as a free surface flow, in which the thickness of the liquid layer is rather small compared to the length of the mold. For this reason, it is rational to expect the momentum in the radial direction to be negligible compared to the momentum in the axial and tangential direction. Taking the 3D Euler equations and the continuity equation leaving out the momentum in the radial direction, integrating momentum and mass equations along the liquid height, and applying kinematic boundary condition on the free surface one obtains the 2D shallow water equations (SWE) originally derived in [9]. From the asymptotic series of the static pressure only the first term, the hydrostatic pressure is considered and terms with higher derivatives are neglected. This as a hydrostatic condition is a leading order approximation to the static pressure and is relevant for flows where a horizontal scale  $L$  is large compared to a characteristic height  $H$ . Note that no assumption is made about amplitudes of waves on the free surface. All the nonlinearities are retained. The original SWE are strictly hyperbolic nonlinear PDEs. In the following text, the SWE are modified to describe the average flow dynamics of the liquid layer inside the horizontally rotating cylinder. Next, an approximate Riemann solver is derived and carefully detailed. Several 1D numerical tests are shown in order to demonstrate the capability of the Riemann solver. In addition, 2D numerical examples are presented showing the simulation of the HSC process. Note that the approximate Riemann solver is used to solve the SWE and the heat advection within the liquid layer. An additional central difference FV model is used to calculate the heat

diffusion and solidification, which is not covered in the present paper. Details about the heat transfer and solidification model are discussed in [10].

## 2. Theory

### 2.1. Original form of shallow water equations

The shallow water equations (SWE) are suitable for a numerical description of so-called gravity waves i.e. waves formed and propagated under action of the gravitational acceleration. The SWE are typically applied in modeling of oceanography [11] and river flows [12]. The SWE can effectively and accurately predict the speed and the amplitude of a propagating tsunami, a tidal bore or any other wave until it breaks into a 3D flow structure [13]. In a 2D Cartesian coordinate system, the continuity and momentum equations take the following form:

$$h_t + (hu)_x + (hv)_y = 0 \tag{1}$$

and

$$\begin{aligned} (hu)_t + \left( hu^2 + \frac{1}{2}gh^2 \right)_x + (huv)_y &= 0 \\ (hv)_t + (huv)_x + \left( hv^2 + \frac{1}{2}gh^2 \right)_y &= 0 \end{aligned} \tag{2}$$

where  $h$  is the liquid height,  $g$  is the gravitational acceleration, and  $u, v$  are the mass-flow averaged velocity components in the  $x$ - and  $y$ -direction, respectively. Note that the indices  $t, x$ , and  $y$  represent temporal and spatial derivatives. Usually, the SWE are solved in the homogeneous form (1), (2). Sometimes, it is however necessary to include momentum source terms such as the bed shear force, wind shear force, etc. In addition, some applications e.g. modeling of landslides require a multilayer approach. In that case, different SWE are used for each layer and coupling terms provide the desired interaction between these layers [14].

### 2.2. Modified shallow water equations

The original SWE (1), (2) were modified to simulate the average flow dynamics of the liquid layer spreading inside a horizontally rotating cylinder. During the observation of the real casting, the liquid melt seems to quickly pick up the speed of the rotating mold [15]. Therefore, the choice of the rotating frame of reference is reasonably advocated and fictitious forces such as the centrifugal force,  $F_c$ , and the Coriolis force,  $F_C$ , have to be taken into account. Since  $h \ll R$ , the coordinate system used for the derivation of the modified SWE is identical to that used in Section 2.1. In other words, the axial  $x$ , tangential  $\theta$ , and radial  $r$  coordinates are mapped (Fig. 2) on the Cartesian plane  $(x, \theta, r) \rightarrow (x, y, z)$  as the following

$$x = x, \quad y = R\theta, \quad z = R - r \tag{3}$$

with  $R$  the radius of the cylinder. Note that this transformation is only possible when  $h \ll R$ . The centrifugal acceleration  $a_c$  acts purely in the radial direction,

$$a_c = \Omega^2(R - z) \tag{4}$$

with  $0 \leq z \leq h$  and  $\Omega$  the angular frequency of the mold. Like any other acceleration acting in the radial direction, also the centrifugal acceleration  $a_c$  contributes to the hydrostatic pressure  $p$

$$p = a_c \rho (h - z) \tag{5}$$

with  $h$  the liquid height, and  $\rho$  the liquid density. Then, the gradient of the hydrostatic pressure  $p$  can be added to the flux function in (2) as the following:

$$\begin{aligned} (hu)_t + \left( hu^2 + \frac{1}{2}\Omega^2Rh^2 - \frac{1}{3}\Omega^2h^3 \right)_x + (huv)_y &= 0 \\ (hv)_t + (huv)_x + \left( hv^2 + \frac{1}{2}\Omega^2Rh^2 - \frac{1}{3}\Omega^2h^3 \right)_y &= 0 \end{aligned} \tag{6}$$

Note that  $h^3 \ll Rh^2$  and therefore, the second term corresponding to the centrifugal acceleration  $a_c$  can be neglected. The momentum equations become:

$$\begin{aligned} (hu)_t + \left( hu^2 + \frac{1}{2}\Omega^2Rh^2 \right)_x + (huv)_y &= 0 \\ (hv)_t + (huv)_x + \left( hv^2 + \frac{1}{2}\Omega^2Rh^2 \right)_y &= 0 \end{aligned} \tag{7}$$

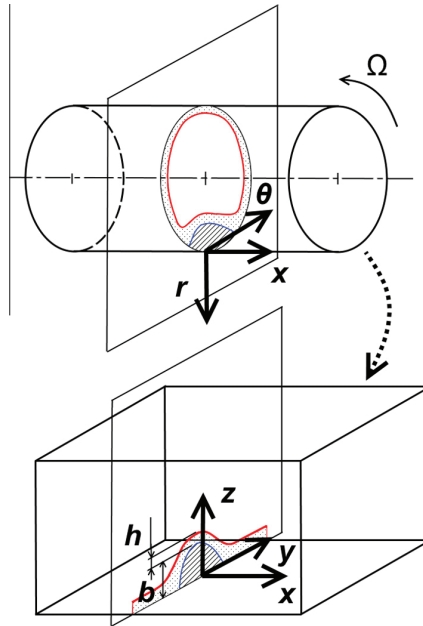


Fig. 2. A sketch of the coordinate system transformation.

The centrifugal term  $1/2\Omega^2 R h^2$  in (7) is the analogy to the gravity term  $1/2 g h^2$  in (2). Despite describing the flow in a cylindrical geometry, note that we keep the 2D Cartesian coordinate system for the derivation of the modified SWE, which is justified by having  $h \ll R$ . To complete the fictitious force terms in (7), the Coriolis force has to be included. Assuming the radial momentum is negligible and the cylinder rotating about its axis, only the radial component of the Coriolis acceleration  $a_c$  is nonzero

$$a_c = -2\Omega v \tag{8}$$

In addition, an assumption about the velocity profile in the radial direction is made. On the cylinder wall a no slip boundary condition is considered i.e.  $u(0) = 0$  and  $v(0) = 0$ . On the free surface, a zero stress boundary condition is considered i.e.  $\partial u(h)/\partial z = 0$  and  $\partial v(h)/\partial z = 0$ . Within  $0 \leq z \leq h$ , a parabolic velocity profile is constructed with the mass-flow averaged velocity components  $u$  and  $v$ .

$$u(z) = 3uz(2h - z)/(2h^2) \tag{9}$$

$v(z)$  can be written analogously. Following the steps used for any acceleration acting in the radial direction, the gradient of the corresponding hydrostatic pressure divided by the density  $\rho$ , denoted  $F_c$ , reads

$$F_c = -\frac{5}{2}\Omega h v \begin{bmatrix} h_x \\ h_y \end{bmatrix} - \frac{5}{4}\Omega h^2 \begin{bmatrix} v_x \\ v_y \end{bmatrix} \tag{10}$$

Later, it will be shown in the algorithm part that it is convenient to take a part of the Coriolis force as a flux function and the rest leave as a source term. In addition to the fictitious forces, several more forces have to be included. Starting with the force of gravity, one has to bear in mind the rotating frame of reference used and the rotating vector of the gravitational acceleration  $\vec{g}(t)$  consequently.

$$\vec{g}(t) = (0, -g \sin(\Omega t), -g \cos(\Omega t)) \tag{11}$$

with zero axial component and the tangential and the radial component different from zero. Taking the radial component of acceleration first and again calculating the gradient of the corresponding hydrostatic pressure divided by the liquid density, denoted  $F_g$ , reads

$$F_g = -g \cos(\Omega t) h \begin{bmatrix} h_x \\ h_y \end{bmatrix} \tag{12}$$

After adding the tangential component integrated over the liquid height  $h$

$$\mathbf{F}_g = -g \cos(\Omega t) h \begin{bmatrix} h_x \\ h_y \end{bmatrix} - g \sin(\Omega t) \begin{bmatrix} 0 \\ h \end{bmatrix} \quad (13)$$

with  $t$  the physical time. Besides, it is no less important to examine various shear stresses that likely appear in the HSC process. In the case of a viscous Newtonian fluid, the bed shear stress is derived from the assumption of a parabolic velocity profile as the following:

$$\boldsymbol{\tau}_b = \boldsymbol{\tau}_\mu = 3\mu/h \begin{bmatrix} u \\ v \end{bmatrix} \quad (14)$$

with  $\mu$  the dynamic viscosity. If  $\boldsymbol{\tau}_b$  only includes turbulent and dispersive effects, the bed shear stress takes the form

$$\boldsymbol{\tau}_b = \boldsymbol{\tau}_t = \rho c_f \begin{bmatrix} u|u| \\ v|v| \end{bmatrix} \quad (15)$$

with  $c_f$  the friction coefficient. In addition to the bed shear stress  $\boldsymbol{\tau}_b$ , the liquid can show other types of flow resistance such as a yield stress  $\boldsymbol{\tau}_{yi}$ . Different types of stresses can be lumped together by a single formula expressing the flow resistance relation. More details about such relations can be found e.g. in [16]. Up to here, the liquid layer was in the contact with the cylindrical wall. However, in the HSC process the solidification takes place from the cylindrical wall and therefore, the underlying topography of the liquid layer varies in time and corresponds to the actual solid height, denoted  $b$ . The solid height  $b$  naturally affects all the forces resulting from any acceleration acting in the radial direction.

Then, assuming the solid height  $b$  greater than zero, the centrifugal force  $\mathbf{F}_c$  becomes:

$$\mathbf{F}_c = -\Omega^2 R h \begin{bmatrix} h_x \\ h_y \end{bmatrix} - \Omega^2 R h \begin{bmatrix} b_x \\ b_y \end{bmatrix} \quad (16)$$

Unlike the first term applied inside the flux function (16), the second term with the gradient of the solid height  $b$  stays on the right-hand side as a source term. The Coriolis force  $\mathbf{F}_c$  is altered by the solid height  $b$  as the following:

$$\mathbf{F}_c = -\frac{5}{2}\Omega h v \begin{bmatrix} h_x \\ h_y \end{bmatrix} - \frac{5}{4}\Omega h^2 \begin{bmatrix} v_x \\ v_y \end{bmatrix} - 2\Omega h v \begin{bmatrix} b_x \\ b_y \end{bmatrix} \quad (17)$$

Finally, the gravity force  $\mathbf{F}_g$  as the last force being affected by the solid height  $b$  takes the form

$$\mathbf{F}_g = -g \cos(\Omega t) h \begin{bmatrix} (h+b)_x \\ (h+b)_y \end{bmatrix} - g \sin(\Omega t) \begin{bmatrix} 0 \\ h \end{bmatrix} \quad (18)$$

### 2.3. Heat advection diffusion equation for modified SWE

The heat advection diffusion equation integrated over the liquid height  $h$  has to be solved simultaneously with the modified SWE. For the average temperature  $T$  of the liquid layer  $h$  the following transport equation holds:

$$hT_t + (huT)_x + (hvT)_y = (h\alpha T_x)_x + (h\alpha T_y)_y + S_T \quad (19)$$

with  $\alpha$  the thermal diffusivity and  $S_T$  the source term due to solidification and heat transfer to the mold.

### 2.4. Complete set of equations

The average flow dynamics of the liquid layer inside the horizontally rotating cylinder coupled with the advection diffusion equation for the average temperature of the liquid layer  $T$  is mathematically described by the following system of equations:

$$\begin{bmatrix} h \\ hu \\ hv \\ hT \end{bmatrix}_t + \begin{bmatrix} hu^2 + \frac{1}{2}\Omega^2 R h^2 + \frac{5}{4}\Omega v h^2 \\ hu v \\ hu T \end{bmatrix}_x + \begin{bmatrix} hv^2 + \frac{1}{2}\Omega^2 R h^2 + \frac{5}{4}\Omega v h^2 \\ hv T \end{bmatrix}_y = \mathbf{S} \quad (20)$$

with  $\mathbf{S}$  the source terms given by:

$$\mathbf{S} = \begin{bmatrix} 0 \\ -\Omega^2 R h b_x - \frac{5}{4}\Omega h^2 v_x - 2\Omega h v b_x - g \cos(\Omega t) h (h+b)_x - 3\frac{\mu}{\rho} \frac{u}{h} - c_f u |u| - \frac{\tau_{yi}}{\rho} \\ -\Omega^2 R h b_y - 2\Omega h v b_y - g \cos(\Omega t) h (h+b)_y - g \sin(\Omega t) h - 3\frac{\mu}{\rho} \frac{v}{h} - c_f v |v| - \frac{\tau_{yi}}{\rho} \\ (h\alpha T_x)_x + (h\alpha T_y)_y + S_T \end{bmatrix} \quad (21)$$

### 2.5. Heat diffusion, solidification, and mold filling

In addition to the average flow dynamics and heat transport of the liquid layer, the heat diffusion inside the cylinder and the continuously solidifying liquid has to be solved with appropriate thermal boundary conditions at the walls and the free surface. Convective and radiative heat losses are taken into account. The solidification of the liquid layer starts exclusively from the inner wall of the cylinder as a moving planar liquid/solid interface. The 3D heat diffusion equation is solved on a finite volume grid in the cylindrical coordinates along with the Stefan condition applied at the liquid/solid interface. The initially empty mold is continuously filled with the hot liquid approximately in the center of the mold. The heat diffusion, the solidification, and the mold filling are out of the scope of this paper and are described in detail in [10].

## 3. Calculation

### 3.1. Approximate Riemann solver

The original SWE (1), (2) is a system of strictly hyperbolic non-linear PDEs, whereas (20) is a system of conditionally hyperbolic PDEs due to the presence of the Coriolis term in the flux function. The benefit from applying the Coriolis term in the flux function and not as a source term will be clearly demonstrated later by a 1D numerical test. The homogeneous system of (20) can be symbolically written as

$$\mathbf{Q}_t + \mathbf{A}(\mathbf{Q})_x + \mathbf{B}(\mathbf{Q})_y = \mathbf{0} \quad (22)$$

with  $\mathbf{Q}$  the vector of conserved quantities  $\mathbf{Q} = [h, hu, hv, hT]^T$  and  $\mathbf{A}$  and  $\mathbf{B}$  flux functions. The 2D set of Eq. (22) can be broken down to two 1D sets of equations by the dimensional splitting [17].

$$\begin{aligned} \mathbf{Q}_t + \mathbf{A}(\mathbf{Q})_x &= \mathbf{0} \\ \mathbf{Q}_t + \mathbf{B}(\mathbf{Q})_y &= \mathbf{0} \end{aligned} \quad (23)$$

The fluxes  $\mathbf{A}(\mathbf{Q})_x$  and  $\mathbf{B}(\mathbf{Q})_y$  can be replaced by  $\mathbf{A}'(\mathbf{Q})\mathbf{Q}_x$  and  $\mathbf{B}'(\mathbf{Q})\mathbf{Q}_y$  respectively with  $\mathbf{A}'(\mathbf{Q})$  and  $\mathbf{B}'(\mathbf{Q})$  Jacobian matrices. Both Jacobian matrices are diagonalizable with conditionally real eigenvalues  $\lambda^{A,B}$  and corresponding eigenvectors.

$$\begin{aligned} \lambda^A &= \left[ u - \sqrt{h\left(\Omega^2 R + \frac{5}{2}\Omega v\right)}, u + \sqrt{h\left(\Omega^2 R + \frac{5}{2}\Omega v\right)}, u, u \right] \\ \lambda^B &= \left[ v + \frac{5}{8}\Omega h - \sqrt{h\left(\Omega^2 R + \frac{5}{2}\Omega v + \frac{25}{64}\Omega^2 h\right)}, v + \frac{5}{8}\Omega h + \sqrt{h\left(\Omega^2 R + \frac{5}{2}\Omega v + \frac{25}{64}\Omega^2 h\right)}, v, v \right] \end{aligned} \quad (24)$$

The hyperbolicity of (20) is lost, when any of the eigenvalues (24) is a complex number. From (24), a critical velocity  $v_c$  can be calculated

$$v_c = -2/5\Omega R, \quad (25)$$

below which the system of PDEs is no longer hyperbolic. In the HSC process, the order of magnitude of  $v_c$  is 10 m/s, which can hardly be reached due to the fact that the liquid rotates nearly at the same speed as the mold. Since the solution procedure is very similar for both,  $x$  and  $y$ , directions, only the  $y$  direction is detailed here. Each eigenvalue corresponds to a finite wave speed at which the information travels through the domain. The first two waves from  $\lambda$  are analogous to nonlinear gravity waves in the original SWE and the last two waves are linearly degenerate. In the tangential ( $y$ ) direction, the following set of equations is solved

$$\mathbf{Q}_t + \mathbf{B}'(\mathbf{Q})\mathbf{Q}_y = \mathbf{0} \quad (26)$$

using an approximate Riemann solver. On each face of a 1D grid with a uniform spacing a 1D Riemann problem is solved in order to get the wave strengths  $\alpha$  each corresponding to its wave speed  $\lambda$  and eigenvector  $r$ . The wave strengths are obtained by solving the system of linear equations

$$\mathbf{r}\alpha = \Delta\mathbf{Q} \quad (27)$$

with  $\Delta\mathbf{Q} (= \mathbf{Q}_R - \mathbf{Q}_L)$  the jump in  $\mathbf{Q}$  over the cell face and  $\mathbf{r}$  being a matrix of column eigenvectors  $r$ .

$$\mathbf{r} = \begin{bmatrix} 1 & 1 & 0 & 0 \\ u & u & 1 & 0 \\ \lambda_1 & \lambda_2 & 0 & 0 \\ T & T & 0 & 1 \end{bmatrix} \quad (28)$$

A linearization of  $u$ ,  $v$ ,  $T$ , and  $h$  is required for both  $\lambda$  and  $\mathbf{r}$ . A Roe linearization [18] is applied in order to find special averages  $\hat{u}$ ,  $\hat{v}$ ,  $\hat{T}$  and  $\hat{h}$ . The Roe averages of  $\hat{u}$ ,  $\hat{T}$  and  $\hat{h}$  are identical to those for the original SWE (1), (2), given by:

$$\hat{u} = \frac{\sqrt{h_L}u_L + \sqrt{h_R}u_R}{\sqrt{h_L} + \sqrt{h_R}}, \quad \hat{T} = \frac{\sqrt{h_L}T_L + \sqrt{h_R}T_R}{\sqrt{h_L} + \sqrt{h_R}}, \quad \hat{h} = (h_L + h_R)/2, \tag{29}$$

whereas  $\hat{v}$  is modified by adding a correction to the original Roe average.

$$\hat{v} = \frac{\sqrt{h_L}v_L + \sqrt{h_R}v_R}{\sqrt{h_L} + \sqrt{h_R}} + \frac{(v_R - v_L)(\sqrt{h_L}h_R - \sqrt{h_R}h_L)}{2(h_R + h_L)(\sqrt{h_R} + \sqrt{h_L})} \tag{30}$$

After using the Roe averages in the matrix of eigenvectors  $\mathbf{r}$  (28) the system of linear equations (26) is solved for the wave strengths  $\alpha$ .

$$\alpha = \left[ \frac{\Delta h \lambda_2 - \Delta h v}{\lambda_2 - \lambda_1}, \quad -\frac{\Delta h \lambda_1 - \Delta h v}{\lambda_2 - \lambda_1}, \quad \Delta h u - \hat{u} \Delta h, \quad \Delta h T - \hat{T} \Delta h \right]^T \tag{31}$$

The centrifugal waves are connected by intermediate states  $h_m$  and  $h v_m$  (Fig. 3) as the following:

$$\begin{aligned} h_m &= h_L + \alpha_1 \\ h_m &= h_R - \alpha_2 \\ h v_m &= h v_L + \alpha_1 \lambda_1 \\ h v_m &= h v_R - \alpha_2 \lambda_2 \end{aligned} \tag{32}$$

Approximate Riemann solvers generally do not distinguish between a shock wave and a rarefaction and treat each wave as a shock wave. To treat a subsonic or a supersonic rarefaction as a shock wave usually does not cause any troubles in the solution especially in the case of a narrow rarefaction fan. However, if the rarefaction occurs in the transonic regime, one widely reported problem is the entropy violation resulting in unphysical expansion shocks. In the present paper, the correct solution is restored by applying the Harten–Hyman entropy fix [19].

The source term  $\mathbf{S}$  (21) can be applied using several different methods. The fractional-step method [20] is a popular method, in which we alternate between solving a homogeneous conservation law and a simple ODE. This approach is simple to use and implement. However, if the solution is close to a steady state i.e. the gradient of the flux almost balances the source term, which cannot be correctly captured by the fractional-step method. Moreover, the fractional-step method often generates unphysical oscillations in the solution. In the present paper, only the source term  $S_4$  in the heat advection diffusion equation (19) is solved using this method namely the BDF implicit method. The rest of the source term  $\mathbf{S}$  ( $S_1$ – $S_3$ ) is directly included in the Riemann solver as a singular source at each discontinuity without modifying the original solution vector of conserved quantities  $\mathbf{Q}$ . This approach is said to upwind the source term by means of projecting it onto the matrix of eigenvectors  $\mathbf{r}$  and propagating it at the wave speeds  $\lambda$ . As shown in Fig. 3, in the homogeneous case the centrifugal waves are connected by the intermediate states  $h_m$  and  $h v_m$ , whereas in the nonhomogeneous case with the source terms the intermediate state  $h_m$  is split into two intermediate states  $h_{Lm}$  and  $h_{Rm}$  separated by a stationary jump discontinuity corresponding to

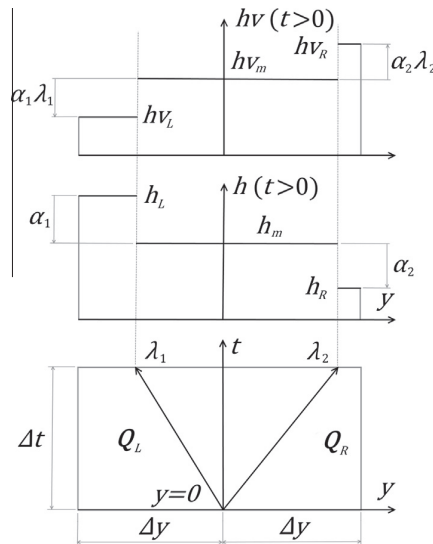


Fig. 3. Solution of the Riemann problem at  $y = 0$  without the source term  $S_3$ . Discontinuities  $\lambda_1$  and  $\lambda_2$  are connected by constant intermediate states  $h_m$  and  $h v_m$ .

the source term (Fig. 4). The momentum is conserved through the stationary discontinuity meaning that the centrifugal waves  $\lambda_1$  and  $\lambda_2$  are still connected by a single intermediate state  $h v_m$  (32), however modified by the effect of the source term. In the tangential ( $y$ ) direction, the following set of nonhomogeneous equations is solved.

$$\mathbf{Q}_t + \mathbf{B}'(\mathbf{Q})\mathbf{Q}_y = [0 \ 0 \ S_3 \ 0]^T \tag{33}$$

The wave speeds  $\lambda$  remain unchanged, while the source strengths  $\beta$  are added to the wave strengths  $\alpha$

$$\beta = \left[ \frac{S_3}{(\lambda_2 - \lambda_1)\lambda_1}, \ -\frac{S_3}{(\lambda_2 - \lambda_1)\lambda_2}, \ 0, \ 0 \right]^T \tag{34}$$

The intermediate states  $h_{Lm}$ ,  $h_{Rm}$ , and  $h v_m^*$  become

$$\begin{aligned} h_{Lm} &= h_L + \alpha_1 + \beta_1 \\ h_{Rm} &= h_R - \alpha_2 - \beta_2 \\ h v_m^* &= h v_L + \alpha_1 \lambda_1 + \beta_1 \lambda_1 \\ h v_m^* &= h v_R - \alpha_2 \lambda_2 - \beta_2 \lambda_2 \end{aligned} \tag{35}$$

Even in the less complex case, without the source terms, a Riemann solver linearized using the Roe average can fail completely. It can give a nonphysical solution such as a negative liquid height ( $h < 0$ ) especially when the solution is close to a vacuum state. Using modified wave speeds  $\lambda$  defined according to HLLC solver, which is positively conservative, is a possible remedy. Here, a different approach was however employed in which a minimum liquid height  $h_{min}$  was used to identify a threshold for a dry cell. Then, any  $h < h_{min}$  and the corresponding velocity  $v$  were set to zero when solving the Riemann problem. Note that this procedure is used to determine the solution of the Riemann problem. It does not modify the vector of conserved quantities  $\mathbf{Q}$ . This approach has been recently advocated e.g. in [21]. When dealing with the source term in (33), the positivity of both,  $h_{Lm}$  and  $h_{Rm}$ , needs to be checked and an adequate numerical limit has to be applied. In Fig. 5, the limiting strategy is shown for  $h_{Lm} < 0$ . The source strength  $\beta_1$  has to be limited as the following

$$\beta_1 = -h_m, \quad \beta_2 = -\beta_1 \lambda_1 / \lambda_2 \tag{36}$$

Similarly, in case that  $h_{Rm} < 0$  the source strength  $\beta_2$  is modified

$$\beta_2 = h_m, \quad \beta_1 = -\beta_2 \lambda_2 / \lambda_1 \tag{37}$$

In addition to the numerical limit due to the occurrence of the negative height [22], a physical limit is applied to prevent incorrect evaluation of the friction source term [16] based on the fact that none of the friction terms cannot change the sign of the intermediate state  $h v_m$  (32). Therefore, in case that  $(h v_m)(h v_m^*) < 0$  the following physical limit has to be applied.

$$\beta_1 = -h v_m / \lambda_1, \quad \beta_2 = h v_m / \lambda_2 \tag{38}$$

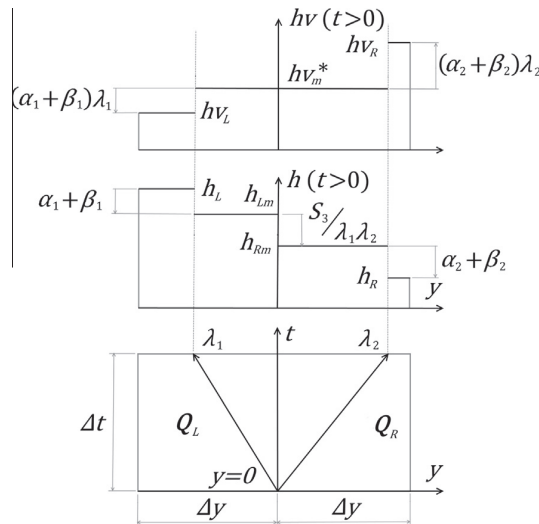


Fig. 4. Solution of the Riemann problem at  $y = 0$  with the source term  $S_3$  as a stationary discontinuity. However, the stationary discontinuity appears only in the liquid height  $h$ , separating intermediate states  $h_{Lm}$  and  $h_{Rm}$ . In the tangential momentum  $h v$  still a single intermediate state  $h v_m^*$  exists altered by the effect of the source term  $S_3$ .

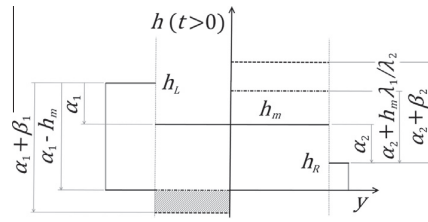


Fig. 5. Negative liquid height  $h$  (hatched region) generated by the source strength  $\beta_1$ . A numerical limit  $\beta_1 = -h_m$  applied, forcing  $h_{lm}$  to 0.

### 3.2. Wave-propagation algorithm

After solving the Riemann problem at each face of the cell in the tangential ( $y$ ) direction, the complete information about the wave speeds  $\lambda$  (24), the matrix of eigenvectors  $\mathbf{r}$  (28), the wave strengths  $\alpha$  (31), and the source strengths  $\beta$  (34) is obtained. To update the solution it is straightforward to apply the Godunov's explicit updating formula, which is basically the first order accurate upwind method. To reconstruct the vector of quantities in a cell  $c_{ij}$  only waves entering this cell are used to update the solution, whereas waves leaving the cell  $c_{ij}$  have no effect. After performing  $n + 1$  time steps  $\Delta t$ , the vector of quantities  $(\mathbf{Q})_{ij}^{n+1}$  reads

$$(\mathbf{Q})_{ij}^{n+1} = (\mathbf{Q})_{ij}^n - \frac{\Delta t}{\Delta y} \left( \mathbf{B}^+ (\Delta \mathbf{Q})_{ij-1/2}^n + \mathbf{B}^- (\Delta \mathbf{Q})_{ij+1/2}^n \right) \quad (39)$$

with  $\Delta y$  the grid size in the tangential direction,  $\mathbf{B}^+ (\Delta \mathbf{Q})_{ij-1/2}^n$  the right going fluctuations, and  $\mathbf{B}^- (\Delta \mathbf{Q})_{ij+1/2}^n$  the left going fluctuation corresponding to the waves entering the cell  $c_{ij}$  from the left and right respectively, given by the following formulas

$$\begin{aligned} \mathbf{B}^+ (\Delta \mathbf{Q})_{ij-1/2}^n &= \sum_{p: \lambda_p > 0} \lambda_p r_p (\alpha_p + \beta_p) \\ \mathbf{B}^- (\Delta \mathbf{Q})_{ij+1/2}^n &= \sum_{p: \lambda_p < 0} \lambda_p r_p (\alpha_p + \beta_p) \end{aligned} \quad (40)$$

evaluated at the cell faces  $f_{ij-1/2}$  and  $f_{ij+1/2}$  respectively. Although the Godunov's method is non-dispersive and does not produce phase errors in treating the wave speeds, it shows a great deal of a numerical diffusion. In order to avoid the numerical diffusion and dispersion at the same time, so-called high resolution (HR) corrections with flux limiters can be applied, increasing the order of accuracy by assuming a piece-wise linear  $\mathbf{Q}$  instead of piece-wise constant. On smooth solutions the HR corrections are second order accurate, while at sharp discontinuities, where the flux limiters are applied in order to avoid an overshooting (or dispersion), it is only first order accurate. One of the advantages of this approach is that each wave is upwinded and limited separately which contributes significantly to the overall accuracy of the algorithm. The HR corrections are added to the Godunov's updating formula (39) as the following:

$$(\mathbf{Q})_{ij}^{n+1} = (\mathbf{Q})_{ij}^n - \frac{\Delta t}{\Delta y} \left( \mathbf{B}^+ (\Delta \mathbf{Q})_{ij-\frac{1}{2}}^n + \mathbf{B}^- (\Delta \mathbf{Q})_{ij+\frac{1}{2}}^n \right) - \frac{\Delta t}{\Delta y} \left( (\mathbf{G})_{ij+1/2}^n - (\mathbf{G})_{ij-1/2}^n \right) \quad (41)$$

with  $\mathbf{G}$  the correction term calculated at  $f_{ij-1/2}$  and  $f_{ij+1/2}$  takes the form

$$G = \frac{1}{2} \sum_{p=1}^4 |\lambda_p| \left( 1 - \frac{\Delta t}{\Delta y} |\lambda_p| \right) r_p (\alpha_p + \beta_p) \phi(\theta_p) \quad (42)$$

with  $\phi(\theta_p)$  the limiter function located within the TVD region [23]. In the present model, the MC flux limiter was considered [24]. The stability region is controlled by the convective limit CFL (Courant–Friedrichs–Lewy) [25] and the time step  $\Delta t$  is determined as the following:

$$\Delta t = CFL \Delta y / \max |\lambda_p| \quad (43)$$

In case that friction terms (14), (15) are used,  $CFL \leq 1/2$ , else  $CFL$  can be increased up to 1.

## 4. Results and discussion

### 4.1. Grid size sensitivity study

The grid size sensitivity study was performed on a 1D grid,  $2\pi R$  long, with a uniformly spaced grid points (100, 400, or 1000), aligned with the tangential direction i.e. with periodic boundary conditions applied. Eq. (33) was solved without the

heat advection, the Coriolis force, and the source term  $\mathbf{S}$  except of the term  $-\Omega^2 R h b_y$  corresponding to the part of the centrifugal force due to the variable topography  $b$ . The chosen initial liquid height  $h$  has a parabolic shape given by

$$h(y, t = 0) = \begin{cases} f(y) & \text{if } f(y) \geq 0 \\ 0 & \text{otherwise} \end{cases} \quad (44)$$

with  $f(y) = 0.1 - 5(y - 1.8)^2$ . Also the solid height  $b$  has initially a parabolic shape

$$b(y, t = 0) = \begin{cases} g(y) & \text{if } g(y) \geq 0 \\ 0 & \text{otherwise} \end{cases} \quad (45)$$

with  $g(y) = 0.02 - 1(y - 1.0)^2$ .

The initial momentum of the liquid layer is zero ( $h v(y, t = 0) = 0$ ). During  $t > 0$ , the parabolic liquid column collapses with two shocks propagating to the left and right. The shocks travel through the periodic extremities, pass each other and reflect from the solid obstacle. After 10 s corresponding to multiple reflections of the shocks from the solid obstacle (approximately 20 reflections), the free surface pattern is compared for each grid size. From Fig. 6, it is obvious that after 10 s only a single moving discontinuity remains in the solution. For a larger number of grid points the wave speed error can be neglected.

#### 4.2. Preserving steady state over variable topography

It is well documented that the fractional-step methods for applying source terms can produce inaccurate results especially when the solution is close to a steady state. In the present algorithm, the source terms are however completely embedded inside the approximate Riemann solver and therefore, the well-balancing of the source term  $\mathbf{S}$  is maintained. A typical test was performed on the lake in rest with a variable topography  $b$ . The same equations, the same grid (400 grid points), and initial conditions as in Section 4.1 were used for this test except of the initial distribution of the liquid height, which was given by

$$h(y, t = 0) = 0.4 - b(y, t = 0) \quad (46)$$

In Fig. 7, the  $y$ -axis on the left and right shows the total height and velocity, respectively. At  $t = 10$  s, the velocity magnitude is everywhere nearly zero, within the round-off error of the algorithm used.

#### 4.3. Stop-and-go mechanism

Although the liquid layer is usually modeled as a Newtonian fluid, a more complicated rheological model might be required when the liquid comprises e.g. a mixture of the liquid metal and free-floating equiaxed crystals. The stop-and-go mechanism is applicable to a non-Newtonian liquid which refuses to flow until a certain level of stress, the yield stress  $\tau_y$ , is exceeded. Thus by applying a sufficiently large yield stress  $\tau_y$  in the source term  $\mathbf{S}$ , the algorithm should be capable of stopping a moving liquid front, all velocities should ultimately decay to zero. The verification of the stop-and-go mechanism was performed on a collapsing parabola given by (44) with  $f(y)$  equal to

$$f(y) = 0.05 - 5(y - 1.2)^2 \quad (47)$$

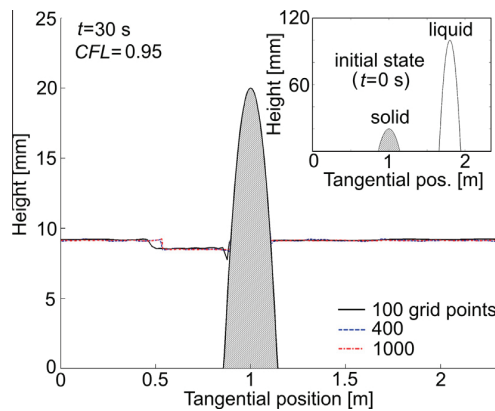


Fig. 6. Grid size sensitivity study showing a wave speed error for different number of grid points (100, 400, and 1000 g.p.).

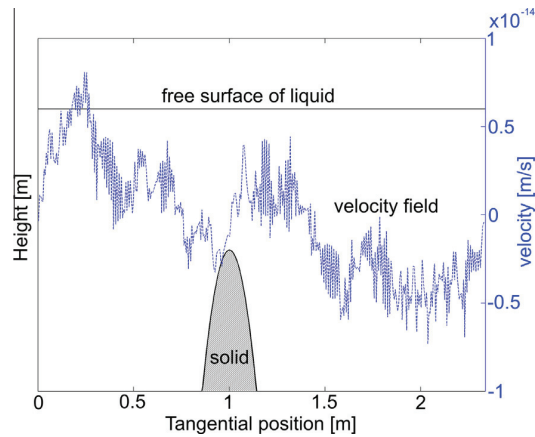


Fig. 7. Preserving steady state over variable topography (a lake in rest). Magnitudes of velocity are nearly zero, within the bounds of the round-off error.

Other parameters and settings were the same as in Section 4.1 except that  $b(y, t = 0) = 0$ . The yield stress  $\tau_y$  was defined using the following formula

$$\tau_y = \Omega^2 R \tan(\gamma), \tag{48}$$

meaning that the front of the liquid layer in rest with the density  $\rho = 1$  should be inclined by angle  $\gamma$ [rad] at the liquid height  $h = 1$ . In other words, the liquid does not move and the centrifugal force exactly balances the yield stress ( $\rho\Omega^2 R h \partial h / \partial y = -\tau_y$ ), which is illustratively shown in Fig. 8.

Here, in the numerical test the angle  $\gamma$  and the density  $\rho$  were set to  $1^\circ$  and  $6800 \text{ kg/m}^3$  respectively. In Fig. 9, the initial conditions are shown in the upper left corner. In addition, the actual shape of the free surface and the corresponding velocity field is shown at  $t = 0.07 \text{ s}$ . Despite a nonzero slope of the free surface in the central part, the liquid already stopped moving there, whereas the fronts still propagate to the left and right. Finally, a steady state is shown at  $t = 0.5 \text{ s}$ , at which the centrifugal pressure exactly balances the effect of the yield stress  $\tau_y$  and therefore the liquid layer shows no movement.

#### 4.4. Coriolis force effect

The Coriolis acceleration  $a_c$  has the only nonzero component in the radial direction, pushing the liquid either towards or outwards the cylinder wall depending on whether the liquid velocity  $v$  is positive or negative. The best demonstration of the Coriolis effect is again on the collapsing parabola given by (44) with  $f(y)$  equal to

$$f(y) = 0.01 - 5(y - 1.2)^2 \tag{49}$$

Other parameters and settings were the same as in Section 4.1 except that  $b(y, t = 0) = 0$ . In Fig. 10, the dashed lines correspond to the case with the Coriolis force at  $t = 0.07 \text{ s}$ . For a better comparison, also the case without the Coriolis force is presented by solid lines. The Coriolis force obviously breaks the symmetry of the collapsing parabola. The liquid naturally propagates faster to the right than to the left.

As shown in Section 2.4, the Coriolis force is put inside the flux function, on the left-hand side of (26), instead of applying it fully as a source term. Both approaches have however their pros and cons. The Coriolis force inside the flux function can turn the eigenvalues from real to complex numbers, meaning that the hyperbolicity can be lost. On the other hand, there is no need for the space integration and any physical or numerical limit, which is generally required when dealing with source

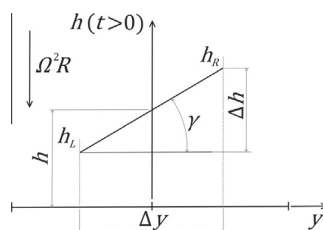


Fig. 8. A schematic of the force balance between the centrifugal force and the yield stress for the liquid height  $h$  and the liquid density  $\rho$ .

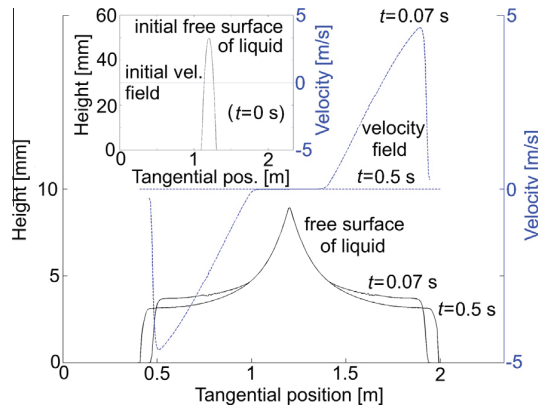


Fig. 9. Initially static liquid parabola collapsing until the balance between the centrifugal pressure and the yield stress  $\tau_y$  restored.

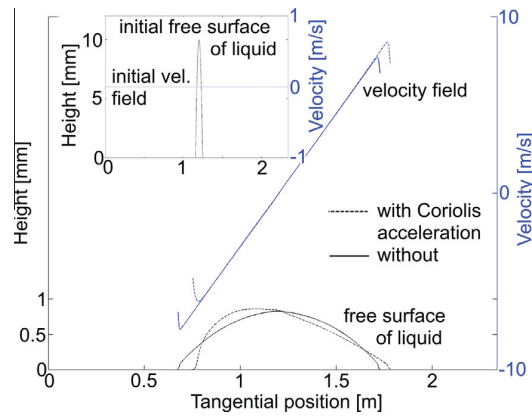


Fig. 10. Effect of the Coriolis force. Dashed and solid lines represent the case with and without the Coriolis force at  $t = 0.07$  s.

terms. When treating the Coriolis force as a source term, the hyperbolicity is strictly preserved, however; the integration is not clear because of the appearance of the velocity  $v$  in the source term. These two approaches are compared to each other in Figs. 11 and 12. The initial conditions is again a liquid parabola given by (44) with  $f(y)$  equal to

$$f(y) = 0.02 - 0.25(y - 1.5)^2 \tag{50}$$

In the early stage ( $t = 0.06$  s) of the liquid spreading shown in Fig. 11, both approaches give almost identical results. However, as the time  $t$  proceeds, spurious oscillations occur in the case of the Coriolis force applied as a source term and gradually grow in time. Although the spurious oscillations extend over the whole domain, the wave speed error is still negligible. See the comparison in Fig. 12 at  $t = 5$  s.

#### 4.5. Heat advection test

The average temperature  $T$  of the liquid layer is required for the heat diffusion and solidification model mentioned in Section 2.5. Although  $hT$  is a conserved quantity (not  $T$ ), the algorithm should be also able to recover  $T$  without any over/undershooting especially near the dry cells. The heat advection test was performed on the collapsing parabola identical to that used in Section 4.4. The average temperature  $T$  of the liquid was set to 100 °C. In order to generalize the numerical test, the parabola was collapsing over a solid hump  $b$  given by (45) with  $g(y)$  equal to

$$g(y) = 0.005 - 0.25(y - 0.8)^2 \tag{51}$$

In Fig. 13, the liquid is just overtopping the hump  $b$  at  $t = 0.08$  s and the temperature  $T$  is obviously advected correctly, without any over/undershooting.

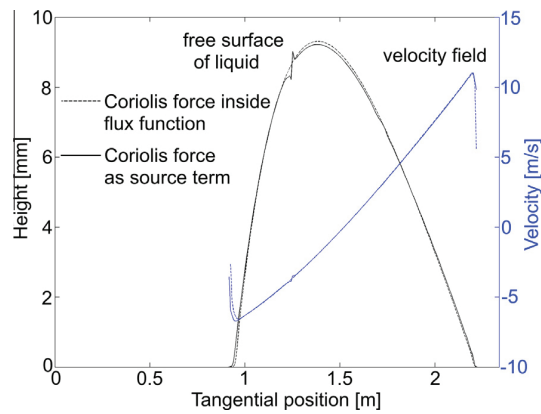


Fig. 11. Coriolis force as a source (the solid line) and as a part of the flux function (the dashed line) at  $t = 0.06$  s.

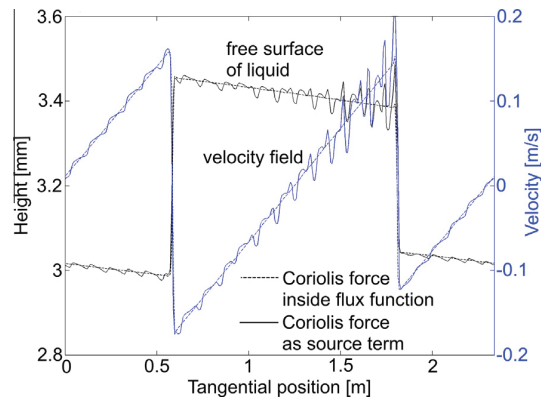


Fig. 12. Coriolis force as a source (the solid line) and as a part of the flux function (the dashed line) at  $t = 5$  s.

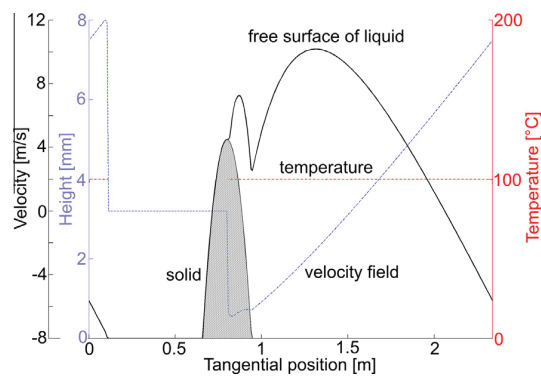
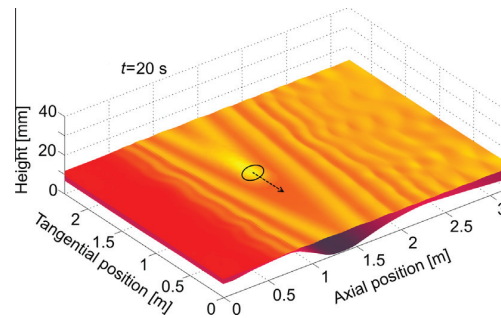


Fig. 13. Heat advection test of a collapsing liquid parabola with the constant temperature of  $T = 100$  °C at  $t = 0.08$  s. The solution is free of undershooting in the temperature  $T$ , especially near dry cells.

#### 4.6. Full simulation

In addition to the 1D numerical tests discussed in Sections 4.1–4.5, the full set of equations (20) (not only the tangential direction) was solved on a 2D Cartesian grid with the axial and tangential dimension corresponding to the cylinder length  $L$  and the cylinder circumference  $2\pi R$  respectively. Eq. (20) were simultaneously solved with the heat diffusion and



**Fig. 14.** Contours of the free surface, disturbed by wave patterns, and the liquid/solid interface with the trench formed due to the localized position of the filling jet. At  $t = 20$  s, the actual position and the apparent velocity of the filling jet are shown as a solid circle and a dashed arrow.

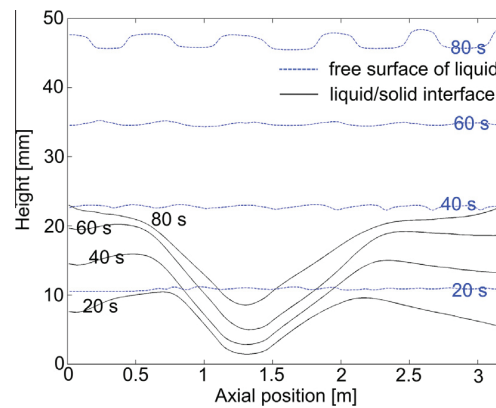


**Fig. 15.** A time evolution of the free surface (dashed lines) and the liquid/solid interface (solid lines) along the axis of the cylindrical model at the tangential position  $y = 1$  m at different times.

solidification model mentioned in Section 2.5. In Fig. 14, the upper and the lower surface represent the actual shape of the free surface of the liquid and the liquid/solid interface respectively at 20 s. Starting with the liquid/solid interface, approximately in the center of the mold (cylinder), exactly below the footprint of the filling jet (Fig. 1), the solidification is suppressed due to the newly incoming hot liquid and a trench is formed around the circumference. The actual position of the filling jet is shown as a solid circle with a dashed arrow signifying the apparent velocity of the filling jet. As approaching both extremities of the mold, the solidification rate increases due to the larger distance from the hot filling and increasing radiative heat losses due to the growing view factor between the free surface and the mold opening. The liquid/solid interface continues growing, until the liquid solidifies completely. In the same figure (Fig. 14), the waves are induced by the filling jet and travel mainly in the axial direction, slightly inclined by the effect of the apparently traveling filling jet. The spacing between waves is larger in the vicinity of the filling jet, where the liquid height  $h$  is large. On the contrary, the wave spacing is small, when the liquid  $h$  is small. The wave spacing is directly linked with the speed of sound, which is proportional to the square root of the liquid height  $h$ .

In Fig. 15, the 2D plot shows a time evolution of both, the liquid/solid interface and the free surface, along the axial direction and at the constant tangential position ( $y = 1$  m). The liquid/solid interface is not symmetric especially due to the off-centered filling.

## 5. Conclusions

During the HSC process, a uniform film of liquid layer is formed around a circumference of the cylindrical mold horizontally spinning around its axis of rotation. The liquid layer is not however motionless which is especially caused by the localized filling, the uneven profile of the liquid/solid interface interacting with the gravity force. The liquid flow can be grouped in the category of free surface flows, in which the momentum along the liquid height  $h$  is negligible compared to momentum components in other directions, the axial and tangential. Instead of solving a complete set of Navier–Stokes equations, we integrate them over the liquid height  $h$  and apply the kinematic boundary condition on the free surface. Only the first order

approximation of the static pressure, the hydrostatic pressure, is considered, leading us to the set of modified shallow water equations (SWE). The modified SWE derived in the present paper include forces such as the centrifugal force, the Coriolis force, the bed shear stress, the yield stress, turbulent and dispersive effects, and variable topography representing the liquid/solid interface. Unlike the original set of SWE, the modified SWE belong to the group of conditionally hyperbolic nonlinear PDEs. In the hyperbolic system shocks and rarefactions propagate at finite wave speeds. In the present paper, an approximate Riemann solver was developed the modified SWE together with the heat advection equation integrated over the liquid height  $h$ . To update the solution in time, we adopted explicit updating formulas originally developed by Godunov. The Godunov's method is only first order accurate and due to the piece-wise constant approximation of data the method possesses a significant numerical diffusion. We applied so-called high resolution corrections with flux limiters (MC limiter) so that the order of accuracy was formally increased up to the second order. To update the solution in two space dimensions, we used the simplest Godunov's splitting algorithm to keep the efficiency of the code. In the approximate Riemann solver, the eigenstructure of the SWE was explicitly calculated from the Jacobian matrices linearized with the help of Roe averages. A special correction for the velocity related to the Coriolis force had to be applied in order to fulfill the Roe's linearization. The algorithm was however not depth-positive i.e. negative liquid heights can occur. To prevent negative heights, a minimum liquid height  $h_{min}$ , a certain threshold, was defined below which all quantities were set to zero when solving the Riemann problem. All the source terms were included in the Riemann solver as a stationary wave. When a transonic rarefaction was detected, the Harten–Hyman entropy fix was applied in order to prevent expansion shocks. The stability of the explicit algorithm was fully controlled by the convective limit  $CFL$ . If a rheological model is included, the algorithm is stable for  $CFL \leq 1/2$ . Otherwise, it is possible to use values of  $CFL$  up to 1.

The capabilities of the algorithm were tested on several 1D simulation. In the grid size sensitivity study (Section 4.1), the wave speed error was qualitatively compared for three different grid sizes, showing only slight differences especially for a larger number of grid points (400 and 1000 g.p.). In Section 4.2, preserving of steady state was verified on the benchmark – the lake in rest with the variable topography  $b$ . All velocities were within the round-off error. Note that this is a typical example where the fractional step method for applying a source term would fail. A next 1D numerical test (Section 4.3) was focused on the stop-and-go mechanism applicable when e.g. a yield stress  $\tau_y$  is considered. An initially patched parabola was collapsing due to the centrifugal force winning over the effect of the yield stress  $\tau_y$  until a balance between them was restored and a new static shape of the liquid was formed. The main idea of applying any type of friction is a physical limit saying that the friction cannot change the sign of the momentum within each intermediate state ( $hu_m$  and  $h\nu_m$ ). In Section 4.4, the effect of the Coriolis force was described by means of 1D simulation performed in the tangential direction. Two cases, with and without the Coriolis force, were compared. When only the centrifugal force is applied, the liquid is naturally spreading in a symmetrical manner. Once the Coriolis force comes in the play, the liquid propagates faster when moving in the positive (rotational) direction and vice versa. In addition, a test was performed demonstrating how important is putting the Coriolis force on the left-hand side of the momentum equation and treat it as a part of the flux function. After letting the parabola to collapse, certain waves survive for a very long time because no other force makes them disappear. In the case with the Coriolis as a source term, parasitic oscillations pollute the solution, which does not happen with the Coriolis inside the flux function. The last 1D test (Section 4.5) targeted on testing the performance of the heat advection model fully coupled with the modified SWE, both solved using the Riemann solver. Solving the heat advection equation along with other transport equations (the SWE) using a Riemann solver is only sporadically discussed in the literature. The behavior of the algorithm was checked especially near dry cells, where the over/undershooting in the temperature  $T$  would be expected the most. The temperature field was advected correctly, including the region near dry cells. Finally, all the particular properties of the proposed algorithm discussed in Sections 4.1–4.5 were successfully combined in the simulation of the HSC process, a real industrial application (Section 4.6).

## Acknowledgments

Financial support by the Austrian Federal Government (in particular from the Bundesministerium fuer Verkehr, Innovation und Technologie and the Bundesministerium fuer Wirtschaft, Familie und Jugend) and the Styrian Provincial Government, represented by Oesterreichische Forschungsforderungsgesellschaft mbH and by Steirische Wirtschaftsforderungsgesellschaft mbH, within the research activities of the K2 Competence Centre on “Integrated Research in Materials, Processing and Product Engineering”, operated by the Materials Center Leoben Forschung GmbH in the framework of the Austrian COMET Competence Centre Programme, is gratefully acknowledged. This work is also financially supported by the Eisenwerk Sulzau-Werfen R. & E. Weinberger AG.

## References

- [1] G. Chirita, I. Stefanescu, J. Barbosa, H. Puga, D. Soares, F.S. Silva, On assessment of processing variables in vertical centrifugal casting technique, *Int. J. Cast Met. Res.* 22 (2009) 382–389.
- [2] C.W. Hirt, B.D. Nichols, Volume of fluid (VOF) method for the dynamics of free boundaries, *J. Comput. Phys.* 39 (1981) 201–225.
- [3] Z. Xu, N. Song, R.V. Tol, Y. Luan, D. Li, Modelling of horizontal centrifugal casting of work roll, *Mater. Sci. Eng.* 33 (2012) 012030.
- [4] E. Kaschnitz, Numerical simulation of centrifugal casting of pipes, *Mater. Sci. Eng.* 33 (2012) 012031.
- [5] K.S. Keerthiprasad, M.S. Murali, P.G. Mukunda, S. Majumdar, Numerical simulation and cold modeling experiments on centrifugal casting, *Metall. Mater. Trans.* B 42 (2010) 144–155.

- [6] L. Drenchev, J. Sobczak, S. Malinoc, W. Sha, Numerical simulation of macrostructure formation in centrifugal casting of particle reinforced metal matrix composites. Part 1: model description, *Modell. Simul. Mater. Sci. Eng.* 11 (2003) 635–649.
- [7] L. Drenchev, J. Sobczak, S. Malinoc, W. Sha, Numerical simulation of macrostructure formation in centrifugal casting of particle reinforced metal matrix composites. Part 2: simulation and practical applications, *Modell. Simul. Mater. Sci. Eng.* 11 (2003) 651–674.
- [8] N. Song, Y. Luan, Y. Bai, Z.A. Xu, X. Kang, D. Li, Numerical simulation of solidification of work roll in centrifugal casting process, *J. Mater. Sci. Technol.* 28 (2) (2012) 147–154.
- [9] A.J.C. Saint-Venant, *Théorie du mouvement non permanent des eaux, avec application aux crues de rivières et à l'introduction des marées dans leur lit*, C. R. Acad. Sci. Paris 73 (1871) 147–154.
- [10] J. Bohacek, A. Kharicha, A. Ludwig, M. Wu, Simulation of horizontal centrifugal casting: mold filling and solidification, *ISIJ Int.* 54 (2) (2014) 266–274.
- [11] D.L. George, Augmented Riemann solvers for the shallow water equations over variable topography with steady states and inundation, *J. Comput. Phys.* 227 (2008) 3089–3113.
- [12] M.-O. Bristeau, B. Coussin, *Boundary conditions for the shallow water equations solved by kinetic schemes*, Rapport de recherché 4282 (2001) 1–28.
- [13] D.L. George, *Finite volume methods and adaptive refinement for tsunami propagation and inundation* (Ph.D. thesis), submitted at University of Washington, 2006.
- [14] E. Audusse, M.-O. Bristeau, B. Perthame, J. Sainte-Marie, A multilayer Saint-Venant system with mass exchanges for shallow water flows. Derivation and numerical validation, *ESAIM: Math. Modell. Numer. Anal.* 45 (2011) 169–200.
- [15] J. Bohacek, A. Kharicha, A. Ludwig, M. Wu, Shallow water model for horizontal centrifugal casting, *Mater. Sci. Eng.* 33 (2012) 012032 (*Int. Conf. MCWSP XIII* published in IOP Conf. Series).
- [16] J. Murillo, P. Garcia-Navarro, Wave Riemann description of friction terms in unsteady shallows: application to water and mud/debris floods, *J. Comput. Phys.* 231 (2012) 1963–2001.
- [17] R.J. Leveque, *Finite Volume Methods for Hyperbolic Systems*, Cambridge University Press, New York, 2002 (p. 447).
- [18] P.L. Roe, Upwind differencing schemes for hyperbolic conservation laws with source terms, *Lect. Notes Math.* 1270 (1987) 41–51.
- [19] A. Harten, J.M. Hyman, Self-adjusting grid methods for one-dimensional hyperbolic conservation laws, *J. Comput. Phys.* 50 (1983) 235–269.
- [20] R.J. Leveque, *Finite Volume Methods for Hyperbolic Systems*, Cambridge University Press, New York, 2002 (p. 377).
- [21] K. T. Mandli, *Finite volume methods for the multilayer shallow water equations with applications to storm surges* (Ph.D. thesis) submitted at University of Washington, 2011.
- [22] J. Murillo, P. Garcia-Navarro, Weak solutions for partial differential equations with source terms: application to the shallow water equations, *J. Comput. Phys.* 229 (2010) 4327–4368.
- [23] A. Harten, High resolution schemes for hyperbolic schemes for hyperbolic conservation laws, *J. Comput. Phys.* 49 (1983) 357–393.
- [24] B. van Leer, Towards the ultimate conservative difference scheme IV. A new approach to numerical convection, *J. Comput. Phys.* 23 (1977) 276–299.
- [25] R. Courant, E. Isaacson, M. Rees, On the solution of nonlinear hyperbolic differential equations by finite differences, *Commun. Pure Appl. Math.* 5 (1952) 243–252.

**STEELSIM**

**2015**

6<sup>th</sup> International Conference on

**MODELLING and SIMULATION of  
METALLURGICAL PROCESSES in  
STEELMAKING**

Bardolino, Garda Lake, Italy, 23-25 September 2015

## AN APPROXIMATE RIEMANN SOLVER FOR TWO LAYER SHALLOW WATER EQUATIONS IN HORIZONTAL CENTRIFUGAL CASTING

J. Bohacek<sup>1</sup>, A. Kharicha<sup>1\*</sup>, A. Ludwig<sup>1</sup>, M. Wu<sup>1,2</sup>, A. Paar<sup>3</sup>, M. Brandner<sup>3</sup>, L. Elizondo<sup>3</sup>, T. Trickl<sup>3</sup>

<sup>1</sup> Chair of Simulation and Modelling of Metallurgical Processes, Montanuniversitaet Leoben, Austria

<sup>2</sup> Christian Doppler Laboratory for Advanced Process Simulation of Solidification and Melting, Montanuniversitaet Leoben, Austria

<sup>3</sup> Research & Development, Eisenwerk Sulzau-Werfen, R. & E. Weinberger AG, Austria

\* Corresponding author: [abdellah.kharicha@unileoben.ac.at](mailto:abdellah.kharicha@unileoben.ac.at)

S

### ABSTRACT

An approximate Riemann solver was developed for solving the shallow water equations (SWE) and energy transport describing the average flow dynamics of two liquid layers spreading inside a horizontally rotating cylinder. The numerical model was particularly developed for simulating the horizontal centrifugal casting (HSC) of the outer layer and the intermediate layer of a work roll. The SWE were derived in the rotating frame of reference; therefore, fictitious forces (the centrifugal force and the Coriolis force) were considered. In addition, other forces such as the bed shear force, the force of gravity, and forces arising from the variable liquid/solid interface were taken into account. The mould filling was realized through a Gaussian mass source applied in the centre of the mould. In addition to the flow solver, the enthalpy equation with the appropriate boundary conditions was solved inside the mould, end cores, and the casting. The solidification progress was studied by means of plotting the time dependent solid shell thickness at selected locations. The calculations were successfully validated with the pyrometer and thermo-camera measurements.

### KEYWORDS

steel, centrifugal casting, numerical modelling, shallow water equations, mould filling

### INTRODUCTION

In the present paper a numerical simulation of the horizontal centrifugal casting (HSC) of the outer layer and the intermediate layer of a work roll is concerned. In short, the HSC process can be outlined as the following: An initially empty cylindrical mould is from inside painted with the refractory material and laid on four carrying rollers, from which two coaxial rollers are driven and the other two are driving. Prior to the casting, the mould is preheated to a desired temperature and the driving rollers gradually bring the mould into the rotational motion. When the desired rounds per minutes is reached the casting of the outer shell can start. A liquid metal is poured from the crucible via the statically mounted runner approximately in the centre of the mould. Due to high centrifugal forces (>100g) the liquid metal spreads uniformly and

generates a sleeve of constant thickness. The solidification front proceeds from the relatively cold wall of the mould. After some period of time, the outer layer is partially solidified and the pouring of the intermediate layer begins. The centrifuging continues until the solidification is completed inside both layers.

Among other research papers published recently, numerical models differ mainly in whether the flow was solved or not. All research papers we mention here deal with a single layer casting i.e., in none of them the casting of two layers is discussed. Most of the numerical studies solving the flow dynamics used the VOF method [1] to capture the interface between the melt and the surrounding air. Xu [2] introduced an interesting numerical model of the HSC process. The full set of Navier-Stokes equations was solved along with the heat advection-diffusion equation. The main focus of the paper dwells in

studying different gating systems for the filling. Simulations were terminated at 30 seconds, when the filling was completed. The solidification model is not discussed in the paper. Next interesting paper on the HSC process namely on the centrifugal casting of seamless pipes was written by Kaschnitz [3]. In this case, a commercial package FLOW-3D was used. In order to avoid extremely small time steps, momentum equations were solved in the rotating frame of reference. However, due to a very small wall-to-length thickness ratio, one simulation still took considerably long time (~20 days).

A commercial package (STAR-CD V4) was also used in a paper by Keerthiprasad [4]. An effort was spent on comparing the cold flow simulations of the single layer HSC with the experimental castings. The mesh inside the mould was entirely constructed out of rather coarse polyhedral elements, which allowed notably large time steps (~0.01 s). Only the continuity and momentum equations were solved for the flow. Heat transfer and solidification were not discussed in the paper.

Results from simulations showed roughly how the melt is spreading during the filling stage, however no details are given on how the filling was imposed and whether the model could capture some free surface patterns or not. From the literature survey it can be concluded that when the main objective of the research paper is a simulation of the free-surface, the heat transfer and the solidification are usually ignored. The main reason for this is different characteristic times for the free-surface motion and the solidification. In addition to free-surface simulations, several research papers can be listed, which neglect the flow, do not consider mould filling, or assume a static flat free-surface. Such works generally target on simulation of the solidification of the whole liquid layer, very often accompanied by a segregation of some element due to a density difference and extremely high centrifugal pressure. For example in [5], Drenchev introduced a numerical model discussing some aspects of macrosegregation of reinforcing particles in a metal matrix. The enthalpy equation was the primary equation to solve with thermal physical properties determined from the segregation model. Since the flow (or the mould filling) was not included, the initial thickness of the liquid layer

was uniform and identical to the final thickness of the shell. Similar numerical models can be found in [6, 7]. The main bottleneck is the fact that the model lacks variances in the mould and shell temperatures due to the localized filling, which in turn affects the local thickness of the solidified shell and the macrostructure pattern consequently.

In the present paper, we introduce a novel approach for modelling of average flow dynamics of both, the outer and the intermediate, layers. These two layers are immiscible. Here, the two layer model is an extension of the single layer model detailed e.g. in [8, 9]. Moreover, the top layer has lower density than the bottom layer. Instead of solving the full set of Navier-Stokes equations with the advection equation for the volume fraction (VOF method), which is inherently computationally expensive, we make assumption that the flow obeys so-called two layer shallow water equations (SWE). The flow during the HSC process can be characterized as a free surface flow with the moving interface between two layers, in which the thickness of each layer is rather small compared to the length of the mould. For this reason, it is rational to expect the momentum in the radial direction to be negligible compared to the momentum in the axial and tangential direction. Taking the 3D Navier-Stokes equations and the continuity equation leaving out the momentum equation in the radial direction, replacing the pressure term with the hydrostatic pressure, and integrating momentum and continuity equations along the liquid height of each layer, and applying kinematic boundary condition on the free surface and at the interface between two layers one obtains the two layer 2D shallow water equations [10]. The two layer SWE are conditionally hyperbolic non-linear PDEs. In our case the range of parameters preserves hyperbolicity and for this reason, we calculate the fluxes using the approximate Riemann solver. The two layer SWE are coupled with the heat advection-diffusion equation containing the latent heat source term due to solidification. The heat diffusion is also solved with the appropriate thermal boundary conditions inside the mould and both end cores. The numerical simulation is performed with the industrial input parameters. Results are validated against pyrometer and thermo-camera measurements.

## 1. THEORY

### 1.1 Two layer shallow water equations

In the present paper, the two layer shallow water equations are derived only in one dimension namely the axial direction  $x$  (Fig. 1). By replacing the pressure term in the 2D Navier-Stokes equations for the axial and the radial direction with the hydrostatic pressure, applying the kinematic boundary condition at the free-surface and at the interface between each layer, and integrating both momentum equations and the continuity equation over the height of each liquid, one yields the set of two layer one dimensional shallow water equations in the axial direction. The hydrostatic pressure is equivalent to the centrifugal pressure. In the plane defined by the radial and the axial direction, the Coriolis force as a next fictitious force does not have any non-zero component, as long as the rotation axis is coincident with the mould axis. Therefore, the Coriolis

force does not appear in the momentum equations. The continuity equations for the outer layer (denoted by subscript 1) and the intermediate layer (denoted by subscript 2) take the form

$$(h_1)_t + (h_1 u_1)_x = 0 \quad (1)$$

$$(h_2)_t + (h_2 u_2)_x = 0 \quad (2)$$

where  $h$  is the height of a layer, and  $u$  is the mass-flow averaged velocity of the corresponding layer. In this paper, the notation  $(\cdot)_t$  stands for the partial time derivative and  $(\cdot)_x$  for the derivative in  $x$ -direction. Note that since  $h_1 + h_2 \ll R$ , the axial and radial coordinates are mapped onto the Cartesian plane  $\{x, r\} \rightarrow \{x, z\}$  as the following

$$x = x \quad \text{and} \quad z = R - r \quad (3)$$

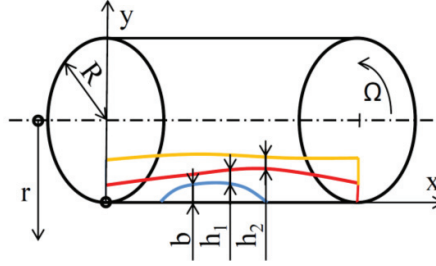


**Figure 1.** Schematic of the HSC process depicting two liquid layers and solidified shell denoted by  $h_1$ ,  $h_2$ , and  $b$ , respectively.

The momentum equations for each layer are given by

$$(h_1 u_1)_t + \left( h_1 u_1^2 + \frac{1}{2} \Omega^2 R h_1^2 \right)_x = -\Omega^2 R h_1 (b)_x - \frac{\rho_1}{\rho_2} \Omega^2 R h_1 (h_2)_x - \frac{\tau_b}{\rho_1} + \frac{\tau_i}{\rho_1} \quad (4)$$

$$(h_2 u_2)_t + \left( h_2 u_2^2 + \frac{1}{2} \Omega^2 R h_2^2 \right)_x = -\Omega^2 R h_2 (b)_x - \frac{\rho_1}{\rho_2} \Omega^2 R h_2 (h_1)_x - \frac{\tau_i}{\rho_2} \quad (5)$$

with  $\Omega$  the angular frequency of the mould,  $R$  the inner radius of the mould,  $b$  is the height of the solid layer growing from the mould wall,  $\rho$  the density of the liquid layer,  $\tau_b$  and  $\tau_i$  the bed shear stress and the shear stress between the lay-

ers both derived by assuming a parabolic velocity profiles in each layer. The bottom shear stress  $\tau_b$  and the shear stress  $\tau_i$  between the layers are expressed by the following formulas

$$\tau_b = 3 \frac{\mu_1}{h_1} u_1 \quad (6)$$

$$\tau_i = 3 \frac{\mu_2}{h_2} \{u_2 - u_1\} \quad (7)$$

The momentum exchange between two layers is thus realized through two mechanisms. The first mechanism is hydrostatic, meaning that any slope of the layer 1 will influence the layer 2 and vice versa. The second mechanism is kinetic,

meaning that the moving layer 1 will drag the layer 2 and vice versa. Note that the two layer SWE are only applicable when the density of the layer 1 is larger than the density of the layer 2 at the top  $\rho_1 > \rho_2$ . When  $\rho_1 < \rho_2$  the heavier liquid at the top will penetrate the lighter liquid at the bottom via the mechanism of Kelvin-Helmholtz instability [11]. In the HSC process, it is naturally desired that the density of the outer layer  $\rho_1$  is larger than the density of the intermediate layer  $\rho_2$ .

### 1.2 Heat advection equation for each layer

Due to the fact that the horizontal velocity field is solved by the SWE, the advection of the temperature field has to be solved correspondingly. In other words, the mass-flow averaged velocities  $u_1$  and  $u_2$  are used to advect the temperature field averaged over the height of each layer. For each layer we therefore solve the advection equation given by:

$$(h_1 \bar{T}_1)_t + (h_1 u_1 \bar{T}_1)_x = 0 \quad (8)$$

$$(h_2 \bar{T}_2)_t + (h_2 u_2 \bar{T}_2)_x = 0 \quad (9)$$

where  $\bar{T}$  is the temperature averaged over the liquid height. Note that the heat advection is solved together with the two layer SWE. The heat diffusion inside layers, the mould, and the end cores is solved in a fractional step approach along with the solidification.

### 1.3 Heat diffusion, solidification, and mould filling

After the average flow dynamics is solved together with the heat advection in each layer, the heat diffusion is solved with the appropriate thermal boundary conditions (Table 1). A refractory coating applied in the contact between the casting and the mould is taken into account via a thin wall model. In order to correctly mimic the latent heat release due to the solidification, the source of the latent heat is added to the heat diffusion equation, which written in the cylindrical coordinates takes the following form:

$$\rho c_p (T)_t = \frac{1}{r} (kr (T)_r)_r - \rho L f_t \quad (10)$$

with  $r$  the radial distance from the mould axis,  $k$  the thermal conductivity of the actual material,  $L$  the latent heat, and  $f$  the liquid fraction. The term with the latent heat is potentially a stiff

source term and special care has to be taken in order to avoid numerical instabilities and too expensive iterative algorithms. In the present paper we adopted an approach by Voller [12], which usually requires only a few iterations ( $\sim 3$ ) to converge the solution. For each layer a different liquid fraction-to-temperature relationship was used to mimic solidification of different materials (shown later in Sec. 3). After the temperature field is obtained, the solid height  $b$  is updated by using the new position of the solidification front corresponding to the isoline of solidus temperature. Note that the solid height  $b$  appears in the SWE, Eqs. (4)-(5).

The pouring of the outer and the intermediate layer is realized through the mass source term with the normal distribution placed in the mould centre. The initial momentum of newly incoming mass can be neglected when compared to the centrifugal pressure immediately exerted on the liquid body.

## 2. CALCULATION

All equations mentioned in Sec. 1 were solved in finite volume framework. The implicit backward Euler method [13] was applied to discretize the heat diffusion Eq. (10). The symmetric linear system of equations was solved with the help of the preconditioned conjugate gradient solver. The latent heat source term was split into an implicit and explicit part, which very much improved the convergence. Only a few iterations were necessary in order to drop residuals below the specified value.

Due to the hyperbolicity of the SWE, explicit updating formulas were used namely the first order Godunov's scheme with the high resolution corrections (MC limiter) [14]. The fluxes were determined from the approximate solution of the Riemann problem.

### 1.3 Approximate Riemann solver + fractional stepping

Symbolically, the SWE can be written as the following

$$\mathbf{Q}_t + \mathbf{A}(\mathbf{Q})_x = \mathbf{S} \quad (11)$$

where  $\mathbf{Q}$  represents the vector of conserved quantities  $\mathbf{Q} = [h_1, h_1 u_1, h_1 \bar{T}_1, h_2, h_2 u_2, h_2 \bar{T}_2]^T$ ,  $\mathbf{A}$  the vector of flux functions, and  $\mathbf{S}$  the vector of

source terms. Eq. (11) can be rewritten in the following form

$$\mathbf{Q}_t + \mathbf{A}'(\mathbf{Q}) \cdot \mathbf{Q}_x = \mathbf{S} \quad (12)$$

where  $\mathbf{A}'(\mathbf{Q})$  is the Jacobian matrix with conditionally real eigenvalues. For the two layer SWE, a direct evaluation of the eigenspace is prohibitively very expensive. Instead, an approximation is more favourable. In the present paper, we expand about differences in the layer speeds and calculate first order approximations of eigenspeeds as

$$\lambda_{1,2} = \frac{h_1 u_1 + h_2 u_2}{h_1 + h_2} \pm \sqrt{\Omega^2 R \{h_1 + h_2\}} \quad (13)$$

$$\lambda_{3,4} = \frac{h_1 u_1 + h_2 u_2}{h_1 + h_2} \quad (14)$$

$$\pm \sqrt{\frac{h_1 h_2}{h_1 + h_2} \left\{ \left[ 1 - \frac{\rho_2}{\rho_1} \right] \Omega^2 R - \frac{\{u_2 - u_1\}^2}{h_1 + h_2} \right\}} \\ \lambda_{5,6} = [u_1, u_2]^T \quad (15)$$

where  $\lambda_{1,2}$  and  $\lambda_{3,4}$  represent the external and internal eigenspeeds, respectively. The external eigenspeeds correspond to the speeds of free-surface waves induced by the centrifugal pressure, whereas the internal waves are much smaller and correspond to waves due to the density and the velocity difference. The eigenspeeds  $\lambda_{5,6}$  represent linearly degenerate waves passively carrying jumps in  $h_1 T_1$  and  $h_2 T_2$ . From Eq. (14) the condition for the loss of hyperbolicity can be calculated

$$\kappa = \frac{\{u_2 - u_1\}^2}{\left[ 1 - \frac{\rho_2}{\rho_1} \right] \Omega^2 R \{h_1 + h_2\}} \leq 1 \quad (16)$$

which is nearly the inverse of the Richardson number defining the transition to Kelvin-Helmholtz instability [15]. In the present paper, the hyperbolicity of Eq. (12) is however preserved and thus, an approximate Riemann solver can be used. By using the Jacobian matrix  $\mathbf{A}'(\mathbf{Q})$  from Eq. (12), the eigenvalues, Eqs. (13)-(14), and operation of linear algebra, the space of eigenvectors can be obtained. The following system of linear equations has to be solved for each eigenspeed in order to calculate corresponding columns of eigenvector space  $\mathbf{R}$ .

$$\mathbf{A}'(\mathbf{Q}) \cdot [1, \alpha_1, \alpha_2, \alpha_3, \alpha_4, \alpha_5]^T = [1, \lambda \alpha_1, \lambda \alpha_2, \lambda \alpha_3, \lambda \alpha_4, \lambda \alpha_5]^T \quad (17)$$

The final form of each of the eigenvectors is

$$\mathbf{r} = [1, \lambda, T_1, \alpha_3, \lambda \alpha_4, \alpha_5 T_2]^T. \quad (18)$$

Knowing the complete eigenspace of the hyperbolic system, Eq. (12), the strength of each wave can be obtained by solving the linear system of equations [16]

$$\mathbf{R} \alpha = \Delta \mathbf{Q} \quad (19)$$

with  $\Delta \mathbf{Q}$  being the jump of conserved quantities  $\mathbf{Q}$  over the face of a finite volume element. After that, the fluxes can be obtained [17]. So far, only the homogeneous case of Eq. (11) was discussed ( $\mathbf{S} = 0$ ). The first two terms on the right hand side of Eqs. (4) and (5) are upwinded by means of projecting it onto the matrix of eigenvectors and propagating it at the eigenspeeds, which result in a stationary discontinuity. Close to the numerical cells that are nearly empty it is crucial to apply a physical limit preventing from the occurrence of negative heights. The stationary discontinuity modifies the wave strengths of the homogeneous case, which in turn changes the resulting fluxes. A fractional stepping had to be applied for the remaining terms of the source  $\mathbf{S}$ , namely all friction terms, as the following

$$(h_1 u_1)_t = -\frac{\tau_b}{\rho_1} + \frac{\tau_i}{\rho_1} \quad (20)$$

$$(h_2 u_2)_t = -\frac{\tau_i}{\rho_2} \quad (21)$$

The main reason for this is that it is not yet clear how to handle physical limits. As long as the friction terms stay weak compared to the convective and the centrifugal pressure terms, the fractional stepping will maintain a reasonable accuracy.

### 3. RESULTS AND DISCUSSION

The numerical model was verified against the pyrometer and the thermo-camera measurements conducted during the industrial HSC process. The important dimensions and the main process parameters are summarized in Table 1. The physical properties are listed in Table 2. The simulation was performed on a structured grid with around 20 000 volume elements. The calculation

was terminated by the user at 3300 s of physical time.

**Table 1.** Dimensions and process parameters

Parameter	value	unit
Length of mould	3.78	m
Inner radius of mould	0.424	m
Mass flow rate of outer layer	75	kg/s
Start of filling outer layer	0	s
Mass flow rate of outer layer	9.7	kg/s
Ambient temperature	25	°C
HTC <sup>a</sup> at outer surfaces	40	W/m <sup>2</sup> /K
HTC at roller tracks	500	W/m <sup>2</sup> /K

<sup>a</sup> heat transfer coefficient

**Table 2.** Physical properties of materials

	Outer layer	Intermediate layer	mould	end core	coating
Specific heat [J/kg/K]	430	450	490	650	
Thermal conductivity [W/m <sup>2</sup> /K]	22	25	58.6	2.3	2.5
Density [kg/m <sup>3</sup> ]	7700	7200	7850	2200	
Latent heat [kJ/kg]	280	200			<sup>a</sup>
Dynamic viscosity [Pa s]	0.006	0.006			

<sup>a</sup> blank entries are irrelevant i.e. not used in the numerical model

The simulation results were compared with the pyrometer and thermo-camera measurements. The pyrometer was used to record the free-surface temperature of the casting. The aiming position of the pyrometer was located approximately in 1/3rd of the mould length. In addition, the thermo-camera was recording the outer temperature of the mould. From the thermo-camera pictures the average temperature of the mould wall was calculated and used for the comparison. In Fig. 2, cooling curves from several castings of the same work roll obtained from the pyrometer are shown in thin solid lines. The cooling curve from the simulation is shown in a thick solid line. On a second y-axis, average temperatures of the external mould wall are compared. Simulation

and experimental data are in a quite good agreement. Next, Fig. 3 shows the computational domain with the volume elements partially visible. At ~35 min., temperature contours are given along with important lines such as the free-surface line, the interface between the outer and intermediate layer, and isolines of liquidus and solidus temperatures.

In Fig. 3, the actual height  $h_2$  of the intermediate layer is not uniform due to the intermediate layer spreading from the mould centre towards the end cores and the intermediate layer interacting with the outer layer through the friction and centrifugal pressure terms.

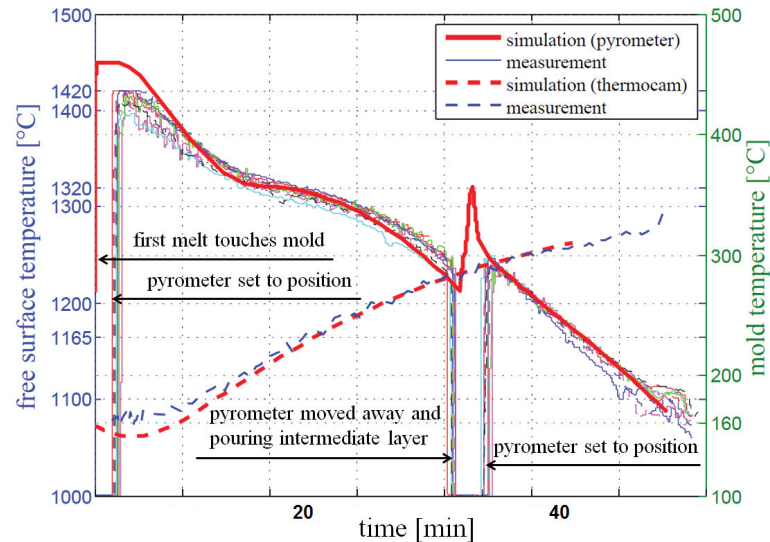


**Figure 2.** Comparison of cooling curves obtained from simulation and experiments (solid line – pyrometer, dashed line – thermo-camera).

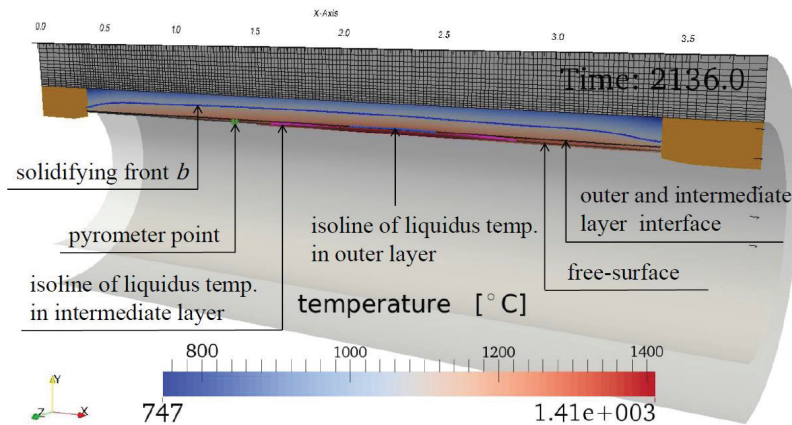


**Figure 3.** Temperature distribution in the outer and intermediate layer at ~35 min.

#### 4. CONCLUSION

A simple algorithm was introduced allowing the calculation of the whole HSC process of the outer and intermediate layer of a work roll (~55 min) in a reasonable enough time, while still resolving main aspects of the flow. The Navier-Stokes equations were substituted by the two layer shallow water equations. The solidification (remelting) was solved with the help of the enthalpy method in finite volume framework considering the prescribed liquid fraction-to-temperature relationships. The numerical model was successfully verified against the pyrometer and

thermo-camera measurements. The mixing due the density differences cannot be captured by the present approach, which can be marked as a main drawback of the model.

#### ACKNOWLEDGEMENT

Financial support by the Austrian Federal Government (in particular from the Bundesministerium fuer Verkehr, Innovation und Technologie and the Bundesministerium fuer Wirtschaft, Familie und Jugend) and the Styrian Provincial Government, represented by Oesterreichische Forschungsfoerderungsgesellschaft mbH and by

Steirische Wirtschaftsfoerderungsgesellschaft mbH, within the research activities of the K2 Competence Centre on "Integrated Research in Materials, Processing and Product Engineering", operated by the Materials Center Leoben Forschung GmbH in the framework of the Austrian COMET Competence Centre Programme, is gratefully acknowledged.

## REFERENCES

- [1] C.W. Hirt, and B.D. Nichols, *J. Comp. Physics*, 39 (1981) pp 201-225.
- [2] Z. Xu, N. Song, R.V. Tol, Y. Luan and D. Li, *Mater. Sci. Eng.*, 33 (2012) pp. 012030.
- [3] E. Kaschnitz, *Mater. Sci. Eng.*, 33 (2012) pp. 012031.
- [4] K.S. Keerthiprasad, M.S. Murali, P.G. Mukunda and S. Majumdar, *Metall. Mater. Trans.B*, 42 (2010) pp 144-155.
- [5] L. Drenchev, J. Sobczak, S. Malinoc and W. Sha, *Modell. Sim. Mater. Sci. Eng.*, 11 (2003) pp 635-649.
- [6] L. Drenchev, J. Sobczak, S. Malinoc and W. Sha, *Modell. Sim. Mater. Sci. Eng.*, 11 (2003) pp 651-674
- [7] N. Song, Y. Luan, Y. Bai, Z.A. Xu, X. Kang and D. Li, *J. Mater. Sci. Tech.*, 28 (2012) pp 147-154.
- [8] J. Bohacek, A. Kharicha, A. Ludwig and M. Wu, *ISIJ Int.*, 54 (2014) pp 266-274.
- [9] J. Bohacek, A. Kharicha, A. Ludwig and M. Wu, *Mater. Sci. Eng.*, 33 (2013) pp. 012032.
- [10] V.V. Ostapenko, *J. Appl. Mech. Tech. Physics*, 20 (1997) pp 127-135.
- [11] W. Thomson, *Phil. Mag.*, 42 (1871) pp 362-377.
- [12] V.R. Voller and C.R. Swaminathan, *Num. Heat Transfer B*, 19 (1991) pp 175-189.
- [13] J.C. Butcher: *Numerical methods Ordinary Differential Equations*, New York: John Wiley & Sons (2003)
- [14] B. Van Leer, *J. Comp. Physics*, 23 (1977) pp 276-299.
- [15] K.T. Mandli, PhD thesis, University of Washington (2011) p 57.
- [16] R.J. Leveque, *Finite Volume Methods for Hyperbolic Problems*, New York: Cambridge University Press (2002) p 54.
- [17] D.L. George, PhD thesis University of Washington (2006) p 31

## 2.3 (Non-)hydrostatic free-surface model to model

Efforts concerning simulation of the horizontal centrifugal casting of the work roll are summarized in 2.4. It started with 2D Volume of Fluid model in ANSYS FLUENT in 2009. It came to an end, temporarily, with the own free-surface flow solver in 2018. It is about to continue again in autumn of 2021, being again funded by the Austrian COMET; however, there will be a new postdoc coming.

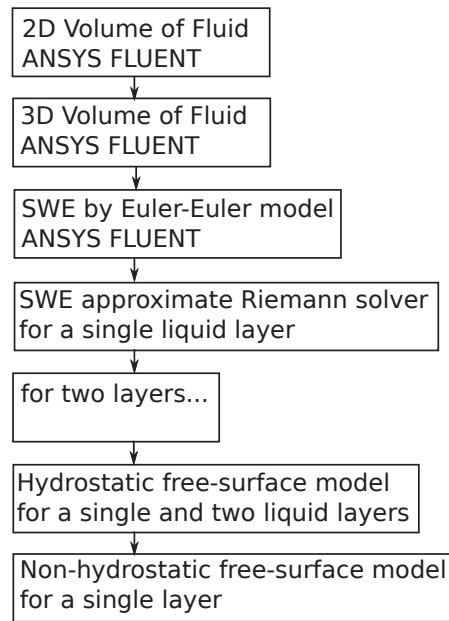


Fig. 2.4: A chronological chart of HSC solver developments

In order to address the drawbacks of the SWE model, as summarized in the previous section 2.2, the free-surface model was developed according to the original paper by Casulli [23]. The free-surface model was published in the article entitled "A (non-)hydrostatic free-surface numerical model for two-layer flows" and it is given on subsequent pages. It was derived from the 3D Navier-Stokes equations and the continuity equations by applying the kinematic boundary condition on the free-surface and the moving interface between the layers. The central idea is splitting of the pressure term into the hydrostatic and hydrodynamic part. Four different examples are shown:

1. The shallow water equation provide a good approximation when waves on the free-surface are long. In the opposite case, the hydrodynamic part of the pressure plays an important role; hence, should not be ignored.
2. In configuration with two liquid layers, the SWE provide accurate results as long as the densities of the liquids are similar. In the opposite case, the wave speeds of the Riemann solver namely those responsible for the momentum

transfer between the layers cannot be correctly approximated. Therefore, the Casulli's approach should be preferred.

3. Free-surface buoyant free-surface flow is shown on two examples. In the first one, the cooling is applied on the free surface. In the second one, the cooling is applied at the bottom wall. The latter is compared against ANSYS FLUENT.
4. Finally, the HSC simulation was performed with data from the plant. Results were successfully verified with the temperature measurements.

On request of the industry partner, the solver was wrapped into a graphical user interface. More details are given in section 2.5.

To the present time, the algorithm can handle non-hydrostatic flow (e.g. the buoyant effects) only with a single layer. When the case with two layers is to be solved, only the hydrostatic option works reliably. It is to be noted that to maintain the stability of the algorithm, the time step must be chosen such that the radial component of the velocity does not lead to crossing more than one computational cell. It should be also noted, although the algorithm can handle non-hydrostatic free-surface flows, it is not capable of simulating 3D liquid splashing or breakup of the main flow into smaller droplets.



Volume 319, 15 February 2018

ISSN 0096-3003

APPLIED  
MATHEMATICS  
AND  
COMPUTATION



Contents lists available at ScienceDirect

## Applied Mathematics and Computation

journal homepage: [www.elsevier.com/locate/amc](http://www.elsevier.com/locate/amc)

## A (non-)hydrostatic free-surface numerical model for two-layer flows



Jan Bohacek<sup>a,\*</sup>, Abdellah Kharicha<sup>b</sup>, Andreas Ludwig<sup>a</sup>, Menghuai Wu<sup>b</sup>,  
Ebrahim Karimi-Sibaki<sup>b</sup>, Armin Paar<sup>c</sup>, Michael Brandner<sup>c</sup>, Leonel Elizondo<sup>c</sup>,  
Thomas Trickl<sup>c</sup>

<sup>a</sup> Department of Metallurgy, Montanuniversitaet Leoben, Franz-Joseph Strasse 18, 8700 Leoben, Austria

<sup>b</sup> Christian Doppler Lab for Advanced Simulation of Solidification and Melting, Dept. of Metallurgy, Montanuniversitaet Leoben, Franz-Joseph Strasse 18, 8700 Leoben, Austria

<sup>c</sup> Eisenwerk Sulzau-Werfen, R.&E. Weinberger AG, A-5441 Tenneck, Austria

### ARTICLE INFO

#### Article history:

Available online 18 April 2017

#### Keywords:

numerical modeling  
free-surface model  
centrifugal casting  
solidification  
advection-diffusion equation  
shallow water equations

### ABSTRACT

A semi-implicit (non-)hydrostatic free-surface numerical model for two layer flows is derived from the Navier–Stokes equations by applying kinematic boundary conditions at moving interfaces and by decomposing the pressure into the hydrostatic and the hydrodynamic part. When the latter is ignored, the algorithm conveniently transforms into a solver for a hydrostatic flow. In addition, when the vertical grid spacing is larger than the layer depths, the algorithm naturally degenerates into a solver for the shallow water equations. In this paper, the presented numerical model is developed for the horizontal centrifugal casting, a metallurgical process, in which a liquid metal is poured into a horizontally rotating cylindrical mold. The centrifugal force pushes the liquid metal toward the mold wall resulting in a formation of a sleeve with a uniform thickness. The mold gradually extracts the sensible and the latent heat from the sleeve, which eventually becomes solid. Often a second layer of another material is introduced during the solidification of the first layer. The proposed free-surface model is therefore coupled with the heat advection-diffusion equation with a stiff latent heat source term representing the solidification. The numerical results show a good agreement with measurements of temperatures performed in the plant. A validation of the proposed model is also provided with the help of using other numerical techniques such as the approximate Riemann solver for the two layer shallow water equations and the volume of fluid method.

© 2017 Elsevier Inc. All rights reserved.

### 1. Introduction

Quite a few numerical models have been derived from the Navier–Stokes (N–S) equations to study free-surface flows. The main task of these models is to account for the interface separating fluid domains and being generally in motion. A typical fluid flow problem may involve one, two or more immiscible fluids. No matter the numerical method used, calculation steps can be summarized as: (a) set the boundary conditions at the interface; (b) advance the interface in time; (c) identify the position of the interface. According to [1,2], the most common numerical methods in this field are

\* Corresponding author.

E-mail address: [bohacekjan@gmail.com](mailto:bohacekjan@gmail.com) (J. Bohacek).

<http://dx.doi.org/10.1016/j.amc.2017.03.030>

0096-3003/© 2017 Elsevier Inc. All rights reserved.

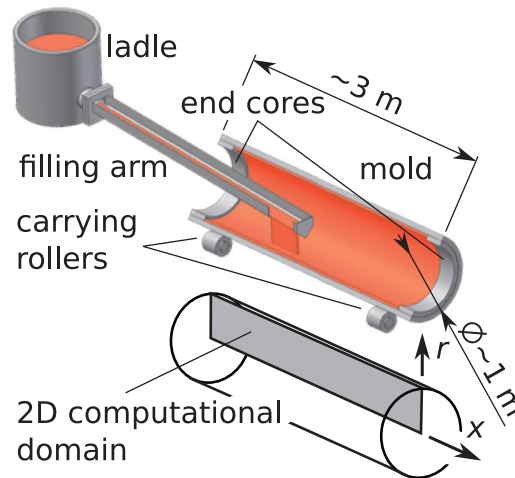


Fig. 1. A scheme of the horizontal centrifugal casting process with a computational domain and coordinates shown below it.

level-set [3,4], volume-of-fluid (VOF) [5], phase-field [6,7], particle method (marker-and-cell) [8], and the interface tracking [9]. Depending on the viewpoint of the observer—Eulerian or Lagrangian—interface capturing (VOF) and interface tracking approach can be distinguished respectively [10]. A main advantage of the earlier over the latter is that the topology of the interface is inherently treated, which allows for a description of much more complex interfaces. On the other hand, since the exact position of the interface is not exactly known, the treatment of boundary conditions, discontinuities across the interface and mass conservation still remain a challenge. For comparable grid sizes, interface tracking methods yield more accurate representation of the interface. Free-surface flows with less complicated interface topologies are generally solved by interface tracking methods, in which all grid points are treated either in a Lagrangian fashion or in an Arbitrary Lagrangian-Eulerian (ALE) approach [11], at which only the grid points close to the free-surface are being relocated. The ALE approach is advantageous when the liquid layer thickness goes to zero. In that case, the entire thickness of the layer is contained within a single cell along the vertical direction. Therefore, the 3D N-S equations collapse into the 2D shallow water equations (SWE) [12,13] due to the hydrostatic pressure assumption commonly applied within the interface cell.

In the present paper, a numerical model of horizontal centrifugal casting (HCC) process is introduced. In the HCC process [14–18], the liquid metal is poured inside a horizontal cylindrical mold rotating at high rates. Centrifugal forces push the liquid metal toward the wall of the mold with the radius  $R$ , resulting in a uniform thickness of the layer. The relatively cold mold extracts the heat from the liquid metal; therefore, solidification gradually proceeds toward the free-surface of the layer (Fig. 1). Often, when the liquid metal is partially solidified, an additional liquid of a different material is poured in. Most of the numerical studies solve the heat diffusion equation with a phase change source term. In order to account for the heat advection due to the flow, the thermal conductivity is artificially increased in the liquid region [19]. Several works in this area can be also found dedicated to the flow simulation, from which some of them rely on commercial CFD packages [20] and some on in-house codes, for example [21,22].

In the HCC, as a simple, nearly flat, free-surface and rather a weak effect of the surrounding air on dynamics of the liquid layer can be anticipated, an interface tracking approach is adopted here, inspired by Casulli [23–25] and further extended to account for two immiscible liquid layers. A robust finite difference-finite volume algorithm is derived from the non-hydrostatic N-S equations and it is suitable for structured and also unstructured grids provided the orthogonal layering of elements in the radial direction (Fig. 2). Due to the geometry configuration of the HCC, the cylindrical coordinates are used. Therefore, the axial, radial, and tangential axis notation can be seen throughout this paper. The pressure term is conveniently decomposed into the hydrostatic and the hydrodynamic part, which makes the algorithm very efficient especially when dealing with hydrostatic or nearly hydrostatic flows. The convective term and the axial viscous term are discretized explicitly using the reconstruction of the Lagrangian trajectory, especially popular in atmosphere modeling [26,27]. The resulting algorithm is mass conservative. In addition, when only a single layer of volume elements is considered, the algorithm degenerates into the shallow water equations. The proposed formulation can inherently handle drying and flooding of dry surfaces. In a subsequent step, the flow algorithm is followed by a stable finite volume scheme for the heat advection-diffusion equation with the solidification source term. Consequently, temperature differences result in thermal convection, which is in the N-S equations realized through a baroclinic pressure term.

In the next sections, the governing equations are firstly introduced, followed by detailed steps of the algorithm. Finally, results are presented in the form of numerical examples, some of them verified against temperature measurements from the plant and some against other numerical techniques.

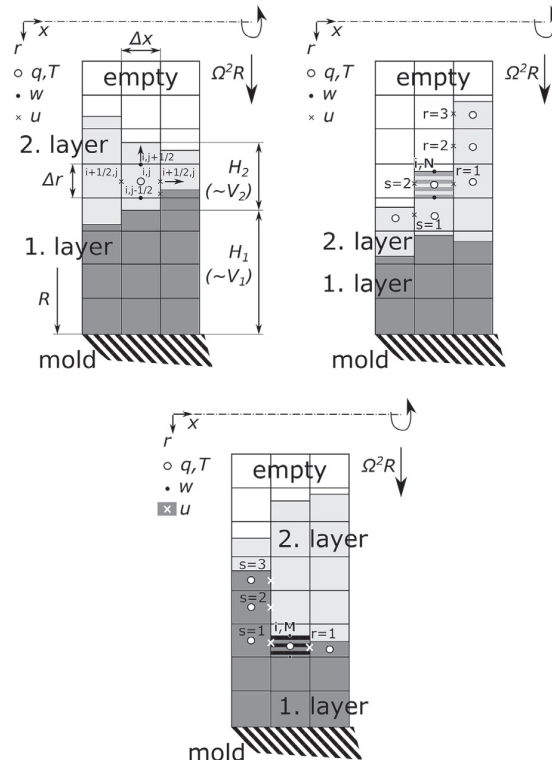


Fig. 2. Two-dimensional structured orthogonal staggered grid; (a) fluctuations of the free-surface/the interface confined within a single layer of cells in the radial direction; (b) the free-surface surpassing more than one layer of cells; (c) the interface surpassing more than one layer of cells.

## 2. Governing equations

For the sake of clarity, not losing generality, the algorithm is presented in a two-dimensional axisymmetric form, for the axial and the radial coordinate,  $x$  and  $r$ , respectively. (The size of the tangential sector is 1 rad.) Conservation of mass, momentum, and energy are governed by transport equations. Starting with the momentum equations, due to the high rotation rate  $\Omega$  they are written in the rotating frame i.e. fictitious forces must be accounted for. In the cylindrical coordinates the momentum equations can be written as:

$$\frac{\partial u}{\partial t} + u \frac{\partial u}{\partial x} + w \frac{\partial u}{\partial r} = -\frac{\partial p}{\partial x} + \nu \left[ \frac{\partial^2 u}{\partial x^2} + \frac{1}{r} \frac{\partial}{\partial r} \left( r \frac{\partial u}{\partial r} \right) \right] - \frac{\nu}{K} u \quad (1)$$

$$\frac{\partial w}{\partial t} + u \frac{\partial w}{\partial x} + w \frac{\partial w}{\partial r} = -\frac{\partial p}{\partial r} + \frac{\rho}{\rho_0} \Omega^2 r + \nu \left[ \frac{\partial^2 w}{\partial x^2} + \frac{1}{r} \frac{\partial}{\partial r} \left( r \frac{\partial w}{\partial r} \right) - \frac{w}{r^2} \right] - \frac{\nu}{K} w, \quad (2)$$

where  $u$  and  $w$  are the axial and radial components of velocity and  $p$  the normalized pressure respectively. The kinematic viscosity and the density, which may depend on temperature ( $\rho = \rho(T)$ ), are denoted by Greek symbols  $\nu$  and  $\rho$ . The permeability,  $K$ , is a part of the momentum sink due to the drag of solidifying dendrites and is defined as a function of the primary dendrite arm spacing and the liquid fraction,  $g_l$  [28,29]. Such momentum sink is only active in the solidifying region. The normalized pressure  $p$  is defined as a ratio between the pressure and a constant reference density  $\rho_0$ . The tangential component of the Coriolis acceleration is the only one different from zero. As the tangential dimension is omitted in this study, the Coriolis term does not appear in (1)-(2). Compared to the centrifugal force, expressed by the second term on the rhs of (2), the force of gravity is small and can be thus neglected. In fact, it cannot be present in (2) due to the rotating frame used and the two-dimensional ( $x, r$ ) case. The mass conservation obeys the incompressibility condition, given by:

$$\frac{\partial u}{\partial x} + \frac{1}{r} \frac{\partial (rw)}{\partial r} = 0 \quad (3)$$

In addition, the energy transport equation represented by the heat advection–diffusion equation takes the following form:

$$\rho c_p \left( \frac{\partial T}{\partial t} + u \frac{\partial T}{\partial x} + w \frac{\partial T}{\partial r} \right) = \frac{\partial}{\partial x} \left( k \frac{\partial T}{\partial x} \right) + \frac{1}{r} \frac{\partial}{\partial r} \left( r k \frac{\partial T}{\partial r} \right) - \rho L_f \frac{\partial g_i}{\partial t} \quad (4)$$

where  $c_p$ ,  $k$ , and  $L_f$  are the specific heat, the thermal conductivity, and the latent heat respectively. In order to describe deformations of the free-surface and the interface between the outer and the inner layer (in the following text referred to as the interface) combining kinematic boundary conditions and the continuity Eq. (3) integrated over the depth of each layer gives a set of free-surface equations, written as:

$$\frac{\partial V_1}{\partial t} + \sum_R^{R-H_1} u r dr = 0 \quad (5)$$

$$\frac{\partial V_2}{\partial t} + \sum_{R-H_1}^{R-H_1-H_2} u r dr = 0, \quad (6)$$

where  $H$  and  $V$  are the local depth of the layer and its corresponding volume calculated for the element size  $dx$ . The indices  $[\dots]_{1,2}$  signify the outer and the inner layer respectively.

In (1)–(2), the pressure  $p$  is decomposed into the sum of the hydrostatic and the hydrodynamic part  $q$ . Unlike the hydrostatic pressure induced by the gravitational acceleration, its centrifugal counterpart is a nonlinear function of radial position  $r$ . If the depths  $H_{1,2}$  are  $\ll R$ , it is advisable to replace the centrifugal term  $\Omega^2 r$  with  $\Omega^2 R$ , where  $R$  is the radius of the cylindrical wall (Fig. 2). This strategy is also convenient in order to avoid lengthy formulas and thus maintain readability of the present text. Then, the pressure  $p_{1,2}$  scaled by the reference density of each layer  $\rho_{01,02}$  takes the following form:

$$p_1 = \Omega^2 R \left( r - R + H_1 + \frac{\rho_{02}}{\rho_{01}} H_2 \right) + \Omega^2 R \sum_{R-H_1}^{R-H_1-H_2} \frac{\rho_{01} - \rho_1}{\rho_{01}} dr + \Omega^2 R \sum_r^{R-H_1} \frac{\rho_{01} - \rho_1}{\rho_{01}} dr + q \quad (7)$$

$$p_2 = \Omega^2 R (r - R + H_1 + H_2) + \Omega^2 R \sum_r^{R-H_1-H_2} \frac{\rho_{02} - \rho_2}{\rho_{02}} dr + q. \quad (8)$$

Due to the variable density  $\rho(T)$ , it is common to further split the hydrostatic pressure into the barotropic component, represented by the first terms of (7)–(8), and the baroclinic component, represented by the terms with integrals. The atmospheric pressure is set to zero, thus not appearing in (7)–(8). Eqs. (7)–(8) are substituted into (1)–(2) for each layer separately. Note that the gradient of the hydrostatic pressure cancels out with the centrifugal term  $\rho/\rho_0 \Omega^2 R$  in (2); therefore, only the hydrodynamic part  $q$  remains.

### 3. Numerical algorithm

The spatial discretization of the physical domain is realized by dividing it into  $N_x N_r$  orthogonal structured cells with an axial and radial size,  $\Delta x$  and  $\Delta r$ . Unlike  $\Delta x$  being fixed, the radial size  $\Delta r$  is only constant in the bulk, equal to the difference between the outer and the inner level surface (Fig. 2). At the free-surface and the interface it is calculated as a difference between the outer level surface and the free-surface or the interface respectively. Cell centers are consecutively numbered with indices  $i, j$ . The field variables are stored in a staggered manner. While the velocities are defined at the cell faces using half indices, other scalar fields such as the hydrodynamic pressure  $q$ , the temperature  $T$ , and the liquid fraction  $g_i$  are located at the cell centers. Finally, the depth and the volume of each layer are indexed along the axial coordinate as  $H_i$  and  $V_i$  respectively.

Here, a semi-implicit Eulerian–Lagrangian fractional step scheme is adopted in order to arrive at stable and efficient numerical algorithm. The pressure is discretized by the  $\theta$ -method [30]. In a predictor step, the preliminary velocity field and positions of the free-surface and the interface are calculated by neglecting the implicit contribution of the hydrodynamic pressure  $q$ . Secondly, the Poisson's equation is solved for the pressure  $q$  in a corrector step, which is finally used to correct the preliminary quantities obtained in the predictor step. The resulting velocity field is mass conservative.

#### 3.1. Predictor step

By discretizing (1) e.g. for the inner layer (2) using a semi-implicit finite-difference scheme, the axial velocity component  $u$  at radial faces  $i + 1/2, j$  yields the following form:

$$\begin{aligned} \tilde{u}_{i+1/2,j}^{n+1} = & F u_{i+1/2,j}^n - \theta \frac{\Delta t}{\Delta x} \left( \Omega^2 R (H_{1,i+1}^{n+1} - H_{1,i}^{n+1} + H_{2,i}^{n+1} - H_{2,i}^{n+1}) \right) - \Delta t \frac{v}{K} \tilde{u}_{i+1/2,j}^{n+1} \\ & + v \frac{\Delta t}{\Delta r_{i+1/2,j}^n} \frac{1}{r_{i+1/2,j}^n} \left( r_{i+1/2,j+1/2}^n \frac{\tilde{u}_{i+1/2,j+1}^{n+1} - \tilde{u}_{i+1/2,j}^{n+1}}{\Delta r_{i+1/2,j+1/2}^n} - r_{i+1/2,j-1/2}^n \frac{\tilde{u}_{i+1/2,j}^{n+1} - \tilde{u}_{i+1/2,j-1}^{n+1}}{\Delta r_{i+1/2,j-1/2}^n} \right) \end{aligned} \quad (9)$$

Discretization of (1) for the outer layer (1) is an analogy. The tilde symbol denotes a preliminary unknown calculated in the predictor step going to be later updated in the corrector step. The current and the old time step are denoted by  $n + 1$  and  $n$  superscripts. The implicit factor  $\theta$  is used to split both, the barotropic and the hydrodynamic pressure, into an implicit and an explicit contribution scaled by  $\theta$  and  $(1 - \theta)$  respectively. The implicit factor  $\theta$  has to be chosen in the range  $1/2 \leq \theta \leq 1$ . In the predictor step, only the barotropic part of the pressure  $p_2$  (8) is treated implicitly multiplied by the implicit factor  $\theta$  and appears as a second term on the rhs of (9). The implicit hydrodynamic part  $q$  of the pressure  $p_2$  is considered separately in the corrector step. The explicit part of the barotropic and the hydrodynamic pressure multiplied by  $(1 - \theta)$  is hidden in the term  $Fu_{i+1/2,j}^n$ , see the third term on the rhs of (11). The baroclinic pressure, the term with an integral in (8), is handled fully explicitly and is also hidden in the term  $Fu_{i+1/2,j}^n$ , see the last term on the rhs of (11). In addition, since the layer depths are significantly smaller than the axial scale, axial viscosity terms are treated explicitly and also enter the term  $Fu_{i+1/2,j}^n$ . Finally, the lhs of (1) is discretized by reconstructing the Lagrangian trajectory. The total derivative of the axial velocity component  $u$  can be written as the following:

$$\frac{du}{dt} = \frac{\tilde{u}_{i+1/2,j}^{n+1} - u_{i+1/2,j}^*}{\Delta t}, \tag{10}$$

where  $u_{i+1/2,j}^*$  is the interpolated axial velocity component recorded at time  $t_n$  at the end of the Lagrangian trajectory and again goes inside the term  $Fu_{i+1/2,j}^n$  and can be expressed as

$$\begin{aligned} Fu_{i+1/2,j}^n &= u_{i+1/2,j}^* + \Delta t v \frac{u_{i+3/2,j}^* - 2u_{i+1/2,j}^* + u_{i-1/2,j}^*}{\Delta x^2} \\ &\quad - (1 - \theta)\Omega^2 R \frac{\Delta t}{\Delta x} (\Omega^2 R (H_{1,i+1}^n - H_{1,i}^n + H_{2,i}^n - H_{2,i}^n) + q_{i+1,j}^n - q_{i,j}^n) \\ &\quad - \Omega^2 R \frac{\Delta t}{\Delta x} \left( \sum_{r_{i+1,j}^n}^{R-H_{1,i+1}^n-H_{2,i+1}^n} \frac{\rho_{02} - \rho_{2,i+1,j}^n}{\rho_{02}} dr - \sum_{r_{i,j}^n}^{R-H_{1,i}^n-H_{2,i}^n} \frac{\rho_{02} - \rho_{2,i,j}^n}{\rho_{02}} dr \right) \end{aligned} \tag{11}$$

Similarly to (1), (2) can be discretized as

$$\begin{aligned} \tilde{w}_{i,j+1/2}^{n+1} &= Fw_{i,j+1/2}^n - \Delta t \frac{v}{K} \tilde{w}_{i,j+1/2}^{n+1} \\ &\quad + v \frac{\Delta t}{\Delta r_{i,j+1/2}^n} \frac{1}{r_{i,j+1/2}^n} \left( r_{i,j+1}^n \frac{\tilde{w}_{i,j+3/2}^{n+1} - \tilde{w}_{i,j+1/2}^{n+1}}{\Delta r_{i,j+1}^n} - r_{i,j}^n \frac{\tilde{w}_{i,j+1/2}^{n+1} - \tilde{w}_{i,j-1/2}^{n+1}}{\Delta r_{i,j}^n} \right) - v \Delta t \frac{\tilde{w}_{i,j+1/2}^{n+1}}{r_{i,j+1/2}^{2,n}} \end{aligned} \tag{12}$$

where  $Fw_{i,j+1/2}^n$  is again the finite difference operator similar to that in (9). It comprises axial viscous terms, the interpolated radial velocity component  $w_{i,j+1/2}^*$  and the explicit contribution of the hydrodynamic pressure  $q$ . In the predictor step, since the implicit contribution of the hydrodynamic pressure is neglected, the momentum equations (9) and (12) are independent of each other and can be therefore solved separately. Eq. (12) forms a symmetric tridiagonal system, which can be easily solved by preconditioned conjugate gradient method [31]. Unlike (12), Eq. (9) cannot be readily solved, as it is coupled to the unknown layer depths  $\tilde{H}_{1,2,i}^{n+1}$ . In order to determine  $\tilde{H}_{1,2,i}^{n+1}$ , the preliminary field of the axial velocity component  $\tilde{u}_{i+1/2,j}^{n+1}$  must satisfy discrete versions of free-surface equations (5)-(6) for each layer.

$$\begin{aligned} \tilde{V}_{1,i}^{n+1} &= V_{1,i}^n - \theta \Delta t \left( \sum_{j=1}^M r_{i+1/2,j}^n \Delta r_{i+1/2,j}^n \tilde{u}_{i+1/2,j}^{n+1} - \sum_{j=1}^M r_{i-1/2,j}^n \Delta r_{i-1/2,j}^n \tilde{u}_{i-1/2,j}^{n+1} \right) \\ &\quad - (1 - \theta) \Delta t \left( \sum_{j=1}^M r_{i+1/2,j}^n \Delta r_{i+1/2,j}^n u_{i+1/2,j}^n - \sum_{j=1}^M r_{i-1/2,j}^n \Delta r_{i-1/2,j}^n u_{i-1/2,j}^n \right) \end{aligned} \tag{13}$$

$$\begin{aligned} \tilde{V}_{2,i}^{n+1} &= V_{2,i}^n - \theta \Delta t \left( \sum_{j=M+1}^N r_{i+1/2,j}^n \Delta r_{i+1/2,j}^n \tilde{u}_{i+1/2,j}^{n+1} - \sum_{j=M+1}^N r_{i-1/2,j}^n \Delta r_{i-1/2,j}^n \tilde{u}_{i-1/2,j}^{n+1} \right) \\ &\quad - (1 - \theta) \Delta t \left( \sum_{j=M+1}^N r_{i+1/2,j}^n \Delta r_{i+1/2,j}^n u_{i+1/2,j}^n - \sum_{j=M+1}^N r_{i-1/2,j}^n \Delta r_{i-1/2,j}^n u_{i-1/2,j}^n \right) \end{aligned} \tag{14}$$

where  $M$  and  $N$ ,  $1 \leq M \leq N \leq N_r$ , may vary both in time and space and denote the radial index  $j$  of the interface cell and the free-surface respectively. After multiplying the momentum equation (9) by  $\Delta r_{i+1/2,j}^n$  and substituting for the pressure  $p$  from (7)-(8) for the outer (1) and the inner layer (2) respectively, we will arrive at the set of linear equations, which written in matrix notation take the following form

$$\mathbf{A}_{i+1/2}^n \tilde{\mathbf{U}}_{i+1/2}^{n+1} = \mathbf{G}_{i+1/2}^n - \Omega^2 R \frac{\Delta t}{\Delta x} (\tilde{H}_{1,i+1}^{n+1} - \tilde{H}_{1,i}^{n+1}) \Delta \mathbf{R}_{i+1/2}^n - \Omega^2 R \frac{\Delta t}{\Delta x} (\tilde{H}_{2,i+1}^{n+1} - \tilde{H}_{2,i}^{n+1}) \Theta_{i+1/2}^n * \Delta \mathbf{R}_{i+1/2}^n \tag{15}$$

where  $\tilde{\mathbf{U}}_{i+1/2}^{n+1}$ ,  $\mathbf{G}_{i+1/2}^n$ ,  $\Delta\mathbf{R}_{i+1/2}^n$ ,  $\Theta_{i+1/2}^n$  are column vectors and  $\mathbf{A}_{i+1/2}^n$  is a tridiagonal coefficient matrix. Explicit terms are contained in  $\mathbf{G}_{i+1/2}^n$ . Implicit terms are reflected in  $\mathbf{A}_{i+1/2}^n$ . In each layer, barotropic parts of the hydrostatic pressure (7)-(8), namely the terms with  $\tilde{H}_2$ , differ only by the scale of density ratio  $\rho_{02}/\rho_{01}$ , which is included in the column vector  $\Theta_{i+1/2}^n$ . The operator [\*] signifies a piecewise-element multiplication. Omitting the subscripts and the superscripts, the vectors  $\tilde{\mathbf{U}}, \Delta\mathbf{R}, \Theta$  are defined as the following:

$$\tilde{\mathbf{U}} = \begin{bmatrix} \tilde{u}_1 \\ \vdots \\ \tilde{u}_M \\ \tilde{u}_{M+1} \\ \vdots \\ \tilde{u}_N \end{bmatrix}, \quad \Delta\mathbf{R} = \Delta\mathbf{R}_1 + \Delta\mathbf{R}_2 = \begin{bmatrix} \Delta r_1 \\ \vdots \\ \Delta r_M \\ 0 \\ \vdots \\ 0 \end{bmatrix} + \begin{bmatrix} 0 \\ \vdots \\ 0 \\ \Delta r_{M+1} \\ \vdots \\ \Delta r_N \end{bmatrix},$$

$$\Theta = \begin{bmatrix} \rho_{02}/\rho_{01} \\ \vdots \\ \rho_{02}/\rho_{01} \\ 1 \\ \vdots \\ 1 \end{bmatrix}. \quad (16)$$

Although it is straightforward to construct the coefficient matrix of implicit terms  $\mathbf{A}$  and the vector of explicit terms  $\mathbf{G}$  using (9), they are too long to be shown here. The coefficient  $\mathbf{A}$  matrix is a tridiagonal positive definite matrix. Note that the size of vectors  $\tilde{\mathbf{U}}, \mathbf{G}, \Delta\mathbf{R}, \Theta$  and the matrix  $\mathbf{A}$  may vary or even disappear depending on actual layer depths  $H_{1,2}$ .

Similarly to (9), (13) and (14) can also be written using vector notation as

$$\tilde{V}_{1,i}^{n+1} = V_{1,i}^n - \theta \Delta t \left( (\mathbf{R}_{i+1/2}^n * \Delta\mathbf{R}_{1,i+1/2}^n)^T \tilde{\mathbf{U}}_{i+1/2}^{n+1} - (\mathbf{R}_{i-1/2}^n * \Delta\mathbf{R}_{1,i-1/2}^n)^T \tilde{\mathbf{U}}_{i-1/2}^{n+1} \right) - (1-\theta) \Delta t \left( (\mathbf{R}_{i+1/2}^n * \Delta\mathbf{R}_{1,i+1/2}^n)^T \mathbf{U}_{i+1/2}^n - (\mathbf{R}_{i-1/2}^n * \Delta\mathbf{R}_{1,i-1/2}^n)^T \mathbf{U}_{i-1/2}^n \right) \quad (17)$$

$$\tilde{V}_{2,i}^{n+1} = V_{2,i}^n - \theta \Delta t \left( (\mathbf{R}_{i+1/2}^n * \Delta\mathbf{R}_{2,i+1/2}^n)^T \tilde{\mathbf{U}}_{i+1/2}^{n+1} - (\mathbf{R}_{i-1/2}^n * \Delta\mathbf{R}_{2,i-1/2}^n)^T \tilde{\mathbf{U}}_{i-1/2}^{n+1} \right) - (1-\theta) \Delta t \left( (\mathbf{R}_{i+1/2}^n * \Delta\mathbf{R}_{2,i+1/2}^n)^T \mathbf{U}_{i+1/2}^n - (\mathbf{R}_{i-1/2}^n * \Delta\mathbf{R}_{2,i-1/2}^n)^T \mathbf{U}_{i-1/2}^n \right) \quad (18)$$

Formal substitution for  $\tilde{\mathbf{U}}_{i+1/2}^{n+1}$  from (15) into (17) and (18) yields

$$\tilde{V}_{1,i}^{n+1} = V_{1,i}^n - \theta \Omega^2 R \frac{\Delta t^2}{\Delta X} \left( [(\mathbf{R} * \Delta\mathbf{R}_1)^T \mathbf{A}^{-1} \Delta\mathbf{R}]_{i+1/2}^n (\tilde{H}_{1,i+1}^{n+1} - \tilde{H}_{1,i}^{n+1}) - [(\mathbf{R} * \Delta\mathbf{R}_1)^T \mathbf{A}^{-1} \Delta\mathbf{R}]_{i-1/2}^n (\tilde{H}_{1,i}^{n+1} - \tilde{H}_{1,i-1}^{n+1}) \right) - \theta \Omega^2 R \frac{\Delta t^2}{\Delta X} \left( [(\mathbf{R} * \Delta\mathbf{R}_1)^T \mathbf{A}^{-1} (\Theta * \Delta\mathbf{R})]_{i+1/2}^n (\tilde{H}_{2,i+1}^{n+1} - \tilde{H}_{2,i}^{n+1}) - [(\mathbf{R} * \Delta\mathbf{R}_1)^T \mathbf{A}^{-1} (\Theta * \Delta\mathbf{R})]_{i-1/2}^n (\tilde{H}_{2,i}^{n+1} - \tilde{H}_{2,i-1}^{n+1}) \right) - \theta \Delta t \left( [(\mathbf{R} * \Delta\mathbf{R}_1)^T \mathbf{A}^{-1} \mathbf{G}]_{i+1/2}^n - [(\mathbf{R} * \Delta\mathbf{R}_1)^T \mathbf{A}^{-1} \mathbf{G}]_{i-1/2}^n \right) - (1-\theta) \Delta t \left( [(\mathbf{R} * \Delta\mathbf{R}_1)^T \mathbf{U}]_{i+1/2}^n - [(\mathbf{R} * \Delta\mathbf{R}_1)^T \mathbf{U}]_{i-1/2}^n \right) \quad (19)$$

$$\tilde{V}_{2,i}^{n+1} = V_{2,i}^n - \theta \Omega^2 R \frac{\Delta t^2}{\Delta X} \left( [(\mathbf{R} * \Delta\mathbf{R}_2)^T \mathbf{A}^{-1} \Delta\mathbf{R}]_{i+1/2}^n (\tilde{H}_{1,i+1}^{n+1} - \tilde{H}_{1,i}^{n+1}) - [(\mathbf{R} * \Delta\mathbf{R}_2)^T \mathbf{A}^{-1} \Delta\mathbf{R}]_{i-1/2}^n (\tilde{H}_{1,i}^{n+1} - \tilde{H}_{1,i-1}^{n+1}) \right) - \theta \Omega^2 R \frac{\Delta t^2}{\Delta X} \left( [(\mathbf{R} * \Delta\mathbf{R}_2)^T \mathbf{A}^{-1} (\Theta * \Delta\mathbf{R})]_{i+1/2}^n (\tilde{H}_{2,i+1}^{n+1} - \tilde{H}_{2,i}^{n+1}) - [(\mathbf{R} * \Delta\mathbf{R}_2)^T \mathbf{A}^{-1} (\Theta * \Delta\mathbf{R})]_{i-1/2}^n (\tilde{H}_{2,i}^{n+1} - \tilde{H}_{2,i-1}^{n+1}) \right) - \theta \Delta t \left( [(\mathbf{R} * \Delta\mathbf{R}_2)^T \mathbf{A}^{-1} \mathbf{G}]_{i+1/2}^n - [(\mathbf{R} * \Delta\mathbf{R}_2)^T \mathbf{A}^{-1} \mathbf{G}]_{i-1/2}^n \right) - (1-\theta) \Delta t \left( [(\mathbf{R} * \Delta\mathbf{R}_2)^T \mathbf{U}]_{i+1/2}^n - [(\mathbf{R} * \Delta\mathbf{R}_2)^T \mathbf{U}]_{i-1/2}^n \right) \quad (20)$$

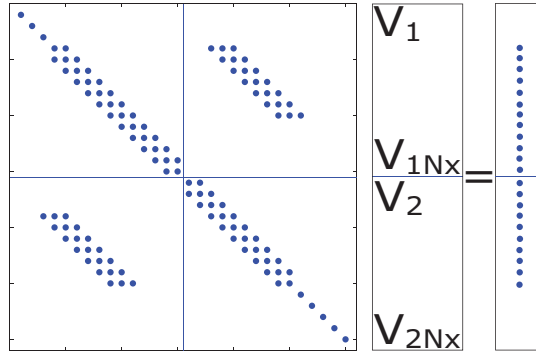


Fig. 3. A visualization of the system of coupled equations (19)-(20) for  $\tilde{V}_{1,j}^{n+1}$  and  $\tilde{V}_{1,j}^{n+1}$  with an illustrative demonstration of vanishing depth of each layer.

In order to allow us to solve (19) and (20) for  $V_{1,2}$ , the layer depths  $H_{1,2}$  has to be firstly replaced by axisymmetric relations linking  $H_{1,2}$  with  $V_{1,2}$ , which read

$$H_1 = R - \sqrt{R^2 - \frac{2V_1}{\Delta x}}, H_2 = R - H_1 - \sqrt{(R - H_1)^2 - \frac{2V_2}{\Delta x}} \tag{21}$$

As the formulas given by (21) are nonlinear, a linearization technique is applied and (21) become

$$H_1^{n+1} = H_1^n + H_1^n (V_1^{n+1} - V_1^n), \quad H_2^{n+1} = H_2^n + H_2^n (V_2^{n+1} - V_2^n), \tag{22}$$

where  $H_1^n$  and  $H_2^n$  are  $H_1^n = \frac{1}{\Delta x \sqrt{R^2 - \frac{2V_1^n}{\Delta x}}}$  and  $H_2^n = \frac{1}{\Delta x \sqrt{(R - H_1^n)^2 - \frac{2V_2^n}{\Delta x}}}$  respectively.

In (19) and (20), we substitute for  $\tilde{H}_{1,2}^{n+1}$  from (22) and rearrange implicit and explicit terms. Due to the properties of the matrix  $\mathbf{A}$ , the terms  $(\mathbf{R}^* \Delta \mathbf{R}_1)^T \mathbf{A}^{-1} (\Theta^* \Delta \mathbf{R})$ ,  $(\mathbf{R}^* \Delta \mathbf{R}_1)^T \mathbf{A}^{-1} \Delta \mathbf{R}$ ,  $(\mathbf{R}^* \Delta \mathbf{R}_2)^T \mathbf{A}^{-1} (\Theta^* \Delta \mathbf{R})$ , and  $(\mathbf{R}^* \Delta \mathbf{R}_2)^T \mathbf{A}^{-1} \Delta \mathbf{R}$  are non-negative. Therefore, (19) and (20) constitute a nine-diagonal system of linear equations for  $\tilde{V}_{1,2}^{n+1}$ , which is schematically drawn for a general configuration with dry regions in Fig. 3. The system is strictly diagonally dominant, generally non-symmetric due to the coupling bands and can be solved by biconjugate gradient (stabilized) method [32].

Before solving (15) for axial velocities  $\tilde{\mathbf{U}}_{i+1/2}^{n+1}$ , it is recommended to replace  $\tilde{H}_{1,2}^{n+1}$  with  $\tilde{V}_{1,2}^{n+1}$  using (22) in order to maintain mass conservation. After having determined preliminary fields  $\tilde{u}$ ,  $\tilde{w}$ , and  $\tilde{V}_{1,2}$ , the predictor step is finished and we may proceed to the corrector step.

### 3.2. Corrector step

After the predictor step, it is necessary to calculate hydrodynamic pressure  $q$  in a way that the continuity equation (3) is fulfilled. New fields  $u$ ,  $w$ , and  $V_{1,2}$  are found by correcting the preliminary fields  $\tilde{u}$ ,  $\tilde{w}$ , and  $\tilde{V}_{1,2}$  using the continuity equation given by (3) and the following fractional step equations

$$u_{i+1/2,j}^{n+1} = \tilde{u}_{i+1/2,j}^{n+1} - \theta \frac{\Delta t}{\Delta x} (q_{i+1,j}^{n+1} - q_{i,j}^{n+1}) \tag{23}$$

$$w_{i,j+1/2}^{n+1} = \tilde{w}_{i,j+1/2}^{n+1} - \theta \frac{\Delta t}{\Delta x} (q_{i,j+1}^{n+1} - q_{i,j}^{n+1}) \tag{24}$$

In each bulk cell i.e. a cell other than that at the free-surface, the discretized form of the continuity equation can be expressed by

$$u_{i+1/2,j}^{n+1} r_{i+1/2,j}^n \Delta r_{i+1/2,j}^n - u_{i-1/2,j}^{n+1} r_{i-1/2,j}^n \Delta r_{i-1/2,j}^n + w_{i,j+1/2}^{n+1} r_{i,j+1/2}^n \Delta x - w_{i,j-1/2}^{n+1} r_{i,j-1/2}^n \Delta x = 0 \tag{25}$$

At the free-surface, the incompressibility condition can be written as

$$(V_1 + V_2)_i^{n+1} = (V_1 + V_2)_i^n + \theta \Delta t w_{i,N-1/2}^{n+1} r_{i,N-1/2}^n \Delta x - \theta \Delta t (u_{i+1/2,N}^{n+1} r_{i+1/2,N}^n \Delta r_{i+1/2,N}^n - u_{i-1/2,N}^{n+1} r_{i-1/2,N}^n \Delta r_{i-1/2,N}^n) \tag{26}$$

Assuming the pressure  $p$  being hydrostatic in the free-surface cells, the following condition applies

$$\Omega^2 R (r - R + H_1 + H_2) = \Omega^2 R (r - R + \tilde{H}_1 + \tilde{H}_2) + q \tag{27}$$

In order to be applied in (26), the hydrostatic condition (27) needs to be however reformulated in terms of replacing  $H$  with  $V$  at timestep  $n + 1$ . Using geometrical relations, (27) can be transformed into

$$V_1 + V_2 = \tilde{V}_1 + \tilde{V}_2 + \Delta x \left( R - \tilde{H}_1 - \tilde{H}_2 - \frac{q}{2\Omega^2 R} \right) \frac{q}{\Omega^2 R} \quad (28)$$

Similarly to (21), (28) is also non-linear and thus, a linearization is again applied to it. Then,  $(V_1 + V_2)_i^{n+1}$  in (26) can be substituted with the linearized form of (28). Substituting (23)–(24) into (25) and (26), keeping terms with  $q$  on the lhs, and moving all other to the rhs, yields the system of Poisson's equations approximated by finite differences. The properties of the system are dependent on the geometric configuration of the free-surface and the interface. When fluctuations of both, the free-surface and the interface, stay within two distinct radial layers or within a single radial layer of cells, the system of Poisson's equations is diagonally dominant and symmetric. On the contrary, when the fluctuations of either of them become larger and spread over more than one radial layer of cells, the system is still diagonally dominant, no longer symmetric though. Both scenarios are depicted in Fig. 2. Concerning the scenario shown in Fig. 2b, the incompressibility condition for the highlighted free-surface cell takes slightly different form than (26), given by

$$(V_1 + V_2)_i^{n+1} = (V_1 + V_2)_i^n + \theta \Delta t w_{i,N-1/2}^{n+1} r_{i,N-1/2}^n \Delta x - \theta \Delta t \left( \sum_r u_{i+1/2,r}^{n+1} r_{i+1/2,r}^n \Delta r_{i+1/2,r}^n - \sum_s u_{i-1/2,s}^{n+1} r_{i-1/2,s}^n \Delta r_{i-1/2,s}^n \right), \quad (29)$$

where indices  $r, s$  are schematically explained in Fig. 2b. In Fig. 2b, the shaded cells are also considered as free-surface cells and therefore; the pressure  $p$  inside them is hydrostatic. This implies that the hydrodynamic pressure  $q$  is shared among all such free-surface cells at a given axial position  $i + 1$ . This approach greatly simplifies assembling of the system of Poisson's equations as well as improves the convergence rate of finding the solution. A similar situation can be encountered at the interface, when its fluctuations surpass a single radial layer of cells (Fig. 2c). The incompressibility condition, given by (25), has to be modified and takes the following form

$$\sum_r u_{i+1/2,r}^{n+1} r_{i+1/2,r}^n \Delta r_{i+1/2,r}^n - \sum_s u_{i-1/2,s}^{n+1} r_{i-1/2,s}^n \Delta r_{i-1/2,s}^n + w_{i,M+1/2}^{n+1} r_{i,M+1/2}^n \Delta x - w_{i,M-1/2}^{n+1} r_{i,M-1/2}^n \Delta x = 0, \quad (30)$$

where  $r, s$  are again schematically explained in Fig. 2c. In addition, a similar assumption is applied to the hydrodynamic pressure  $q$  at pseudo-interface cells at a given axial position  $i + 1$  such that it is constant.

Once the field of the hydrodynamic pressure  $q$  is determined, axial velocities  $u$  can be corrected using (23). In order to ensure divergence free velocity field, radial velocities  $w$  should be determined using the incompressibility condition rather than (24). By setting  $w_{i,1/2}^{n+1}$  to zero, such condition can be written in the following form

$$w_{i,j+1/2}^{n+1} = \frac{1}{r_{i,j+1/2}^n \Delta x} \left( w_{i,j-1/2}^{n+1} r_{i,j-1/2}^n \Delta x - u_{i+1/2,j}^{n+1} r_{i+1/2,j}^n \Delta r_{i+1/2,j}^n + u_{i-1/2,j}^{n+1} r_{i-1/2,j}^n \Delta r_{i-1/2,j}^n \right) \quad (31)$$

Note that in free-surface cells and interface cells, the incompressibility condition may differ from (31). Finally,  $V_{1,2}$  are recomputed using the following formulas

$$V_1^{n+1} = V_1^n - \Delta t \left( \sum_{j=1}^M r_{i+1/2,j}^n \Delta r_{i+1/2,j}^n u_{i+1/2,j}^{n+1} - \sum_{j=1}^M r_{i-1/2,j}^n \Delta r_{i-1/2,j}^n u_{i-1/2,j}^{n+1} \right) \quad (32)$$

$$V_2^{n+1} = V_2^n - \Delta t \left( \sum_{j=M+1}^N r_{i+1/2,j}^n \Delta r_{i+1/2,j}^n u_{i+1/2,j}^{n+1} - \sum_{j=M+1}^N r_{i-1/2,j}^n \Delta r_{i-1/2,j}^n u_{i-1/2,j}^{n+1} \right) \quad (33)$$

and the radial elements  $\Delta r$  are updated using the new values of  $V_{1,2}$  from (32)–(33).

The heat advection–diffusion equation (4) is discretized in a finite volume framework as the following

$$\begin{aligned} & \rho_{i,j} c_{pi,j} \left( \Delta x r_{i,j}^{n+1} \Delta r_{i,j}^{n+1} T_{i,j}^{n+1,m+1} + \Delta t \left[ \left( \rho_{i,j+1/2} c_{pi,j+1/2} \Delta x r_{i,j+1/2}^n w_{i,j+1/2}^{n+1} T_{i,j+1/2}^{n+1,m+1} - \rho_{i,j-1/2} c_{pi,j-1/2} \Delta x r_{i,j-1/2}^n w_{i,j-1/2}^{n+1} T_{i,j-1/2}^{n+1,m+1} \right) \right. \right. \\ & \quad + \left( \rho_{i+1/2,j} c_{pi,i+1/2,j} r_{i+1/2,j}^n \Delta r_{i+1/2,j}^n u_{i+1/2,j}^{n+1} T_{i+1/2,j}^{n+1,m+1} - \rho_{i-1/2,j} c_{pi,i-1/2,j} r_{i-1/2,j}^n \Delta r_{i-1/2,j}^n u_{i-1/2,j}^{n+1} T_{i-1/2,j}^{n+1,m+1} \right) \\ & \quad - \left( k_{i,j+1/2} \Delta x r_{i,j+1/2}^{n+1} \frac{T_{i,j+1}^{n+1,m+1} - T_{i,j}^{n+1,m+1}}{\Delta r_{i,j+1/2}^{n+1}} - k_{i,j-1/2} \Delta x r_{i,j-1/2}^{n+1} \frac{T_{i,j}^{n+1,m+1} - T_{i,j-1}^{n+1,m+1}}{\Delta r_{i,j-1/2}^{n+1}} \right) \\ & \quad \left. - \left( k_{i+1/2,j} r_{i+1/2,j}^{n+1} \Delta r_{i+1/2,j}^{n+1} \frac{T_{i+1,j}^{n+1,m+1} - T_{i,j}^{n+1,m+1}}{\Delta x} - k_{i-1/2,j} r_{i-1/2,j}^{n+1} \Delta r_{i-1/2,j}^{n+1} \frac{T_{i,j}^{n+1,m+1} - T_{i-1,j}^{n+1,m+1}}{\Delta x} \right) \right] \\ & = \rho_{i,j} c_{pi,j} \left( \Delta x r_{i,j}^n \Delta r_{i,j}^n T_{i,j}^n + S_{i,j}^{m+1} \right) \end{aligned} \quad (34)$$

Both the thermal diffusion and the advection term are treated implicitly. At the cell faces, physical properties are determined using the upwind method, which naturally ensures the boundedness for the temperature field. The term,  $S_{i,j}^{m+1}$ , represents the latent heat source term due to solidification and, as explained later, a special scheme is required for  $S_{i,j}^{m+1}$ . Briefly, when the phase change takes place within a narrow range of temperatures denoted as the liquidus temperature and the solidus temperature, the source term is stiff and the algorithm should be able to prevent numerical oscillations of the solution, namely permanent switching between the liquid and the solid during two subsequent iterations. In order to achieve convergence between the temperature  $T$  and the liquid fraction  $g_l$ , (34) must be solved iteratively for a number of iterations, each denoted by the letter  $m$ . An appropriate discretization of  $S_{i,j}^{m+1}$  may be of the following form [33]

$$S_{i,j}^{m+1} = -\rho_{i,j}L_f(\Delta x r_{i,j}^{n+1} \Delta r_{i,j}^{n+1}) \frac{dF}{dT} T_{i,j}^{n+1,m+1} + \rho_{i,j}L_f(\Delta x r_{i,j}^{n+1} \Delta r_{i,j}^{n+1}) \left[ g_{l,i,j}^n - g_{l,i,j}^m + \frac{dF}{dT} F^{-1} \right], \tag{35}$$

where  $\frac{dF}{dT}$  and  $F^{-1}$  are respectively the slope of the temperature dependent liquid fraction curve and the inverse of the liquid fraction  $g_l$ , both evaluated at  $g_{l,i,j}^m$  from previous iteration. After solving (34) with  $S_{i,j}^{m+1}$  given by (35), it is necessary to update the liquid fraction  $g_{l,i,j}^{m+1}$  using the following formula

$$g_{i,j}^{m+1} = g_{i,j}^m + \frac{dF}{dT} (T_{i,j}^{n+1,m+1} - F^{-1}) \tag{36}$$

When the convergence is reached,  $g_{i,j}^{n+1}$  is set equal to  $g_{i,j}^{m+1}$  and we may proceed to the next time step.

Until here, the boundary conditions were not discussed except for those related to movement of the free-surface and the interface, known as the kinematic boundary conditions. Imposing other flow-related boundary conditions is quite straightforward. Along the normal direction to fixed walls, a zero flux is applied for both the velocity component and the hydrodynamic pressure. In addition, the tangential component of velocity is set zero there. Although not used in this study, discretization of the radial viscous term in the momentum equation for the axial component of velocity may be for example realized through the Manning–Chezy formula [34]. Similar formulas may be applied at the free-surface to mimic a stress resulting from a relative motion between the liquid layer and the surrounding gas. It is also possible to design an empirical formula for the viscous stress at the interface between the layers. In the present study namely in the numerical examples, viscous stresses are directly determined using the physical viscosity and dimensions of the finite-difference grid. At the free-surface, a zero stress is considered. In addition, the boundary conditions are also required for the heat-advection diffusion equation given by (4). Here, at the free-surface a Robin-type boundary condition is imposed to account for a convective heat transfer. At the walls, either a Neumann-type boundary condition or a coupled boundary condition is considered.

Concerning the properties of the method, it should be pointed out that by skipping the corrector step and setting the initial value of the hydrodynamic pressure  $q_{i,j}^0$  to zero a hydrostatic velocity field is obtained. This feature of the method is beneficial in cases, when the type of flow is known in advance or can be estimated to be approximately hydrostatic. In such cases, computational costs drop significantly, as it is no longer necessary to solve the set of Poisson’s equations for the hydrodynamic pressure  $q$ , which is the most computationally expensive part of the algorithm.

The presented method can deal with two immiscible layers, from which the inner (top) layer must be lighter ( $\rho_2 < \rho_1$ ) than the outer (bottom) layer. Opposite scenarios, when  $\rho_2 \geq \rho_1$  and the Rayleigh–Taylor instability is expected to happen, cannot be however handled. Another important feature of the method is related to the layer depths  $H_{1,2}$  extending only over a single layer of cells along the radial direction. The algorithm conveniently transforms into the shallow water equations, often used in oceanography and meteorology e.g. in modeling of geostrophic flows.

When it comes to implicit coupling of the free-surface/interface position and the velocity field, the method turns out to be unconditionally stable for  $1/2 \leq \theta \leq 1$ . Therefore, the time step is independent of the free-surface/interface wave speeds and radial viscosity terms. Due to explicit treatment of the axial viscosity terms, a time step restriction however exists and is given by [35].

$$\Delta t \leq \Delta x^2 / (4\nu) \tag{37}$$

As long as the axial grid size  $\Delta x$  stays much larger, the time step restriction (37) stays rather weak. Currently, there appears to be a second restriction of the time step related to the radial velocity  $w$ , namely the radial velocity of the free-surface and the interface, and solving the heat advection–diffusion equation (34). As the algorithm requires both the free-surface and the interface not to cross more than one layer of cells in radial direction, the following convective limit CFL applies

$$\Delta t^{n+1} \leq \min \left( \frac{\Delta r}{H_1^{n+1} - H_1^n}, \frac{\Delta r}{H_1^{n+1} + H_2^{n+1} - H_1^n - H_2^n} \right) \tag{38}$$

where  $\Delta r$  is the radial size of the background grid cell rather than the radial size of the actual element. The last stability limit (38) could be possibly removed by splitting the time step  $\Delta t$  into a number of equal-size substeps and use a subcycling when solving (34).

#### 4. Numerical examples and discussion of results

This section demonstrates the capabilities of the proposed method on several numerical examples. Some examples are compared with results of other numerical techniques and some are verified against experimental data.

##### 4.1. Example 1: single-layer hydrostatic vs. full model

The first example is intended to show that when the ratio of radial and axial characteristic scales is small ( $\ll 1$ ), the flow is nearly hydrostatic. Therefore, it is possible to omit the hydrodynamic pressure  $q$  from the momentum equations. In the present method it is realized by setting the initial value  $q_{i,j}^0$  to zero and skipping the corrector step. Here, two different single-layer cases (a) and (b) are considered with a short and a long wave initial disturbance of the free-surface respectively, given by the following formulas

$$\begin{aligned} (a) : H_1^0(x) &= 0.06 + \max(0.02 - 5(x - 0.5)^2, 0) \\ (b) : H_1^0(x) &= 0.06 + \max(0.02 - 5(x - 5)^2, 0) \end{aligned} \quad (39)$$

In addition to the free-surface, fixed walls with no-slip condition are bounding the finite-volume grid with  $100 \times 100$  cells. Physical properties such as the density and the dynamic viscosity are set to  $7700 \text{ kgm}^{-3}$  and  $0.006 \text{ Pas}$  respectively. The size of the time step  $\Delta t$  is adjusted during the calculation in order to maintain  $CFL = 0.95$ . The implicitness factor  $\theta$  is set to 0.55. At  $t = 0 \text{ s}$ , the free-surface is described by (39). Later, due to the g-force (100g) the parabolic disturbance collapses and waves propagate toward the left and the right wall. The g-force is a term often used by centrifugal casting community to express the centrifugal acceleration  $\Omega^2 R$  as a multiple of the gravitational acceleration  $g$ . The g-force of 100g is a typical value encountered during the centrifugal casting. In Fig. 4a and b, the scenarios are depicted respectively for the case (a) and (b). The contours represent a distribution of the hydrodynamic pressure  $q$ . While the hydrostatic assumption is obviously justified in the case (a), in the case (b) such assumption is clearly incorrect, meaning that the hydrodynamic pressure has to be accounted for. As a result, the hydrostatic model, greatly saving the computational resources, should only be used, when the ratio of radial and axial characteristic scales  $\ll 1$ . Otherwise, it is necessary to consider the full model with the hydrodynamic pressure included.

##### 4.2. Example 2: two-layer hydrostatic model vs. shallow water equations

Here, a test case with two layers is suggested with initial conditions shown in Fig. 5. Gradients of the hydrostatic pressure again serve as a driving force for a fluid motion and also provide a momentum coupling between the layers. The coupling is also realized through a viscous stress term. A simulation work was performed using the hydrostatic model, followed by the numerical verification conducted with the help of the radially averaged shallow water equations solved using the approximate Riemann solver with high resolution corrections [36] developed earlier by the authors [37]. Initially, the bottom layer is flat, whereas the top layer is disturbed with a parabolic hump. Initial conditions are patched on the domain using the following formulas

$$\begin{aligned} \text{the bottom layer} : H_1^0(x) &= 0.045 \\ \text{the top layer} : H_2^0(x) &= 0.015 + \max(0.03 - 500(x - 0.05)^2, 0) \end{aligned} \quad (40)$$

The densities,  $\rho_1$  and  $\rho_2$ , are set to  $7700 \text{ kgm}^{-3}$  and  $7600 \text{ kgm}^{-3}$  respectively. The dynamic viscosities are identical, equal to  $0.006 \text{ Pas}$ . In Fig. 5, it is shown that both techniques produce almost identical results at  $t = 0 \text{ s}$ . Later, the deviations will certainly grow. The reader should be reminded that it is difficult to say, which algorithm is more accurate namely for the following reasons. Unlike the hydrostatic model discretized on a two-dimensional finite-volume grid, the SWE model requires only one (axial) space dimension. On the other hand, the approximate Riemann solver physically correctly decomposes the hyperbolic PDEs into a set of discontinuities moving with certain wave speeds. The solution is found using TVD updating formulas with limiters, unwinding each discontinuity separately. One significant drawback of the two-layer approximate Riemann solver for the SWE is a way of determining the wave speeds, namely the one representing the momentum transfer between the layers. It was shown that when  $\rho_2$  is significantly smaller than  $\rho_1$ , than such a wave speed is not correctly approximated [38]. In Fig. 5, the layer densities are quite similar and both methods deliver almost identical results. In Fig. 6,  $\rho_2 \ll \rho_1$  such that  $\rho_1 = 7700 \text{ kgm}^{-3}$  and  $\rho_2 = 1000 \text{ kgm}^{-3}$ , the results are hardly comparable due the erroneous wave speed approximation in the SWE model. Only the hydrostatic model thus gives a physically reasonable propagation of waves (solid lines in Fig. 6).

##### 4.3. Example 3: thermal convection

This example shows two cases with the thermal convection. In both cases, the free-surface is initially disturbed by the following function

$$H_1^0(x) = 0.03 + 0.005 \sin(2\pi x/L) \quad (41)$$

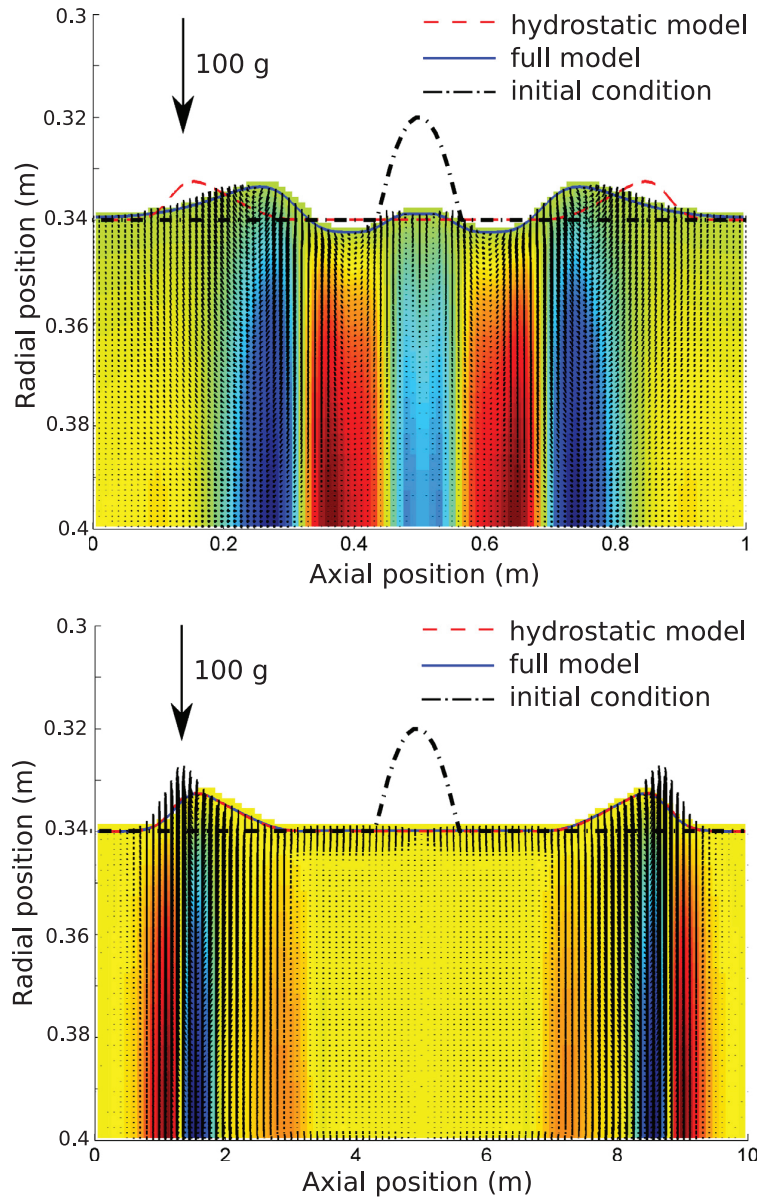


**Fig. 4.** An initial parabolic perturbation of the free-surface producing waves propagating to the left and to the right; (a) a short wave case  $t = 0.125$  s; (b) a long wave case ( $\sim$ hydrostatic) at  $t = 1.25$  s.

where  $L(L = 0.1\text{m})$  denotes the axial dimension of the computational domain. In the first case, the thermal convection is induced by cooling applied at the free-surface, numerically represented by a constant heat transfer coefficient  $htc$ . Remaining boundaries are treated as adiabatic walls. The characteristic time of the free-surface motion is set close to that of the thermal convection, so that both phenomena can be observed at the same time. Material properties and other parameters are listed in Table 1. As the time proceeds, due to the cooling the liquid close to the free-surface becomes heavier and starts sinking toward the bottom. The instability, also known as the Rayleigh–Bénard instability, is triggered by oscillations of the free-surface. Eventually, the gravity waves, dictating the actual shape of the free-surface, are taken over by the thermal convection in this case. In Fig. 7, thermal convection patterns interacting with the free-surface are shown at time  $t = 1$  s.

In the second case, the cooling of the same intensity  $htc$  is applied at the bottom, while the cooling at the free-surface is stopped. In order to promote rising plumes of the colder liquid within the bulk of the hot liquid, the sign of the

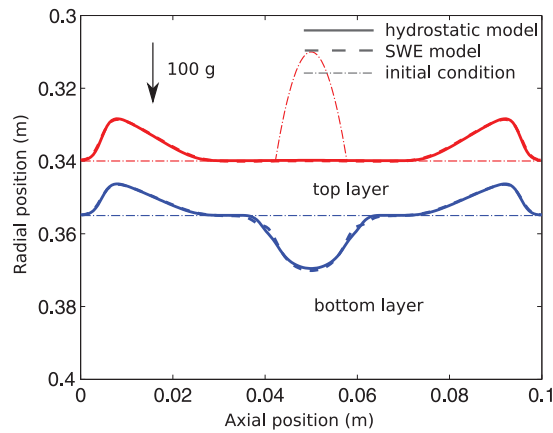


Fig. 5. The present numerical model vs. the approximate Riemann solver for the shallow water equations with two layers of similar densities ( $\rho_1 = 7700 \text{ kgm}^{-3}$ ,  $\rho_2 = 7600 \text{ kgm}^{-3}$ ) at  $t = 0.014 \text{ s}$ .

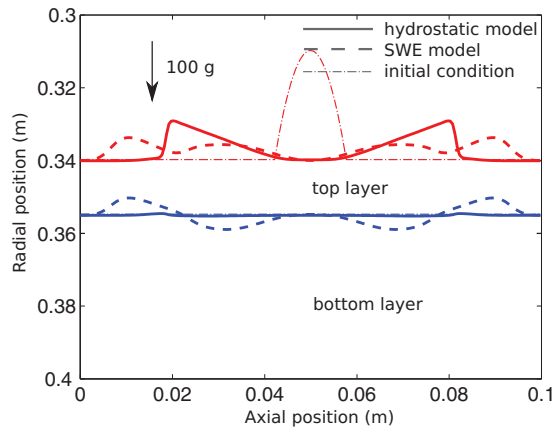


Fig. 6. The present numerical model vs. the approximate Riemann solver for the shallow water equations with two layers of significantly different densities ( $\rho_1 = 7700 \text{ kgm}^{-3}$ ,  $\rho_2 = 1000 \text{ kgm}^{-3}$ ) at  $t = 0.014 \text{ s}$ .

**Table 1**  
Physical properties and parameters used in Example 3.

Property/parameter name	Symbol	Value	Unit
Grid	$N_x \times N_y$	$100 \times 100$	–
Convective time step limit	$CFL$	0.95	–
Implicitness factor	$\theta$	0.55	–
Gravitational acceleration	$g$	10	$\text{m s}^{-2}$
Density	$\rho$	7700	$\text{kg m}^{-3}$
Dynamic viscosity	$\mu$	0.006	$\text{Pa s}$
Thermal conductivity	$k$	20	$\text{W m}^{-1} \text{K}^{-1}$
Specific heat	$c_p$	500	$\text{J kg}^{-1} \text{K}^{-1}$
Heat transfer coefficient	$htc$	10	$\text{kW m}^{-2} \text{K}^{-1}$
Ambient temperature	$T_a$	25	$^{\circ}\text{C}$
Reference temperature	$T_{ref}$	1450	$^{\circ}\text{C}$
Thermal expansion coefficient	$\beta$	0.001	$\text{K}^{-1}$

thermal expansion coefficient  $\beta$  has to be switched so that the colder liquid becomes lighter ( $\beta \rightarrow -\beta$ ). Other material properties and parameters are identical to those summarized in Table 1. In Fig. 8, again a snapshot of the temperature field reflecting the thermal convection is presented at time  $t = 1 \text{ s}$ . In addition, the position of the free-surface is also plotted at  $t = 0.25 \text{ s}$ . The dashed lines indicate the position of the free-surface calculated using the volume of fluid model available in ANSYS FLUENT 14.5 with the properties and parameters given in Table 1. Note that here  $\beta$  is referred to as a thermal

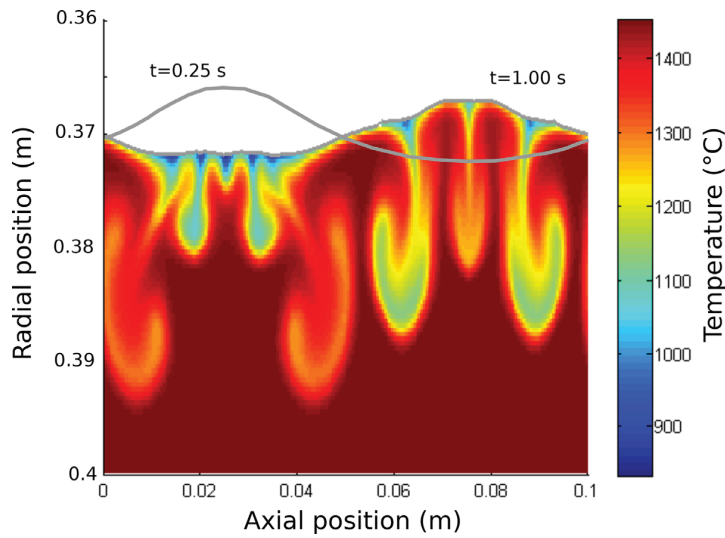


Fig. 7. An example of a thermal convection induced by the cooling applied at the free-surface, initially disturbed by (41), at  $t = 1$  s.

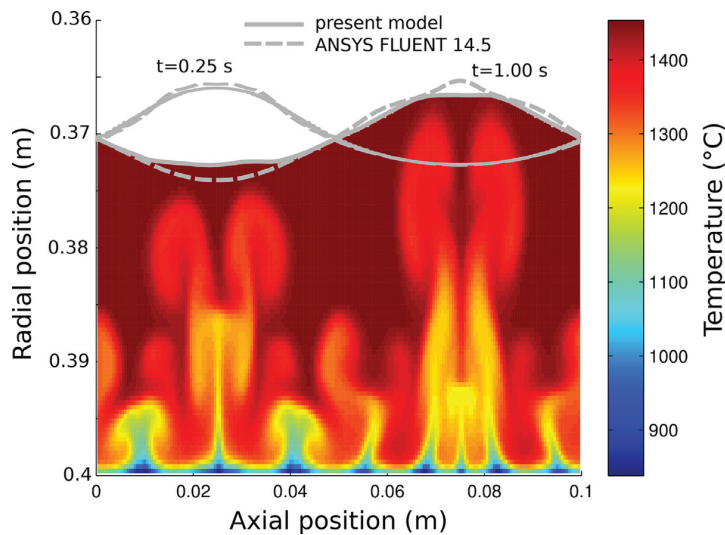


Fig. 8. Thermal convection at  $t = 1$  s induced by the cooling applied at the bottom wall. A free-surface calculated by the present numerical model (solid line) compared to that obtained using ANSYS FLUENT 14.5 (dashed line).

expansion coefficient. It could however also represent a solutal expansion coefficient. In that case the corresponding advection-diffusion equation would be solved for the concentration and not for the temperature.

#### 4.4. Example 4: horizontal centrifugal casting (HCC)

A simulation of the HCC process, shortly described in Section 1, is presented here. The results are validated against in terms of comparing calculated and measured temperatures. A pyrometer and a thermo-camera were used to continuously record temperatures of a single point at the free-surface of the casting and the outer wall of the cylindrical mold respectively. The simulation was set up using a multi-region approach. The numerical model, detailed in the section Numerical algorithm, was employed only in the fluid region indicating the room for the casting. The solid regions such as the mold and both end cores were also discretized using finite-volume grids; however, only the heat diffusion equation was solved there for the temperature  $T$  with appropriate material properties and boundary conditions, which are due to confidentiality of industry data only roughly introduced in Table 2. The heat transport was solved simultaneously in all regions; therefore, there was no need for otherwise typical Neumann–Dirichlet coupling at the common walls.

**Table 2**  
Physical properties and other parameters used in Example 4.

	symbol	value	Unit
Simulation settings			
Total number of cells	$N_x \times N_r$	~100k	–
Convective time step limit	$CFL$	0.95	–
Implicitness factor	$\theta$	0.55	–
Thermal boundary conditions			
Free-surface	$htc_{fs}$	0	$W m^{-2} K^{-1}$
Mold and end core walls	$htc_{m,en}$	40	$W m^{-2} K^{-1}$
Ambient temperature	$T_a$	25	$^{\circ}C$
First layer			
Casting length	$h$	3	m
Layer thickness	$H_1$	0.1	m
Outer radius	$R$	0.4	m
Density	$\rho$	7600	$kg m^{-3}$
Dynamic viscosity	$\mu$	0.006	Pa s
Thermal conductivity	$k$	22	$W m^{-1} K^{-1}$
Specific heat	$c_p$	600	$J kg^{-1} K^{-1}$
Reference temperature	$T_{ref}$	1450	$^{\circ}C$
Filling temperature	$T_{fill}$	1450	$^{\circ}C$
Thermal expansion coefficient	$\beta$	0.0001	$K^{-1}$
Latent heat	$L_f$	280	$kJ kg^{-1}$
Solidus temperature	$T_s$	1165	$^{\circ}C$
Liquidus temperature	$T_l$	1322	$^{\circ}C$
Liquid fraction	–	Linear	–
Second layer			
Layer thickness	$H_2$	0.15	m
Density	$\rho$	7200	$kg m^{-3}$
Dynamic viscosity	$\mu$	0.006	Pa s
Thermal conductivity	$k$	25	$W m^{-1} K^{-1}$
Specific heat	$c_p$	450	$J kg^{-1} K^{-1}$
Reference temperature	$T_{ref}$	1450	$^{\circ}C$
Filling temperature	$T_{fill}$	1420	$^{\circ}C$
Thermal expansion coefficient	$\beta$	0.0001	$K^{-1}$
Latent heat	$L_f$	200	$kJ kg^{-1}$
Solidus temperature	$T_s$	1080	$^{\circ}C$
Liquidus temperature	$T_l$	1250	$^{\circ}C$
Liquid fraction	–	Linear	–
Mold			
Rotation rate	$\Omega$	70	$rad s^{-1}$
Mold thickness	$mt$	0.2	m
Density	$\rho$	7850	$kg m^{-3}$
Thermal conductivity	$k$	60	$W m^{-1} K^{-1}$
Specific heat	$c_p$	490	$J kg^{-1} K^{-1}$
End cores			
Density	$\rho$	2200	$kg m^{-3}$
Thermal conductivity	$k$	10	$W m^{-1} K^{-1}$
Specific heat	$c_p$	200	$J kg^{-1} K^{-1}$
Coating			
Thermal conductivity	$k$	5	$W m^{-1} K^{-1}$
Coating thickness	$ct$	0.004	m

A layout of the computational domain is obvious from looking at Fig. 9, with the mold at the top, the end cores at both sides, and the casting region in the center. In addition, temperature contours are shown inside both layers at  $v t \approx 35$ min along with isolines of liquid fraction, namely  $g_l = 0.01$  (solid line) and  $g_l = 0.99$  (dash line). The marker at the free-surface denotes the target point of a single channel IR thermometer, at which the temperature was recorded with frequency of 100 Hz. The IR thermometer (Infratherm ISQ 5) was calibrated to a single temperature of  $\sim 1450^{\circ}C$  and it was mounted at a fixed position schematically shown in Fig. 9. In Fig. 10, the calculated cooling curve (thick solid line) quite reasonably follows IR thermometer curve (thin solid line) obtained by averaging temperature records from several castings of the same product. The error bars corresponds to relative errors of  $\pm 5\%$ . The sudden jump of the temperature at  $t = 33$  min is caused by pouring the second layer. During the pouring, the IR thermometer measurement was interrupted; data is therefore not available. The experimental data is also missing at the early stage of the casting namely during the pouring of the first layer. In addition to IR thermometer measurements, a thermal camera (FLIR ThermoCAM 540; frequency 0.1 Hz) was employed to monitor temperatures of the entire surface of the mold visible from outside (Fig. 11). For comparison with the numerical results, only a single value of temperature was however used, obtained by averaging temperature field along the black solid line shown in Fig. 11. Looking at the evolution of the average temperature of the outer mold surface in Fig. 10, it can be concluded that the calculated and the measured data are in a good agreement. Relative errors

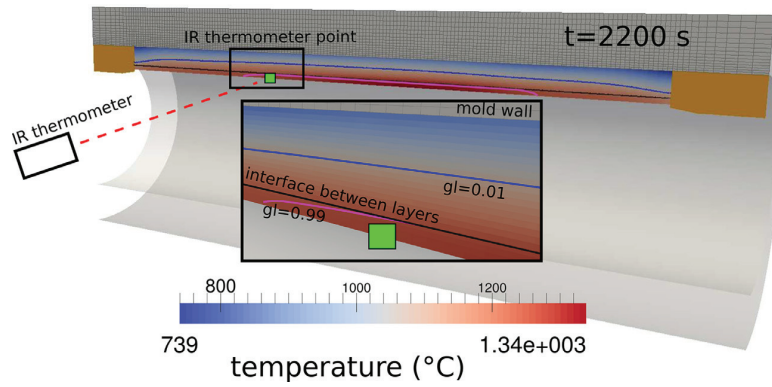


**Fig. 9.** Results of horizontal centrifugal casting simulation namely temperature contours and isolines of the liquid fraction  $g_l = 0.01$ (solid line) and  $g_l = 0.99$ (dashed line) demarcating the mushy zone at  $t = 35$ min. The circle marker denotes the target point of the pyrometer. In addition to the casting region, the mold and two end cores are visible.

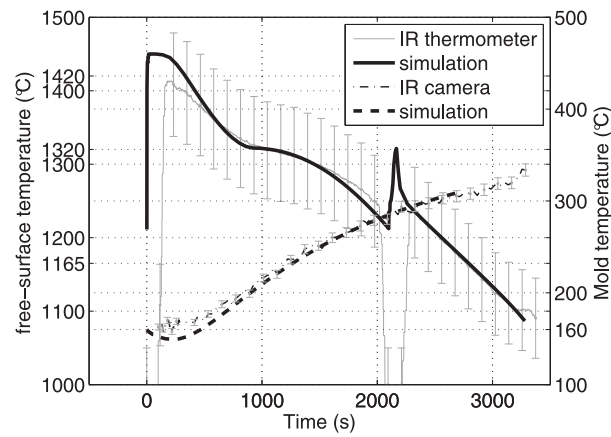


**Fig. 10.** Cooling curves calculated using the present numerical model plotted against those obtained from the pyrometer and thermo-camera measurements.

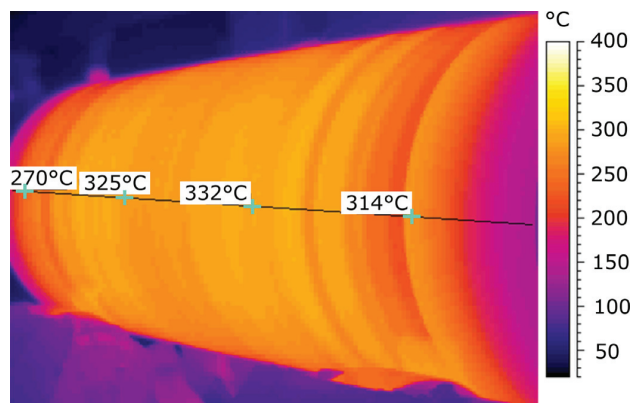


**Fig. 11.** Thermal camera image taken at around 35min.

of thermal camera measurements are expected to fall into a typical range  $\pm 2\%$  [39]. Although the numerical results were successfully compared against two different kinds of temperature measurement techniques, further verifications are still required mainly for the following reasons. Excellent match of temperatures of the outer surface of the mold cannot be considered as a conclusive and sufficient verification, as it is located far from the casting and at the same time it is very much influenced by the accuracy of the thermal boundary condition imposed there. Concerning IR thermometer measurements, these were performed exclusively at a single location at the free-surface. The reader should be reminded of two things. Firstly, the flow was solved in  $x - r$  plane and thus some features, peculiarities caused by the Coriolis force may have been missed. Secondly, in this study the solutal transport was not taken into account. However, during the real casting the solutal convection will be quite pronounced especially due to significant centrifugal forces, providing a good mixing in the liquid.

## 5. Conclusions

A semi-implicit finite-difference/volume-based model has been proposed to numerically investigate a free-surface flow of a single or two immiscible liquid layers, with a special focus on the horizontal centrifugal casting process. The numerical model is based on valuable and comprehensively processed works done by Casulli [23–25]. Here, the governing equations and the numerical algorithm were derived in the cylindrical coordinate system in two space dimensions, namely the axial and the radial coordinates. Switching to the Cartesian coordinate system is straightforward and in fact, it eventually results in a simpler algorithm, as all the linearization steps described earlier in section Numerical algorithm drop out. The main idea of the algorithm is to split the pressure term into the hydrostatic pressure and the hydrodynamic pressure. The algorithm is divided into two steps, the predictor step and the corrector step. The pressure is discretized by the  $\theta$ -method, allowing the user to set the level of its implicitness. Both explicit and implicit contributions of the hydrostatic pressure are included in the predictor step. While the explicit part of the hydrodynamic pressure is applied there also, the implicit part is determined separately in the corrector step. The convective term, the axial viscous terms, the gradient of the baroclinic pressure are discretized explicitly in the predictor step. Preliminary fields of the layer depths and velocity obtained in the predictor step are subsequently updated in the corrector step. In addition to the flow, the heat advection-diffusion equation is solved in a fractional step. When the solidification is taken into account through the latent heat source term, generally several iterations ( $\sim 3$ ) are needed to reach a convergence between the liquid fraction  $g_l$  and the temperature  $T$ . Concerning the stability, due to the implicit discretization of the gradient of the hydrostatic pressure the proposed algorithm is unconditionally stable with respect to the free-surface/interface wave speed. Yet a certain restriction on the time step exists due to the explicit discretization of the axial viscous terms. As long as the axial grid spacing is large compared to the radial one, such a time step restriction is rather weak. In addition, the time step is restricted also by the convective limit (CFL) arising when solving the heat advection-diffusion equation. In that case, the free-surface or the interface should not cross more than one computational cell in the radial direction within a single time step ( $CFL < 1$ ).

As shown in the numerical examples, the algorithm can be easily modified into a hydrostatic model by setting the initial value of the hydrodynamic pressure to zero and skipping the corrector step. It was also mentioned that when the liquid layer(s) fits into a single layer of radial computational cells, the algorithm naturally converts into a solver for the single or the two-layer shallow water equations. The algorithm has been successfully validated against the experimental data obtained during the horizontal centrifugal casting process.

## Acknowledgments

Financial support by the Austrian Federal Government (in particular from the Bundesministerium fuer Verkehr, Innovation und Technologie and the Bundesministerium fuer Wirtschaft, Familie und Jugend) and the Styrian Provincial Government, represented by Oesterreichische Forschungsfoerderungsgesellschaft mbH and by Steirische Wirtschaftsforderungsgesellschaft mbH, within the research activities of the K2 Competence Centre on "Integrated Research in Materials, Processing and Product Engineering", operated by the Materials Center Leoben Forschung GmbH in the framework of the Austrian COMET Competence Centre Programme, is gratefully acknowledged. This work is also financially supported by the Eisenwerk Sulzau-Werfen R. & E. Weinberger AG.

## References

- [1] A. Coutinho, Some reflections on big data and computational mechanics, *IACM Expressions* 35 (2014) 5–7.
- [2] S. Elgeti, H. Sauerland, Deforming fluid domains within the finite element method: five mesh-based tracking methods in comparison, *Arch. Comput. Method Eng.* 23 (2) (2015) 1–39.
- [3] S. Osher, J.A. Sethian, Fronts propagating with curvature-dependent speed: algorithms based on Hamilton–Jacobi formulations, *J. Comput. Phys.* 79 (1988) 12–49.
- [4] J.A. Sethian, Level set methods and fast marching methods: evolving interfaces in computational geometry, *Fluid Mechanics, Computer Vision, and Materials Science*, Cambridge University Press, 1999 ISBN 0-521-64557-3.
- [5] H.C.W. Hirt, B.D. Nichols, Volume of fluid (VOF) method for the dynamics of free boundaries, *J. Comput. Phys.* 39 (1) (1981) 201–225.
- [6] W.J. Boettinger, J.A. Warren, C. Beckermann, A. Karma, Phase-field simulation of solidification, *Annu. Rev. Mater. Res.* 32 (2002) 163.
- [7] R. Folch, J. Casademunt, A. Hernández-Machado, L. Ramírez-Piscina, Phase-field model for Hele-Shaw flows with arbitrary viscosity contrast. II. Numerical study, *Phys. Rev. E* 60 (2) (1999) 1734.
- [8] F.H. Harlow, J.E. Welch, Numerical calculation of time-dependent viscous incompressible flow of fluid with a free surface, *Phys. Fluids* 8 (1965) 2182–2189.

- [9] J.H. Ferziger, M. Perić, *Computational Methods for Fluid Dynamics*, vol. 3, Springer, Berlin, 2002.
- [10] T.E. Tezduyar, Interface-tracking, interface-capturing and enhanced solution techniques, *Mecanica Comput.* 21 (2002) 116–135.
- [11] T. Bjontegaard, E.M. Ronquist, Accurate interface-tracking for arbitrary, Lagrangian-Eulerian Schemes 228 (12) (2009) 4379–4399.
- [12] R.J. Leveque, *Finite Volume Methods For Hyperbolic Problems*, Cambridge University Press, 2002, p. 429.
- [13] D. George, *Finite volume Methods and adaptive refinement for tsunami propagation and inundation* Ph.D. thesis, University of Washington, 2006, p. 6.
- [14] J. Bohacek, A. Kharicha, A. Ludwig, M. Wu, Simulation of horizontal centrifugal casting: mold filling and solidification, *ISIJ Int.* 54 (2) (2014) 266–274.
- [15] J. Bohacek, A. Kharicha, A. Ludwig, M. Wu, Shallow water model for horizontal centrifugal casting, *IOP Conf. Ser.: Mater. Sci. Eng.* 33 (2012) 012032.
- [16] E. Kaschnitz, Numerical simulation of centrifugal casting of pipes, *IOP Conf. Ser.: Mater. Sci. Eng.* 33 (2012) 012031.
- [17] H. Esaka, K. Kawai, H. Kaneko, K. Shinozuka, In-situ observation of horizontal centrifugal casting using a high-speed camera, *IOP Conf. Ser.: Mater. Sci. Eng.* 33 (2012) 012041.
- [18] L. Nastac, Numerical modeling of carbide redistribution during centrifugal casting of HSS shell rolls, *ISIJ Int.* 54 (6) (2014) 1294–1303.
- [19] S. Vacca, M.A. Martorano, R. Heringer, M. Bocallini, Determination of the heat transfer coefficient at the metal-mold interface during centrifugal casting, *Metall. Mater. Trans. A* 46A (2015) 2238–2248.
- [20] K.S. Keerthi Prasad, M.S. Murali, P.G. Mukunda, Analysis of fluid flow in centrifugal casting, *Front. Mater. Sci. China* 4 (1) (2010) 103–110.
- [21] D. McBride, N. Humphreys, T. Croft, N. Green, M. Cross, P. Withey, Complex free surface flows in centrifugal casting: computational modelling and validation experiments, *Comput. Fluids* 82 (2013) 63–72.
- [22] Z. Xu, N. Song, R.V. Tol, Y. Luan, D. Li, Modelling of horizontal centrifugal casting of work roll, *IOP Conf. Ser.: Mater. Sci. Eng.* 33 (2012) 01203.
- [23] V. Casulli, P. Zanolli, Semi-implicit numerical modeling of nonhydrostatic free-surface flows for environmental problems, *Math. Comput. Modell.* 36 (2002) 1131–1149.
- [24] V. Casulli, A semi-implicit finite difference method for non-hydrostatic, free-surface flows, *Int. J. Numer. Methods Fluids* 30 (1999) 425–440.
- [25] V. Casulli, A semi-implicit numerical method for the free-surface Navier–Stokes equations, *Int. J. Numer. Methods Fluids* 74 (8) (2014) 605–622.
- [26] A. Staniforth, A. White, N. Wood, Analysis of semi-Lagrangian trajectory computations, *Q. J. R. Meteorol. Soc.* 129 (591) (2003) 2065–2085.
- [27] I.G. Gospodinov, V.G. Spiridonov, J.-F. Geleyn, Second-order accuracy of two-time-level semi-Lagrangian schemes, *Q. J. R. Meteorol. Soc.* 127 (573) (2001) 1017–1033.
- [28] J.P. Gu, C. Beckermann, Simulation of convection and macrosegregation in a large steel ingot, *Metall. Mater. Trans. A* 30A (1999) 1357–1366.
- [29] M. Wu, A. Vakhrusev, G. Nunner, C. Pfeiler, A. Kharicha, A. Ludwig, Importance of melt flow in solidifying mushy zone, *Open Transp. Phenom. J.* 2 (2010) 16–23.
- [30] S. Vitousek, O.B. Fringer, Stability and consistency of nonhydrostatic free-surface models using semi-implicit  $\theta$ -method, *Int. J. Numer. Methods Fluids* 72 (2013) 550–582.
- [31] M.R. Hestenes, E. Stiefel, Methods of conjugate gradients for solving linear systems, *J. Nat. Bur. Stand.* 49 (6) (1952) 409–436.
- [32] H.A. Van der Vorst, Bi-CGSTAB: a fast and smoothly converging variant of Bi-CG for the solution of nonsymmetric linear systems, *SIAM J. Sci. Stat. Comput.* 13 (2) (1992) 631–644.
- [33] V.R. Voller, C.R. Swaminathan, General source-based method for solidification phase change, *Numer. Heat Transfer B* 19 (1991) 175–189.
- [34] J. Murillo, P. Garcia-Navarro, Wave Riemann description of friction terms in unsteady shallow flows: Application to water and mud/debris floods, *J. Comput. Phys.* 231 (2012) 1963–2001.
- [35] H. Johnston, J.-G. Liu, Accurate, stable and efficient Navier-Stokes solvers based on explicit treatment of the pressure term, *J. Comput. Phys.* 199 (2004) 221–259.
- [36] B. Van Leer, Towards the ultimate conservative difference scheme III. Upstream-centered finite-difference schemes for ideal compressible flow, *J. Comput. Phys.* 23 (3) (1977) 263–275.
- [37] J. Bohacek, A. Kharicha, A. Ludwig, M. Wu, A. Paar, M. Brandner, L. Elizondo, T. Trickl, An approximate Riemann solver for two layer shallow water equations in horizontal centrifugal casting, in: *6th Int. Conf. Modelling and Simulation of Metall. Processes in Steelmaking*, 2015, pp. 1–8.
- [38] K.T. Mandli, *Finite volume methods for the multilayer shallow water equations with applications to storm surges* Ph.D. thesis, University of Washington, 2011, p. 52.
- [39] K. Pacholski, B. Wiecek, Practical assessment of accuracy of thermographic indirect measurements, *Meas. Autom. Monit.* 61 (2015) 278–281.

## 2.4 Air gap modeling

During the horizontal centrifugal casting, the liquid steel is pressed towards the wall of the mould by extreme centrifugal forces (100G). In spite of it, a perfect contact can get lost when the solid shell is formed which can withstand such forces. Due to the temperature dependent density the solid shell gradually shrinks. The air gap is formed and acts as a thermal resistance for the heat transfer between the mould and the solidifying shell. Moreover, it can potentially be a source of inadmissible vibrations of the whole casting machine.

The formation of an air gap as well as its effect on heat transfer and solidification is discussed in the following article entitled "Heat Transfer Coefficient at Cast-Mold Interface During Centrifugal Casting: Calculation of Air Gap". Numerical models of other research groups generally rely on explicit time-dependent formulas to describe the heat resistance caused by the air gaps. The introductory part of the author's article reveals that researchers interestingly apparently inherited one formula from each other, some of them just rewrote it into a different form.

After Introduction, a shrinkage model was developed based on the equilibrium equation for radial and tangential stresses, the Hooke's law with thermoelastic term and plastic strains. The differential equation for the total displacement was solved in the solidifying shell as well as in the mould. It was coupled with solving the heat conduction equation with solidification.

It is very important to make the following note. The numerical model was derived as a axisymmetric one in the radial-tangential plane. However, imagine when the air gap is formed, the solidifying shell must touch the mould at one point. Such event will lead to a mass imbalance and subsequent vibrations. Moreover, the contact point may theoretically either remain static in the rotating frame of reference or it can azimuthally travel. These phenomena naturally cannot be captured with the present model.

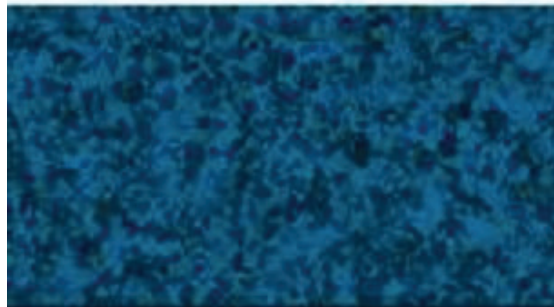
In addition to that, a research was done focused on finding time-dependent formulas for the heat transfer coefficient in the air gap. Results of our simulations agree qualitatively well with the explicit formulas. For this reason, the GUI presented in the next section 2.5 only uses the explicit formula for the thermal resistance at the cast-mould interface.

Volume 49, 12 March 2018

# Metallurgical and Materials Transactions



Process Metallurgy and  
Materials Processing Science



 Springer

TMS

 ASM  
INTERNATIONAL

# Heat Transfer Coefficient at Cast-Mold Interface During Centrifugal Casting: Calculation of Air Gap



JAN BOHACEK, ABDELLAH KHARICHA, ANDREAS LUDWIG, MENGHUAI WU,  
and EBRAHIM KARIMI-SIBAKI

During centrifugal casting, the thermal resistance at the cast-mold interface represents a main blockage mechanism for heat transfer. In addition to the refractory coating, an air gap begins to form due to the shrinkage of the casting and the mold expansion, under the continuous influence of strong centrifugal forces. Here, the heat transfer coefficient at the cast-mold interface  $h$  has been determined from calculations of the air gap thickness  $d_a$  based on a plane stress model taking into account thermoelastic stresses, centrifugal forces, plastic deformations, and a temperature-dependent Young's modulus. The numerical approach proposed here is rather novel and tries to offer an alternative to the empirical formulas usually used in numerical simulations for a description of a time-dependent heat transfer coefficient  $h$ . Several numerical tests were performed for different coating thicknesses  $d_c$ , rotation rates  $\Omega$ , and temperatures of solidus  $T_{sol}$ . Results demonstrated that the scenario at the interface is unique for each set of parameters, hindering the possibility of employing empirical formulas without a preceding experiment being performed. Initial values of  $h$  are simply equivalent to the ratio of the coating thermal conductivity and its thickness ( $\sim 1000 \text{ Wm}^{-2} \text{ K}^{-1}$ ). Later, when the air gap is formed,  $h$  drops exponentially to values at least one order of magnitude smaller ( $\sim 100 \text{ Wm}^{-2} \text{ K}^{-1}$ ).

<https://doi.org/10.1007/s11663-018-1220-0>

© The Author(s) 2018. This article is an open access publication

## I. INTRODUCTION

HORIZONTAL centrifugal casting is an important industrial process used especially for the production of high-quality seamless tubes and outer shells of work rolls. In this process, the effect of centrifuging is twofold. First, it is the fictitious centrifugal force making the production of axisymmetric hollow castings even possible by pushing the molten metal against the inner wall of the cylindrical mold. Second, the interaction between inertial forces and the vector of the gravitational acceleration induces the so-called pumping effect, responsible for thorough mixing,<sup>[1]</sup> the growth of fine equiaxed grains, and superior mechanical properties of the cast.<sup>[2,3]</sup>

As with many other industrial processes, horizontal centrifugal casting has been studied with increased

attention, with the help of various numerical techniques, in order to gain a better understanding of the process and underlying physical phenomena. While some of the numerical studies concentrate more on simulating flow dynamics, such as the mold filling, waves propagating over the free surface, and complex buoyant flow patterns inside the molten metal,<sup>[4-11]</sup> others focus more on heat transfer and solidification, often assuming coupling with simple segregation models.<sup>[12-14]</sup> The latter is naturally more frequent within the centrifugal casting community. Solidification is usually modeled by means of applying the enthalpy method with appropriate rules for a liquid fraction evolution in the mushy zone. In order to construct useful and realistic heat transfer models, precise and accurate material properties and boundary conditions are necessary. Heat transfer coefficients are usually imposed at boundaries, generally being determined from empirical formulas for the Nusselt number. Materials properties are generally temperature dependent and must be specified for all zones, *i.e.*, the casting, the mold, and the coating. The thickness of the coating, a kind of a refractory material, such as  $\text{ZrO}_2$ , is usually small ( $\sim 1 \text{ mm}$ ); therefore, in numerical models, it is often simplified by an assumption of the thin-wall (zero-capacity) model. The coating is applied on the inner surface of the mold in order to insulate the mold from high temperatures and also to control to a certain extent the solidification rate. The

---

JAN BOHACEK, ABDELLAH KHARICHA, and ANDREAS LUDWIG are with the Chair of Simulation and Modeling Metallurgical Processes, Metallurgy Department, Montanuniversitaet Leoben, Franz-Josef-Str. 18/III, 8700 Leoben, Austria. Contact e-mail: jan.bohacek@unileoben.ac.at MENGHUAI WU and EBRAHIM KARIMI-SIBAKI are with the Christian Doppler Laboratory for "Advanced Process Simulation of Solidification and Melting.", Franz-Josef-Str. 18/III, 8700 Leoben, Austria.  
Manuscript submitted October 26, 2016.

general consensus is that it tends to stick firmly to the mold surface. A time-dependent scenario at the contact between the casting and the coating attached to the mold surface is perhaps one of the weakest points of all currently available heat transfer models.

Only during the first seconds of the casting, the molten metal is in perfect contact with the coating, as pointed out in Reference 15. Immediately after that, a so-called microscopic air gap is formed, whose properties such as thickness and temporal growth are strongly influenced by a surface roughness of the mold and the coating eventually. Earlier studies<sup>[16]</sup> show that the importance of the surface roughness has been for many years underestimated. Furthermore, in the literature (*e.g.*, Reference 17), there are interesting numerical works available, taking into account the surface roughness and trying to evaluate the effective thickness of the microscopic air gap by using simple geometrical operations. As time proceeds, the first layer of the solid has enough strength to withstand the metallostatic pressure, whereby the air gap thickness gradually grows and the microscopically thin contact is permanently lost. Such an air gap is often referred to as the macroscopic air gap. Please note that while the cast-mold contact has been extensively studied in static castings and a large body of experimental evidence of microscopic and macroscopic air gap behavior has been presented, it is not yet clear whether at least qualitatively the same observations would apply to the centrifugal casting. Unlike static casting, extreme centrifugal forces are exerted on the liquid metal being cast, which strive to delay the subsequent air gap formation. We deduce that the high centrifugal pressure may be able to significantly reduce the microscopic air gap. Furthermore, we also believe—and this has been proven in this article—that once the macroscopic air gap is formed, the centrifugal force has a negligible impact on its growth.

In order to cope with time-dependent thermal resistance induced by the formation of an air gap, various approaches have been adopted in earlier numerical studies of centrifugal casting. Naturally, a simplest approach would be an assumption of a perfect contact formed throughout the entire casting, which was used, *e.g.*, by Xu *et al.*,<sup>[18]</sup> Gao and Wang,<sup>[19]</sup> and Cook *et al.*<sup>[20]</sup> Bohacek *et al.*<sup>[21]</sup> pointed out the importance of an air gap in their findings and conclusions, yet in the numerical model, it was not taken into account. Humphreys *et al.*<sup>[22]</sup> calculated the heat transfer at the interface by employing a “virtual wall” technique with cumulative thermal resistances; however, they did not provide parameters to calculate them. Chang *et al.*<sup>[23]</sup> used arbitrary values of heat transfer coefficients at the interface, constant during the casting and increasing for higher rotation rates. Other researchers, such as Kang *et al.*<sup>[24]</sup> and Kang and Rohatgi,<sup>[25]</sup> have also used time-independent heat transfer coefficients. Ebisu<sup>[26]</sup> and Kamlesh<sup>[27]</sup> assumed an exponential decay of the radiative heat flux through the interface as follows:

$$q = q_0 e^{-\beta s(t)}, \quad [1]$$

where  $q_0$ ,  $\beta$ , and  $s(t)$  are the initial heat flux through the interface, a damping coefficient, and the current

solidified thickness, respectively. A similar approach was adopted by Lajoie and Suery<sup>[28]</sup> and was later widely used by other authors such as Raju and Mehrotra,<sup>[29]</sup> Drenchev *et al.*,<sup>[30]</sup> Panda *et al.*<sup>[31]</sup> Instead of the heat flux, a time-dependent heat transfer coefficient  $h$  was considered at the interface and defined by the following formula:

$$h = h_0 \left( \frac{h_f}{h_0} \right)^{s(t)/d}, \quad [2]$$

where  $h_0$ ,  $h_f$ , and  $d$  are the initial and the final heat transfer coefficient and the casting thickness, respectively. Naturally, Eqs. [1] and [2] are not equivalent. However, it is worth noting that when the heat flux  $q$  was replaced with the heat transfer coefficient  $h$ , Eqs. [1] and [2] would become identical provided that the damping coefficient was defined as

$$\beta = -\frac{1}{d} \log \left( \frac{h_f}{h_0} \right). \quad [3]$$

Recently, Nastac<sup>[32]</sup> applied a different approach based on calculating an equivalent convective heat transfer coefficient  $h$  to simulate the effect of the coating and the air gap, which can be written as

$$h = \frac{h_a k_C}{k_C + d_C h_a}, \quad [4]$$

where  $k_C$ ,  $d_C$ , and  $h_a$  represent thermal conductivity and thickness of the coating and the heat transfer coefficient between the casting and the coating, which is defined as follows:

$$h_a = h_0 + (h_f - h_0) \left\{ 1 - \left[ \min \left( 1, \frac{t_0}{t} \right) \right]^\gamma \right\}, \quad [5]$$

where  $t_0$ ,  $t$ , and  $\gamma$  stand for the time to initiation of solidification, the current time, and a constant exponent. Table I summarizes the values of  $h$  adopted by the aforementioned authors. Obviously, all of the aforementioned approaches contain at least one unknown parameter, which needs to be adjusted, *e.g.*, by means of an experiment. Although especially the choice of the function given by Eq. [2] appears to be a reasonable solution, a careful fine-tuning of  $h_f$  is required in order to reflect, or at least approximate, real-life conditions. According to Vacca *et al.*,<sup>[33]</sup> who performed a valuable experimental study of the heat transfer coefficient at the interface involving the inverse task, values of the heat transfer coefficient adopted in centrifugal casting simulations are unreliable and usually arbitrary. A similar approach combining a simulation and experiment was employed by Susac *et al.*<sup>[34]</sup> and Sahin *et al.*<sup>[35]</sup> The inverse task is, however, in general, computationally very intensive. Moreover, time-dependent experimental data are necessary at least at one point, located close to the cast-mold interface. While the inverse task cannot be practically applied in a typical centrifugal casting simulation, it is an excellent tool for validating other numerical models or determining constants in

empirical models. In Reference 36, the inverse task, the inverse heat conduction problem (IHCP), was solved by a popular nonlinear estimation technique, originally developed by Beck.<sup>[37]</sup> The casting material, A356 Al alloy, was cast into a carbon steel mold. The IHCP proved that the heat transfer to the mold can be significantly improved by applying the pressure load during solidification in terms of restoring a contact between the mold and the casting.

In Reference 38, the research concerns the simulation of trip continuous casting. An engineering approach was employed to approximate the thermal resistance at the strip-mold interface from the heat transferred to the cooling water. The water flow rate and temperature were recorded at different positions along the length of the strip for this purpose. At selected points in the liquid pool, the calculated cooling curves agreed strongly with those obtained from Inconel (American Special Metals, Corp., Miami, FL) sheathed thermocouples.

In addition, a direct measurement of the macroscopic air gap can be performed by using linear variable differential transformers (LVDTs). However, this technique during the centrifugal casting is limited to static castings due to high rotations of the mold during centrifugal casting. For example, in Reference 39, the heat transfer coefficient at the cast-mold interface of a static casting was determined from the inverse task. The air gap thickness was measured with the help of the LVDTs. Finally, a correlation was found, defining the heat transfer coefficient as a function of the air gap thickness. The effect of the surface roughness of the mold was analyzed. As expected, during formation of the microscopic air gap, findings showed that the smaller degree of roughness provides stronger contact with the mold and that the heat transfer coefficient is, therefore, higher. Consequently, the smaller the surface roughness of the mold, the earlier the macroscopic air gap occurs. On the other hand, the ultimate heat transfer coefficient, when solidification is nearly complete, is insignificantly influenced by the surface roughness.

As a numerical alternative of estimating the air gap thickness, one could suggest ignoring stresses built up in the casting and the mold and using the thermal expansion coefficient to calculate the shrinkage simply by assuming displacements, independent of direction, *i.e.*, uniform rate of deformation of control volume. This technique was applied, *e.g.*, by Taha *et al.*,<sup>[40]</sup> for a static casting. Accuracy and reliability are, however, doubtful due to the missing thermal stresses, which may significantly alter total displacements. In addition, unlike static castings, extreme forces in the centrifugal casting process act on the casting, leading to yielding of the material especially at early stages. In addition, for this reason, the aforementioned approach should be avoided. A strategy that incorporates a more complete and holistic model of physics was outlined by Kron,<sup>[41]</sup> who suggested taking into account vacancies formed due to the thermal expansion of the mold and the material being cast, as well as elastic stresses acting as a consequence of thermally induced strains. Kron *et al.*<sup>[42]</sup> developed the thermomechanical model, based on the plane stress model, assuming elastic materials. They showed that the model predicts accurately the casting scenario only for grain-refined alloys such as Al-4.5 pct Mg. When the solid grains are surrounded by liquid, the material becomes more ductile and consequently the microscopic air gap is suppressed. On the other hand, in the non-grain-refined case, the elastic thermomechanical model does not perform particularly effectively. However, one may wish to interpret these findings, the important message of Reference 42 could be formulated as follows: The peak value of the heat transfer coefficient is larger for the grain-refined alloy due to ductile suppression of the microscopic air gap, but since the formation of the macroscopic air gap starts earlier in this case, total solidification times are almost identical. Lagerstedt, a colleague of Kron, pointed out in the future work chapter of his doctoral thesis<sup>[43]</sup> that including plasticity in the stress model probably should be the next step in developing an accurate shrinkage model.

Table I. Values of  $h$  Adopted by Different Authors

Authors	Type of $h$	Value ( $\text{W m}^{-2} \text{K}^{-1}$ )
Xu <i>et al.</i> <sup>[18]</sup>	—	perfect contact
Gao and Wang <sup>[19]</sup>	—	perfect contact
Cook <i>et al.</i> <sup>[20]</sup>	—	perfect contact
Bohacek <i>et al.</i> <sup>[21]</sup>	—	perfect contact
Humphreys <i>et al.</i> <sup>[22]</sup>	—	not available
Chang <i>et al.</i> <sup>[23]</sup>	constant	1000 to 2600
Kang <i>et al.</i> , <sup>[24]</sup> Kang and Rohatgi <sup>[25]</sup>	constant	1000
Ebisu <sup>[26]</sup>	variable	not available
Kamlesh <sup>[27]</sup>	variable	not available
Lajoie and Suery <sup>[28]</sup>	variable	400 to 80,000 (1/10)*
Raju and Mehrotra <sup>[29]</sup>	variable	100 to 10,000 (1/10)
Drenchev <i>et al.</i> <sup>[30]</sup>	variable	420 to 84,000 (1/10)
Panda <i>et al.</i> <sup>[31]</sup>	variable	50 to 5000 (1/10)
Nastac <sup>[32]</sup>	variable	90 to 6000 (3/100)
Vacca <i>et al.</i> <sup>[33]</sup>	variable (exp.)	50 to 870 (6/100)

\* $h_i/h_0$  ratio.

In Reference 44, Schwerdtfeger *et al.* underlined the importance of the displacement reference. Classically, in stress theory, the displacement is the distance of a specified atom from the position it had assumed when the entire solid body was stress free. Such a situation, however, does not occur during solidification; therefore, they recommended defining the displacement as the distance of a specified atom from the position where it was at the moment of solidification. Consequently, one should work with stress rates and strain rates rather than with stresses and strains. In their study, plastic deformations were also considered and added to the elastic ones by assuming an empirical strain-hardening equation.

Nowadays, most of the commercial software available on the market, including MAGMASOFT (MAGMA in Aachen, North Rhine-Westphalia, Germany), PROCAST (ESI Group, Paris, France), and THERCAST (TRANSVALOR S.A., Mougins, France), offers modules for thermomechanical calculations, and often the user can choose from several elastic-plastic models. In Reference 45, in conclusion, Kron *et al.* stated that an accurate modeling of the air gap formation can only be realized through fully coupled thermomechanical models. They highlighted that the prediction of the air gap, done with the commercial codes, is not satisfactory, suggesting that the solidification shrinkage in the air gap vicinity should be relaxed by the liquid and, therefore, contribute more to a cavity formed in the top of the casting or to the porosity. In conclusion, the entire strain model needs to be defined more precisely. Difficulties associated with air gap modeling were summarized in Reference 46 as the following. High-temperature elastic constants are generally hard to obtain. Defining material properties of the mushy zone remains a challenging topic. Currently, a transition model is available described by the Percolation theory. Next, obtaining proper values of rheological parameters in the power law equation is difficult. Finally, other difficulties or discrepancies, common to all numerical models, are related to oversimplifying assumptions and numerical errors.

In the article by Nayak and Sundarraj,<sup>[47]</sup> it was shown that while it is accurate enough to assume a constant value of the interface heat transfer coefficient during the entire casting into the sand mold, it is not the case with the metal mold. Furthermore, the rate of gap formation significantly affects the solidification process.

The cast-mold interface, namely, the coating and an air gap, represents a significant blockage for the heat transfer and solidification. The thermal resistance of the coating is often negligible compared to that of the air gap. Therefore, a thermal resistance of such an interface has to be carefully determined in order to allow reliable and trustworthy numerical simulations. Existing empirical formulas describing the heat transfer scenario at the interface should only be applied when validated against experimental data. The formation of an air gap depends on many factors such as material and mechanical properties of the casting and the mold, the coating properties, and the process parameters (initial temperatures, the pouring temperature, the casting geometry, and the rotation rate). Obviously, setting up a generalized and unique formula for the heat transfer coefficient at the

interface a priori would be very hard, if not impossible. In the present article, we target developing a simple, computationally cheap, and robust algorithm for calculating the air gap at the cast-mold interface during the centrifugal casting, which could be used as an alternative to often doubtful empirical formulas. A schematic of the configuration at the interface is shown in Figure 1.

## II. NUMERICAL MODEL

During the centrifugal casting of cylindrical parts, it is reasonable to assume that fields of variables and other properties are uniform in the tangential direction. In fact, also, axial variations will be often small and, therefore, could be neglected, too. This finding directly suggests using a plane stress model. Although different variations of plane stress models have been used in diverse industrial applications, such as autofrettage of gun barrels, strain-hardened pressure vessels, and multilayer seamless pipes, in the past,<sup>[48–51]</sup> they have rarely been employed in air gap thickness calculations. Especially, concerning the centrifugal casting, to the best of our knowledge, not a single match was found in the literature survey.

Radial and tangential stresses,  $\sigma_r$  and  $\sigma_t$ , are coupled through the equilibrium equation:

$$\frac{d\sigma_r}{dr} + \frac{\sigma_r - \sigma_t}{r} + \rho\Omega^2 r = 0, \quad [6]$$

where  $\rho$ ,  $\Omega$ , and  $r$  are the density, the rotation rate, and the radial coordinate, respectively. When only elastic deformations are considered, stresses are coupled with strains *via* the Hooke's law with the thermoelastic term. Such a relationship takes the following form:

$$\begin{aligned} \varepsilon_t &= \frac{1}{E} [\sigma_t - \nu\sigma_r] + \alpha T, \\ \varepsilon_r &= \frac{1}{E} [\sigma_r - \nu\sigma_t] + \alpha T, \end{aligned} \quad [7]$$

where  $\nu$ ,  $E$ ,  $\alpha$ , and  $T$  are Poisson's ratio, Young's modulus, the thermal expansion coefficient, and the temperature, respectively. Strains and total radial displacements are related through the following laws:

$$\varepsilon_t = \frac{u}{r}, \quad \varepsilon_r = \frac{du}{dr}. \quad [8]$$

It would, however, be incorrect to only consider elastic strains. Since the casting in a semisolid state can easily yield under strong centrifugal forces, plastic deformations also must be taken into account. Then, total strains can be conveniently expressed as a sum of elastic and plastic strains as follows:

$$\begin{aligned} \varepsilon_t &= \frac{1}{E} [\sigma_t - \nu\sigma_r] + \alpha T + \varepsilon_t^p, \\ \varepsilon_r &= \frac{1}{E} [\sigma_r - \nu\sigma_t] + \alpha T + \varepsilon_r^p, \end{aligned} \quad [9]$$

where  $\varepsilon_t^p$  and  $\varepsilon_r^p$  represent plastic strains in corresponding directions. In addition, it is also physically meaningful to consider a temperature-dependent Young's modulus. Substituting total strains in Eq. [9] with displacements from Eq. [8], and by combining the

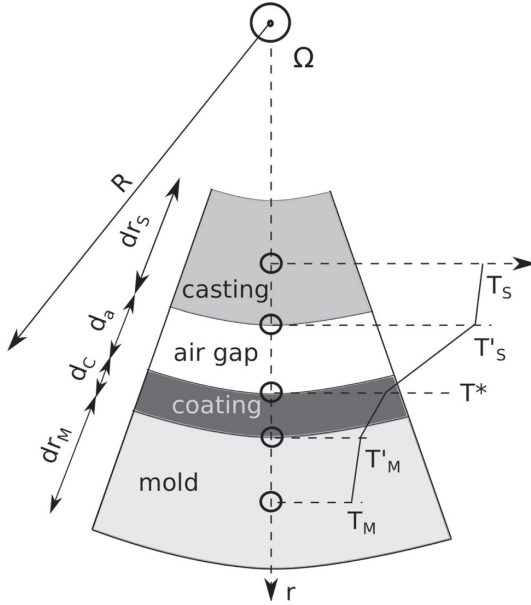


Fig. 1—Schematic of the configuration at the cast-mold interface. In the case of perfect contact, the air gap disappears.

resulting equations with Eq. [6], we can arrive at the following ordinary differential equation for the total displacement  $u$  in the casting:

$$\begin{aligned} & \frac{d^2u}{dr^2} + \frac{1}{r} \frac{du}{dr} \left( 1 + r \frac{1}{E} \frac{dE}{dr} \right) - \frac{u}{r^2} \left( 1 - rv \frac{1}{E} \frac{dE}{dr} \right) \\ & = \alpha(1+v) \left( \frac{dT}{dr} + T \frac{1}{E} \frac{dE}{dr} \right) - \rho r \Omega^2 (1-v^2) \frac{1}{E} \\ & + F(\varepsilon_r^p, \varepsilon_t^p) \text{ with } F = \frac{1}{E} \frac{dE}{dr} (\varepsilon_r^p + v\varepsilon_t^p) + \frac{d\varepsilon_r^p}{dr} + v \frac{d\varepsilon_t^p}{dr} \\ & + \frac{1-v}{r} \varepsilon_r^p - \frac{1-v}{r} \varepsilon_t^p. \end{aligned} \quad [10]$$

In the mold, Eq. [10] is considerably simplified because one assumes a constant Young's modulus and pure elastic deformations. The differential equation for the total displacement  $u$  in the mold becomes

$$\frac{d^2u}{dr^2} + \frac{1}{r} \frac{du}{dr} - \frac{u}{r^2} = \alpha(1+v) \frac{dT}{dr} - \rho r \Omega^2 (1-v^2) \frac{1}{E}. \quad [11]$$

Note that in Eqs. [10] and [11], subscripts [...] <sub>S</sub> and [...] <sub>M</sub> denoting the mold and the casting are omitted for the sake of brevity. Equations [10] and [11] can be solved provided that plastic strains  $\varepsilon_r^p$  and  $\varepsilon_t^p$  are known. In order to determine them, a universal stress-strain curve, usually assumed to be equivalent to the stress-strain curve obtained from the uniaxial loading test, must be known in advance. The universal stress-strain curve relates two scalar quantities: the effective stress  $\bar{\sigma}$  and the effective plastic strain  $\bar{\varepsilon}^p$ . Several models of the effective stress  $\bar{\sigma}$  exist. Here, the von Mises stress,

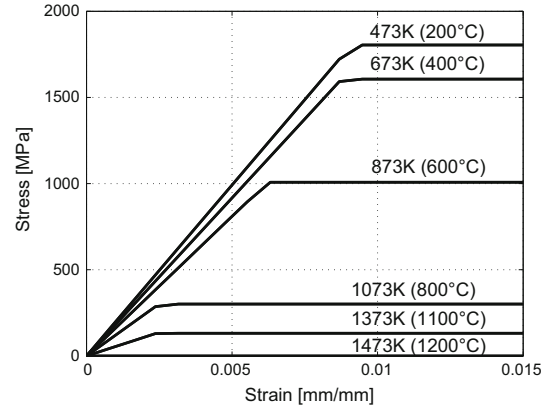


Fig. 2—Uniaxial stress-strain curves of elastic-perfectly plastic material used in the present study.

calculated by assuming a principal stress loading, was used in the following form:

$$\bar{\sigma} = \frac{1}{\sqrt{2}} \sqrt{(\sigma_r - \sigma_t)^2 + \sigma_r^2 + \sigma_t^2}. \quad [12]$$

The von Mises stress  $\bar{\sigma}$  is coupled with the increment of the effective plastic strain  $d\bar{\varepsilon}^p$  by the Prandtl–Reuss (Levy–Mises) flow rule as follows:

$$d\varepsilon_r^p = \frac{d\bar{\varepsilon}^p}{\bar{\sigma}} (\sigma_r - 0.5\sigma_t) \quad [13]$$

and

$$d\varepsilon_t^p = \frac{d\bar{\varepsilon}^p}{\bar{\sigma}} (\sigma_t - 0.5\sigma_r). \quad [14]$$

Knowing or assuming  $d\bar{\varepsilon}^p$ , the plastic strains  $d\varepsilon_r^p$  and  $d\varepsilon_t^p$  can be easily calculated and then used in Eq. [10] to extrapolate the total displacement  $u$ . In Eqs. [13] and [14], the increment of the effective plastic strain  $d\bar{\varepsilon}^p$  is used and not the effective plastic strain  $\bar{\varepsilon}^p$ , which means that the plastic strain history (or the loading path) is very important. Correspondingly, a progressive load must be also applied in the simulation. Here, such loading is automatically realized by a time-dependent temperature field and a gradual progress of solidification.

In the present study, a temperature-dependent, perfectly elastic-plastic material is used, as shown in Figure 2. At a given temperature, the material deforms elastically until a certain threshold of the effective stress, known as the yield strength, is reached, at which point the material starts yielding with no further increase of the effective stress. Instead of the elastic-perfectly plastic material, any kind of other material could be used such as a strain-hardening or a strain-softening material.

In the following text, we summarize all the facts, assumptions, and solution strategy necessary to run a successful numerical simulation and obtain a reasonable air gap.

Facts:

- (1) The mold constantly expands during the entire casting process.
- (2) The casting also expands but only during the early stage of casting. Later, the strength of the solidified part of the casting is sufficient to withstand centrifugal forces; therefore, the casting contracts. Consequently, the air gap forms.

Assumptions:

- (1) The mold undergoes purely elastic deformations. (In reality, it may not be true, especially in the vicinity of the cast-mold interface. At the initial stage of casting, extreme stresses may occur, causing a type of damage known as “fire cracks,” to the inner part of the mold.)
- (2) Mechanical properties of the mold material are constant. Thermophysical properties may vary with the temperature.
- (3) The casting may deform both elastically and plastically. A temperature-dependent, perfectly elastic-plastic material is assumed (Figure 2).
- (4) Mechanical properties (Young’s modulus  $E$  and yield strength  $Y$ ) of the casting material are temperature dependent. Thermophysical properties may also vary with the temperature.
- (5) Only the radiative and the conductive heat transfer mechanisms are expected within the air gap. The convective mechanism is neglected due to the small size of the air gap.

In addition to Eqs. [10] and [11], we also need to solve the heat conduction for the temperature  $T$ . In the cylindrical coordinate system, it takes this form in the mold:

$$\rho_M c_{pM} \frac{\partial T}{\partial t} = \frac{1}{r} \frac{\partial}{\partial r} \left( k_M \frac{\partial T}{\partial r} \right), \quad [15]$$

where  $\rho_M$ ,  $c_{pM}$ , and  $k_M$  are the density, specific heat, and thermal conductivity of the mold material, respectively. Similarly, in the casting, it can be written as

$$\rho_S c_{pS} \frac{\partial T}{\partial t} = \frac{1}{r} \frac{\partial}{\partial r} \left( k_S \frac{\partial T}{\partial r} \right) + \rho_S L_f \frac{\partial g_s}{\partial t}, \quad [16]$$

where  $\rho_S$ ,  $c_{pS}$ , and  $k_S$  are density, specific heat, and thermal conductivity of the casting material, respectively. The last term is a latent heat source term due to the phase change, in which  $L_f$  and  $g_s$  represent the latent heat and the solid fraction, respectively. In the present study, a simple linear relationship is considered between the solid fraction  $g_s$  and the temperature  $T$ . Other relationships, however, could also be considered (e.g., the lever rule or the Gulliver–Scheil equation). The heat conduction equations, Eqs. [15] and [16], are coupled *via* the heat flux at the cast-mold interface. A thin-wall model, also known as a zero-capacity model, was used to numerically simplify the situation at the interface by considering only a thermal resistance,

exerted by the coating and possibly the air gap. Then, the heat flux at the interface reads as

$$q = k_{\text{ifc}} \frac{T_S - T_M}{dr_M + dr_S}, \quad [17]$$

$$k_{\text{ifc}} = \frac{k_S k_M k_C k_a (dr_M + dr_S)}{(k_C k_a (dr_M k_S + dr_S k_M) + k_S k_M (dc k_a + d_a k_C))}, \quad [18]$$

where  $k_{\text{ifc}}$ ,  $k_C$ , and  $k_a$  denote the effective thermal conductivity, the thermal conductivity of the coating, and the air gap, respectively. Other quantities are explained in Figure 1. The air gap thermal conductivity  $k_a$  is, in fact, the sum of the thermal conductivity of air  $k_{a,\text{phys}}$  and a thermal conductivity, which is equivalent to the radiative heat transfer through the air gap, given by

$$k_a = k_{a,\text{phys}} + \sigma d_a (T_S' + T^*) (T_S'^2 + T^{*2}), \quad [19]$$

where  $\sigma$  is the Stefan–Boltzman constant ( $5.67 \times 10^{-8} \text{ W m}^{-2} \text{ K}^{-4}$ ). The temperatures  $T_S'$  and  $T^*$  must be given in Kelvin. Note that without the air gap ( $d_a = 0$ ), Eq. [18] is still valid and represents the effective thermal conductivity only in the presence of the coating. The reader should be reminded that in this study, the black body radiation model has been taken for its simplicity and convenience. However, when targeting more accurate results, considering gray bodies is better justified and Eq. [19] would then become

$$k_a = k_{a,\text{phys}} + \sigma d_a (T_S' + T^*) (T_S'^2 + T^{*2}) (1/\varepsilon_S + 1/\varepsilon_C - 1)^{-1}, \quad [20]$$

where  $\varepsilon_S$  and  $\varepsilon_C$  are emissivity coefficients of both surfaces enclosing the air gap, which belong to the casting and the coating, respectively. Using Eq. [20], instead of Eq. [19] will naturally reduce the radiative heat transfer. In reality, the air between the casting and the shell may, as a participating gas, further reduce the radiative heat transfer. A description of the corresponding mathematical model can be found, e.g., in Reference 52.

Concerning thermal boundary conditions, both the free surface of the casting and the outer surface of the mold are considered to be adiabatic:

$$\begin{aligned} \frac{dT}{dr}(r_i) &= 0, \\ \frac{dT}{dr}(r_o) &= 0. \end{aligned} \quad [21]$$

In simulations focused on a comparison with experimental data, thermal boundary conditions, however, should be specified more precisely, e.g., with the help of existing empirical formulas for the Nusselt number<sup>[53,54]</sup> in rotating geometries.

In addition to Eq. [21], boundary conditions have to be specified also for Eqs. [10] and [11]. Here, we have to distinguish between two cases: a perfect contact or an air

gap. In the case of the contact, appropriate boundary conditions take the following form:

$$\begin{aligned}\sigma_{rS}(r_i) &= 0 \\ u_S(R) &= u_M(R) \\ \sigma_{rM}(r_o) &= 0.\end{aligned}\quad [22]$$

Otherwise (the air gap),

$$\begin{aligned}\sigma_{rS}(r_i) &= 0 \\ \sigma_{rS}(R) &= 0 \\ \sigma_{rM}(R) &= 0 \\ \sigma_{rM}(r_o) &= 0.\end{aligned}\quad [23]$$

Differential equations for total displacements, Eqs. [10] and [11], and temperature, Eqs. [15] and [16], were all solved using the finite difference method with second-order accurate central difference schemes for derivatives (including points at the boundaries). In the radial direction, the casting and the mold were divided into  $N_S$  and  $N_M$  uniformly spaced grid points with the dimensions  $dr_S$  and  $dr_M$  of 1 mm (Figure 1). The same grids with uniform spacing were used for both quantities  $u$  and  $T$ . For Eqs. [15] and [16], the implicit backward Euler method was used for time-stepping. In addition, an iterative approach was necessary for heat conduction equations due to temperature-dependent thermophysical properties, the nonlinear heat flux  $q$  at the cast-mold interface (Eq. [17]), and especially the stiff, latent heat source term. Treatment of the latent heat source term was realized by using a semi-implicit method proposed by Voller and Swaminathan.<sup>[55]</sup> A detailed description of the discretization can be found in Reference 56. Although systems of equations are unconditionally stable, the time-step size should be small enough so that the loading rate still allows finding correct and physically meaningful increments of plastic strains. Here, the time-step of 0.1 seconds was found to be reasonable.

Solution strategy:

- (1) Initialize fields of temperature, solid fraction, plastic strains, stresses, and air gap thickness.
- (2) For time  $t_{n+1}$ , solve heat conduction equations, Eqs. [15] and [16], coupled by the heat flux at the interface (Eq. [17]), with the air gap thickness  $d_a$  from the previous time  $t_n$  and obtain new temperature  $T$  and solid fraction  $g_s$  fields. In our numerical tests, usually between two and five iterations were necessary to drop scaled residuals below  $10 \times 10^{-8}$  for the latent heat source term and the nonlinear heat flux  $q$ , respectively. The residuals were calculated according to the following formula:

$$\text{res} = \frac{\sqrt{N \sum_i (T_i - T_i^{\text{old}})^2}}{\sum_i T_i^{\text{old}}}\quad [24]$$

where  $N$  is the total number of cells ( $N_S + N_M$ ).  $T_i$  and  $T_i^{\text{old}}$  are the current temperature and the

temperature from the previous iteration both taken at the grid point with the index  $i$

- (3) Use Figures 3 and 4 to find new values of yield strength  $Y$  and Young's modulus  $E$  of the casting material.
- (4) Assume an air gap. For time  $t_{n+1}$ , solve Eq. [11] for total displacements  $u$  of mold with the boundary conditions for the radial stress  $\sigma_{rM}$  in Eq. [23]. Similarly, for time  $t_{n+1}$ , solve Eq. [10] for total displacements  $u$  of the casting with the boundary conditions for the radial stress  $\sigma_{rS}$  in Eq. [23] and the plastic strains  $\epsilon_r^p$  and  $\epsilon_t^p$  from the previous time  $t_n$ .
- (5) If the total displacement of the casting at the interface is greater than that of the mold, the casting and the mold are in perfect contact, *i.e.*, no air gap is formed. Otherwise, the cast-mold contact is lost and the air gap is formed. If the earlier is true (perfect contact), recalculate Eqs. [10] and [11] with the boundary conditions given in Eq. [22]. Otherwise, evaluate the air gap thickness as

$$d_a = u_M(R) - u_S(R)\quad [25]$$

- (6) In the casting, evaluate radial and tangential stresses by using the following explicit formulas, which can be obtained by straightforward manipulations of Eqs. [8] and [9]:

$$\begin{aligned}\sigma_{rS} &= \frac{E}{1-\nu^2} \left[ \left( \frac{du}{dr} - \epsilon_r^p \right) + \nu \left( \frac{u}{r} - \epsilon_t^p \right) \right] - \alpha E \frac{1}{1-\nu} T, \\ \sigma_{tS} &= \frac{E}{1-\nu^2} \left[ \left( \frac{u}{r} - \epsilon_t^p \right) + \nu \left( \frac{du}{dr} - \epsilon_r^p \right) \right] - \alpha E \frac{1}{1-\nu} T.\end{aligned}\quad [26]$$

- (7) Using Eq. [26] in Eq. [12], calculate von Mises stresses  $\bar{\sigma}$  in the casting and compare them with yield stresses  $Y$  obtained from the stress-strain curve (Figure 3). Then, identify only the points  $P$  that yield ( $P = \bar{\sigma} \geq Y$ ).
- (8) For the points  $P$ , new increments  $\overline{d\epsilon^p}$  of the effective plastic strain  $\bar{\epsilon}^p$  must be calculated so that

$$\bar{\sigma} - Y = 0\quad [27]$$

This is realized through an optimization loop, in which Eq. [27] is the objective function and  $\overline{d\epsilon^p}$  is constrained to values greater than zero. Then, one iteration sequence could have the following form: Estimate increments  $\overline{d\epsilon^p}$ ; using Eqs. [13] and [14], calculate increments  $d\epsilon_r^p$  and  $d\epsilon_t^p$  and update the plastic strains  $\epsilon_r^p$  and  $\epsilon_t^p$  ( $\epsilon_r^p = \epsilon_r^p + d\epsilon_r^p$ ,  $\epsilon_t^p = \epsilon_t^p + d\epsilon_t^p$ ); solve Eq. [10] for new displacements  $u$  in the casting and get new stresses (Eq. [26]); and recalculate von Mises stresses  $\bar{\sigma}$  and repeat until the convergence of Eq. [27] is attained. In the present article, a nonlinear least-squares optimization algorithm, known as the trust-region-reflective algorithm,<sup>[57,58]</sup> was applied. In order to reduce dispersive errors of  $\overline{d\epsilon^p}$  appearing due to complex loading and, consequently, yielding on a discrete grid, the Savitzky-Golay filter<sup>[59]</sup> was applied on a temporally overlaid  $\overline{d\epsilon^p}$  signal.

- (9) Proceed to the next time-step.

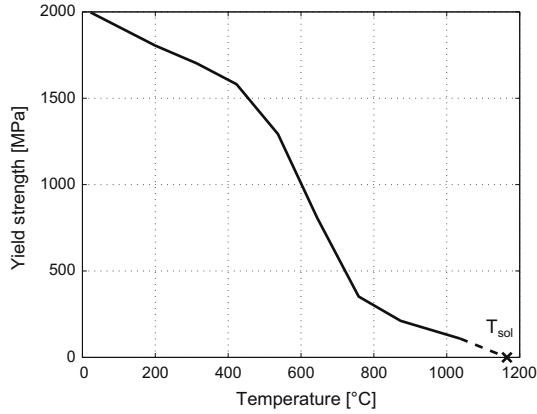


Fig. 3—Temperature-dependent yield strength of the casting material.<sup>[60]</sup> The dashed line represents data reconstructed using the extrapolation until the temperature of solidus  $T_{sol}$ .

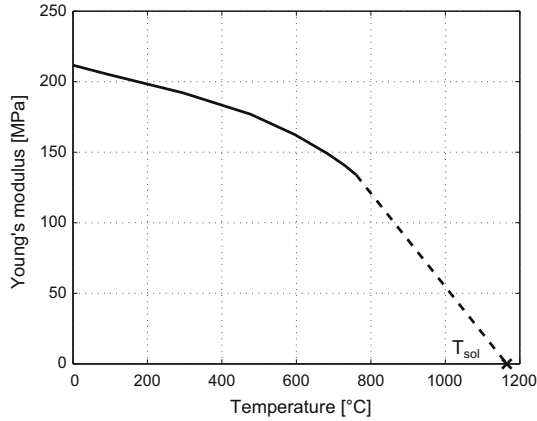


Fig. 4—Temperature-dependent Young's modulus of the casting material.<sup>[60]</sup> The dashed line represents data reconstructed by means of extrapolation until the solidus temperature  $T_{sol}$ .

### III. RESULTS AND DISCUSSION

As the main objective of the present study is to propose and test a novel approach of calculating an air gap rather than numerically analyzing a particular process, material and mechanical properties used in the simulations only roughly correspond to those of real materials (Table II). The geometry, initial conditions, and other casting parameters are given in Table III.

First, numerical tests were performed for different coating thicknesses (0.5, 1, 2, and 4 mm) and all other parameters were fixed. Total displacements  $u$  of the mold and the casting at the interface are shown as a function of time  $t$  in Figure 5. As one would expect, initially, the mold and the casting are in contact. At a certain moment, they detach and their displacements follow different paths. This is clearly shown by bifurcating curves in Figure 5. A difference between the casting and the mold displacement corresponds to the

Table II. Properties of Materials Used in the Simulations

Material	Property	Value	Unit
Casting[...] <sub>S</sub>	$\alpha$	$5 \times 10^{-6}$	$K^{-1}$
	$\rho$	7860	$kg\ m^{-3}$
	$c_p$	500	$J\ kg^{-1}\ K^{-1}$
	$\nu$	0.5	—
	$E$	Fig. 4	Pa
	$g_s$	linear between $T_{liq}$ and $T_{sol}$	—
	$k$	22	$W\ m^{-1}\ K^{-1}$
	$L_f$	280	$kJ\ kg^{-1}$
	$T_{liq}$	1593 (1320)	$K\ (^{\circ}C)$
	$T_{sol}$	1438 (1165)	$K\ (^{\circ}C)$
Mold [...] <sub>M</sub>	$Y$	Fig. 3	Pa
	$\alpha$	$5 \times 10^{-6}$	$K^{-1}$
	$\nu$	0.5	—
	$\rho$	7850	$kg\ m^{-3}$
	$c_p$	490	$J\ kg^{-1}\ K^{-1}$
	$E$	$200 \times 10^9$	Pa
Coating	$k$	58.6	$W\ m^{-1}\ K^{-1}$
	$k_C$	2	$W\ m^{-1}\ K^{-1}$
Air	$k_{a,phys}$	0.02	$W\ m^{-1}\ K^{-1}$

Table III. Geometry, Initial Conditions, and Other Casting Parameters

Property	Value	Unit
$\Omega$	71	$rad\ s^{-1}$
$d$	65	mm
$d_C$	2	mm
$L$	165	mm
$R$	400	mm
$T_{fill}$	1623 (1350)	$K\ (^{\circ}C)$
$T_{mold}$	433 (160)	$K\ (^{\circ}C)$

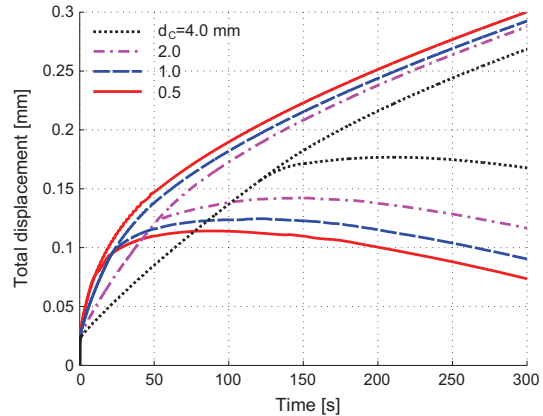


Fig. 5—Total displacements  $u$  at the cast-mold interface for different coating thicknesses of 0.5, 1, 2, and 4 mm. Bifurcation corresponds to the first appearance of the air gap.

air gap thickness  $d_a$ . Obviously, the air gap appears earlier in the case of a thin coating than that of a thick one. Consequently, the heat transfer coefficient  $h$  at the

interface will drop faster in the case of a thin coating than that of a thick one, which can be seen in Figure 6. The heat transfer coefficient  $h$  was simply calculated as

$$h = \frac{q}{T_S - T_M} = \frac{k_{ifc}}{dr_M + dr_S}. \quad [28]$$

For each configuration ( $d_C = 0.5, 1, 2,$  and  $4$  mm), the time evolution of the heat transfer coefficient  $h$  is, therefore, unique. Ultimately, it seems that after 300 seconds, the heat transfer coefficients are almost identical, close to  $200 \text{ W m}^{-2} \text{ K}^{-1}$ .

Similar tests with similar outputs were performed for different values of the rotation rate  $\Omega$  (50, 71, and  $90 \text{ rad s}^{-1}$ ). Naturally, the higher the centrifugal force, the better the contact between the casting and the mold. Concerning the elastic deformations of the mold, displacements  $u$  are larger at higher rotation rates  $\Omega$  (Figure 7). Higher centrifugal forces are also responsible for stronger and longer yielding of the partly solidified casting, which delays a formation of the air gap. Consequently, at a given instance, the heat transfer coefficient  $h$  is higher in the case of a higher rotation rate  $\Omega$  (Figure 8).

A similar study was carried out for different values of solidus temperature  $T_{sol}$  such that  $T_{liq} - T_{sol} = 10 \text{ K}, 50 \text{ K}, 100 \text{ K},$  and  $200 \text{ K}$  ( $10 \text{ }^\circ\text{C}, 50 \text{ }^\circ\text{C}, 100 \text{ }^\circ\text{C},$  and  $200 \text{ }^\circ\text{C}$ ). Although it is a somewhat intuitive, one could confidently state that the smaller the difference is, the earlier the air gap occurs. Again, we provide total displacements and heat transfer coefficients at the interface in Figures 9 and 10, respectively. Since coating parameters are fixed this time, initial heat transfer coefficients are all identical, equal to  $1000 \text{ W m}^{-2} \text{ K}^{-1}$ . Later, they significantly deviate. While the curves referring to mold displacements at the interface have a similar trend, indicating a continuous thermoelastic expansion of the mold, those corresponding to casting displacements exhibit more complex scenarios due to the combination of plastic and elastic deformations. In

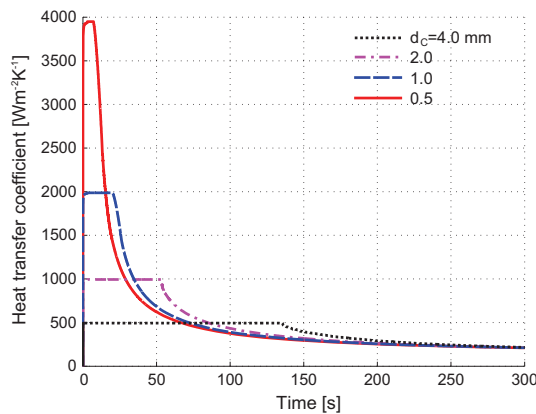


Fig. 6—Heat transfer coefficients  $h$  at the cast-mold interface for different coating thicknesses of 0.5, 1, 2, and 4 mm. Before the air gap is formed,  $h$  is constant defined as  $k_C d_C$ .

METALLURGICAL AND MATERIALS TRANSACTIONS B

Figure 9, e.g., the dash-dot line representing  $T_{liq} - T_{sol} = 200 \text{ K}$  ( $200 \text{ }^\circ\text{C}$ ) indicates the yielding of the casting material within the entire time span simulated. On the contrary, the dash line  $T_{liq} - T_{sol} = 50 \text{ K}$  ( $50 \text{ }^\circ\text{C}$ ) displays only slight yielding in the beginning, immediately followed by thermoelastic contraction.

Although the quantities calculated at the interface, such as the air gap thickness  $d_a$  and the heat transfer coefficient  $h$ , are of primary interest here, the numerical model also provides other quantities such as stresses and elastic/plastic strains. In Figure 11, a typical example of temperature and strains appears at 50 seconds. The gray zone on the right represents the mold. The rest on the left belongs to the casting. A temperature drop can be seen at the interface due to a large thermal resistance. As the time proceeds, total strains grow quite uniformly throughout the entire thickness of the mold. The same applies also to the casting but only at the early stage. Later, when the casting is partly solidified and the yield

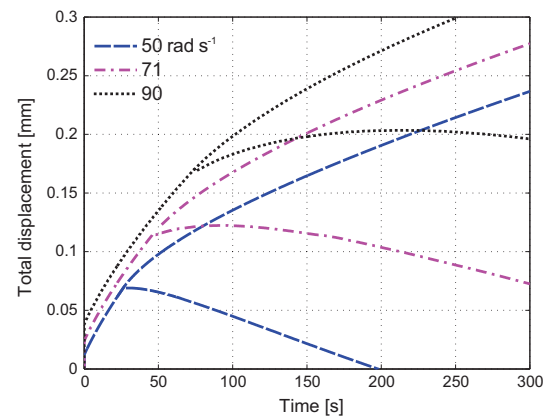


Fig. 7—Total displacements  $u$  at the cast-mold interface for different values of rotation rate  $\Omega$  such that  $\Omega = 50, 71, 90 \text{ rad s}^{-1}$ .

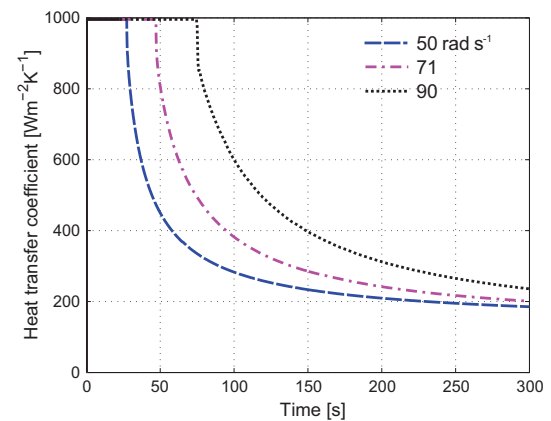


Fig. 8—Heat transfer coefficients  $h$  at the cast-mold interface for different values of rotation rate  $\Omega$  such that  $\Omega = 50, 71,$  and  $90 \text{ rad s}^{-1}$ .

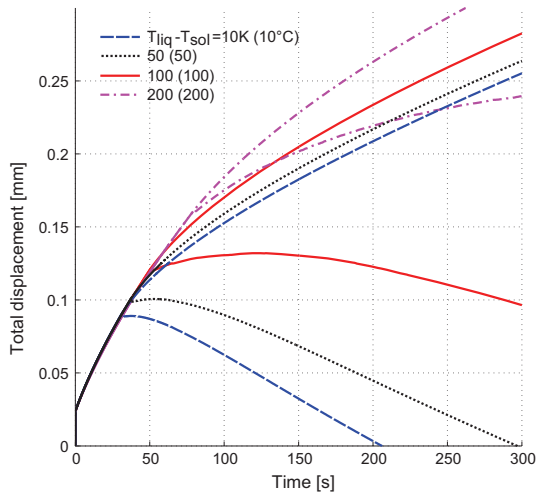


Fig. 9—Total displacements  $u$  at the cast-mold interface for different values of solidus temperature  $T_{sol}$  such that  $T_{liq} - T_{sol} = 10$  K, 50 K, 100 K, and 200 K (10 °C, 50 °C, 100 °C, and 200 °C).

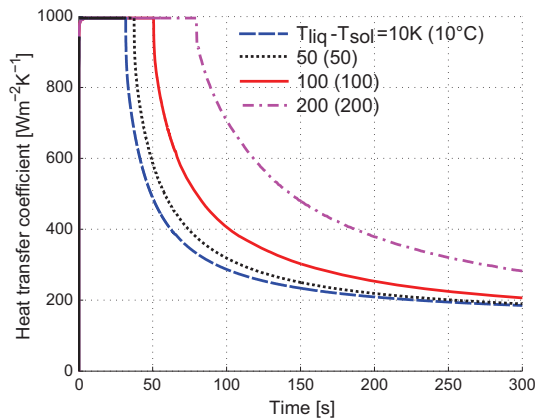


Fig. 10—Heat transfer coefficients  $h$  at the cast-mold interface for different values of solidus temperature  $T_{sol}$  such that  $T_{liq} - T_{sol} = 10$  K, 50 K, 100 K, and 200 K (10 °C, 50 °C, 100 °C, and 200 °C).

strength  $Y$  increased, total strains start dropping and the casting contracts consequently.

In addition to strains (Figure 11), stresses are shown in Figure 12. A typical distribution of stresses can be seen in the mold. While the radial stresses are exclusively compressive, the tangential stresses are compressive close to the inner surface of the mold and become tensile as they approach the outer surface of the mold. The greatest stresses the mold must withstand are naturally located at the inner surface due to a sudden temperature loading. In this particular case (Figure 12), they do, in

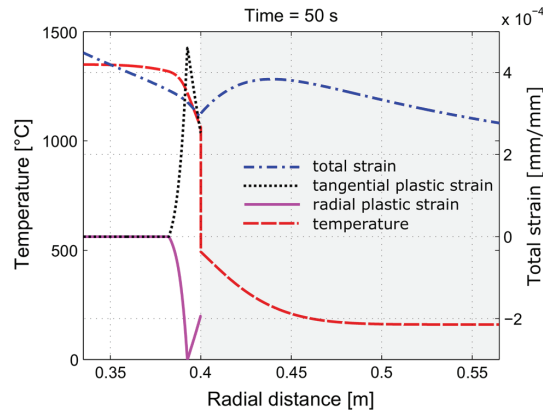


Fig. 11—Distribution of strains and temperature in the radial direction for the case with the coating thickness  $d_C$  of 2.0 mm at 50 s. The zones in white and gray stand for the casting and the mold, respectively.

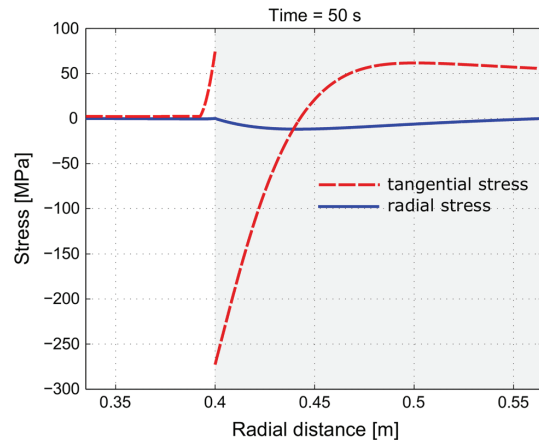


Fig. 12—Distribution of radial and tangential stresses for the case with the coating thickness  $d_C$  of 2.0 mm at 50 s.

fact, reach the yield strength of the material. After several casting cycles, a thermal loading would most likely lead to the formation of fire cracks.<sup>[61]</sup> Concerning stresses in the casting, at the early stage of solidification, they are within the temperature-dependent envelope of the yield strength. The (semi-)solid part of the casting close to the mold can already hold some stresses, whereas the liquid part remains stress free. At later stages of the casting, the stresses in the casting are well below the yield strength and only the elastic loading is present. When the casting procedure is finished and the temperature field becomes uniform, residual stresses remain in the casting. An analysis of stresses and strains is, however, beyond the scope of the present article.

#### IV. CONCLUSIONS

In centrifugal casting simulations, exponential functions are generally used to describe the heat transfer coefficient at the cast-mold interface, varying due to the air gap formation. Such functions contain empirical constants, which must be carefully specified. Unfortunately, this is not an easy task. An experiment alone is not sufficient to determine such constants, and computationally expensive inverse methods should be employed, which is, however, rarely the case. A literature survey performed here reveals an expansive scatter of data used in current and previous research. In the present study, we offer an alternative of calculating an air gap thickness and the corresponding heat transfer coefficient at the interface. The heat transfer model is coupled with a plane stress model, taking into account thermoelastic stresses, centrifugal forces, plastic deformations, and a temperature-dependent Young's modulus. Several numerical tests were performed for different coating thicknesses  $d_C$ , rotation rates  $\Omega$ , and solidus temperatures  $T_{sol}$ . Results were analyzed in the sense of comparing heat transfer coefficients at the interface and air gap thicknesses as a function of time. The numerical model developed here helps demonstrate that the scenario at the interface is unique for each set of parameters. Therefore, deploying any of the exponential functions that explicitly describe the thermal resistance at the cast-mold interface will always give rise to the question about the actual value of empirical constants used in that particular function. Although the material properties taken for this study do not strictly correspond to any particular material, they are obviously not far from material properties of common steels and coatings, and the results obtained here appear to be entirely reasonable and meaningful. In the near future, we plan to verify the current numerical approach against the results obtained from the inverse task run with the experimental data. Finally, possible room for improvement of the presented model remains. For example, some kind of implicit coupling between the heat transfer model and the plane stress model would be beneficial and might even be necessary in order to maintain numerical stability (or suppress unphysical oscillations of calculated displacements), especially at higher cooling rates, *e.g.*, when an air gap is being just formed. In addition, the optimization loop involved in the loading step, *i.e.*, the process of calculating the plastic strains could also be further improved.

#### ACKNOWLEDGMENTS

Open access funding provided by Montanuniversity Leoben. Financial support from the Austrian Federal Government (in particular, from the Bundesministerium fuer Verkehr, Innovation und Technologie and the Bundesministerium fuer Wirtschaft, Familie und Jugend) and the Styrian Provincial Government, represented by Oesterreichische Forschungsfoerderungsgesellschaft

mbH and by Steirische Wirtschaftsforderungsgesellschaft mbH, within the research activities of the K2 Competence Centre on "Integrated Research in Materials, Processing and Product Engineering," operated by the Materials Center Leoben Forschung GmbH in the framework of the Austrian COMET Competence Centre Programme, is gratefully acknowledged. This work is also financially supported by the Eisenwerk Sulzau-Werfen R. & E. Weinberger AG.

#### OPEN ACCESS

This article is distributed under the terms of the Creative Commons Attribution 4.0 International License (<http://creativecommons.org/licenses/by/4.0/>), which permits unrestricted use, distribution, and reproduction in any medium, provided you give appropriate credit to the original author(s) and the source, provide a link to the Creative Commons license, and indicate if changes were made.

#### NOMENCLATURE

[...] $C$	Subscript referring to the coating
[...] $M$	Subscript referring to the mold
[...] $S$	Subscript referring to the casting
$c_p$	Specific heat ( $J kg^{-1} K^{-1}$ )
$d$	Casting thickness (mm)
$d_a$	Air gap thickness (mm)
$d_C$	Coating thickness (mm)
$E$	Young's modulus (Pa)
$g_s$	Solid fraction
$h$	Heat transfer coefficient at the interface ( $W m^{-2} K^{-1}$ )
$h_0$	Initial heat transfer coefficient at the interface ( $W m^{-2} K^{-1}$ )
$h_f$	Final heat transfer coefficient at the interface ( $W m^{-2} K^{-1}$ )
$h_a$	Heat transfer coefficient between the casting and the coating ( $W m^{-2} K^{-1}$ )
$k$	Thermal conductivity ( $W m^{-1} K^{-1}$ )
$k_a$	Effective thermal conductivity of the air gap ( $W m^{-1} K^{-1}$ )
$k_{a,phys}$	Thermal conductivity of air ( $W m^{-1} K^{-1}$ )
$k_C$	Thermal conductivity of the coating ( $W m^{-1} K^{-1}$ )
$k_{ifc}$	Effective thermal conductivity of the control volume built of the mold, coating, air gap, and casting ( $W m^{-1} K^{-1}$ )
$L$	Thickness of the mold (m)
$L_f$	Latent heat of solidification ( $J kg^{-1}$ )
$N$	Number of grid points
$P$	Set of yielding points
$q$	Heat flux through the interface ( $W m^{-2}$ )
$q_0$	Initial heat flux through the interface (only coating present) ( $W m^{-2}$ )
$r$	Radial distance (mm)
$r_i$	Inner radius of the casting (mm)
$r_o$	Outer radius of the mold (mm)

$R$	Inner radius of the mold–radius of the interface (mm)
$s$	Solidified thickness of the casting (mm)
$t$	Time (s)
$t_0$	Time of solidification initiation (s)
$T$	Temperature (K (°C))
$T_{\text{fill}}$	Initial temperature of the liquid metal-filling temperature (K (°C))
$T_{\text{liq}}$	Liquidus temperature of the casting material (K (°C))
$T_{\text{mold}}$	Initial temperature of the mold (K (°C))
$T_{\text{sol}}$	Solidus temperature of the casting material (K (°C))
$T^*$	Temperature between the coating and the air gap (Fig. 1) (K (°C))
$T'_M$	Temperature between the mold and the coating (K (°C))
$T'_S$	Temperature between the casting and the air gap (K (°C))
$u$	Radial displacement (mm)
$Y$	Yield strength (Pa)

#### GREEK SYMBOLS

$\alpha$	Thermal expansion coefficient (K <sup>-1</sup> )
$\beta$	Damping coefficient
$\gamma$	Constant exponent
$\epsilon_r$	Total strains in radial direction (mm mm <sup>-1</sup> )
$\epsilon_t$	Total strains in tangential direction (mm mm <sup>-1</sup> )
$\epsilon_r^p$	Plastic strains in radial direction (mm mm <sup>-1</sup> )
$\epsilon_t^p$	Plastic strains in tangential direction (mm mm <sup>-1</sup> )
$\frac{\epsilon^p}{\epsilon^p}$	Effective plastic strain (mm mm <sup>-1</sup> )
$\epsilon$	Radiative emissivity
$\nu$	Poisson's ratio
$\rho$	Density (kg m <sup>-3</sup> )
$\sigma_r$	Radial stress (Pa)
$\sigma_t$	Tangential stress (Pa)
$\bar{\sigma}$	von Mises (effective stress) (Pa)
$\sigma$	Stefan–Boltzmann constant (W m <sup>-2</sup> K <sup>-4</sup> )
$\Omega$	Rate of rotation (rad s <sup>-1</sup> )

#### REFERENCES

1. H. Esaka, K. Kawai, H. Kaneko, and K. Shinozuka: *IOP Conference Series: Materials Science and Engineering*, 2012, vol. 33, p. 012041.
2. S. Wei: *ASM Int.*, 2008, vol. 15, pp. 667–73.
3. P. Kapranos, C. Carney, A. Pola, and M. Jolly: *Compr. Mater. Process.*, 2014, vol. 5, pp. 39–67.
4. M. Yuan, L. Cao, Y. Xu, and X. Song: *Model. Num. Simul. Mater. Sci.*, 2014, vol. 4, pp. 20–24.
5. E. Kaschnitz: *IOP Conference Series: Materials Science and Engineering*, 2012, vol. 33, p. 012031.
6. T.C. Lebeau: Master's Thesis, University of Alabama, Birmingham, AL, 2008, p. 35.
7. K.S. Keerthi Prasad, M.S. Murali, and P.G. Mukunda: *Front. Mater. Sci. China*, 2010, vol. 4, pp. 103–111.
8. S.-L. Lu, F.-R. Xiao, S.-J. Zhang, Y.-W. Mao, and B. Liao: *Appl. Therm. Eng.*, 2014, vol. 73, pp. 512–21.
9. D. McBride, N.J. Humphreys, T.N. Croft, N.R. Green, M. Cross, and P. Withey: *Comput. Fluids*, 2013, vol. 82, pp. 63–72.
10. J. Bohacek, A. Kharicha, A. Ludwig, and M. Wu: *ISIJ Int.*, 2014, vol. 54, pp. 266–74.
11. J. Bohacek, A. Kharicha, A. Ludwig, and M. Wu: *Appl. Math. Comput.*, 2015, vol. 267, pp. 179–94.
12. N. Song, Y. Luan, Y. Bai, Z.A. Xu, X. Kang, and D. Li: *J. Mater. Sci. Technol.*, 2012, vol. 28, pp. 147–54.
13. H. Fu, Q. Xiao, and J. Xing: *Mater. Sci. Eng. A*, 2008, vol. 479, pp. 253–60.
14. L. Drenchev, J. Sobczak, S. Malinov, and W. Sha: *Model. Simul. Mater. Sci. Eng.*, 2003, vol. 11, pp. 651–74.
15. J.A. Hines: *Metall. Mater. Trans. B*, 2004, vol. 35B, pp. 299–311.
16. W.D. Griffiths and R. Kayikci: *J. Mater. Sci.*, 2007, vol. 42, pp. 4036–43.
17. C.P. Hallam and W.D. Griffiths: *Metall. Mater. Trans. B*, 2004, vol. 35B, pp. 721–33.
18. Z. Xu, N. Song, R.V. Tol, Y. Luan, and D. Li: *IOP Conference Series: Materials Science and Engineering*, 2012, vol. 33, p. 012030.
19. J.W. Gao and C.Y. Wang: *Mater. Sci. Eng. A*, 2000, vol. 292, pp. 207–15.
20. K. Cook, B. Wu, and R.G. Reddy: *Int. J. Manuf. Sci. Prod.*, 2006, vol. 17, pp. 48–59.
21. J. Bohacek, A. Kharicha, A. Ludwig, and Wu M: *IOP Conference Series: Materials Science and Engineering*, 2012, vol. 33, p. 012032.
22. N.J. Humphreys, D. McBride, D.M. Shevchenko, T.N. Croft, P. Withey, N.R. Green, and M. Cross: *Appl. Math. Model.*, 2013, vol. 37, pp. 7633–43.
23. S.R. Chang, J.M. Kim, and C.P. Hong: *ISIJ Int.*, 2001, vol. 41, pp. 738–47.
24. C.G. Kang, P.K. Rohatgi, C.S. Narendranath, and G.S. Cole: *ISIJ Int.*, 1994, vol. 34, pp. 247–54.
25. C.G. Kang and P.K. Rohatgi: *Metall. Mater. Trans. B*, 1996, vol. 27B, pp. 277–85.
26. Y. Ebisu: *AFS Trans.*, 1977, pp. 643–54.
27. Kamlesh: Ph.D. Thesis, BVM Engineering College, Gujarat, India, 2001, p. 35.
28. L. Lajoie, and M. Suery: *Proc. Int. Symp. on Advances in Cast Reinforced Metal Composites*, ASM International, Chicago, IL, 1988, pp. 15–20.
29. P.S.S. Raju and S.P. Mehrotra: *Mater. Trans. JIM*, 2000, vol. 41, pp. 1626–35.
30. L. Drenchev, J. Sobczak, S. Malinov, and W. Sha: *Model. Simul. Mater. Sci. Eng.*, 2003, vol. 11, pp. 635–49.
31. E. Panda, D. Mazumdar, and S.P. Mehrotra: *Metall. Mater. Trans. A*, 2006, vol. 37A, pp. 1675–87.
32. L. Nastac: *ISIJ Int.*, 2014, vol. 54 (6), pp. 1294–1303.
33. S. Vacca, M.A. Martorano, R. Heringer, and M. Boccacini, Jr: *Metall. Mater. Trans. A*, 2015, vol. 46A, pp. 2238–48.
34. F. Susac, K. Ohura, M. Banu, and A. Makinouchi: *VCAD System Res.*, 2009, pp. 69–70.
35. H.M. Sahin, K. Kocatepe, R. Kayikci, and N. Akar: *Energy Convers. Manag.*, 2006, vol. 47, pp. 19–34.
36. A.F. Ilkhchy, N. Varahraam, and P. Davami: *Iran. J. Mater. Sci. Eng.*, 2012, vol. 9, pp. 11–20.
37. J.V. Beck, B. Blackwell, and C. Clair: *Inverse Heat Conduction: Ill-Posed Problems*, Wiley, New York, NY, 1985.
38. J. Mahmoudi: *Int. J. Cast. Met. Res.*, 2006, vol. 19, pp. 223–36.
39. B. Coates and S.A. Argyropoulos: *Metall. Mater. Trans. B*, 2007, vol. 38B, pp. 243–55.
40. M.A. Taha, N.A. El-Mahallawy, M.T. El-Mestekawi, and A.A. Hassan: *Mater. Sci. Technol.*, 2001, vol. 17, pp. 1093–1101.
41. J. Kron: Ph.D. Thesis, Royal Institute of Technology, Stockholm, 2004, p. 15.
42. J. Kron, A. Lagerstedt, and H. Frederiksson: *Int. J. Cast. Met. Res.*, 2005, vol. 18, pp. 29–40.
43. A. Lagerstedt: Ph.D. Thesis, Royal Institute of Technology, Stockholm, 2004, p. 41.
44. K. Schwerdtfeger, M. Sato, and K.-H. Tacke: *Metall. Mater. Trans. B*, 1998, vol. 29B, pp. 1057–68.
45. J. Kron, M. Bellet, A. Ludwig, B. Pustal, J. Wendt, and H. Fredriksson: *Int. J. Cast. Met. Res.*, 2004, vol. 17, pp. 295–310.
46. M. Trovant and S.A. Argyropoulos: *Can. Metall. Q.*, 1998, vol. 37, pp. 185–96.
47. R.K. Nayak and S. Sundarraj: *Metall. Mater. Trans. B*, 2010, vol. 41B, pp. 151–60.

48. A. Kandil, A.A. El-Kady, and A. El-Kafrawy: *Int. J. Mech. Sci.*, 1995, vol. 37, pp. 721–32.
49. X.-L. Gao: *Int. J. Solid Struct.*, 2003, vol. 40, pp. 6445–55.
50. A. Loghman and M.A. Wahab: *J. Press. Vess.-Trans. ASME*, 1994, vol. 116, pp. 105–09.
51. J. Perry and J. Aboudi: *J. Press. Vess.-Trans. ASME*, 2003, vol. 125, pp. 248–52.
52. G.H. Geiger and D.R. Poirier: *Transport Phenomena in Metallurgy*, Addison-Wesley Publishing Company, Reading, MA, 1973, p. 396.
53. S. Seghir-Ouali, D. Saury, S. Harmand, O. Phillipart, and D. Laloy: *Int. J. Therm. Sci.*, 2006, vol. 45, pp. 1166–78.
54. S. Harmand, J. Pelle, S. Poncet, and I.V. Shevchuk: *Int. J. Therm. Sci.*, 2013, vol. 67, pp. 1–30.
55. V.R. Voller and C.R. Swaminathan: *Num. Heat Transfer B*, 1991, vol. 19, pp. 175–89.
56. J. Bohacek, A. Kharicha, A. Ludwig, M. Wu, E. Karimi-Sibaki, A. Paar, M. Brandner, L. Elizondo, and T. Trickl: *Appl. Math. Comp.*, 2017, vol. 319 (C), pp. 301–17.
57. T.F. Coleman and Y. Li: *SIAM J. Optimiz.*, 1996, vol. 6, pp. 418–45.
58. T.F. Coleman and Y. Li: *Math. Program.*, 1994, vol. 67, pp. 189–224.
59. S.J. Orfanidis: *Introduction to Signal Processing*, Prentice-Hall, Englewood Cliffs, NJ, 1996.
60. R. Brockenbrough and F. Merrit: *Structural Steel Designer's Handbook*, 5th ed., McGraw-Hill Education, New York, NY, 2011.
61. A. Weronki and T. Hejwowski: *Thermal Fatigue of Metals*, Marcel Dekker Inc., New York, NY, 1991, p. 223.

## 2.5 Software for industry

As mentioned in section 2.3, a Graphical User Interface (GUI) was developed in MATLAB. The (non-)hydrostatic solver forms the core of the GUI. The post-processing must be done in PARAVIEW with templates. The GUI is simple to control and intuitive. From the following figures, the workflow becomes apparent.

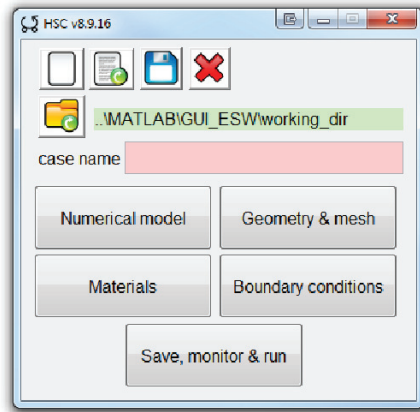


Fig. 2.5: The GUI's main panel.

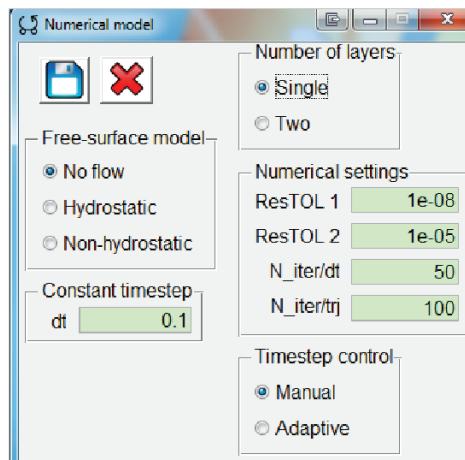


Fig. 2.6: Step 1: solver options

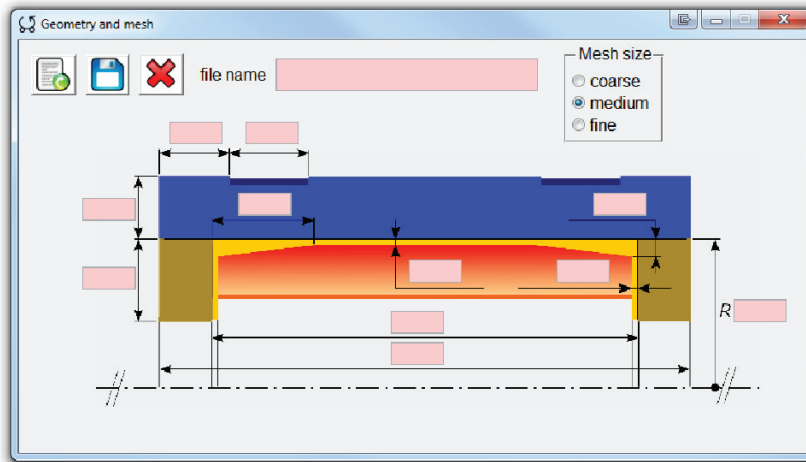


Fig. 2.7: Step 2: setting up the dimensions and the mesh.

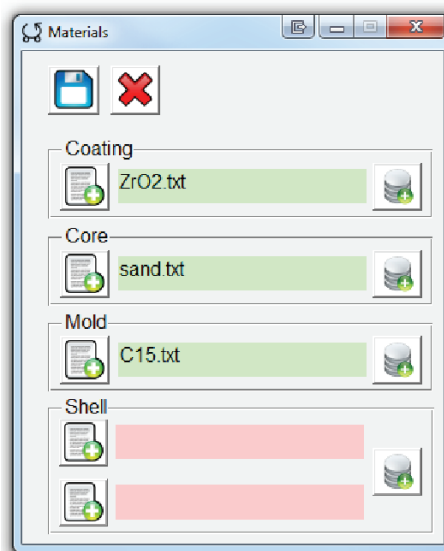


Fig. 2.8: Step 3: reading material from database (or creating a new material).

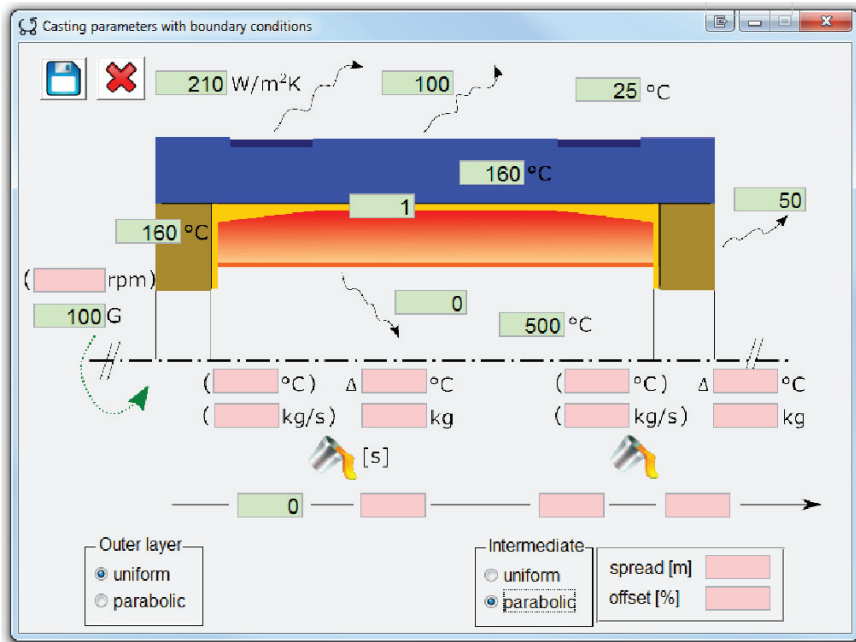


Fig. 2.9: Step 4: imposing initial and boundary conditions.

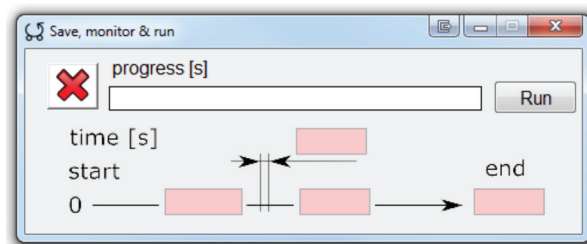


Fig. 2.10: Step 5: Run simulation and save data in *vtk* format.

# Conclusions

The present thesis hopefully coherently delivers to the reader knowledge about the *horizontal centrifugal casting* of rolls collected during projects funded by the Austrian COMET Competence Centre Programme between years 2010 and 2020. The research was mainly focused on development of numerical models of the whole casting process.

Theoretical background, practical aspects and common problems served as a first input for model developments.

When 3D *Volume of Fluid* models prepared in ANSYS FLUENT turned out to be computationally very expensive, the idea about modifying *shallow water equations* (SWE) emerged. A trick of solving SWE by using the *Euler-Euler model* was applied. Despite having a comprehensive model of horizontal centrifugal casting, several drawbacks were identified, which eventually led to development of more accurate and much faster approximate Riemann solver. The main advantage was that a 3D scenario about spreading the liquid metal along with a gradually solidifying shell could be captured in a fair amount of time. However, some missing parts of physics and a certain pressure by the industry partner resulted into a development of a 2D *free-surface model* based on the full Navier-Stokes equations, which was eventually incorporated into a user-friendly graphical-user interface. The code was further extended to consider a shrinkage of the solidifying shell.

The numerical model is able to capture various wave patterns on the free-surface that interacts with the solidifying liquid metal. The numerical model amply demonstrates the oscillating trajectory of an equiaxed crystal carried by the melt. The numerical can simulate the whole horizontal centrifugal casting process including pouring the outer (first) layer as well as the intermediate (second) layer until solidification is finished.

The present work hopefully stands as a good starting point for someone who is going to start with CFD simulations of horizontal centrifugal casting or simulations of rotating rotating flows in general.



# Bibliography

- [1] KURZ W., FISHER D.: Fundamentals of Solidification, *Trans. Tech. Publications*, 4th edition: Aedermannsdorf, 1998.
- [2] DANTZIG J., RAPPAZ M.: Solidification, *EPFL Press*: Lausanne, 2009.
- [3] BOUSSINESQ, J.: Theorie Analytique de la Chaleur, vol. II., *Gauthier-Villars*: Paris, 1903.
- [4] CHILDS P.R.N.: Rotating Flow: Chapter 2 - Laws of Motion, *Butterworth-Heinemann*: Oxford, 2011, 17-52.
- [5] LOPEZ J.M., MARQUES F., AVILA M: The Boussinesq approximation in rapidly rotating flows, *Journal of Fluid Mechanics* 737, 2013, 56-77.
- [6] DENTIS: Taylor-Couette Flow (Ultra Laminar Flow) - Smarter Every Day 217 Behind the Scenes, *Retrieved from <<https://www.youtube.com/watch?v=57IMufyoCnQ>>* on 21 May 2019.
- [7] FENSTERMACHER P., SWINNEY H.L., GOLLUB J.P.: Dynamical instabilities and the transition to chaotic Taylor vortex flow, *Journal of Fluid Mechanics* 94, 1979, 103-128.
- [8] TENG H., LIU N., LIU X., KHOMAMI B.: Direct numerical simulation of Taylor-Couette flow subjected to a radial temperature gradient, *Physics of fluids* 27, 2015, 125101.
- [9] LOPEZ J. M., MARQUES F., AVILA M.: Conductive and convective heat transfer in fluid flows between differentially heated and rotating cylinders, *International Journal of Heat and Mass Transfer* 90, 2015, 959-967.
- [10] DYAKOVA V., POLEZHAEV D.: Oscillatory and Steady Flows in the Annular Fluid Layer inside a rotating Cylinder, *Shock and Vibration* 2016, 2015, 162368.
- [11] YANG Y., OSTILLA-MONICO R., WU J., ORLANDI P.: Inertial waves and mean velocity profiles in a rotating pipe and a circular annulus with axial flow, *Phys. Rev. E* 91, 2015, 013015.
- [12] 62. IVANOVA A.A. KOZLOV V.G., CHIGRAKOV A.V.: Dynamics of a fluid in a rotating horizontal cylinder, *Fluid Dyn.* 39, 2004, 594-604.
- [13] O.M. PHILLIPS O.M.: Centrifugal waves, *J. of Fluid Mechanics* 21, 1959, 340-352.

- [14] ESAKA H., KAWAI K., KANEKO H., SHINOZUKA K.: In-situ observation of horizontal centrifugal casting using a high-speed camera, *emphIOP Conf. Ser.: Mater. Sci. Eng.* 33, 2012, 012041.
- [15] BEELEY P.: Foundry technology, *Butterworth-Heinemann*, Oxford: 2001, 639.
- [16] DYAKOVA V., KOZLOV V., POLEZHAEV D.: Ripple formation in a librating cylinder filled with fluid, *In Proceedings of XXIV ICTAM Montreal*, Canada, 2016, poster available
- [17] BRANDNER M., NYLEN T., ELIZONDO L., TRICKL T., PAAR A.: Roll grade application for HSM to reduce total cost of ownership, *In Proceedings of the 51 Rolling Seminar*, Brazil, 2014, 178-189.
- [18] EKSTROM T., NYGREN M.: SiAlON ceramics, *Journal of the American Ceramic Society* 75, 1992, 259-276.
- [19] DANZER R., LENGAUER M., ZLEPPNIG W., HARRER W.: Silicon nitrid tools for hot rolling of high-alloyed steel and superalloy wires - Load analysis and first practical tests, *International Journal of Materials Research* 98, 2007, 1104-1114.
- [20] BROOKS R. G., MOORE C., LEATHAM A. G., COOMBS J. S.: The Osprey process, *Powder Metallurgy* 20, 1977, 100-102.
- [21] BRANDNER M., ELIZONDO L., TRICKL T., PAAR A., HARDT S.: Roll grade application for HSM to reduce total cost of ownership, *In Proceedings of the 53 Rolling Seminar*, Brazil, 2016, 146-159.
- [22] LEVEQUE R. J.: Finite volume methods for hyperbolic systems, Cambridge University Press, New York, 2002, 447.
- [23] CASULLI V.: A semi-implicit finite difference method for non-hydrostatic free-surface flows, *Int. J. Numer. Methods Fluids* 30, 1999, 425-440.

## Author's publications on centrifugal casting

- [A1] BOHACEK J., KHARICHA A., LUDWIG A., WU M. ,KARIMI-SIBAKI E., PAAR A., BRANDNER M., ELIZONDO L., TRICKL T.: A (non-)hydrostatic free-surface numerical model for two-layer flows. *Applied Mathematics and Computation*, 319:301–317, 2018.
- [A2] BOHACEK J., KHARICHA A., LUDWIG A., WU M., KARIMI-SIBAKI E.: Heat Transfer Coefficient at Cast-Mold Interface During Centrifugal Casting: Calculation of Air Gap, *Metallurgical and Materials Transactions B: Process Metallurgy and Materials Processing Science* 49(3), 2018, 1421-1433.
- [A3] BOHACEK J., KHARICHA A., LUDWIG A., WU M. , PAAR A., BRANDNER M., ELIZONDO L., TRICKL T.: Free-surface flow in horizontally rotating cylinder: Experiment and simulation. *IOP Conference Series: Materials Science and Engineering*, 143(1), 2016.
- [A4] BOHACEK J., KHARICHA A., LUDWIG A., WU M.: An approximate Riemann solver for shallow water equations and heat advection in horizontal centrifugal casting, *Applied Mathematics and Computation* 267, 2015, 179-194.
- [A5] KHARICHA A., BOHACEK J., LUDWIG A., WU M.: Modified Shallow Water Equations with Application for Horizontal Centrifugal Casting of Rolls, *Journal of Fluids Engineering, Transactions of the ASME* 137, 2015, 111105.
- [A6] BOHACEK J., KHARICHA A., LUDWIG A., WU M.: Simulation of horizontal centrifugal casting: Mold filling and solidification. *ISIJ International*, 54(2), 2014, 266-274.
- [A7] BOHACEK J., KHARICHA A., LUDWIG A., WU M.: Vibrations induced flow in a horizontal centrifugal casting. *Cfd Modeling and Simulation in Materials Processing*, 2012, 227-234.
- [A8] BOHACEK J., KHARICHA A., LUDWIG A., WU M.: Shallow water model for horizontal centrifugal casting, *IOP Conference Series: Materials Science and Engineering* 33, 2012, 012032.



## Authored and co-authored publications on other topics

- [C1] KARIMI-SIBAKI E., KHARICHA A., WU M., LUDWIG A., BOHACEK J.: A numerical investigation on the electrochemical behavior of  $CaO$  and  $Al_2O_3$  in the ESR slags. *Metallurgical and Materials Transactions B: Process Metallurgy and Materials Processing Science*, 51(3), 2020, 871-879.
- [C2] KARIMI-SIBAKI E., KHARICHA A., WU M., LUDWIG A., BOHACEK J.: A Parametric Study of the Vacuum Arc Remelting (VAR) Process: Effects of Arc Radius, Side-Arcing, and Gas Cooling *Metallurgical and Materials Transactions B: Process Metallurgy and Materials Processing Science*, 51(1), 2020, 222-235.
- [C3] KARIMI-SIBAKI E., KHARICHA A., VAKHRUSHEV A., WU M., LUDWIG A., BOHACEK J.: A volume of fluid (VOF) method to model shape change during electrodeposition, *Electrochemistry Communications*, 112, 2020, 106675.
- [C4] BOHACEK J., KHARICHA A., LUDWIG A., WU M., HOLZMANN T., KARIMI-SIBAKI E.: A gpu solver for symmetric positive-definite matrices vs. traditional codes. *Computers and Mathematics with Applications*, 78, 2019, 2933-2943.
- [C5] KARIMI-SIBAKI E., KHARICHA A., WU M., LUDWIG A., BOHACEK J.: Modeling electrochemical transport of ions in the molten  $CaF_2 - FeO$  slag operating under a DC voltage. *Applied Mathematics and Computation*, 357, 2019, 357-373.
- [C6] BOHACEK J., RAUDENSKY M., KARIMI-SIBAKI E.: Polymeric hollow fibers: Uniform temperature of Li-ion cells in battery modules, *Applied Thermal Engineering*, 159, 2019, 113940.
- [C7] BOHACEK J., RAUDENSKY M., KROULIKOVA T., KARIMI-SIBAKI E.: Polymeric hollow fibers: A supercompact cooling of li-ion cells. *International Journal of Thermal Sciences*, 146, 2019, 106060.
- [C8] KARIMI-SIBAKI E., KHARICHA A., ABDI M., WU M., LUDWIG A., BOHACEK J.: A dynamic mesh method to model shape change during electrodeposition. *Journal of the Electrochemical Society*, 166(12), 2019, D521-D529.
- [C9] KARIMI-SIBAKI E., KHARICHA A., WU M., LUDWIG A., BOHACEK J.: Confrontation of the Ohmic approach with the ionic transport approach for

- modeling the electrical behavior of an electrolyte. *Ionics*, 24(7), 2018, 2157-2165.
- [C10] KARIMI-SIBAKI E., KHARICHA A., WU M., LUDWIG A., BOHACEK J.: Contribution of an electro-vortex flow to primary, secondary, and tertiary electric current distribution in an electrolyte. *Journal of the Electrochemical Society*, 165(11), 2018, E604-E615.
- [C11] BOHACEK J., KOUTNA N., LUDWIG A., RODRIGUES C., KARIMI-SIBAKI E., KHARICHA A.: Simulation in metallurgy: Past achievements and future challenges. *27TH International Conference on Metallurgy and Materials (METAL)*, 2018, 28-33.
- [C12] KARIMI-SIBAKI E., KHARICHA A., WU M., LUDWIG A., BOHACEK J., HOLZGRUBER H., OFNER B., SCHERIAU A., KUBIN M.: A multiphysics model of the electroslag rapid remelting (ESRR) process. *Applied Thermal Engineering*, 130, 2018, 1062-1069.
- [C13] KHARICHA A., KARIMI-SIBAKI E., WU M., LUDWIG A., BOHACEK J.: Review on Modeling and Simulation of Electroslag Remelting. *Steel Research International*, 89(1), 2018.
- [C14] KARIMI-SIBAKI E., KHARICHA A., WU M., LUDWIG A., BOHACEK J.: Toward modeling of electrochemical reactions during electroslag remelting (ESR) process. *Steel Research International*, 88(5), 2017.
- [C15] KARIMI-SIBAKI E., KHARICHA A., BOHACEK J., WU M., LUDWIG A.: On Validity of Axisymmetric Assumption for Modeling an Industrial Scale Electroslag Remelting Process. *Advanced Engineering Materials*, 18(2), 2016, 224-230.
- [C16] KARIMI-SIBAKI E., KHARICHA A., BOHACEK J., WU M., LUDWIG A.: Transient melting of an ESR electrode. *IOP Conference Series: Materials Science and Engineering*, 143(1), 2016, 012003.
- [C17] KARIMI-SIBAKI E., KHARICHA A., BOHACEK J., WU M., LUDWIG A.: A dynamic mesh-based approach to model melting and shape of an esr electrode. *Metallurgical and Materials Transactions B: Process Metallurgy and Materials Processing Science*, 46(5), 2015, 2049-2061.
- [C18] ZAHRADNIK R., BOHACEK J., KOTRBACEK P.: Experimental investigation of heat transfer between hot air nozzle flow and cylinder. *EPJ Web of Conferences*, 25, 2012, 1-6.

- [C19] BOHACEK J., HORAK A., Numerical study of droplet dynamics impinging onto steel plate covered with scale layer. *Frontiers of Mechanical Engineering in China*, 5(4), 2010, 389–398.
- [C20] BOHACEK J.: Ejector type cooling nozzle. *Experimental Fluid Mechanics 2006, PROCEEDINGS*, 2006.



## List of symbols, quantities and abbreviations

$\vec{\Omega}$	angular velocity ( $\text{rad} \cdot \text{s}^{-1}$ )
$p$	static pressure (Pa)
$\Phi$	gravitational potential ( $\text{m}^2 \cdot \text{s}^{-2}$ )
$\nu$	kinematic viscosity ( $\text{m}^2 \cdot \text{s}^{-1}$ )
$\vec{g}$	gravitational acceleration ( $\text{m} \cdot \text{s}^{-2}$ )
$z$	vertical coordinate (m)
$\vec{f}$	body forces ( $\text{m} \cdot \text{s}^{-1}$ )
$\rho$	fluid density ( $\text{kg} \cdot \text{m}^{-3}$ )
$\rho_0$	reference fluid density ( $\text{kg} \cdot \text{m}^{-3}$ )
$\rho'$	fluid density fluctuations ( $\text{kg} \cdot \text{m}^{-3}$ )
$Ri$	Richardson number (-)
$Ta_m$	Taylor number (-)
$Ta_{cr}$	critical Taylor number (-)
<b>lhs</b>	left-hand side